FAKULTÄT FÜR PHYSIK

Low-mass dielectron production in proton–proton collisions at $\sqrt{s} = 13$ TeV with ALICE

Ivan Vorobyev

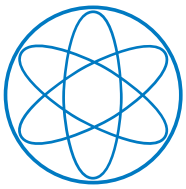

DER TECHNISCHEN UNIVERSITÄT MÜNCHEN

FACHBEREICH: DENSE AND STRANGE HADRONIC MATTER (E62)

2018

FAKULTÄT FÜR PHYSIK

DER TECHNISCHEN UNIVERSITÄT MÜNCHEN

FACHBEREICH: DENSE AND STRANGE HADRONIC MATTER (E62)

Low-mass dielectron production
in proton–proton collisions at $\sqrt{s} = 13$ TeV with ALICE

Ivan Vorobyev

Vollständiger Abdruck der von der Fakultät für Physik der Technischen Universität München zur Erlangung des akademischen Grades eines

Doktors der Naturwissenschaften (Dr. rer. nat.)

genehmigten Dissertation.

Vorsitzende:	Prof. Dr. Nora Brambilla
Prüfer der Dissertation:	1. Prof. Dr. Laura Fabbietti
	2. Prof. Dr. Elisa Resconi

Die Dissertation wurde am 17.09.2018 bei der Technischen Universität München eingereicht und durch die Fakultät für Physik am 01.10.2018 angenommen.

Abstract

Low-mass electron–positron pairs are a unique experimental tool to study the properties of the Quark-Gluon Plasma created in ultra-relativistic heavy-ion collisions at the CERN Large Hadron Collider (LHC). Such pairs are produced during all stages of the collision and carry the information about the whole space-time evolution of the system to the detector unperturbed by strong final-state interactions. The study of dielectron production in inelastic proton–proton (pp) collisions provides crucial vacuum reference needed for the interpretation of the results in heavy-ion collisions and a test of perturbative Quantum Chromodynamics (pQCD).

This work summarises the measurement of low-mass dielectron pairs in pp collisions at a centre-of-mass energy of $\sqrt{s} = 13$ TeV with the ALICE detector. The dielectron production is studied as a function of invariant mass and transverse momentum at midrapidity ($|y_{\mathrm{e}}| < 0.8$). The contributions from light-hadron decays can be calculated from their cross sections independently measured in pp collisions. Correlated electron pairs from semi-leptonic charm and beauty decays, which dominate in the intermediate mass region ($1.1 < m_{\mathrm{ee}} < 2.8$ GeV/c^2), are used to extract the charm and beauty cross sections integrated over all transverse momenta for the first time at this collision energy at midrapidity. The data are fit with templates from two different Monte Carlo event generators, Pythia and Powheg, leading to the following values of heavy-flavour production cross-sections: $\mathrm{d}\sigma_{\mathrm{c\bar{c}}}/\mathrm{d}y|_{y=0} = 974 \pm 138\,(\text{stat.}) \pm 140\,(\text{syst.}) \pm 214\,(\text{B.R.})\ \mu\mathrm{b}$ and $\mathrm{d}\sigma_{\mathrm{b\bar{b}}}/\mathrm{d}y|_{y=0} = 79 \pm 14\,(\text{stat.}) \pm 11\,(\text{syst.}) \pm 5\,(\text{B.R.})\ \mu\mathrm{b}$ using Pythia simulations and $\mathrm{d}\sigma_{\mathrm{c\bar{c}}}/\mathrm{d}y|_{y=0} = 1417 \pm 184\,(\text{stat.}) \pm 204\,(\text{syst.}) \pm 312\,(\text{B.R.})\ \mu\mathrm{b}$ and $\mathrm{d}\sigma_{\mathrm{b\bar{b}}}/\mathrm{d}y|_{y=0} = 48 \pm 14\,(\text{stat.}) \pm 7\,(\text{syst.}) \pm 3\,(\text{B.R.})\ \mu\mathrm{b}$ using Powheg. The difference observed between Pythia and Powheg based results points to different kinematic correlations of the heavy-quark pairs in the two generators. These values, whose uncertainties are fully correlated between the two generators, are consistent with extrapolations from lower energies based on pQCD calculations.

Recent studies of pp collisions with high charged-particle multiplicities showed surprising results similar to previous observations in heavy-ion collisions. Measurements of low-mass dielectrons could provide additional information regarding the underlying physics processes. This work compares the dielectron spectra in inelastic pp collisions and in collisions collected with high charged-particle multiplicities in various transverse-momentum intervals. The differences are consistent with the already mea-

sured multiplicity-dependent production of light and heavy hadrons at lower $\sqrt{s}$. The production of direct photons in inelastic and high-multiplicity collisions is also discussed. Upper limits on the contribution of direct photons to the inclusive photon spectrum are extracted at 90% confidence level and found to be in agreement with pQCD predictions.

Zusamenfassung

Massearme Elektron–Positron Paare sind ein einzigartiges experimentelles Werkzeug, um die Eigenschaften des Quark–Gluon Plasmas, das bei ultrarelativistischen Schwerionenkollisionen am CERN Large Hadron Collider (LHC) entsteht, zu untersuchen. Solche Paare werden in allen Stadien der Kollision erzeugt und tragen die Information über die gesamte Raum–Zeit Entwicklung des Systems ohne Störung durch die starke Wechselwirkung zum Detektor. Die Erforschung der Dielektronen in inelastischen Proton–Proton (pp) Kollisionen dient der Erstellung einer Vakuumreferenz, die für die Interpretation der Ergebnisse in Schwerionenkollisionen benötigt wird. Desweiteren kann man mit ihnen Berechnungen von pp Kollisionen mit pertubativer Quantenchromodynamik (pQCD) testen.

Diese Arbeit behandelt die Messung von massearmen Dielektronen in pp Kollisionen bei einer Kollisionsenergie von $\sqrt{s} = 13$ TeV mit dem ALICE Detektor. Die Produktion der Dielektronen wird als Funktion der invarianten Masse und des Transversalimpulses bei zentraler Rapidität untersucht ($|y_{\mathrm{e}}| < 0.8$). Der Beitrag von Zerfällen leichter Hadronen kann aus ihrer unabhängig gemessenen Produktion in pp Kollisionen berechnet werden. Korrelierte Elektronenpaare von semileptonischen Zerfällen der Charm und Beauty Hadronen, die das Massekontinuum im mittleren Massenbereich ($1.1 < m_{\mathrm{ee}} < 2.8$ GeV/c^2) dominieren, werden zur ersten Messung von Charm und Beauty Wirkungsquerschnitten bei dieser Kollisionsenergie und zentraler Rapidität verwendet. Die Daten werden mit Vorlagen aus zwei verschiedenen Monte-Carlo Ereignisgeneratoren, Pythia und Powheg, gefitted. Dies führt zu folgenden Wirkungsquerschnitten: $\mathrm{d}\sigma_{\mathrm{c\bar{c}}}/\mathrm{d}y|_{y=0} = 974 \pm 138\,(\mathrm{stat.}) \pm 140\,(\mathrm{syst.}) \pm 214\,(\mathrm{B.R.})\ \mu\mathrm{b}$ und $\mathrm{d}\sigma_{\mathrm{b\bar{b}}}/\mathrm{d}y|_{y=0} = 79 \pm 14\,(\mathrm{stat.}) \pm 11\,(\mathrm{syst.}) \pm 5\,(\mathrm{B.R.})\ \mu\mathrm{b}$ mit Pythia Simulationen und $\mathrm{d}\sigma_{\mathrm{c\bar{c}}}/\mathrm{d}y|_{y=0} = 1417 \pm 184\,(\mathrm{stat.}) \pm 204\,(\mathrm{syst.}) \pm 312\,(\mathrm{B.R.})\ \mu\mathrm{b}$ und $\mathrm{d}\sigma_{\mathrm{b\bar{b}}}/\mathrm{d}y|_{y=0} = 48 \pm 14\,(\mathrm{stat.}) \pm 7\,(\mathrm{syst.}) \pm 3\,(\mathrm{B.R.})\ \mu\mathrm{b}$ mit Powheg. Der beobachtete Unterschied zwischen Pythia- und Powheg-basierten Ergebnissen lässt sich auf unterschiedliche kinematische Korrelationen der schweren Quarkpaare in den beiden Generatoren zurückführen. Diese Werte, deren Unsicherheiten vollständig zwischen den beiden Generatoren korreliert sind, sind konsistent mit auf perturbativen QCD-Berechnungen basierten Extrapolationen von Messungen bei niedrigeren Energien.

Neuere Studien von pp Kollisionen mit hoher Multiplizität geladener Teilchen zeigten überraschende Ergebnisse ähnlich den Beobachtungen, die zuvor bei Schwerionenkol-

lisionen gemacht wurden. Die Messungen von Dielektronen könnten hier zusätzliche Information zu den grundliegenden physikalischen Prozessen liefern. Diese Arbeit vergleicht Dielektronenspektren in inelastischen pp Kollisionen und in solchen mit hoher Multiplizität geladener Teilchen in verschiedenen Transversalimpulsintervallen. Die Unterschiede stimmen mit der bereits gemessenen Multiplizitätsabhängigkeit der Produktion leichter und schwerer Hadronen überein. Die Produktion direkter Photonen in pp Kollisionen wird ebenfalls diskutiert. Obergrenzen für den Beitrag von direkten Photonen zum inklusiven Photonspektrum werden bei 90% Konfidenzniveau extrahiert und stimmen mit pQCD-Vorhersagen überein.

Contents

List of Figures

List of Tables

1 Introduction

According to our current knowledge, all interactions in nature are due to the four fundamental forces: gravitational, electromagnetic, weak and strong forces. While the first two act over large distances so that their effects can be directly observed in everyday life, the latter two become relevant only at the subatomic level. Mathematically, these interactions can be described as fields, which for all forces except for gravity are discrete quantum fields with the interactions mediated by elementary particles (so-called gauge bosons). The electromagnetic, weak and strong interactions between all known particles are incorporated into one theory — the Standard Model of particle physics, a quantum field gauge theory based on the symmetry group $G_{\mathrm{SM}} = SU(3)_{\mathrm{C}} \times SU(2)_{\mathrm{L}} \times U(1)_{\mathrm{Y}}$. Here $SU(3)_{\mathrm{C}}$ colour symmetry represents the strong sector of the Standard model — Quantum Chromodynamics (QCD) which describes the interactions of gluons with other quarks and gluons. The $SU(2)_{\mathrm{L}} \times U(1)_{\mathrm{Y}}$ part corresponds to the electroweak sector handling weak and electromagnetic interactions, where the subscript L indicates coupling only to left-handed fermions and weak hypercharge Y is the generator of $U(1)_{\mathrm{Y}}$ group.

At normal temperatures and nuclear matter densities, quarks and gluons are held together by the strong force inside hadrons — composite particles made of either three quarks (baryons) or of one quark and one antiquark (mesons). However, already in the 1960s it was pointed out that at high temperatures beyond some critical value nuclear matter cannot exist in the form of hadrons [1]. The heating of hadronic matter leads to an increase in the kinetic energies of particles and to the production of new states, and statistical-thermodynamical treatment of nuclear matter involving only hadrons breaks beyond some critical temperature T_{C}. Other early theoretical descriptions of nuclear matter, e. g. based on the model of strongly interacting particle in a finite region of

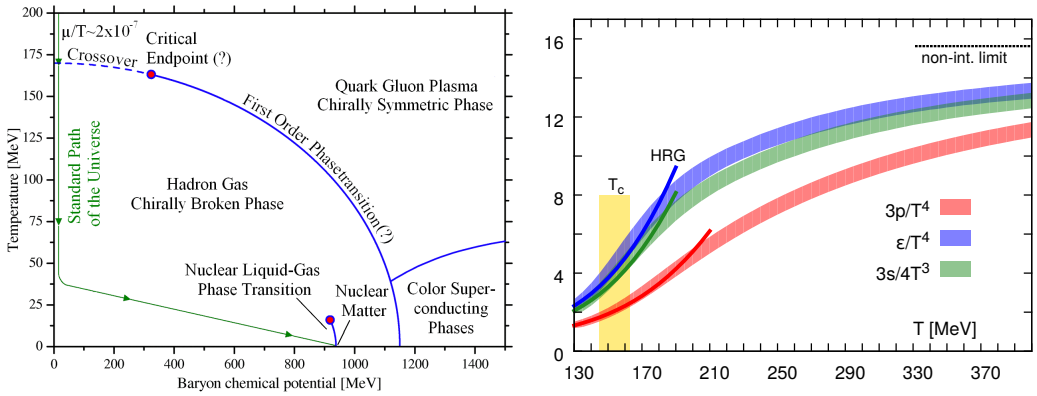

Figure 1.1: Left: schematic QCD phase diagram showing the phases of QCD matter at different temperatures and baryon chemical potentials [8]. The green line shows the commonly accepted evolution path of the Universe as calculated e. g. in [9]. Right: normalised pressure, energy density and entropy density as a function of the temperature [6]. The horizontal dashed line corresponds to the ideal gas limit for the energy density.

space to which fields are confined [2], also implied that at high temperatures and/or baryonic densities a state of heated and/or compressed nuclear matter must be described with partonic (quarks and gluons) degrees of freedom.

The properties of QCD matter can be described through thermodynamics. By analogy with the well-known example of the phase diagram for water, Fig. 1.1 (left) shows a schematic QCD phase diagram as a function of temperature T and baryon chemical potential μ_B, i. e. the amount of energy needed to introduce one additional baryon into the system. According to lattice QCD calculations [3–6], at temperatures[1] around $T \approx 155$ MeV $\approx 10^{12}$ K and $\mu_B \sim 0$ a new state of matter comprising deconfined quarks and gluons is formed. Such hot and dense (with the energy density exceeding $\epsilon \approx 1$ GeV/fm^3) state with net baryon density close to zero may have existed in the early Universe just few microseconds after the Big Bang. In the regime of high T and low μ_B, lattice QCD calculations indicate a smooth crossover from confined nuclear matter to a deconfined phase. At $T \sim T_C$, the normalised system pressure, energy density and entropy density rapidly rise and reach approximately constant values beyond this point (Fig. 1.1 right), which clearly indicates a crossover to a state with more degrees of freedom. However, in the regime of higher μ_B effective field theories are needed, and the order of the phase transition is extremely model dependent, see e. g. [7] for a review. A phase boundary between two states should end up therefore in critical point.

Exact details such as the existence of the critical point or the order of phase transition remain unknown. In the laboratory, the QCD phase diagram can be explored by means of heavy-ion collisions at various collision energies, which for a very short period of

[1] If not stated otherwise, the natural units of $\hbar = c = k_B = 1$ are used in this thesis.

time $\sim\mathcal{O}(10\,\mathrm{fm}/c)$ create a hot and/or dense strongly interacting medium. At lower collision energies, the physics of heavy-ion collisions is defined by large nuclear stopping effect, thus producing hadronic matter at high μ_B and lower T, whereas at relativistic energies, i. e. in regime when the total energy of colliding nuclei is much higher than their rest masses, colliding heavy ions are highly transparent and create hot medium with almost zero net baryon density. Since nuclei are extended objects, such collisions are also characterised in terms of "centrality", i. e. the degree of overlap of the colliding nuclei, which defines directly the volume of the interacting region and the geometrical properties of the collision, such as the number of participating nucleons and the number of binary nucleon–nucleon collisions. In central, head-on collisions, almost all incoming nucleons can contribute their energy to a collision, and the medium is expected to have higher temperatures and a longer lifetime. In peripheral collisions, nuclei only slightly overlap, so a medium is expected to have a smaller lifetime and temperature. In the field of heavy-ion physics, it is customary to introduce the concept of the centrality of the collision, which provides an important tool to compare different measurements from various experiments with each other and with theoretical calculations.

Many experimental results clearly indicate that in relativistic heavy-ion collisions a new state of matter has been created — the Quark-Gluon Plasma (QGP), see e. g. [10, 11] for recent reviews. The name refers to the analogy with the conventional plasma, where nuclei and electrons, normally bound to atoms by electromagnetic forces, can move freely. The QGP is thought to consist of free quarks and gluons, otherwise confined inside hadrons at low temperatures and net baryon densities. In a QGP, quarks and gluons still strongly interact with each other, so the system does not reach an ideal gas approximation, which is also indicated by lattice QCD calculations in Fig. 1.1 (right). Among other properties, this system is characterised by large energy densities well above $\epsilon \approx 1\ \mathrm{GeV/fm}^3$ [12, 13] and by initial temperatures of several hundred MeV [14, 15]. A large elliptic flow is developed on a partonic level indicating early thermalisation of the medium (including heavy charm quarks) and its behaviour as almost perfect liquid with shear-viscosity to entropy-density ratio η/s close to the theoretical lower bound of $1/4\pi$ [13, 16–18]. Fig. 1.2 shows a sketch of the evolution of the system created in central relativistic heavy-ion collisions. However, the correct interpretation of the heavy-ion results would not be possible without extensive studies of the smaller collision systems such as proton–proton (pp) or proton–nucleus collisions. These studies provide necessary vacuum and cold-nuclear matter references for any modifications which can be seen in heavy-ion collisions, allowing us to distinguish the interesting phenomena related to the formation of QGP from other effects. Thanks to large energy transfers reached in the initial hard parton scattering, such studies are also an important medium-free test for perturbative QCD (pQCD) calculations.

Electromagnetic probes such as photons or dilepton pairs ($l^+l^- = \mathrm{e}^+\mathrm{e}^-$ or $\mu^+\mu^-$) have established themselves as a particularly useful experimental tool to study the prop-

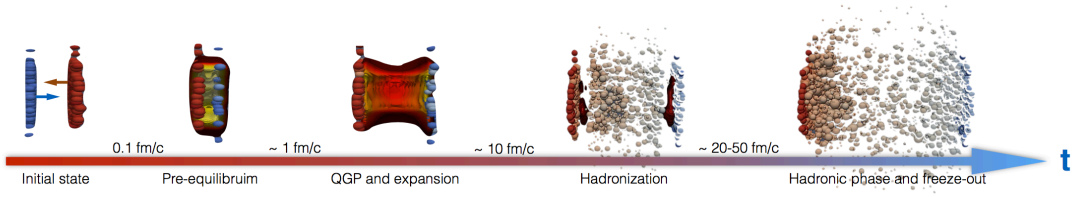

Figure 1.2: Evolution of the system created in relativistic central heavy-ion collisions. Time is advancing from the left to the right, the approximate time scale is shown for each stage. The sketch is based on the simulations by the MADAI Collaboration [19].

erties of the system created in heavy-ion collisions. Once emitted, they carry the information to the detector unaffected by strong final-state interactions with the surrounding hadronic medium, as sketched in Fig. 1.2. Dilepton pairs are created during all stages of heavy-ion collision via various processes with an approximate time ordering in the invariant mass of the dilepton pair: the earlier produced, the higher its invariant mass, thus allowing us to study the whole space-time evolution of the system.

The dielectron continuum is very rich in physics sources. A realistic simulation of the expected dielectron invariant mass spectrum from hadronic sources in pp collisions at the top LHC energy[2] of $\sqrt{s} = 13$ TeV is shown in Fig. 1.3. This simulation includes also the detector effects such as resolution and acceptance. In the low mass region ($m_{\mathrm{ee}} \lesssim 1$ GeV$/c^2$), the dielectron continuum is dominated by light-flavour meson decays, including resonance (e. g. $\rho \rightarrow \mathrm{e^+e^-}$) and Dalitz decays (e. g. $\pi^0 \rightarrow \gamma\mathrm{e^+e^-}$). The latter are in fact two-body decays with one intermediate (virtual) particle immediately decaying into two additional decay products, such as $\pi^0 \rightarrow \gamma\gamma^* \rightarrow \gamma\mathrm{e^+e^-}$. In the intermediate mass range ($1.1 \lesssim m_{\mathrm{ee}} \lesssim 2.8$ GeV$/c^2$), the continuum is dominated by correlated dielectrons from semi-leptonic decays of charm and beauty hadrons, which provide complementary information about heavy-quark production. At higher invariant masses, dielectron studies give also insight into the production of bound heavy-flavour states such as the J$/\psi$ meson, which is a bound state of a charm quark and a charm anti-quark.

Various modifications of the dielectron spectrum in heavy-ion collisions provide a unique information about the properties of hot and dense system created in these collisions. On top of ordinary Dalitz and resonance decays, thermal black-body radiation (from both partonic and hadronic phases [20, 21]) is of particular interest as it contains the information about the temperature of the system created in collisions. In the low mass region, the dielectron invariant-mass distribution is also sensitive to medium modifications of the spectral function of short-lived vector mesons that are linked to the predicted restoration of chiral symmetry at high temperatures [20]. In the intermediate mass range,

[2]The definitions of kinematic variables used in this thesis can be found in Appendix A.

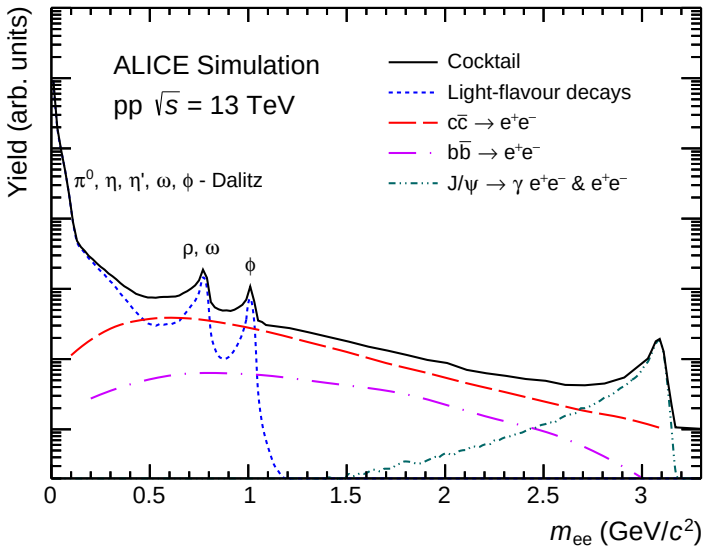

Figure 1.3: Expected contributions to the dielectron mass spectrum from hadron decays in pp collisions at $\sqrt{s} = 13$ TeV.

the mass continuum produced by semi-leptonic heavy-flavour decays is sensitive to the energy loss [22–26] and to the degree of thermalisation of charm and beauty quarks in the medium, as well as to heavy-quark hadronisation mechanism, e.g. recombination of heavy quarks with light quarks from the thermalised medium [27–29].

To single out such effects related to the QGP phase, it is therefore crucial to investigate first heavy-flavour production in pp collisions. At LHC energies, heavy-flavour quarks are copiously produced by inelastic partonic scatterings in these collisions, mostly via gluon fusion $gg \rightarrow Q\overline{Q}$ with a small contribution of quark–antiquark annihilation $q\overline{q} \rightarrow Q\overline{Q}$, where g, q and Q denote gluons, light (up or down) and heavy (charm or beauty) quarks correspondingly. The large masses of heavy quarks, m_{Q}, make it possible to calculate their production cross sections perturbatively [30–32]. Hence, experimental measurements of heavy-quark production in pp collisions provide an excellent test of pQCD and Monte Carlo event generators in this energy regime. Flavour conservation in the strong interaction allows heavy quarks to be only produced in pairs, which then hadronise independently to (anti)charm or (anti)beauty hadrons. Hadrons which contain only one heavy quark or antiquark are referred to as "open charm" or "open beauty" hadrons. Since the mass of charm and beauty quarks is much larger than that of light quarks (up, down or strange), open heavy-flavour hadrons inherit the strong initial correlation of the original heavy-quark pair. Charm hadrons and their decay products reflect the initial angular correlation of the heavy-quark pairs, whereas in the case of beauty hadron decays the correlation of the decay products is weakened due to their large masses. In both cases individual semi-leptonic weak decays of open heavy-flavour hadrons will lead to a

continuum of dielectron pairs, which dominates the spectrum in the intermediate mass region between the ϕ and J/ψ peaks. Therefore, dielectron measurements can be used to study charm and beauty production.

Proton–proton collisions, in which a large number of charged particles are produced, have recently attracted the interest of the heavy-ion community [33, 34]. These events exhibit several features that are similar to those observed in heavy-ion collisions, e. g. collective effects, such as long-range angular correlations [35–40] or enhanced strangeness production [41]. Charged-hadron p_{T} spectra show a hardening with increasing multiplicity, an effect that arises naturally from jet production [42]. Also, heavy-quark production is found to scale faster than linearly with the charged-particle multiplicity [43, 44], which can be explained by a substantial contribution from Multiple Parton Interactions (MPI) [45, 46], i. e. several interactions on the parton level occurring in a single pp collision, which introduce a correlation between particle production and the total event multiplicity [47–49]. Moreover, if a thermalised system were created in such high-multiplicity pp collisions, a signal of (virtual) thermal photons should be present. This motivates the study of dielectron production in high-multiplicity pp collisions, which could bring additional information regarding the underlying physical phenomena.

This work presents the measurements of low-mass dielectron pairs produced in proton–proton collisions at a centre-of-mass energy of $\sqrt{s} = 13\ \mathrm{TeV}$ recorded in 2016 and 2017 with the ALICE detector. The dielectron production has been studied at midrapidity ($|y_{\mathrm{e}}| < 0.8$) as a function of invariant mass, m_{ee}, and pair transverse momentum, $p_{\mathrm{T,\,ee}}$, over a wide range ($m_{\mathrm{ee}} < 4\ \mathrm{GeV}/c^2$ and $p_{\mathrm{T,\,ee}} < 6\ \mathrm{GeV}/c$). The dielectron yield is compared to the expectations from known hadronic sources based on the independently measured hadron cross sections in pp collisions. Heavy-flavour (charm and beauty) production cross sections at midrapidity are extracted in inelastic and high-multiplicity pp collisions by fitting the dielectron spectrum with templates provided by two Monte Carlo event generators. The dielectron spectrum in inelastic collisions is compared with the one obtained in high-multiplicity collisions in various transverse-momentum intervals. The production of direct photons is measured in both event classes as well.

The thesis is organised in the following way: Chapter 1 presents a short theoretical introduction into the physics of the dielectron spectrum. The ALICE detector and its sub-systems relevant for the analysis are described in Chapter 2. The details about the experimental data analysis such as reconstruction and selection of electron/positron candidates as well as the analysis of Monte Carlo simulated data are presented in Chapter 3. Chapter 4 summarises the results obtained in this work: dielectron mass and $p_{\mathrm{T,\,ee}}$ spectra, heavy-flavour production cross sections, fraction of direct photons in inclusive photon spectrum and the comparison of dielectron spectra in high-multiplicity and inelastic collisions. Summary and outlook for future analyses conclude the thesis in Chapter 5.

1.1 Quantum Chromodynamics

The theory of Quantum Chromodynamics is a non-Abelian gauge theory with symmetry group $SU(3)$ that is constructed on the basis of fermion fields (quarks) and boson mediators of the strong force (gluons). The dynamics of a quantum state and the fundamental fields are determined by the Lagrangian which can be written as:

$$\mathcal{L}_{\mathrm{QCD}} = \overline{\psi}_i \left(i(\gamma^\mu D_\mu)_{ij} - M\,\delta_{ij} \right) \psi_j - \frac{1}{4} G^a_{\mu\nu} G^{\mu\nu}_a. \tag{1.1}$$

Here $\psi_i(x)$ are the spin-$1/2$ quark fields, which are distinguished by their flavour (up, down, strange, charm, bottom and top) and carry colour (red, blue or green, in total $N_C = 3$) and electric ($-1/3$ or $+2/3$) charges. $D_\mu = \partial_\mu - igA^\alpha_\mu \lambda_\alpha$ is the gauge covariant derivative with Gell-Mann matrices λ_α, flavour-independent coupling constant $g = \sqrt{4\pi\alpha_s}$ and gluon gauge field A for $N_C^2 - 1 = 8$ different gluons $\alpha = 1...8$. The Dirac matrices γ^μ connect the spinor representation to the vector representation of the Lorentz group. The mass matrix M includes bare masses of quarks ($m_u \simeq 3$, $m_d \simeq 7$, $m_s \simeq 100\ \mathrm{MeV}/c^2$ for light quarks and $m_c \simeq 1.25$, $m_b \simeq 4.1$, $m_t \simeq 175\ \mathrm{GeV}/c^2$ for heavy quarks) along the diagonal. The gluon field strength tensor $G^a_{\mu\nu}$ (analogous to the field strength tensor $F^{\mu\nu}$ in quantum electrodynamics) is given by:

$$G^a_{\mu\nu} = \partial_\mu \mathcal{A}^a_\nu - \partial_\nu \mathcal{A}^a_\mu + g f^{abc} \mathcal{A}^b_\mu \mathcal{A}^c_\nu. \tag{1.2}$$

Here $\mathcal{A}^a_\mu$ are the gluon fields in the adjoint representation of the $SU(3)$ gauge group, and f^{abc} is the structure constant of $SU(3)$. Since gluons carry a gauge symmetry charge (colour), they can also interact among themselves, which is represented by the self-coupling term $g f^{abc} \mathcal{A}^b_\mu \mathcal{A}^c_\nu$. Fig. 1.4 shows the fundamental couplings of the strong interactions.

The fact that gluons carry themselves a non-zero colour charge leads to significant differences in QCD compared to quantum electrodynamics. In QED, (neutrally charged)

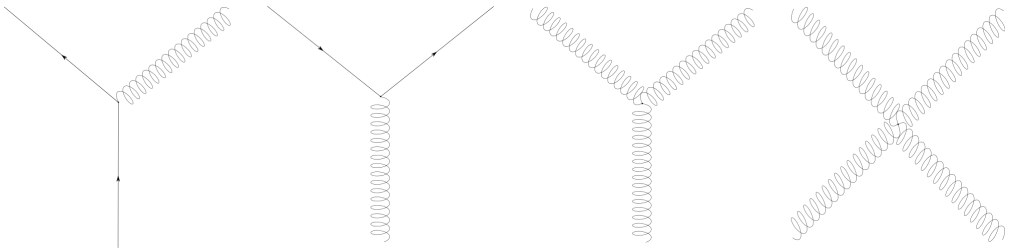

Figure 1.4: The fundamental couplings of the strong interaction (from left to right): gluon radiation, gluon splitting and gluon self-coupling. Time is advancing from bottom to top.

virtual photons carry the interaction between two charges and are allowed to create an electron-positron pair, which consequently annihilates. Such virtual e^+e^- pairs act as electric dipole, screening effectively the two interacting charges and reducing the effective charge of the electron as well as the fine structure constant $\alpha_{\rm QED}$. In QCD, gluons are not only allowed to split into virtual quark-antiquark pairs, but also to split into gluon pairs, which creates the opposite behaviour of the coupling constant compared to QED. Higher order processes of the strong interaction lead to a dependence of the coupling constant on the transferred momentum Q: $\alpha_s = \alpha_s(Q)$, which to first order can be written as:

$$\alpha_s(Q^2) \approx \frac{12\pi}{(11n - 2f)\ln(Q^2/\Lambda^2_{QCD})}. \tag{1.3}$$

Here n is the number of colours, f represents the number of quark flavours, and the value of QCD scale parameter $\Lambda_{QCD} \approx 210 \pm 14$ MeV [50] is the only intrinsic QCD parameter. The dependence of α_s on the momentum transfer Q and the potential between two quarks as a function of distance is shown in Fig. 1.5. At higher momenta, the coupling between quarks becomes weak, and the static local potential at small quark separation r is proportional to $\sim 1/r$. However, at large distances or small momenta the coupling between quarks increases linearly as r, which reflects the non-Abelian nature of the underlying symmetry of QCD. As a result, at small distances or for large transferred momenta quarks and gluons in QCD behave as *asymptotically free*, and the small α_s allows for perturbative expansion around large momentum transfers. For smaller momenta or large distances the perturbative treatment breaks down, and colourless hadrons, to which the quarks and gluons are *confined*, become the relevant degrees of freedom. In this energy regime, lattice QCD is a well-established non-perturbative approach: it describes space and imaginary time with a set of discrete points (lattice) and introduces a natural momentum cut-off of the order of $1/a$, where a is the lattice spacing [51, 52]. Lattice QCD calculations on supercomputers are usually repeated at different lattice spacing a and extrapolated to $a = 0$ and an infinitely large size of the lattice, thus recovering the continuum QCD.

In the limit of zero quark masses in Eq. 1.1, the QCD Lagrangian reveals a symmetry under global vector and axial vector transformation in flavour space defined as:

$$\psi \to e^{-i\alpha^i_V \frac{\lambda^i}{2}}\psi \text{ and } \psi \to e^{-i\alpha^i_A \frac{\lambda^i}{2}}\gamma_5\psi \tag{1.4}$$

The corresponding vector and axial-vector Noether currents associated with this symmetry are:

$$j^\mu_{V,i} = \overline{\psi}\gamma^\mu\frac{\lambda^i}{2}\psi \quad \text{and} \quad j^\mu_{A,i} = \overline{\psi}\gamma^\mu\frac{\lambda^i}{2}\gamma_5\psi \tag{1.5}$$

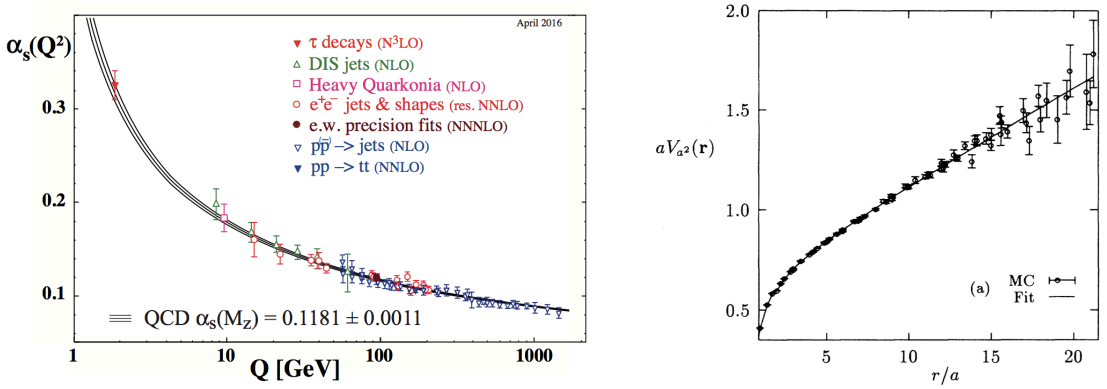

Figure 1.5: Left: summary of experimental measurements of running coupling constant $\alpha_s(Q)$ [50]. Right: quark-quark potential as a function of the distance from lattice QCD calculations [53].

The quark fields in Eq. 1.1 can then be decomposed into left- and right-handed components, which are invariant under the transformations from Eq. 1.5:

$$\psi_{L,R} \rightarrow \frac{1}{2}(1 \mp \gamma_5)\psi \tag{1.6}$$

Here L and R stand for left and right handed quark fields. For massless particles, quark handedness simplifies to the projection of the spin onto the momentum direction of a quark (for momentum transfers of $Q \approx 1$ GeV$/c$ zero quark masses is a good approximation for the light quarks u, d and, to a lesser extend, s). This quantity is conserved under such $SU(3)_L \times SU(3)_R$ chiral symmetry, so left- and right-handed quarks do not mix dynamically. Significant mass differences observed experimentally between chiral partners (e. g. ρ and a_1 mesons with $J^{PC}_{\rho} = 1^{--}$ and $J^{PC}_{a_1} = 1^{++}$ have masses $m_{\rho} = 775$ MeV$/c^2$ and $m_{a_1} = 1230$ MeV$/c^2$ [50]) suggest that chiral symmetry is apparently broken spontaneously due to a non-vanishing vacuum expectation value of the quark condensate $\langle\overline{\psi}\psi\rangle \neq 0$. The quark condensate serves as order parameter analogously to the magnetisation of a ferromagnet, which has no net magnetisation above the Curie temperature T_{C} but spontaneously picks its direction below T_{C}. While the vector current $j_V = j_L + j_R$ is still conserved, the axial-vector symmetry $j_A = j_L - j_R$ is spontaneously broken. This means that axial-vector charge $Q^k_A = \int d^3x \psi^{\dagger} \frac{\lambda^k}{2} \gamma_5 \psi$ still commutes with the Hamiltonian, but ground state has a non-zero expectation value: $Q^k_A|0\rangle \neq 0$ (an often used visualisation is a system with "Mexican hat" potential). An arbitrary choice of the ground state leads to the spontaneous breaking of the chiral symmetry and to the appearance of eight (massless) Goldstone bosons: $\pi^{\pm}, \pi^0, K^{\pm}, K^0, \overline{K^0}$ and η. Since quarks have non-zero masses, the chiral symmetry is also broken explicitly (which leads to massive pseudo-Goldstone bosons), but the effect of explicit breaking is

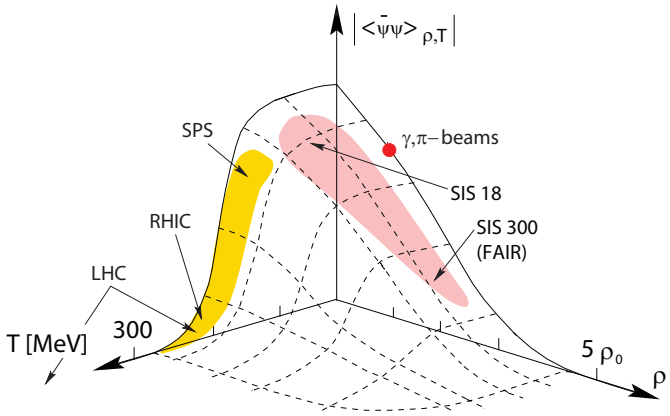

Figure 1.6: Expectation value of the quark condensate as a function of temperature T and nuclear density ρ. Figure is taken from [58] based on theoretical calculations in [55].

small compared to the spontaneous breaking.

According to the calculations based on the $SU(3)$ Nambu and Jona-Lasinio model [54], the quark condensate $\langle\overline{\psi}\psi\rangle$ should melt at high temperatures or densities [55]. Fig. 1.6 shows schematically the expectation value for quark condensate $\langle\overline{\psi}\psi\rangle$ together with the regions accessible by experiments. Even before the deconfinement phase transition, the chiral symmetry is expected to be partially restored [20], which should lead to the change of hadron masses. However, the exact effect of chiral symmetry restoration on hadron masses is a priori not known, and various suggested scenarios include e. g. dropping of ρ meson mass [56] or significant broadening of ρ and ω spectral functions [20, 57]. Here, dilepton decay channel $\rho \to l^+l^-$ provides a unique experimental information about the meson properties in hot and dense medium right at the moment of their decay, since in case of e. g. $\rho \to \pi^+\pi^-$ decay pions are re-scattered in surrounding medium, and the information about ρ meson properties at the moment of the decay is lost.

1.2 Dilepton Pairs

In this Section various dilepton sources contributing to the dilepton continuum will be discussed: Drell-Yan process, correlated semi-leptonic decays of open-heavy flavour hadrons, decays of light-flavour mesons and direct photon production.

1.2.1 Drell-Yan Process

At the very first moments of the collision, a quark in one incoming hadron or nucleus can annihilate with a sea antiquark from the other incoming hadron/nucleus to create a virtual photon, which subsequently converts into dilepton pair — a production mecha-

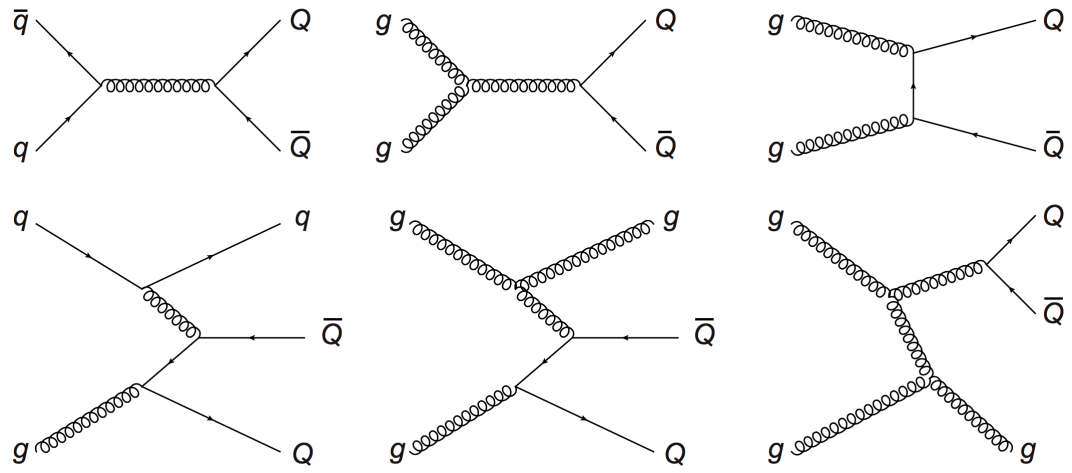

Figure 1.7: Examples of leading-order (top row) and higher-order (bottom row) diagrams for heavy-quark production.

nism known as Drell-Yan process [59]. In pp collisions at the top LHC energies this process is expected to have only very small contribution to the dilepton spectrum in the investigated invariant mass range $m_{\mathrm{ee}} < 4\ \mathrm{GeV}/c^2$ [60, 61].

1.2.2 Open Heavy Flavour

Semi-leptonic decays of open heavy-flavour hadrons are an important source of the dilepton production at LHC energies. Heavy-quark pairs (charm and beauty, $Q\overline{Q}$) are produced via inelastic hard-scattering processes between constituent quarks or gluons of the incoming nucleons. The lowest-order diagrams for heavy-quark production are shown in the top row of Fig. 1.7. Because of the gluon self-coupling, these production mechanisms also include the interaction of a gluon from one incoming nucleon with a gluon from the other nucleon ($gg \rightarrow g^* \rightarrow Q\overline{Q}$).

Once a heavy-quark pair is produced, quark hadronisation can lead to a creation of open-heavy flavour hadrons, e. g. $\mathrm{D}^0\overline{\mathrm{D}^0}$. The quark content of these mesons is one heavy c or b quark (or antiquark) and one light antiquark $\overline{u}, \overline{d}, \overline{s}$ (or quark), e. g. $\mathrm{D}^0 = \mathrm{c}\overline{\mathrm{u}}$ or $\mathrm{B}^+ = \mathrm{u}\overline{\mathrm{b}}$. Open heavy-flavour baryons (such as $\Lambda_c^+ = udc$ or $\Lambda_b^0 = udb$) are composed of in total three quarks, with only one of them being heavy (anti)quark. Due to the large charm quark mass, the $\mathrm{D}^0\overline{\mathrm{D}^0}$ pair inherits the initial strong correlation of $Q\overline{Q}$ pair, which at leading order is back-to-back. With the total branching ratio of about 10%, the D^0 meson can afterwards weakly decay semi-leptonically, $\mathrm{D}^0 \rightarrow \mathrm{K}^-\mathrm{l}^+\nu_\mathrm{l}$, which leads (in case both mesons decay semi-leptonically) to the creation of *correlated* l^+l^- pair. A schematic sketch of full process of such dilepton production mechanism is shown

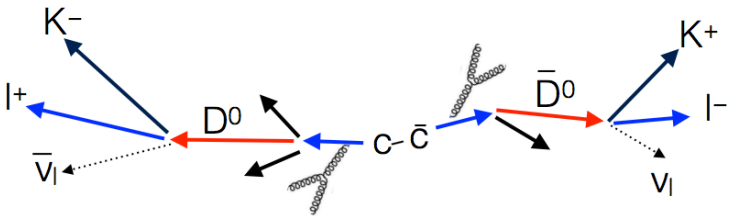

Figure 1.8: Schematic view of dilepton production from correlated semi-leptonic decays of open heavy-flavour hadrons (here for $c\bar{c} \rightarrow D^0\overline{D^0}$ case).

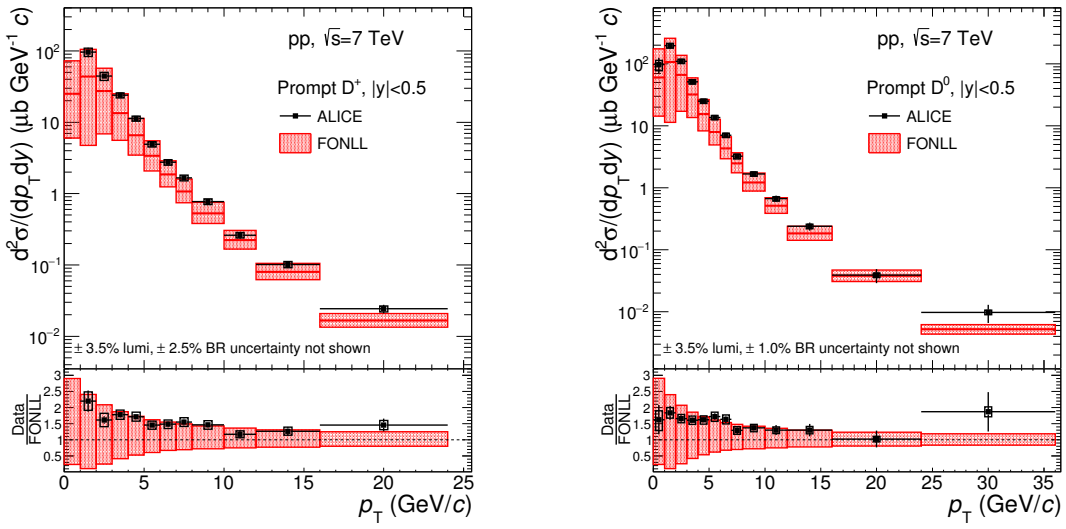

Figure 1.9: p_{T}-differential production cross sections of D mesons in pp collisions at $\sqrt{s} = 7$ TeV [62]. Data are compared to the theoretical prediction from FONLL pQCD calculations [32].

in Fig. 1.8. With different branching ratios for $h^{HF} \rightarrow l^{\pm}$, the same holds true for other open-charm ($\mathrm{D}^{\pm}$, $\Lambda_c^{\pm}$) and open-beauty ($\mathrm{B}^{\pm}$, B^0, Λ_b^0) mesons and baryons. Such dilepton pairs dominate the spectrum in the intermediate mass region between the ϕ and J/ψ resonance peaks (Fig. 1.3).

Thanks to their large masses, the production of heavy quarks can be calculated perturbatively in QCD. However, such calculations to leading order cannot describe fully the production of heavy-flavour quarks in nucleon-nucleon collisions. Higher order calculations such as next-to-leading-order (NLO) or fixed-order-plus-next-to-leading-log-order (FONLL) are in better agreement with the D-meson production cross section measured in experiments (see e. g. [63] for excellent recent review). Theoretical un-

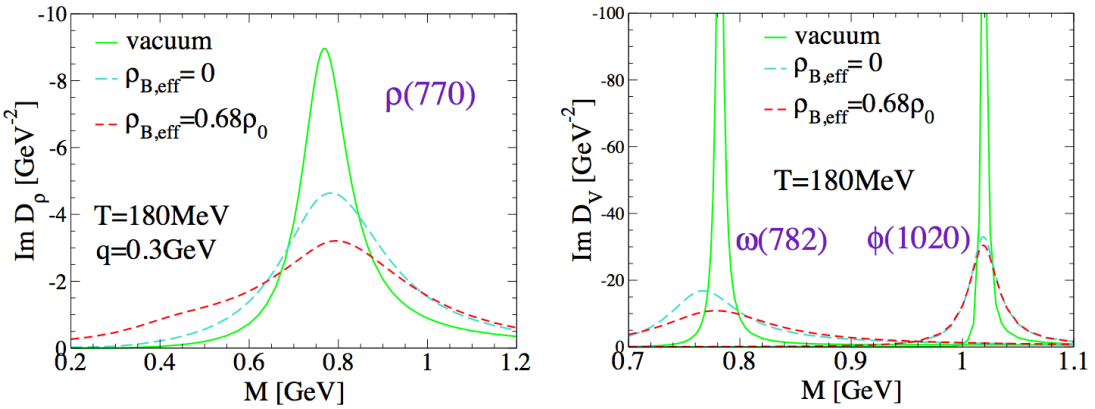

Figure 1.10: In-medium spectral functions of light vector mesons in hot and dense hadronic matter based on the hadronic many-body approach [20]. Short- and long-dashed lines represents the results with and without medium effects induced by baryons.

certainties are nevertheless quite large due to several factors like heavy-quark masses, non-perturbative parameters (parton distribution and fragmentation functions) and relativistic corrections, and the experimental data points constantly lie on the upper edge of uncertainties. Fig. 1.9 shows an example of recent results on D meson production [62] compared to FONLL calculations [32]. Measurements of the heavy-flavour production via dielectrons have the advantage that they probe full p_{T} range of heavy-quark pairs and are additionally sensitive to the initial correlation of charm and beauty quarks, i. e. the underlying production mechanism, which is not accessible in conventional single heavy-flavour measurements. Therefore dilepton measurements provide a complementary information about charm and beauty production and can be used to further test the pQCD and Monte Carlo event generators in pp collisions.

1.2.3 Hadron Decays

At the later stages of heavy-ion collision, the medium cools down and forms an interacting hadron gas. Close to the phase boundary (i. e. shortly after the crossover from QGP to a hadron gas) the spectral functions of vector mesons such as ρ, ω and ϕ are expected to be modified due to many-body properties of hadron interactions in hot hadronic phase [20]. These effects are connected to the partial restoration of chiral symmetry expected at temperatures close to the phase boundary [64–66]. An example of predicted in-medium spectral functions of light vector mesons in hot and dense hadronic matter is shown in Fig. 1.10. In such theoretical calculations, ρ and ω spectral functions (and to a lesser extend also ϕ, due to its longer lifetime) exhibit strong broadening towards higher temperatures and densities.

At this stage, dilepton production from pion annihilation and scattering is expected to be largely mediated by ρ, ω and ϕ. Since these mesons have the same quantum numbers as the photon, they couple directly to dilepton pairs according to the Vector Dominance Model [67], e. g. in $\pi^+\pi^-$ annihilation process: $\pi\pi \rightarrow \rho \rightarrow \gamma^* \rightarrow l^+l^-$. Among these mesons, the ρ meson is an especially useful probe to study the modifications of spectral functions, as its lifetime ($\tau \approx 1.3\,\mathrm{fm}/c$) is smaller than the expected lifetime of the medium in heavy-ion collisions at ultra-relativistic energies ($\approx 10\,\mathrm{fm}/c$ [68]). The invariant mass of the dilepton will directly reflect the mass of vector meson at the time of its decay, providing a unique information about in-medium meson spectral functions.

After the system reaches thermal freeze-out, the dominant sources of dielectron pairs are resonance and Dalitz decays of vector and pseudo-scalar mesons with their vacuum properties: π^0, η, η', ρ, ω, ϕ, J/ψ. In case of Dalitz decays such as $\pi^0 \rightarrow \gamma\,\mathrm{e}^+\mathrm{e}^-$, the relation between hadron production and the associated $\mathrm{e}^+\mathrm{e}^-$ pair production is described by Kroll-Wada equation [69, 70]:

$$\frac{\mathrm{d}^2N}{\mathrm{d}m_{\mathrm{ee}}\mathrm{d}p_{\mathrm{T,\,ee}}} = \frac{2\alpha}{3\pi}\sqrt{1-\frac{4m_{\mathrm{e}}^2}{m_{\mathrm{ee}}^2}}\left(1+\frac{2m_{\mathrm{e}}^2}{m_{\mathrm{ee}}^2}\right)\frac{1}{m_{\mathrm{ee}}}S(m_{\mathrm{ee}},p_{\mathrm{T,\,ee}})\frac{\mathrm{d}N_{\mathrm{h}}}{\mathrm{d}p_{\mathrm{T}}}. \tag{1.7}$$

Here $\alpha \approx 1/137$ is the electromagnetic fine structure constant and $S(m_{\mathrm{ee}}, p_{\mathrm{T,\,ee}}) = |F_h(m_{\mathrm{ee}}^2)|^2(1-\frac{m_{\mathrm{ee}}^2}{m_h^2})^3$ is the electromagnetic form factor, $F_h(m_{\mathrm{ee}}^2)$, and a phase space factor that cuts off the m_{ee} distribution as one approaches the parent hadron mass, m_h. In proton–proton collisions, the measurement of dielectron production from resonance and Dalitz decays of vector and pseudo-scalar mesons provide crucial baseline needed for the interpretation of results in heavy-ion collisions.

1.2.4 Direct Photons

Direct photons (i. e. photons which originate not from hadronic decays, but from inelastic scattering processes between partons) are another important electromagnetic probe to study the system created in heavy-ion collisions. Such photons can be created both in form of real (massless) photons or as virtual photons with non-zero mass [71] converting consequently into dilepton pair, which is allowed by uncertainty principle $\Delta E \Delta t \sim \hbar$. In proton–proton collisions, the measurement of direct photons provides another important test of pQCD calculations, for which the leading-order diagrams are shown in Fig. 1.11. Furthermore, at low $p_{\mathrm{T}} \lesssim 3\ \mathrm{GeV}/c$, where one cannot rely on pQCD calculations, direct photon production in pp collisions provides crucial reference to establish the presence of thermal radiation from hot and dense medium created in heavy-ion collisions [14, 15, 72, 73]. Since the momentum distribution of direct photons is defined by the characteristics of the interacting partons, the momentum distribution of thermal di-

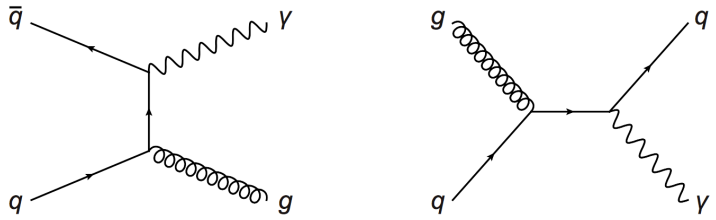

Figure 1.11: Examples for leading-order processes of direct photon production: quark–antiquark annihilation (left) and quark–gluon Compton scattering (right).

rect photons (i. e. produced by partons in a thermalised medium) will reflect the medium temperature, with a black-body radiation spectrum following $\sim e^{-E/T}$.

A measurement of real direct photons at low p_{T} is, however, challenging because of the large background of hadron decay photons, with the main contribution ($\sim$80%) coming from $\pi^0 \to \gamma\gamma$ decays. This background can be largely avoided by measuring the contribution of virtual direct photons, which in contrast to real photons bring an additional observable — the invariant mass of the created $\mathrm{e}^+\mathrm{e}^-$ pair — into the game. In general, any process which creates real direct photons as e. g. in Fig. 1.11 can also produce virtual photon which appears in form of dilepton pair. The relation between real photon production and the associated $\mathrm{e}^+\mathrm{e}^-$ pair production is described by the Kroll-Wada equation as defined in Eq. 1.7, in which case $S(m_{\mathrm{ee}}, p_{\mathrm{T,\,ee}})$ is a process dependent factor that accounts for differences between real and virtual photon production. For direct photon production it approaches unity for $p_{\mathrm{T,\,ee}} \gg m_{\mathrm{ee}}$, and the corresponding dielectron mass spectrum has therefore the same $\sim 1/m_{\mathrm{ee}}$ dependence as $\mathrm{e}^+\mathrm{e}^-$ pairs from Dalitz decays of hadrons at small m_{ee}. The measurements of virtual direct photons allow selecting the mass range $m_{\mathrm{ee}} \gtrsim m_{\pi^0} = 135\ \mathrm{MeV}/c^2$ and therefore improving drastically the signal-to-background ratio compared to measurements of real direct photons. Assuming the equivalence between the fraction of real direct photons and fraction of virtual direct photons with zero mass

$$r_{\mathrm{dir}} = \frac{N^{\gamma}_{\mathrm{dir}}}{N^{\gamma}_{\mathrm{incl}}} \equiv \left.\frac{N^{\gamma^*}_{\mathrm{dir}}}{N^{\gamma^*}_{\mathrm{incl}}}\right|_{m=0}, \tag{1.8}$$

the real direct photon fraction r can be extracted with a fit of the $\mathrm{e}^+\mathrm{e}^-$ invariant mass distribution above the π^0 mass with a virtual photon contribution in addition to hadron decays using the following expression:

$$\mathrm{d}\sigma/\mathrm{d}m_{\mathrm{ee}} = r f_{\mathrm{dir}}(m_{\mathrm{ee}}) + (1-r) f_{\mathrm{LF}}(m_{\mathrm{ee}}) + f_{\mathrm{HF}}(m_{\mathrm{ee}}). \tag{1.9}$$

Here $f_{\mathrm{LF}}(m_{\mathrm{ee}})$ and $f_{\mathrm{HF}}(m_{\mathrm{ee}})$ are contributions from light-flavour and heavy-flavour decays correspondingly, and the shape of virtual direct photon component $f_{\mathrm{dir}}(m_{\mathrm{ee}})$

is described by Eq. 1.7 in the quasi-real virtual photon regime ($p_{\mathrm{T,\,ee}} \gg m_{\mathrm{ee}}$). The drawbacks of this method are the small internal conversion probability for virtual photon ($\sim\alpha_{em} \approx 1/137$) and rapidly decreasing cross section as a function of m_{ee} ($\sim 1/m_{\mathrm{ee}}$).

1.3 High-Multiplicity Proton–Proton Collisions

The phenomena described in previous Section (such as modification of vector meson spectral functions or thermal radiation) are expected to be caused by a hot and dense system. Experimental evidence for a creation of strongly-interacting hot partonic matter is found in many observations, such as the significant energy loss of high-p_{T} colour probes [74], bulk collective effects described by relativistic hydrodynamics [75], high initial temperatures of several hundred MeV [15, 76] and characteristic heavy-flavour production [63] including sequential suppression of quarkonium states [77]. There are only a few yet unresolved problems in the heavy-ion collisions which need to be addressed in the future, but they should not invalidate the general conclusion about the formation of hot strongly-interacting QGP at RHIC and LHC energies.

Proton–proton collisions that produce a large number of charged particles have recently attracted great interest of the heavy-ion community, see e. g. [33, 34] for recent reviews. The observation of a pronounced longitudinal structure in the two-dimensional angular correlation function in high-multiplicity pp events at $\sqrt{s} = 7$ TeV [35] has triggered speculations that physics relevant for heavy-ion collisions is also at work in small collision systems. Soon after that, pp and p–Pb events with high multiplicities were found to exhibit further features that are similar to those observed in heavy-ion collisions, e. g. collective effects [34, 36–40] or enhanced strangeness production [41]. Among the frameworks which aim at description of all collision systems on similar footing, relativistic hydrodynamics seems to be the most promising approach. The studies of high-multiplicity small systems should provide a "bridge" between the dilute pp collisions and the QGP created in heavy-ion collisions. The field of relativistic heavy ion physics is currently continuously evolving towards a possible revolution in the understanding of the conditions, which are necessary for nuclear matter to create a (droplet of) Quark–Gluon plasma.

Since the dilepton mass spectrum reflects directly various sources and physical processes involved in the collision, measurements of dilepton production provide an excellent tool for exploratory studies in high-multiplicity pp collisions. These measurements could give us further insight and shed light on the underlying physics processes, especially regarding the direct photon, vector meson and heavy-flavour production. This work focuses on a comparison of dielectron spectra in inelastic events and in events collected with a trigger on high charged-particle multiplicities. To achieve this, the ratio of properly normalised dielectron spectra in high-multiplicity (HM) and inelastic (INEL) pp events is calculated as following:

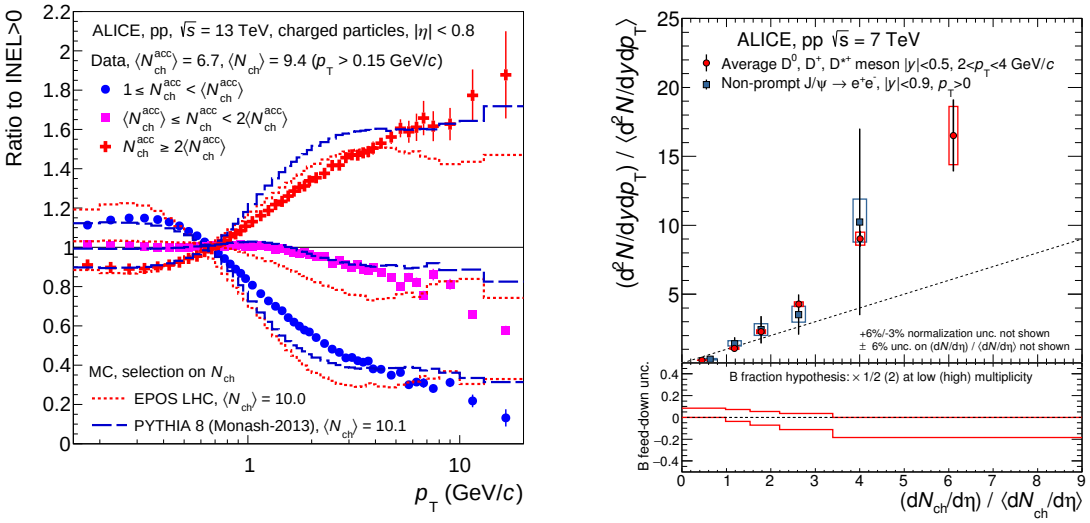

Figure 1.12: Left: the modification of charged-hadron p_{T} spectra in high-multiplicity pp collisions at $\sqrt{s} = 13$ TeV [42]. Right: D meson and non-prompt J/ψ relative yields as a function of the relative charged-particle multiplicity in pp collisions at $\sqrt{s} = 7$ TeV [43].

$$\frac{N_{\mathrm{ee}}(\mathrm{HM})/\langle N_{\mathrm{ch}}(\mathrm{HM})\rangle}{N_{\mathrm{ee}}(\mathrm{INEL})/\langle N_{\mathrm{ch}}(\mathrm{INEL})\rangle} = \frac{\langle N_{\mathrm{ch}}(\mathrm{INEL})\rangle}{\langle N_{\mathrm{ch}}(\mathrm{HM})\rangle} \times \frac{1/N_{\mathrm{HM}}\,\mathrm{d}N_{\mathrm{ee}}/\mathrm{d}m_{\mathrm{ee}}|_{\mathrm{HM}}}{1/N_{\mathrm{INEL}}\,\mathrm{d}N_{\mathrm{ee}}/\mathrm{d}m_{\mathrm{ee}}|_{\mathrm{INEL}}}. \quad (1.10)$$

Here $\langle N_{\mathrm{ch}}\rangle$ is the average charged particle multiplicity and N_{HM} (N_{INEL}) is the number of analysed high-multiplicity (inelastic) events. In such a ratio multiplicity-independent uncertainties of dielectron spectra cancel, and the results reflect directly the dielectron production relative to the charged-particle multiplicity. Naively, one expects the relative yield of dielectrons from light hadron decays to scale linearly — and with slope 1 — with the relative charged particle multiplicity. Deviations from this linear behaviour are caused by modifications of the charged hadron p_{T} spectra [42] and by the unknown chemistry in high-multiplicity events, e. g. by modification of the η/π ratio. The hardening of charged-hadron p_{T} spectra shown in Fig. 1.12 (left) could arise naturally from larger production of jets (bunches of high-p_{T} particles originating from early hard processes and concentrated in small solid angle) in high-multiplicity events. While this hardening of p_{T} spectra is taken into account in the corresponding hadronic cocktail calculations (Section 3.5), possible modification of hadron chemistry can be studied for the first time with dielectrons. Particularly interesting is the production of the ρ meson: will it be suppressed by final state interactions with surrounding charged particles, akin to the comover model in the context of quarkonium suppression [78] or enhanced by an increased final state production via $\pi^+\pi^- \to \rho$ annihilation?

Furthermore, the production of open charm mesons is known to increase faster than linearly with multiplicity for $p_{\mathrm{T}} > 1\ \mathrm{GeV}/c$ [43, 44]. At LHC energies, this effect can be attributed to larger amount of gluon radiation in hard processes or to a substantial contribution from MPI, i. e. several interactions on the parton level in a single pp collision [45, 46]. The charged-particle multiplicity is a direct measurement of the number of partonic interactions in the pp events, and the results on heavy-flavour production in high-multiplicity pp events indicate that the effect of MPI can also extend into the regime of hard processes. Similar dependence is observed for non-prompt J/ψ from B mesons, although the data are compatible within their large uncertainties with the linear slope of 1 (Fig. 1.12 right). Here, dielectrons from correlated semileptonic charm and bottom decays offer a unique window at the production of low-p_{T} charm and beauty hadrons. Above $p_{\mathrm{T,\,ee}}{\sim}3\ \mathrm{GeV}/c$, the dielectron spectrum in the intermediate mass range is dominated by beauty hadron decays, therefore the dielectron measurement can also be used to investigate the production of beauty hadrons in high-multiplicity pp events.

1.4 Previous Experimental Results

Before the Large Hadron Collider at CERN started to take data, several laboratories have been studying the nuclear matter at various T and μ_B in heavy-ion collisions. Among them, the Schwerionen-Synchrotron (SIS, German for Heavy Ion Synchrotron) at GSI, the Super Proton Synchrotron (SPS) at CERN and the Relativistic Heavy Ion Collider (RHIC) at Brookhaven National Laboratory (BNL) have been colliding heavy ions at various centre-of-mass energies. A short selection of previous results from SIS, SPS, RHIC and LHC experiments on photon and dilepton production is presented below.

1.4.1 SIS Accelerator

The High Acceptance DiElectron Spectrometer (HADES) is a fixed-target experiment at SIS, which has systematically measured dielectron production in low-energy collisions of various nuclei: pp/np, C–C, p–Nb and Ar–KCl [79–85], where dielectrons from quasi-free np reactions have been reconstructed by detecting the proton spectator from the deuteron breakup. At bombarding energies of a few GeV per nucleon, i. e. in the regime of nucleon stopping, quantitative descriptions of heavy-ion collisions indicate that the medium radiation is apparently driven by baryonic resonances, and baryon-driven medium effects are expected to be maximal.

Figure 1.13 (left) shows the ratio of dielectron spectra in p–Nb/pp, Ar–KCl and C–C to the corresponding N–N reference. In the momentum range $p_{\mathrm{ee}} < 0.8\ \mathrm{GeV}/c$, the ratio in p–Nb/pp reactions measured at the same kinetic beam energy of $3.5\ \mathrm{GeV}$ is rising to $\sim$1.7, which indicates the onset of processes not accounted for in the pp system. A direct comparison of the experimentally constrained N–N reference spectrum with the

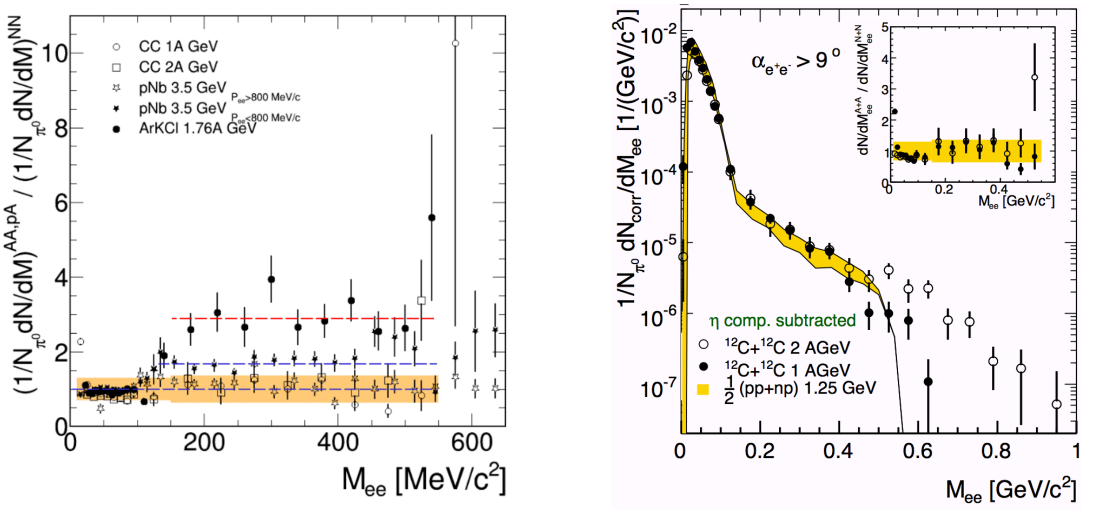

Figure 1.13: Left: ratio of the invariant mass yield in p–Nb/pp, Ar–KCl and C–C collisions to the corresponding N–N reference [79]. Right: comparison of the reference spectrum from elementary collisions with the results for C–C collisions; the inset displays the ratio to the reference spectrum [83]. Contributions from Dalitz decays of η meson are subtracted from all spectra.

e^+e^- invariant mass distribution in the heavier system Ar–KCl at $E_{\mathrm{lab}} = 1.76\,A$ GeV shows an excess yield of about $\sim$3.5 [82], proving a qualitative change in the nature of the excess yield in heavier systems. The dielectron spectra observed by HADES result from a four-volume integral over the emissivity, weighted with the time-dependent temperature and density profile of the hot and dense medium described by microscopic transport calculations [86, 87]. This approach agrees well with experiment in the region $0.4 < m_{\mathrm{ee}} < 0.8$ GeV$/c^2$, but seems to overpredict the results in the lower mass region. The electron pair spectra measured in C–C collisions at $E_{\mathrm{lab}} = 1$ and $2\,A$ GeV are compatible with a superposition of elementary np and pp collisions (Fig. 1.13 right), leaving little room for additional electron pair sources in such light collision systems at SIS energies [83].

In continuation of a systematic investigation of dielectron production at low energies, HADES has recently also collected data from Au–Au collisions at $E_{\mathrm{lab}} = 1.23\,A$ GeV, and preliminary results are available in [79]. The studies will provide an important test of the scenario described above.

1.4.2 Super Proton Synchrotron

The SPS machine at CERN was commissioned in June 1976 and continues to provide fixed-target collisions nowadays, serving at the same time as the pre-accelerator for the

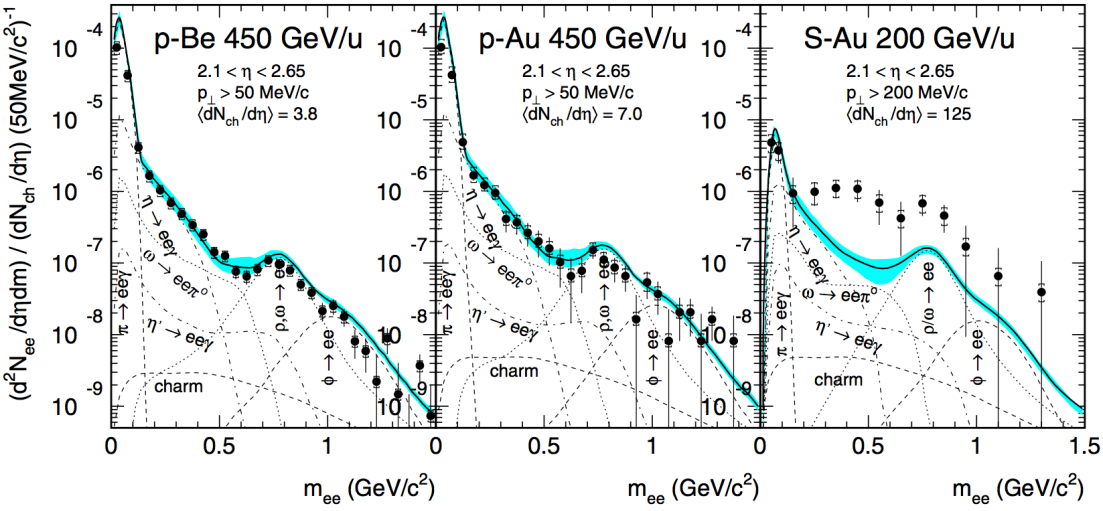

Figure 1.14: Dielectron spectra in p–Be, p–Au and S–Au collisions measured by CERES [88].

Large Hadron Collider. Already first heavy-ion SPS experiments on fixed targets found an indication for an anomalous dielectron production (NA38 [89] and NA45/CERES [88, 90, 91]). While the dielectron yield in proton–nucleus collisions at $E_{\mathrm{lab}} = 450$ GeV was compatible with the expected contributions from hadron decays, results in nucleus–nucleus collisions at $E_{\mathrm{lab}} = 200\,A$ GeV clearly showed an excess over expected hadronic sources, particularly in the mass region below $1\ \mathrm{GeV}/c^2$ (Fig. 1.14). The characteristics of the excess such as the mass distribution and the onset at $m_{\mathrm{ee}} > 2m_{\pi}$ suggested that it originates from two-pion annihilation $\pi\pi \to \rho \to e^+e^-$. Theoretical models used to describe CERES data included two possible scenarios for the modification of ρ meson properties: dropping of ρ mass or the broadening of its width [92–94]. However, the mass resolution and statistical precision of CERES data did not allow to distinguish between these two scenarios, with both models being able to describe the data fairly well. In the intermediate mass region above $1\ \mathrm{GeV}/c^2$, an enhanced dilepton production was also observed by Helios-3 experiment in S–W collisions at $E_{\mathrm{lab}} = 200\,A$ GeV [95, 96] and by NA50 experiment in Pb–Pb collisions at $E_{\mathrm{lab}} = 158\,A$ GeV [97]. Theoretically, this excess was attributed to enhanced open-charm production and/or thermal radiation from the partonic phase, while experimentally this remained an open question.

These ambiguities and unresolved questions motivated the upgrade of the NA50 experiment to construct the NA60 detector: a third-generation heavy-ion experiment which was designed specifically to determine the origin of the enhancement in the intermediate mass region. The NA60 detector complements the muon spectrometer and zero degree calorimeter previously used by NA50 with state-of-the-art silicon detectors placed in the target region, which provided precise information about primary interaction vertex.

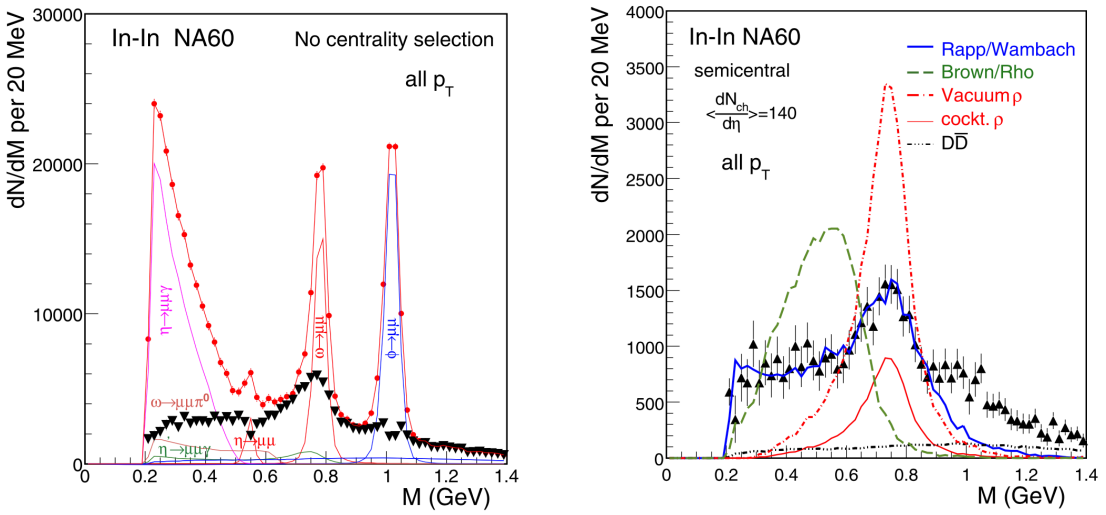

Figure 1.15: Left: background-subtracted dimuon mass spectrum in In–In collisions at $E_{\mathrm{lab}} = 158\,A$ GeV [98]. Dots and triangles show the spectrum before and after the subtraction of all hadron decay sources but ρ. Right: the dimuon excess compared to different model predictions for ρ such as dropping mass (green line) or in-medium broadening (blue).

Commissioned in 2001, it measured the dimuon invariant-mass spectrum in In–In collisions at $E_{\mathrm{lab}} = 158\,A$ GeV with very good mass resolution and statistical precision. Detailed analysis of low-mass region led to clear conclusion regarding the ρ spectral function and the origin of the excess in $m_{\mu\mu} \lesssim 1$ GeV$/c^2$ [98, 100, 101]. Data were in agreement with the in-medium broadening of the ρ meson and thermal radiation from hadronic and/or QGP phase, whereas vacuum ρ and mass shifting scenarios were excluded (Fig. 1.15).

The NA60 Collaboration has also clarified the origin of the excess over the semileptonic decays of heavy-flavour hadrons and Drell-Yan pairs in the intermediate mass range [98, 99, 101, 102]. By using precise information from the silicon tracker placed close to interaction point, it was shown that this excess is associated with a prompt source, as opposed to $\mu^+\mu^-$ pairs from charm hadron pairs that decay further away from the interaction point. Transverse mass spectra were used to extract the slope parameter T_{eff} in different mass windows as shown in Fig. 1.16 (left). The T_{eff} values of the dimuon excess rise nearly linearly with mass up to $\sim$1 GeV$/c^2$, which is consistent with the expectations for radial flow of an in-medium hadron source ($\pi^+\pi^- \to \rho$) decaying continuously into lepton pairs (Fig. 1.16 right). Beyond $m_{\mu\mu} \approx 1$ GeV$/c^2$, T_{eff} drops to a constant value in intermediate mass range. A natural explanation of such behaviour is a transition to a predominantly early, i. e. partonic emission source, where radial flow is not yet built up [101, 102]. This analysis presented the first data-based evidence for

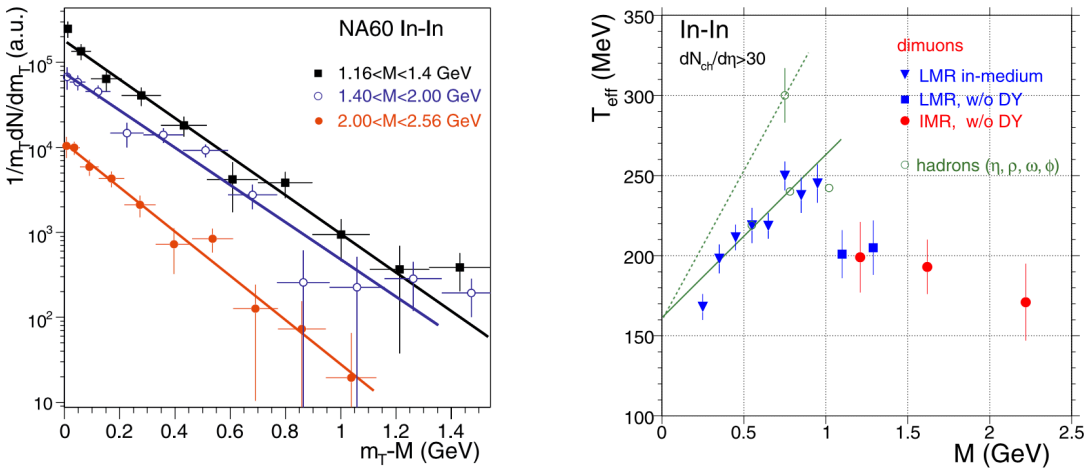

Figure 1.16: Left: transverse mass spectra of the dimuon excess in different mass windows. The lines show fits to the data with the function $\sim e^{-m_{\mathrm{T}}/T_{\mathrm{eff}}}$, with T_{eff} being the inverse slope of the distributions. Right: the dependence of T_{eff} parameter on the invariant mass [99].

thermal radiation of partonic origin in nuclear collisions. Models including thermal radiation from the QGP [103–106] can reproduce the data.

Soon after the NA60 measurements have been published, CERES presented new results from Pb–Au collisions at $E_{\mathrm{lab}} = 158\,A$ GeV [107]. Improved mass resolution and statistical precision after a TPC upgrade allowed solving the ambiguity of the first CERES data regarding the origin of the low-mass excess: the data clearly favoured a substantial in-medium broadening of the ρ spectral function over a density-dependent shift of the ρ pole mass, confirming the NA60 results.

1.4.3 Relativistic Heavy Ion Collider

The studies of dilepton production in nuclear collisions have been continued at RHIC by the PHENIX and STAR Collaborations. RHIC is the first heavy-ion collider ever built, and with energies of Au–Au collisions up to $\sqrt{s_{\mathrm{NN}}} = 200$ GeV it is well suited for the investigations of QGP properties in the regime of high temperature and low net-baryon density.

Both PHENIX and STAR Collaborations have shown that dielectron production in pp collisions at $\sqrt{s} = 200$ GeV is well described by a cocktail of expected hadronic sources [76, 108, 109]. In addition, PHENIX measured the total $\mathrm{c\bar{c}}$ and $\mathrm{b\bar{b}}$ cross sections in pp and d–Au collisions at $\sqrt{s_{\mathrm{NN}}} = 200$ GeV by fitting the spectra of dielectron pairs from heavy-flavour hadron decays simultaneously in invariant mass and pair transverse momentum [108, 110, 111] (Fig. 1.17). At this energy, the yield from correlated pairs

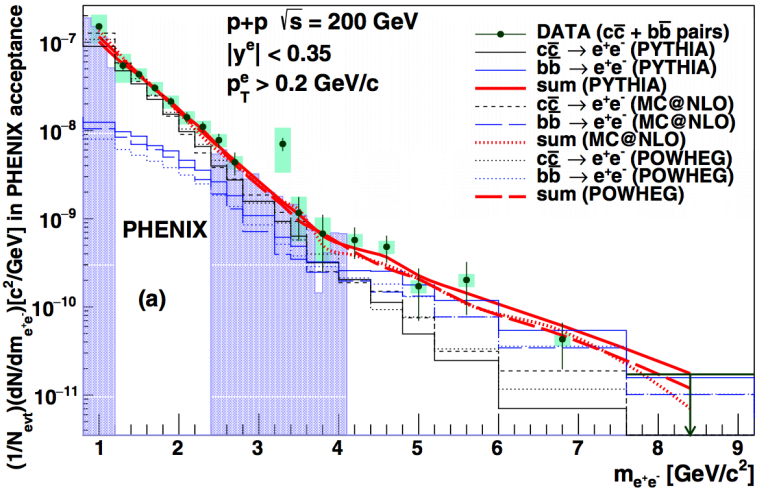

Figure 1.17: Dielectron mass spectrum in pp collisions at $\sqrt{s} = 200$ GeV after subtraction of light-flavour and J/ψ decays compared to different Monte Carlo generators for heavy-flavour production [111]. The mass region shown in blue was excluded from the fit used to extract the charm and beauty production cross sections.

from beauty-hadron decays dominates across all mass regions for $p_{\mathrm{T,\,ee}} \gtrsim 2.5$ GeV/c, whereas the c$\bar{\mathrm{c}}$ contribution is preeminent for $m_{\mathrm{ee}} < 3$ GeV/c^2 and $p_{\mathrm{T,\,ee}} \lesssim 2$ GeV/c. Due to different rapidity and momentum distributions predicted by the models, the extraction of heavy-flavour cross sections, in particular the total c$\bar{\mathrm{c}}$ cross section, depends nevertheless on the event generator used to extrapolate the measurements to full phase space.

At lower masses ($m_{\mathrm{ee}} < 0.3$ GeV/c^2) and high pair transverse momentum ($p_{\mathrm{T,\,ee}} > 1$ GeV/c), i. e. in the quasi-real virtual-photon region where $p_{\mathrm{T,\,ee}} \gg m_{\mathrm{ee}}$, the measured dielectron yield was used to extract the cross section of virtual direct photons. The corresponding yield of real direct photons in pp and d–Au collisions is reproduced by next-to-leading order pQCD calculations [76, 112] (Fig. 1.18 right).

In Au–Au collisions, an enhancement of dielectron production in the low-mass region was also observed by PHENIX and STAR collaborations [76, 113–115]. The first measurement by PHENIX showed a very large excess compared to the hadronic cocktail [76], and all models which successfully described SPS data failed to explain the new PHENIX results [76, 116]. Later, the STAR measurements revealed a much smaller enhancement, compatible with models that involve the broadening of the ρ meson [114]. The inconsistency between these results has been solved with the new data from the PHENIX Collaboration after the installation of the Hadron Blind Detector [113]. The large excess seen previously in old data was not confirmed, and new results were in good agreement with the STAR measurements (Fig. 1.18 left). Data are consistent with

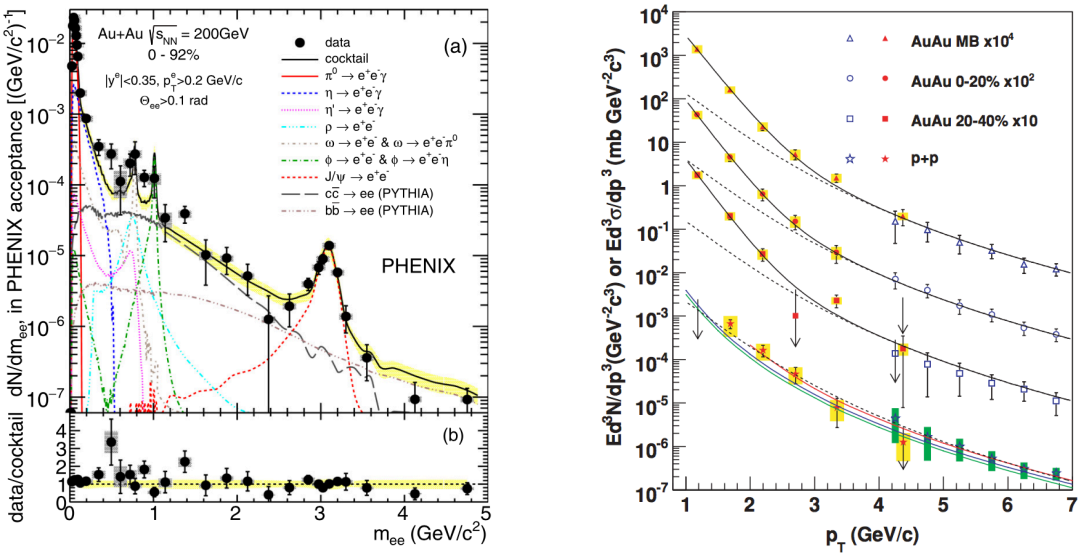

Figure 1.18: Left: dielectron invariant mass spectrum in Au–Au collisions at $\sqrt{s_{\mathrm{NN}}} = 200$ GeV [113]. Right: invariant cross section (pp) and invariant yield (Au–Au) of direct photons as a function of p_{T} [76]. The curves on the pp data represent NLO pQCD calculations, and the dashed curves show a modified power-law fit to the pp data scaled by geometric nuclear overlap function T_{AA}.

models predicting a ρ broadening and thermal radiation from the hadronic and/or QGP phases. The observed strong broadening of ρ meson with essentially no change of the pole mass is consistent with the restoration of chiral symmetry [66].

The dielectron spectra in Au–Au collisions also show a further excess of the direct-photon yield over the pp expectation (Fig. 1.18 right), which is exponential in p_{T} with an inverse slope in central collisions of $T_{\mathrm{eff}} = 221 \pm 19^{stat} \pm 19^{syst}$ MeV [76]. Later, this excess has been also measured using real photon conversions in detector material, which resulted in similar values for the inverse slope parameter in central Au–Au collisions $T_{\mathrm{eff}} = 239 \pm 25^{stat} \pm 7^{syst}$ [117]. This excess can be attributed to thermal radiation from the partonic and/or hadronic phase [118–120]. However, the resulting thermal direct photon spectrum observed in experiment is a sum of all contributions from different stages of the collision after thermalisation. High photon emission rates in the earliest, hottest stage can be compensated by an expanded space-time volume and a blue shift due to radial flow in the later, cooler stages [121]. This complicates the interpretation of inverse slope parameter, but a correlation between the slope parameter and the initial temperature still exists [122]. Models assuming thermal photon emission from hot matter with initial temperatures in the range $300 - 600$ MeV can describe the measured spectrum [76].

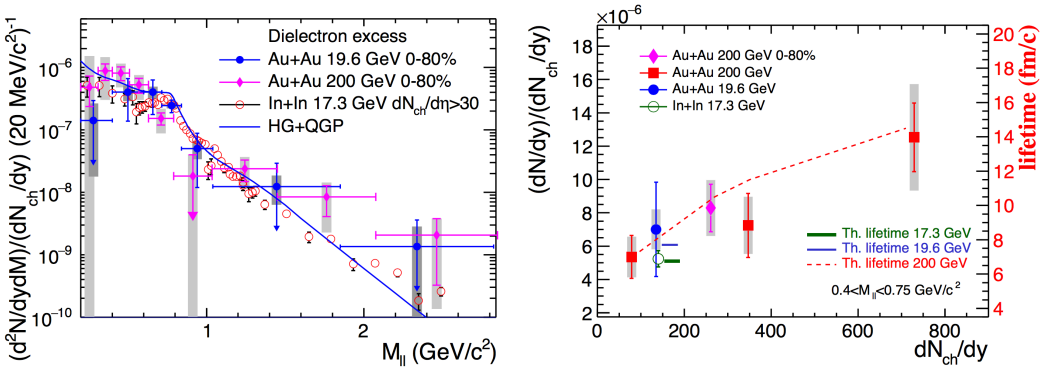

Figure 1.19: Left: the excess dielectron mass spectra in Au–Au and In–In collisions, normalised to the charged particle multiplicity at mid-rapidity [131]. Right: integrated yields of the normalised dilepton excesses for $0.4 < m_{ll} < 0.75$ GeV$/c^2$ as a function of charged particle multiplicity. Dashed curve and horizontal lines show theoretical predictions for a lifetime of the medium [132].

The first measurement of elliptic flow of direct photons in Au–Au collisions by the PHENIX Collaboration revealed, that, surprisingly, it is compatible to the one of hadrons [123]. Further PHENIX results on more precise measurements of elliptic flow extended to lower p_{T} confirmed this early observation [124]. This measurement challenged theoretical models aiming at description of both large direct photon spectra and significant flow of direct photons at the same time. This could be achieved either by an increase of the direct photon emission from the later stages of the collision and/or suppress emission of the initial stage [125–127] or by assuming a new azimuthally asymmetric source of direct photons like jet-matter interactions or synchrotron radiation in the field of colliding nuclei [128–130]. These theoretical efforts considerably reduce the discrepancy of the data, however, consistent reproduction of both the direct photon spectra and flow measured at RHIC is still missing.

In addition to the studies at $\sqrt{s_{\mathrm{NN}}} = 200$ GeV, the excess of dielectron pairs in low-mass region has also been measured in Au–Au collisions at various collision energies by STAR Collaboration [131, 133]: $\sqrt{s_{\mathrm{NN}}} = 19.6$, 27, 39 and 62.4 GeV. The excess mass spectra over the hadronic cocktail prominent at all energies are consistently described in its m_{ee}- and p_{T}-dependence by a model calculation with a broadened ρ spectral function from SPS up to top RHIC energies. The integrated dielectron excess yield at $\sqrt{s_{\mathrm{NN}}} = 19.6$ GeV in mass range $0.4 < m_{\mathrm{ee}} < 0.75$ GeV$/c^2$, normalised to the charged particle multiplicity at mid-rapidity, has a value similar to that in In–In collisions at $\sqrt{s_{\mathrm{NN}}} = 17.3$ GeV measured by NA60 [102, 134] (Fig. 1.19 left). For $\sqrt{s_{\mathrm{NN}}} = 200$ GeV, the normalised excess yield in central collisions is higher than that at lower energies, and increases from peripheral to central collisions (Fig. 1.19 right), indicating that the lifetime of the hot and dense medium created in central Au–Au colli-

sions at top RHIC energies is longer than those in peripheral and lower-energy collisions. Dielectron studies at various collision energies will be continued at RHIC within future Beam Energy Scan (BES) Phase-II program, which can further improve the understanding of enhancement dependence on total baryon densities.

In the intermediate mass region, the detailed analysis of a possible excess at RHIC was complicated due to the much higher production of correlated dilepton pairs from open heavy-flavour decays compared to SPS energies. In absence of precise inner tracking systems, which would allow a separation of prompt and non-prompt dielectron sources, heavy-ion results from PHENIX and STAR can be fairly well described by calculations including heavy-flavour contributions estimated in pp collisions and scaled with the number of binary collisions [76, 113–115].

Recently, STAR observed a significant enhancement of $\mathrm{e^+e^-}$ pair production at very low transverse momentum in non-central Au–Au collisions at $\sqrt{s_{\mathrm{NN}}} = 200$ GeV and U–U collisions at $\sqrt{s_{\mathrm{NN}}} = 193$ GeV [135]. The excess over hadronic cocktail calculations is pronounced over a wide mass range, but is concentrated entirely in $p_{\mathrm{T,\,ee}} < 0.15\ \mathrm{GeV}/c$, with a much weaker centrality dependence compared to the hadronic production. From comparison with model calculations it can be concluded, that the observed excess is very likely due to photon-photon production in hadronic heavy-ion collisions. Future studies of dielectron production in non-central collisions at other heavy-ion experiments should clarify the characteristics of such production mechanism.

1.4.4 Large Hadron Collider

In 2010, the Large Hadron Collider at the European Organisation for Nuclear Research (CERN) brought the heavy-ion physics to TeV scale. Four big experiments (ATLAS, ALICE, CMS and LHCb) study proton–proton, proton–nucleus and lead–lead[3] collisions at unprecedented collision energies and luminosities. The medium created in ultra-relativistic heavy-ion collisions at the LHC energies is expected to reach extreme initial temperatures and essentially zero net baryon density. ALICE is the only large experiment at the LHC designed specifically to study the properties of the hot medium created in such collisions.

The ALICE Collaboration has reported charm and beauty production cross sections at midrapidity ($|y| < 0.5$) in pp collisions at centre-of-mass energies of $\sqrt{s} = 2.76$ and 7 TeV [62, 136–141]. The charm measurement at $\sqrt{s} = 7$ TeV is complemented by ATLAS results extending to higher transverse momentum and $|y| < 2.1$ [142]. Furthermore, the CMS Collaboration has provided a variety of charm and bottom measurements at midrapidity at $\sqrt{s} = 2.76$, 5 and 7 TeV [143–151]. At forward rapidity ($2 < y < 5$), the LHCb Collaboration has measured charm and beauty production cross sections in pp collisions at $\sqrt{s} = 5$, 7, 8 and 13 TeV [152–155]. These results are generally in good

[3] In 2017 LHC has also delivered a short xenon test run.

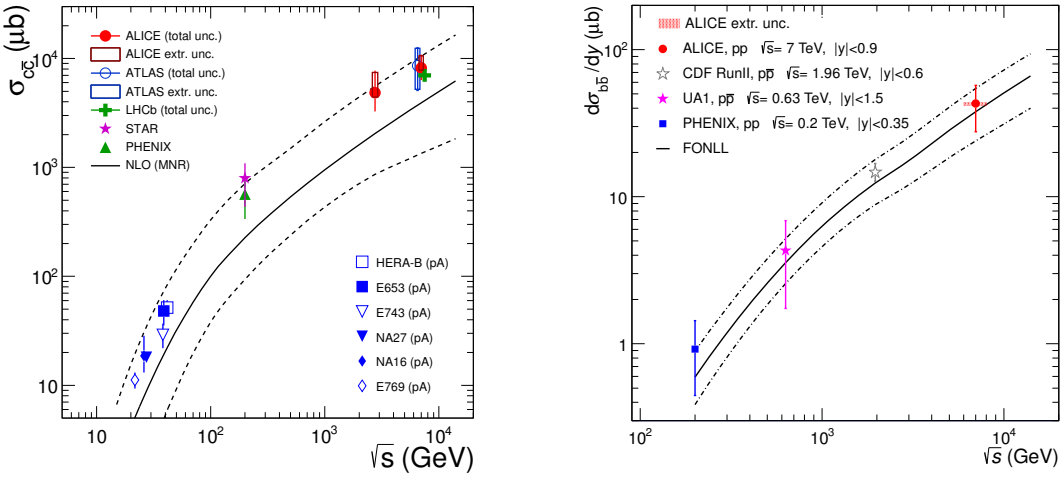

Figure 1.20: Charm (left) and beauty (right) production cross sections in nucleon–nucleon collisions as a function of $\sqrt{s}$ [139, 140]. Results from NLO pQCD calculations and their uncertainties are shown as solid and dashed lines.

agreement with pQCD calculations at next-to-leading order (NLO) in the strong coupling constant α_{s} with all-order resummation of the logarithms of $p_{\mathrm{T}}/m_{\mathrm{Q}}$ (FONLL) [30–32]. However, the measured charm production cross sections consistently lie on the upper edge of the systematic uncertainties of the theory calculations (Fig. 1.20).

In pp collisions at $\sqrt{s} = 2.76$ TeV and 8 TeV, the ALICE Collaboration did not yet observe a significant signal of direct photons for $p_{\mathrm{T}} < 16$ GeV/c in the inclusive photon measurements [73]. However, the results are consistent with expectations from NLO pQCD calculations, which predict a smaller contribution of direct photons to the inclusive photon spectrum with increasing $\sqrt{s}$. In central Pb–Pb collisions at $\sqrt{s_{\mathrm{NN}}} = 2.76$ TeV, an enhancement of the direct photon production similar to that seen at RHIC [76] is observed, with a significance of the direct photon signal in $0.9 < p_{\mathrm{T}} < 2.1$ GeV/c of 2.6σ in central collisions [15]. The inverse slope parameter of $T_{\mathrm{eff}} = 304 \pm 11^{stat} \pm 40^{syst}$ MeV has been extracted with a fit to the data without subtracting contribution from direct pQCD photons (Fig. 1.21). As for the results at RHIC energies, the relation between the initial medium temperature and the inverse slope parameter T_{eff} is not so straightforward due to the large contribution of blue-shifted photons from the late stages of the collision evolution [121]. The results from full direct photon calculations which take into account high radial flow velocities and the photon emission from hadron gas phase have been compared to experimental data. Models assuming the formation of QGP with initial temperatures in the range of $400 - 750$ MeV and early start of hydrodynamical evolution of the system ($\tau_0 = 0.1 - 0.2$ fm/c) are able to describe the spectrum. The elliptic flow of direct photons has been measured

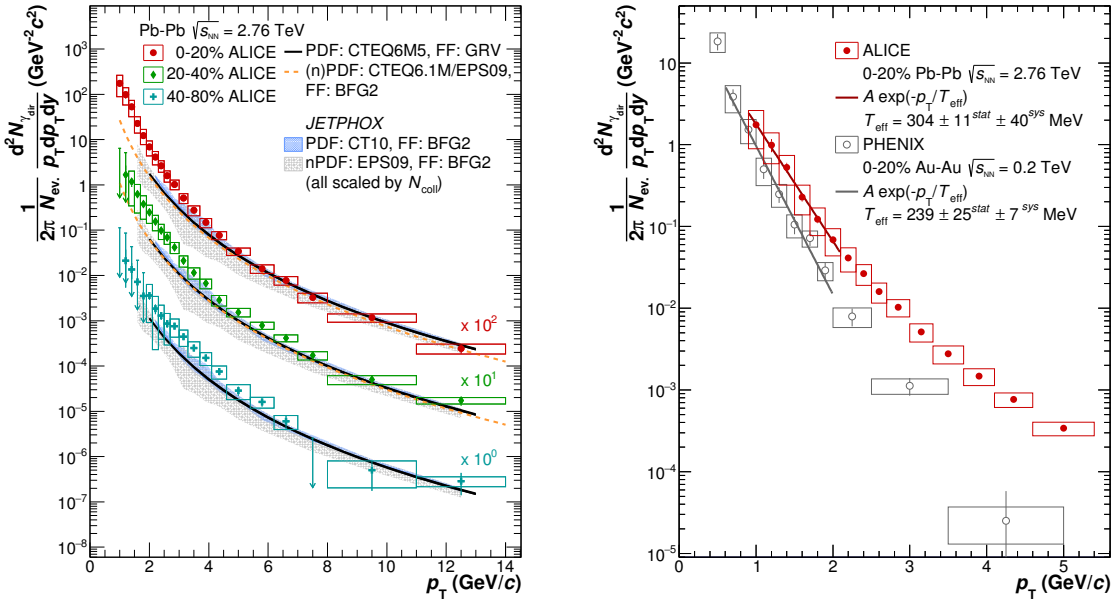

Figure 1.21: Left: the direct photon spectra in Pb–Pb collisions at $\sqrt{s_{\rm NN}} = 2.76$ TeV in different centrality classes compared to NLO pQCD predictions for the direct photon yield in pp collisions at the same energy, scaled by the number of binary nucleon collisions [15]. Right: the direct photon spectra in central heavy-ion collisions at the LHC energy compared to RHIC.

at mid-rapidity in Pb–Pb collisions at $\sqrt{s_{\rm NN}} = 2.76$ TeV and is found to be consistent with zero within (large) uncertainties, with a significance of 1.4σ for central and 1.0σ for semi-central collisions [156]. A comparison to RHIC data shows a similar magnitude of the measured elliptic flow, but large experimental uncertainties prevent any definitive conclusion on direct photon flow at LHC energies. Future measurements using a larger statistics dataset will greatly increase the precision of this measurement.

ALICE Collaboration has recently submitted the results of low-mass dielectron measurements in pp collisions at $\sqrt{s} = 7$ and 13 TeV [157, 158] and in Pb–Pb collisions at $\sqrt{s_{\rm NN}} = 2.76$ TeV [159] for the publication. This thesis presents the results of dielectron production measurements in pp collisions at $\sqrt{s} = 13$ TeV [158]. In inelastic pp collisions, the dielectron yield can be well described by the expectation from a hadronic cocktail calculations based on their independent measurements. The charm and beauty production cross sections at midrapidity have been extracted for the first time at this collision energy by fitting the data in two dimensions, $m_{\rm ee}$ & $p_{\rm T,\,ee}$, using the templates from two Monte Carlo generators (similar to the approach used previously at RHIC [108, 110, 111]). The results are consistent with extrapolations from lower energies based on pQCD calculations, and the sizeable difference in the cross sections between two generators are comparable to what is observed at $\sqrt{s} = 7$ TeV [157]. Fur-

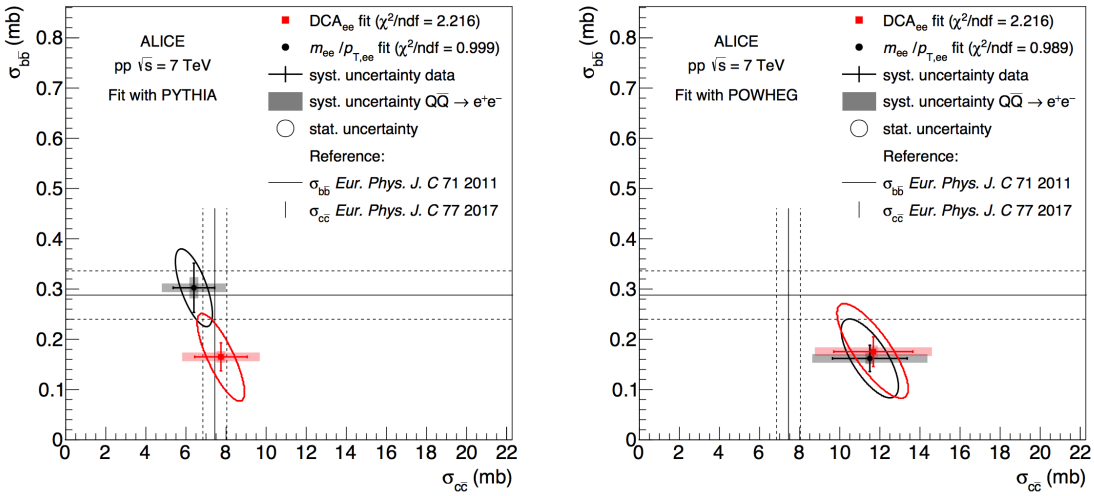

Figure 1.22: Total charm and beauty production cross sections in pp collisions at $\sqrt{s} = 7$ TeV extracted from the fit to the dielectron spectra with Pythia (left) and Powheg (right) [157]. The results are compared to independent single heavy-flavour hadron measurements.

thermore, the dielectron production is studied for the first time in pp collisions with high charged-particle multiplicities. The fraction of direct photons in inclusive photon spectrum is studied in both event classes via the measurement of virtual direct photons in the transverse-momentum range $1 < p_{\mathrm{T}} < 6$ GeV/c, and upper limits for the contribution of virtual direct photons extracted at 90% confidence level are found to be in agreement with pQCD calculations.

In inelastic pp collisions at $\sqrt{s} = 7$ TeV, the dielectron yield can be also described by hadronic cocktail calculations [157]. The total charm and beauty production cross sections have been measured by fitting the data either in two dimensions, m_{ee} & $p_{\mathrm{T,\,ee}}$, or in one dimension, the pair transverse impact parameter[4] $\mathrm{DCA_{ee}}$, using the templates from different Monte Carlo generators. The results agree between two methods within uncertainties, however the extracted charm and beauty cross sections depend on the model used for the fit (Fig. 1.22). In the mass region $0.14 < m_{\mathrm{ee}} < 1.1$ GeV/c^2, the pair $\mathrm{DCA_{ee}}$ variable allows the prompt and non-prompt dielectron sources to be separated and provides an additional variable to disentangle the contributions from $\mathrm{c\bar{c}}$ (with $c\tau \approx 150\,\mu$m for D mesons) and $\mathrm{b\bar{b}}$ (with $c\tau \approx 470\,\mu$m for B mesons). Finally, the ratio of inclusive to decay photons is measured with virtual direct photons in the transverse-momentum range $1 < p_{\mathrm{T}} < 8$ GeV/c. This is found to be unity within the statistical and systematic uncertainties, while also being consistent with expectations

[4] i. e. the average distance of closest approach of the reconstructed electron and positron tracks to the collision vertex normalised by its resolution.

from next-to-leading order pQCD calculations.

The measurement of thermal dielectrons from the QGP is very challenging at the LHC due to the dominant contribution of dilepton pairs from correlated semi-leptonic heavy-flavour decays. In Pb–Pb collisions at $\sqrt{s_{\mathrm{NN}}} = 2.76\ \mathrm{TeV}$, the ratio of the dielectron spectrum and the cocktail of hadronic contributions without vacuum ρ is measured in the invariant mass range $0.15 < m_{\mathrm{ee}} < 0.7\ \mathrm{GeV}/c^2$, where an excess of dielectrons is observed in other experiments, and its value is found to be 1.40 ± 0.28 (stat.) ± 0.08 (syst.) ± 0.27 (cocktail) [159]. The limited sensitivity in the low-mass region due to the low statistics and small signal-to-background ratio prevents any quantitative analysis of a possible excess. The dielectron spectrum measured in the invariant mass range $0 < m_{\mathrm{ee}} < 1\ \mathrm{GeV}/c^2$ is consistent with the predictions from two theoretical model calculations that include thermal dielectron production from both partonic and hadronic phases with in-medium broadened ρ meson [118, 160, 161] (Fig. 1.23). The measured fraction of virtual direct photons is found to be consistent within uncertainties with the measurement of real direct photons and with the expectations from previous dielectron studies at RHIC. The effect of interactions between charm quarks and other partons in the medium was simulated using Pythia event generator assuming two extreme scenarios: complete loss of initial heavy-quark correlation (random correlation for produced $\mathrm{e}^+\mathrm{e}^-$ pair) or absence of any medium modifications (i. e. pure pp simulations scaled by the number of binary nucleon–nucleon collisions). The dielectron yield in the intermediate mass region is found to be consistent with both scenarios and the limited precision prevents any conclusion on energy loss effects on the dielectron spectrum.

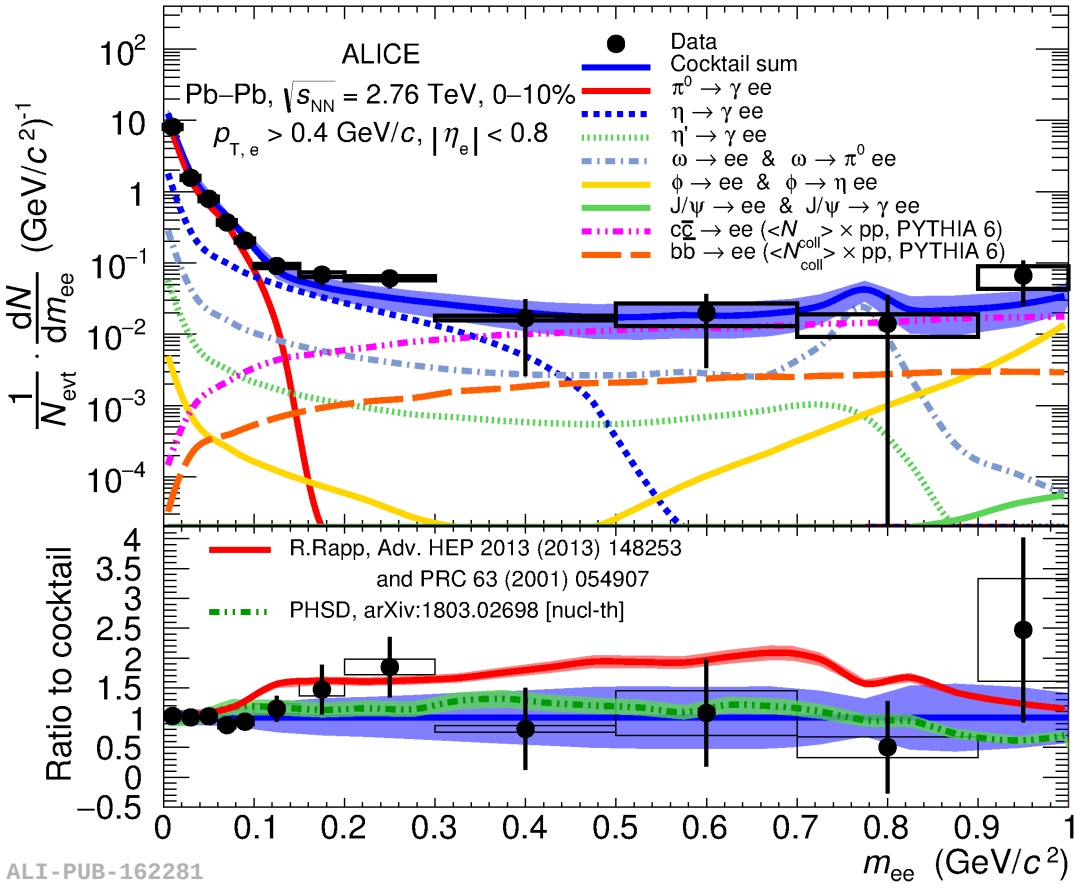

Figure 1.23: Dielectron invariant mass spectrum in Pb–Pb collisions at $\sqrt{s_{\mathrm{NN}}} = 2.76$ TeV in comparison with the predictions from theoretical models that include thermal dielectron production [159].

2
The ALICE Apparatus

ALICE (A Large Ion Collider Experiment) is one of four big experiments situated at the Large Hadron Collider at CERN. With its 10000 tonnes of weight and a size of $26 \times 16 \times 16$ meters it's one of the largest experiment in the world dedicated to the studies of the physics of matter at an infinitely small scale. Its 19 sub-detector systems use different techniques to provide complementary information about each collision happening inside the experiment. ALICE relies on an international collaboration of more than 1800 physicists, engineers and technicians from 176 physics institutes in 41 countries all over the world. The main goal of ALICE is to study the physics of strongly interacting matter at the highest energy densities reached so far in the laboratory and to characterise physical properties of QGP. For this purpose, the experimental data from heavy-ion collisions are studied in details using excellent tracking (down to $p_{\mathrm{T}} = 0.2\,\mathrm{GeV}/c$ at mid-rapidity) and particle identification capabilities of the detector. A detailed description of the ALICE apparatus and its performance can be found in [162–165]. Figure 2.1 shows the schematic view of the ALICE detector during the LHC Run-2 period (2015–2018). The layout of the ALICE detector can be divided into two large parts. The central barrel part, which covers polar angles from 45° to 135° and is embedded in a large solenoid magnet, is used in this thesis to reconstruct charged particle tracks and to identify electrons and positrons produced in collisions. The forward muon arm located at small azimuthal angles ($2^\circ - 9^\circ$) is not used in this thesis and will be mentioned below only shortly.

Trajectories of charged particles are reconstructed in the ALICE central barrel with the Inner Tracking System (ITS) and the Time Projection Chamber (TPC) that reside within a large solenoid re-used from the L3 experiment, which provides a homogeneous magnetic field of $0.5\,\mathrm{T}$ along the beam direction. The track finding and fitting in TPC

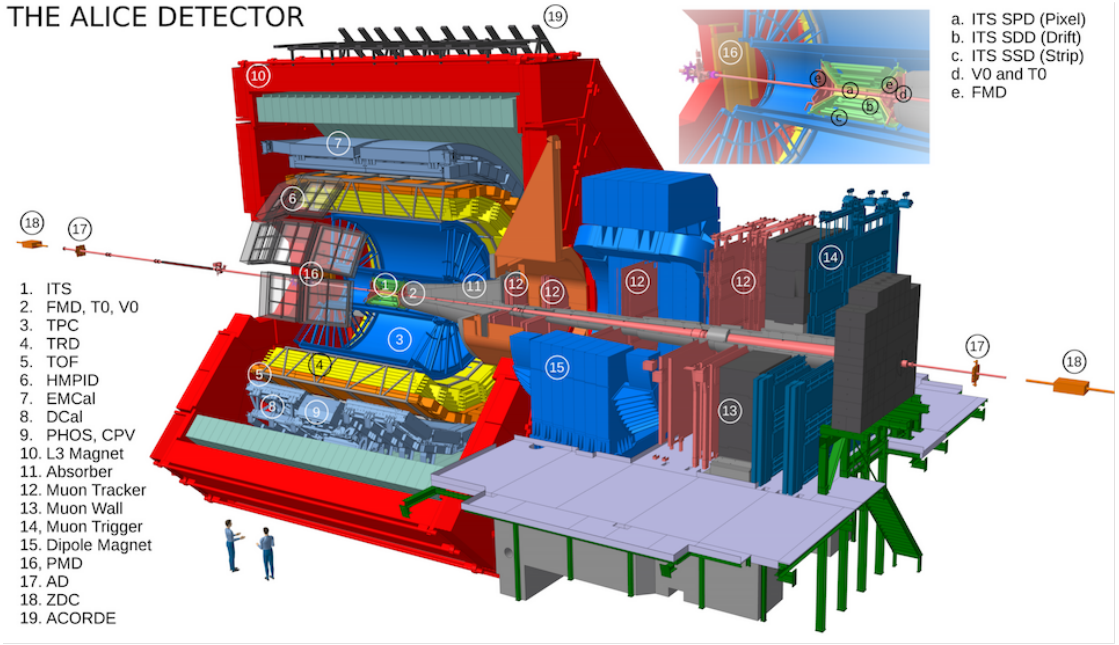

Figure 2.1: Schematic view of the ALICE detector during the Run-2 data taking period (2015–2018) [166]. The Inner Tracking System is shown in more details in the inlay in the top right corner together with some forward detectors located nearby.

and ITS is performed with the help of the Kalman filter technique [167], and the found tracks are matched afterwards to the other central-barrel detectors such as Time-of-Flight (TOF) or Transition Radiation Detector (TRD). Before tracking, the primary interaction vertex is determined using clusters in the first two ITS layers, and its position is then further improved using the fully reconstructed tracks. A search for photon conversions and decays of strange hadrons far from the interaction vertex concludes the central-barrel tracking procedure. After track reconstruction, the bending radius r of the track is used to determine its transverse momentum, which is independent of the particle mass:

$$p_{\mathrm{T}} = 0.3 \frac{\mathrm{GeV}}{\mathrm{Tm}} \cdot qrB, \tag{2.1}$$

where q is the particle charge and B is the magnetic field.

Particle identification (PID) capabilities over a large part of the phase space and for many different particle species is a key design feature of ALICE. Both TPC and ITS detectors provide the PID information through the measurement of specific energy loss of charged particles, either in gas (TPC) or in silicon of the ITS layers. PID at mid-rapidity is complemented by TOF located at larger radial distance, and by TRD, which is optimised to distinguish electrons and pions at momenta above $1\ \mathrm{GeV}/c$ using

Xe/CO_2-filled wire chambers and fibre radiator. A single-arm High-Momentum Particle Identification Detector (HMPID) consists of a $10\,\mathrm{m}^2$ array of ring imaging Cherenkov counters and extends hadron identification capabilities toward higher momenta in about 10% of the central barrel acceptance.

Photons and neutral mesons are measured in a small single-arm PHOton Spectrometer (PHOS) — a high-resolution and high-granularity electromagnetic calorimeter made of dense scintillating crystals ($PbW0_4$). A set of multiwire chambers in front of PHOS acts as a charged particle veto (CPV). An ElectroMagnetic CALorimeter (EMCAL) with lower granularity and energy resolution than PHOS, but much larger acceptance, is a Pb-scintillator calorimeter optimised to measure jet production and fragmentation functions in conjunction with the charged particle tracking in other barrel detectors. In order to extend jet measurements to di-jet studies, a second (identical, but with smaller acceptance) calorimeter has been installed in the central barrel opposite to the EMCAL — the Di-Jet CALorimeter (DCAL). Forming together with EMCAL a two-arm electromagnetic calorimeter, it provides larger acceptance and much stronger capabilities for back-to-back correlation measurements of jets, photons and neutral mesons.

The charm and bottom resonance states J/ψ, ψ' and Υ, Υ', Υ'' are studied in ALICE with the muon arm located at forward rapidity ($-4 < \eta < -2.4$), which provides good acceptance down to zero p_T and a mass resolution sufficient enough to separate all states. It consists of composite absorber, a large dipole magnet (placed outside the L3 magnet) and 10 planes of thin cathode strip tracking stations with high granularity. A second absorber behind the spectrometer and four planes of Resistive Plate Chambers are used for muon identification and triggering.

A number of small detectors located close to the beam pipe are used for triggering and to measure global event characteristics. The event collision time is measured with very good precision ($< 25\,\mathrm{ps}$) by T0 detector comprising two sets of 12 Cherenkov counters each. The V0 detector, two arrays of segmented scintillator counters, is used as minimum-bias trigger and for rejection of background events such as beam–gas interactions. The multiplicity information at large rapidities is provided by the Forward Multiplicity Detector (FMD), which counts charged particles in rings made of silicon strip detectors. The Photon Multiplicity Detector (PMD) consists of two planes of gas proportional counters and measures the multiplicity and spatial distribution of photons in the region $2.3 < \eta < 3.7$. The Zero Degree Calorimeter (ZDC) comprises two sets of two compact calorimeters each, which are used to measure the impact parameter of collision. Since protons which did not participate in a collision are spatially separated from neutrons by the magnetic elements of the LHC beam line, each ZDC set is made by two distinct detectors: one for spectator neutrons (ZN), placed between the beam pipes at 0° relative to the LHC axis, and one for spectator protons (ZP), placed externally to the outgoing beam pipe on the side where positive particles are deflected. On top of the L3 magnet an array of scintillators called ACORDE (ALICE COsmic Ray DEtector) is

used to trigger on cosmic ray particles for calibration and alignment purposes [168], as well as for cosmic ray physics [169].

The hardware trigger in ALICE combines the input from many detectors with fast trigger capability (T0, V0, ZDC, SPD, TOF, TRD, PHOS, EMCal, Muons, ACORDE). The trigger system includes a flexible protection against pile-up and background events and an event priority scheme to optimise the acceptance of rare triggers as well as the overall throughput of accepted events. The High-Level Trigger (HLT), a computing farm currently consisting of 4480 CPU cores operating at $2.7\,\mathrm{GHz}$, selects on-the-fly the relevant part of the huge amount of incoming data and reduces the data volume by orders of magnitude while preserving the physics information of interest. During heavy-ion data taking, the Data AcQuisition system (DAQ) copes with very large data flow of up to several GB/s from detector to permanent storage, which is achieved by combination of a custom optical data link, used throughout the experiment, with commodity equipment (PCs and network switches) in a highly parallel and scalable architecture.

ALICE is studying proton–proton and proton–nucleus collisions both as a baseline for the interpretation of results from nucleus–nucleus collisions and in their own right. Experimental data from different collision systems (pp, p–Pb and Pb–Pb) at various collision energies provided by the LHC have been recorded during several periods of LHC operations, which can be denoted as Run-1 (2010–2013), Run-2 (2015–2018) and, in future, Run-3 (2021–2023) and beyond. Four detector sub-systems used extensively in this analysis are described below in more detail: the Inner Tracking System, the Time Projection Chamber, the Time-of-Flight detector and the V0 scintillators.

2.1 Inner Tracking System

The ITS consists of six cylindrical layers of silicon detectors, with radial distances from the beam axis of 4, 7, 15, 24, 39 and 44 cm (Fig. 2.2). It covers the rapidity range of $|\eta| < 0.9$ for all vertices located within the length of the interaction diamond, i.e. $\pm 10\,\mathrm{cm}$ around the nominal interaction point along the beam direction. It is the detector closest to the collision vertex and, therefore, is exposed to large particle densities, especially in Pb–Pb collisions (as many as 50 particles per cm^2 for the innermost layer). This drives the design of the four innermost layers as truly two-dimensional devices, which are based on silicon pixel (SPD, two innermost ITS layers) and silicon drift detectors (SDD, two intermediate ITS layers). In such semiconductor detectors, ionising radiation is measured by the number of charge carriers (electrons and holes) set free in the material arranged between two electrodes, with the number of electron-hole pairs proportional to the energy of the radiation. Electrons which are transferred from the valence band to the conduction band travel to the electrodes under the influence of an electric field, where they result in a pulse that can be measured. SPD consists of a two-dimensional matrix of reverse-biased silicon detector diodes with binary readout: in each cell, a threshold

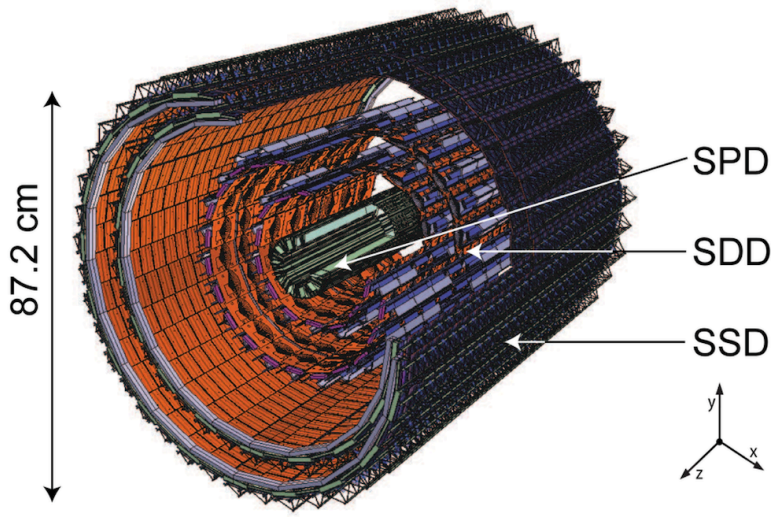

Figure 2.2: Layout of the ITS detector [168].

is applied to the pre-amplified and shaped signal. The digital output level changes when the signal is above a set threshold. SDDs, like gaseous drift detectors, exploit the measurement of the transport time of the charge deposited by a traversing particle to localise the impact point in one of the dimensions, thus enhancing resolution and multi-track capability at the expense of speed. The two outer layers are equipped with double-sided silicon micro-strips (SSD). The four outer layers have analogue readout, with a signal amplitude proportional to the energy loss in detector material. Therefore, SDD and SSD layers can be used for particle identification via the measurement of specific energy loss in the non-relativistic region.

The basic tasks of the inner tracker include the following:

- Localisation of the primary collision vertex and secondary vertices from charmed meson and hyperon decays with a resolution better than $100\,\mu\mathrm{m}$
- Improvement of the impact parameter and momentum resolution of charged particle tracks reconstructed in the TPC
- Tracking and identification of particles with $p_{\mathrm{T}} < 200\ \mathrm{MeV}/c$ which are not detected in the TPC

The ITS therefore contributes to practically all physics topics addressed by the ALICE experiment. For this thesis, the ITS detector is used for the reconstruction of the primary collision vertex as well as for the rejection of pile-up and background events as discussed in Chapter 3. Together with the TPC detector it is used for the charged-particle tracking in the ALICE central barrel acceptance ($p_{\mathrm{T}} > 0.2\,\mathrm{MeV}/c$ and $|\eta| < 0.8$). For minimum ionising particles with transverse momenta between $100\ \mathrm{MeV}/c$ and $3\ \mathrm{GeV}/c$ the relative momentum resolution achievable with the ITS is better than 2% [162]. For charged

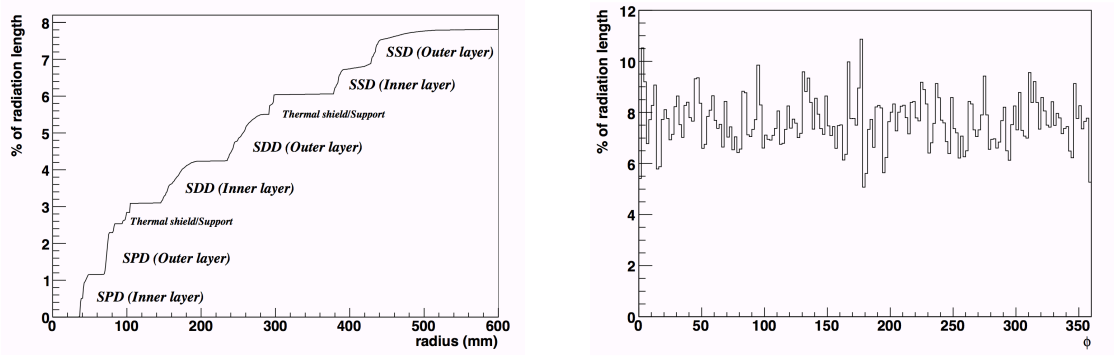

Figure 2.3: ITS material thickness traversed by a perpendicular track originating from the primary vertex versus radius (left) and azimuthal angle (right) [164].

particles with transverse momenta $p_{\mathrm{T}} > 1\ \mathrm{GeV}/c$, the distance of closest approach (DCA) resolution in the plane transverse to the beam direction is better than $75\,\mu\mathrm{m}$.

Since the momentum and impact parameter resolution for low-momentum particles are dominated by multiple scattering effects in the detector material, the amount of material has been kept to a minimum, which is another key feature of the ITS detector. The effective integrated thickness, including electronics, cabling, support structure, and cooling system, amounts to just $\sim 8\%$ of radiation length X_0. Fig. 2.3 shows the ITS material thickness as a function of radius and azimuthal angle for a perpendicular track originating from the primary vertex. For this analysis, the low ITS material budget is of importance as it reduces the conversion probability for real photons, which are reconstructed as $\mathrm{e}^+\mathrm{e}^-$ pairs. Such pairs do not only contaminate the physical signal at very low ($m_{\mathrm{ee}} < 100\ \mathrm{MeV}/c^2$) invariant mass, but also contribute to the combinatorial background (Chapter 3).

2.2 Time Projection Chamber

The TPC is the main charged-particle tracking device in the ALICE central barrel and is with $5\,\mathrm{m}$ length and a radius extending from $85\,\mathrm{cm}$ to $247\,\mathrm{cm}$ the largest TPC detector in the world. Despite of the drawbacks concerning speed and data volume, only such a device can guarantee efficient and robust tracking with reliable PID performance when $\sim$10000 charged particles are produced within its acceptance in central Pb–Pb collisions. Figure 2.4 (left) shows a schematic view of the ALICE TPC. A large cylindrical field cage of the TPC surrounds the gas volume, which was Ar/CO_2 gas mixture (with abundances of 88/12) in 2016 and Ne/CO_2/N_2 (90/10/5) in 2017. Both gas mixtures are characterised by low diffusion, low atomic number and large ion mobility. These requirements are needed for a good momentum and PID resolution, and to guarantee the

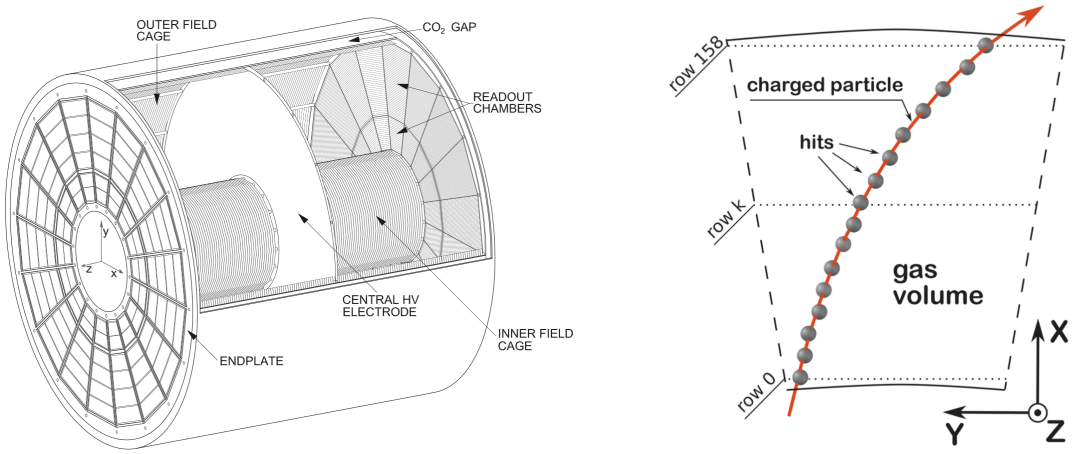

Figure 2.4: Schematic layout of the ALICE TPC (left) and the sketch of TPC tracking (right) [164].

highest possible data acquisition rate. Charged particles traversing the gaseous volume of the TPC cause an ionisation of gas atoms and produce electrons and ions. The electric field of $400\,\mathrm{V/cm}$, applied between the central electrode and the end plates, transports the electrons towards the endplates with a drift velocity of $2.7\,\mathrm{cm/\mu s}$ ($92\,\mu\mathrm{s}$ maximum drift time). To keep the occupancy low and to ensure necessary energy loss, position and two-track resolution, there are about 560 000 readout pads on both end plates grouped in 18 azimuthal sectors.

The position measurement at the endplates allows the reconstruction of a two dimensional projection of the particle trajectory in the xy plane, transverse to the beam direction (Fig. 2.4 right). The third dimension along the beam direction is reconstructed from the arrival time at the endplates relative to the event collision time. For this measurement, it is important to ensure an approximately constant drift velocity of the electrons from ionisation, which depends on several external parameters such as temperature or pressure. These parameters are constantly monitored during the data taking, and the corresponding calibrations are continually applied to the drift velocity. In this way the complete trajectory in space is precisely determined for all charged particles. In total, the TPC provides up to 159 spacial points per track for charged-particle reconstruction and particle identification, each point being provided by a pad row.

The PID is performed by simultaneously measuring the specific energy loss $\mathrm{d}E/\mathrm{d}x$ and momentum of each particle traversing the detector gas. The mean rate of energy loss by a relativistic charged-particle is well described by the Bethe-Bloch formula:

$$\left\langle -\frac{dE}{dx} \right\rangle = Kz^2 \frac{Z}{A} \frac{1}{\beta^2} \left[\frac{1}{2} \ln \frac{2m_e c^2 \beta^2 \gamma^2 W_{max}}{I^2} - \beta^2 - \frac{\delta(\beta\gamma)}{2} \right] \tag{2.2}$$

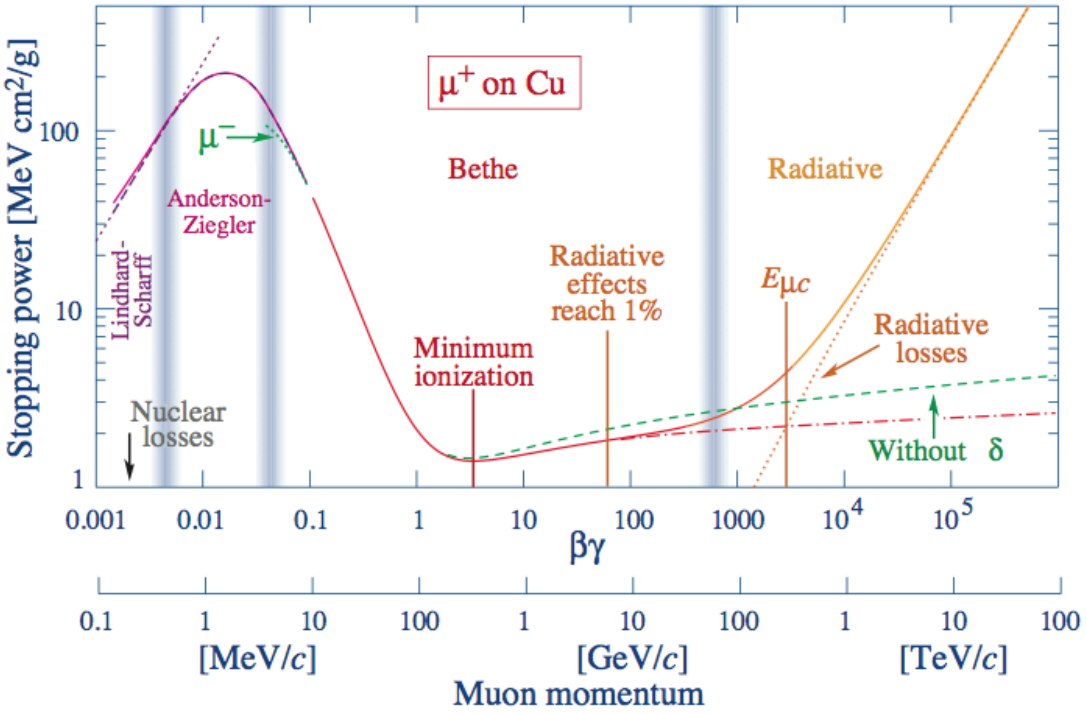

Figure 2.5: Specific energy loss $\mathrm{d}E/\mathrm{d}x$ for positive muons in copper as a function of $\beta\gamma = p/Mc$ over the wide range of muon's kinetic energy. The region between second and third vertical bands denoted as "Bethe" corresponds to the kinetic range in which Bethe-Bloch parametrisation is applicable.

Here β and γ are particle velocity $\beta = v/c$ and Lorentz factor $\gamma = 1/\sqrt{1-\beta^2}$ correspondingly, and Z denotes the atomic number of the absorbing material. In the region $0.1 \lesssim \beta\gamma \lesssim 1000$ and for intermediate-Z materials it describes the mean rate of energy loss with an accuracy of a few percent [50]. Fig. 2.5 shows an example of $\mathrm{d}E/\mathrm{d}x$ for the positive muons in copper over wide range of muon's kinetic energy. In a given material and in the momentum range of $0.1 \lesssim \beta\gamma \lesssim 1000$, $\mathrm{d}E/\mathrm{d}x$ is approximately a function of particle $\beta \cdot \gamma$ only, therefore for fixed momentum $p = m\beta\gamma$ particles with different mass m will have different energy loss. Formula in Eq. 2.2 can be parametrised by the following function originally proposed by the ALEPH collaboration [170]:

$$f(\beta\gamma) = \frac{P_1}{\beta^{P_4}} \left(P_2 - \beta^{P_4} - \ln(P_3 + \frac{1}{(\beta\gamma)^{P_5}}) \right), \tag{2.3}$$

where P_{1-5} are fit parameters. Fig. 2.6 shows $\mathrm{d}E/\mathrm{d}x$ in the TPC measured in pp collisions at $\sqrt{s} = 13$ TeV as a function of the particle momentum. It also clearly demonstrates the separation between electrons and pions over the wide momentum range, which

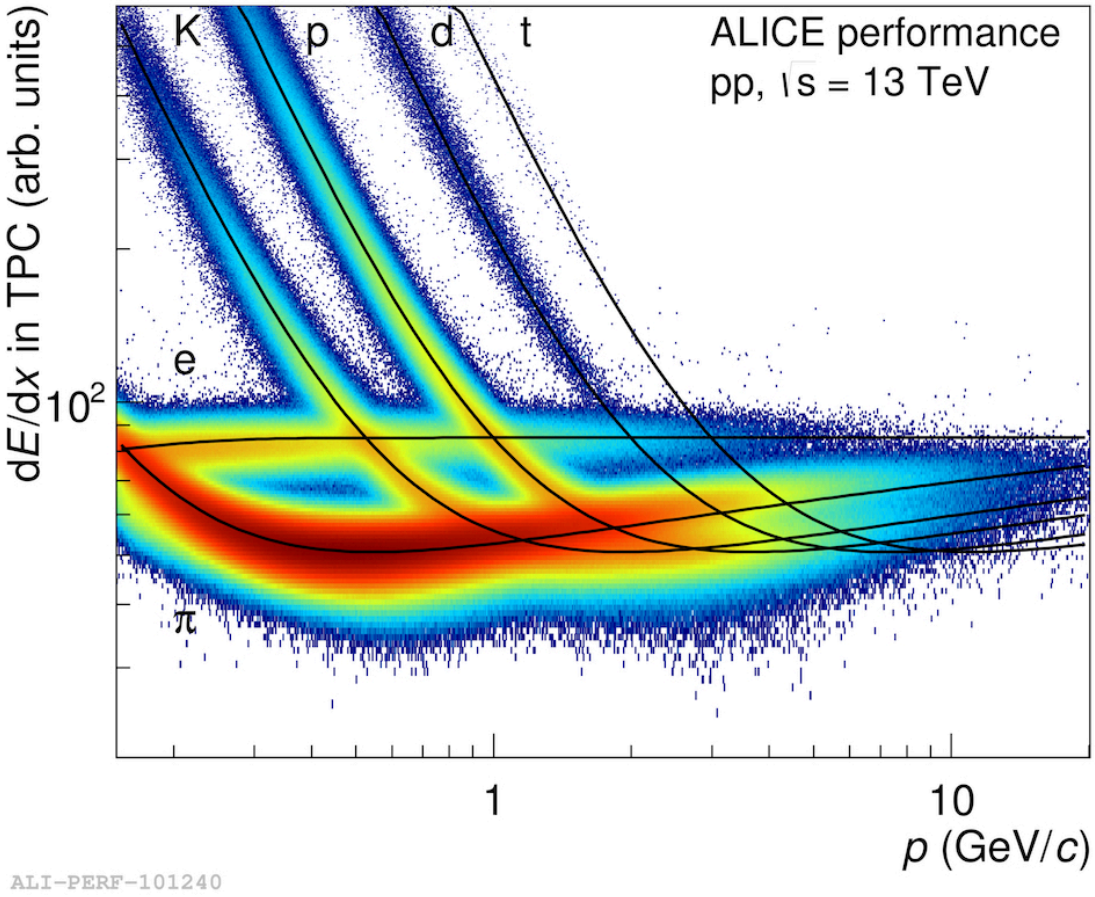

Figure 2.6: Specific energy loss $\mathrm{d}E/\mathrm{d}x$ in the TPC as a function of particle momentum in pp collisions at $\sqrt{s} = 13$ TeV [166]. The lines show the parameterisations of the expected mean energy loss for a given particle specie according to the Eq. 2.3.

is essential for this analysis. However, at $p \approx 0.5$ and $1\ \mathrm{GeV}/c$ electrons in the TPC are indistinguishable from kaons and protons correspondingly. To suppress hadron contamination in these regions, a complementary PID information from the TOF detector is used in this thesis.

The inner radius of the TPC is determined by the maximum acceptable hit density, the outer radius of $2.5\ \mathrm{m}$ by the length required for achieving $\mathrm{d}E/\mathrm{d}x$ resolution of better than 5–7% [164]. This resolution is necessary to provide particle identification in the region of the relativistic rise up to momenta of $\sim 50\ \mathrm{GeV}/c$. Good two-track resolution is provided by position resolution of 1100 to $800\ \mu\mathrm{m}$ (at inner/outer radius) in $r\phi$ direction and 1250 to $1100\ \mu\mathrm{m}$ in z. The TPC-standalone momentum resolution (better than 5% for the momentum region below $20\ \mathrm{GeV}/c$) can be significantly improved with the usage of combined ITS+TPC information (Fig. 2.7).

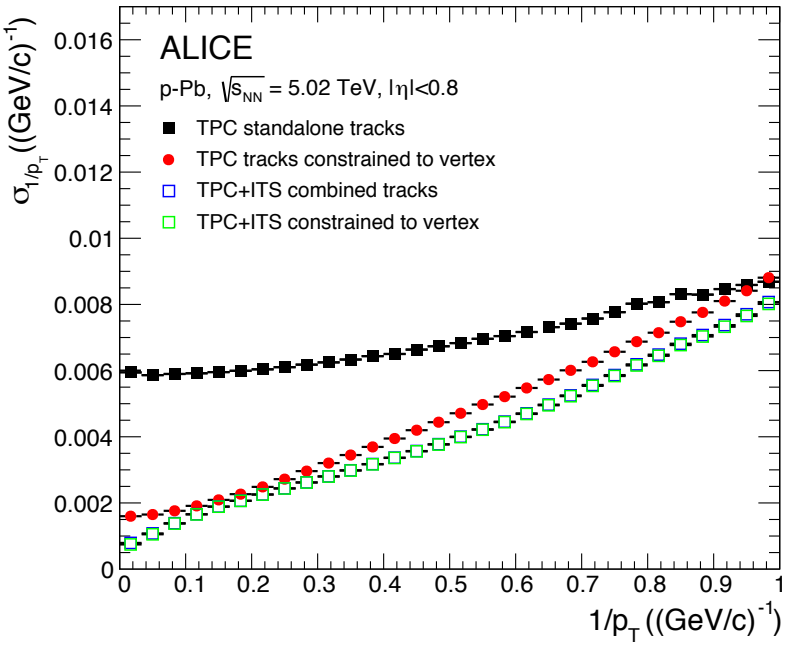

Figure 2.7: The transverse momentum resolution for standalone TPC and for TPC+ITS matched tracks with and without constraint to the vertex [165].

2.3 Time-of-Flight Detector

In the ALICE central barrel the particle identification capabilities of ITS and TPC are complemented by the Time-Of-Flight detector. It provides the arrival time of the particle, which together with the event collision time is used to define the time of flight from the interaction point up to the detector itself. The TOF array covers an area of $\approx 140\,\mathrm{m}^2$ with 160 000 individual cells at a radial distance from $370\,\mathrm{cm}$ to $399\,\mathrm{cm}$ from the nominal interaction point. The requirement for an affordable system with a large number of channels, an occupancy at around 10% or below as well as time resolution of better than $100\,\mathrm{ps}$, was accomplished with Multigap Resistive Plate Chambers (MRPC) [171]. The key aspect of these chambers is that the electric field is high and uniform over the full sensitive gaseous volume of the detector. Any ionisation produced by a traversing charged particle immediately starts a gas avalanche process which generates the observed signals on the pick-up electrodes, so that, unlike other types of gaseous detectors, there is no drift time associated with the movement of the electrons to a region of high electric field. Double-stack MRPC strips each $122\,\mathrm{cm}$ long and $13\,\mathrm{cm}$ wide are placed inside the gas-tight modules and are positioned transversely to the beam direction. Five such modules in a row compose one supermodule, which is installed inside a framework of longitudinal and transverse aluminium beams in each of the 18 sectors matching the TPC sectors. A schematic layout of one supermodule inside the ALICE spaceframe is shown

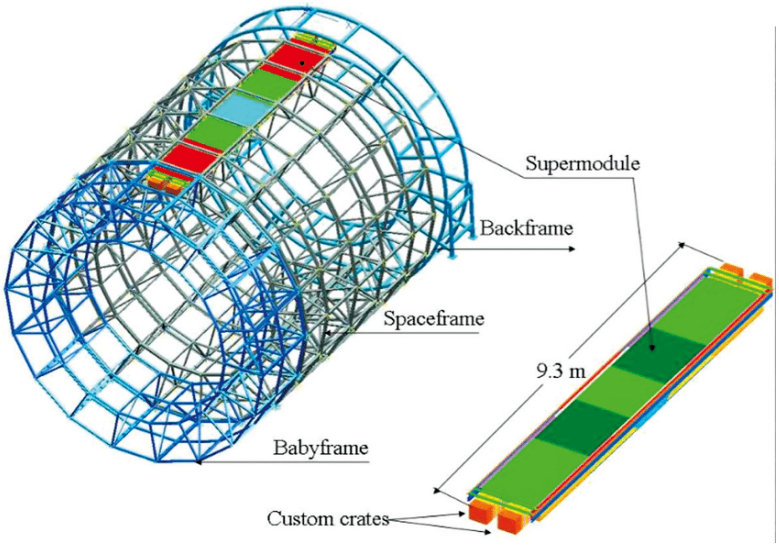

Figure 2.8: Schematic drawing of one TOF supermodule in the ALICE spaceframe [164].

in Fig. 2.8.

The arrival time of the particles is measured relative to the event collision time provided by the T0 detectors with very good precision (< 25 ps) as $t_{\mathrm{ev}}^{\mathrm{T0}} = (t_{\mathrm{T0A}} + t_{\mathrm{T0C}})/2$, where t_{T0A} and t_{T0C} correspond to the fastest signals among T0A and T0C photomultipliers correspondingly. The event collision time can be also estimated by the TOF detector itself on an event-by-event basis by means of a χ^2-minimisation procedure [172]. For a known momentum p and track length l, the time of flight can be related to the particle velocity and mass as:

$$\beta = \frac{l}{t_{TOF}c} \tag{2.4}$$

$$m = \frac{p}{\beta\gamma} = \frac{p}{c}\sqrt{\frac{c^2 t_{TOF}^2}{l^2} - 1}. \tag{2.5}$$

Due to their curved paths in the magnetic field of the solenoidal magnet, charged particles need a minimum p_{T} of about 300 MeV/c to reach the TOF detector. For particle momenta below $\sim$2.5 GeV/c TOF is capable to distinguish between electrons/pions and kaons, and below $\sim$4 GeV/c between kaons and protons, with a π/K and K/p separation better than 3σ [163], where σ denotes the detector resolution. The resulting $\beta = v/c$ of charged particles produced in pp collisions at $\sqrt{s} = 13$ TeV is shown in Fig. 2.9.

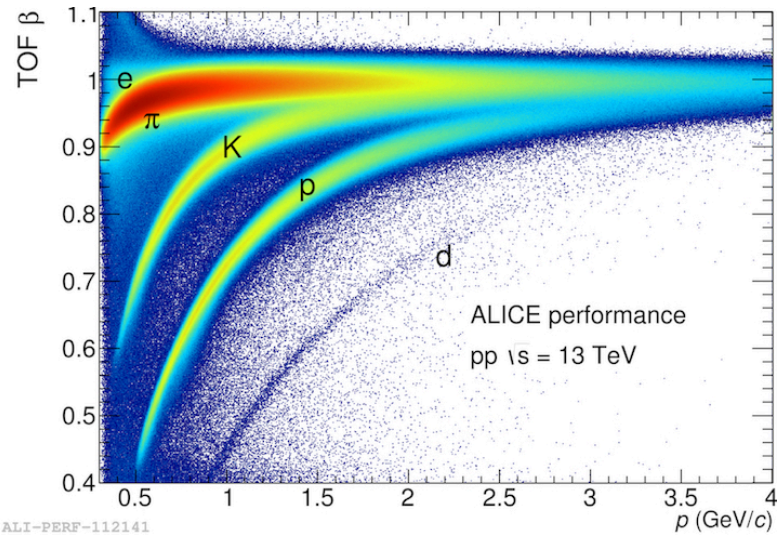

Figure 2.9: TOF β as a function of particle momentum in pp collisions at $\sqrt{s} = 13\,\mathrm{TeV}$ [166].

2.4 V0 Scintillators

The V0 detector comprises two plastic scintillator arrays (V0A and V0C) placed on both sides of the interaction point at $340\,\mathrm{cm}$ (V0A) and at $-90\,\mathrm{cm}$ (V0C) from the interaction vertex covering the pseudorapidities $2.8 < \eta < 5.1$ and $-3.7 < \eta < -1.7$ respectively (Fig. 2.10). The material consists of BC404 scintillating material ($2.5\,\mathrm{cm}$ and $2.0\,\mathrm{cm}$ in thickness for V0A and V0C respectively) with Wave-Length Shifting (WLS) fibres of $1\,\mathrm{mm}$ diameter. In total there are 32 elementary counters arranged in 4 rings and 8 sectors of $45°$.

The V0 detector has several functions. First, it provides fast "minimum-bias" trigger for inelastic pp collisions for the central barrel detector, i. e. a trigger aiming at detection of possibly largest fraction of inelastic events without introducing significant selection bias. This trigger requires coincident signal[1] on both sides of V0 detector ("V0AND" trigger logic). This requirement reduces significantly the amount of triggered background events like interactions of the beam with residual gas inside the beam pipe or with mechanical structures of the beam line, since such collisions do not produce particles in both V0A and V0C detectors.

As the dependence between the number of registered particles on the V0 arrays and the number of primary emitted particles is monotone, the V0 serves as an indicator of the event activity via the multiplicity recorded in the event. Cuts on the number of fired counters and on the total charge can be applied to achieve rough multiplicity triggers.

[1] More precisely, $11\,\mathrm{ns}$ after the collision on V0A and $3\,\mathrm{ns}$ after the collision on V0C due to the non-symmetric detector geometry.

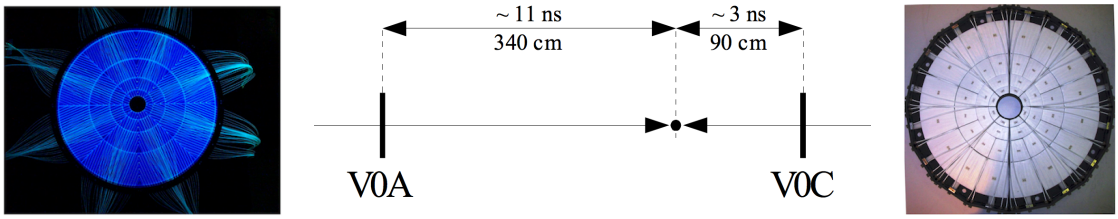

Figure 2.10: Schematic view of the V0 detector geometry. Front views of each individual scintillator array are shown on the left (V0A) and right (V0C) sides. [164]

In this analysis the V0 detector provides also high-multiplicity trigger for pp collisions, which follow the same trigger logic as minimum-bias one by requiring coincident signal on both V0 sides, with a total measured V0 multiplicity (V0M) above a certain threshold.

3 Analysis

This Chapter discusses the analysis of experimental data in detail. The analysis of inelastic and high-multiplicity data samples follow essentially the same technique, so they are discussed in parallel, with the differences highlighted if present. The data analysis begins with the selection of good collision events (Section 3.1), followed by the charged-particle track and electron selection discussed in Section 3.2. The pairing of single electron and positron candidates and the pair analysis is described in Section 3.3. The resulting raw dielectron distributions are corrected for the reconstruction and trigger efficiencies as discussed in Section 3.4 and Section 3.5 presents the calculation of expected dielectron production from hadron decays (the so-called hadronic "cocktail"). Systematic checks and the evaluation of systematic uncertainties conclude this Chapter in Section 3.6.

3.1 Datasets and Event Selection

The data samples used in this analysis have been recorded with the ALICE detector in 2016 and 2017 during the LHC proton–proton run at $\sqrt{s} = 13\ \mathrm{TeV}$ (with the nominal B-field strength of $0.5\ \mathrm{T}$ in the ALICE central barrel). The minimum-bias event trigger, which is used to define the data sample for the analysis of inelastic pp collisions, require coincident signals in both V0 scintillators to be synchronous with the beam crossing time defined by the LHC clock. On average, an inelastic pp collision at $\sqrt{s} = 13\ \mathrm{TeV}$ produces at mid-rapidity about 5 charged particles per unit of rapidity [42]. To enhance the sample of events with high multiplicities, these events are triggered on with V0 de-

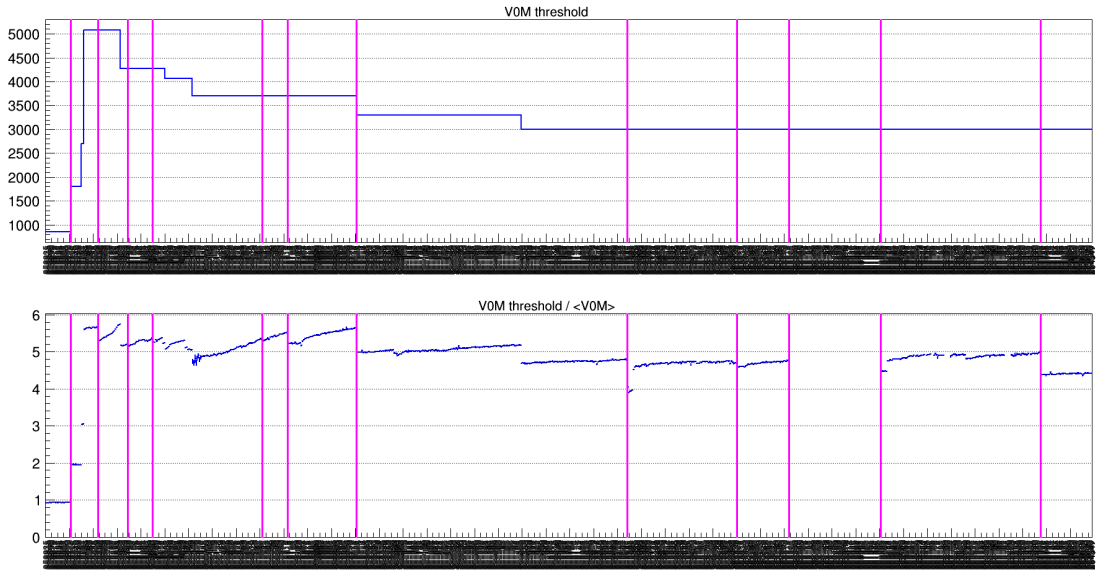

Figure 3.1: V0 high-multiplicity trigger threshold (top) and the ratio "threshold / mean multiplicity" (bottom) as a function of run number during 2016 pp data taking [173]. All 2016 data are shown, including some periods which are not used for the analysis.

tector by additionally requiring the total signal amplitude measured in the V0 detector (V0M) to exceed a certain threshold, i. e. by triggering on events located in the tail of V0M distribution.

Due to the continuous ageing effect in V0 photomultipliers[1], high-multiplicity trigger threshold has been adjusted several times in order to keep the trigger selection factor at around the same level of $\sim 0.1\%$, which corresponds to a factor of ~ 5 in the V0M multiplicity (Fig. 3.1). In order to avoid trigger inefficiencies due to threshold variations during data taking, an information from the V0 detector is used for triggered events to select 0.05% of events with the highest V0 multiplicity. In this interval, the V0 multiplicity percentile distribution is flat and the high-multiplicity trigger is fully efficient (Fig. 3.2). For the calibration of events in each run, the mean V0 multiplicity is used as reference point, so the overall V0 ageing effect is taken into account in the percentile distribution. No V0 multiplicity selection is applied for the minimum-bias event class.

Figure 3.2 also shows the V0M distributions in high-multiplicity and minimum-bias events. Since the V0M distribution in high-multiplicity events corresponds to the tail of the minimum-bias distribution, no additional bias is introduced by such a selection. The resulting correlation between the V0M and the charged-particle reference multiplicity at mid-rapidity $|\eta| < 0.5$ is shown in Fig. 3.3. In both event classes a monotonic increase of reference multiplicity at mid-rapidity with V0M amplitude is found in wide V0M

[1]For minimum-bias trigger V0 ageing effect didn't play any significant role.

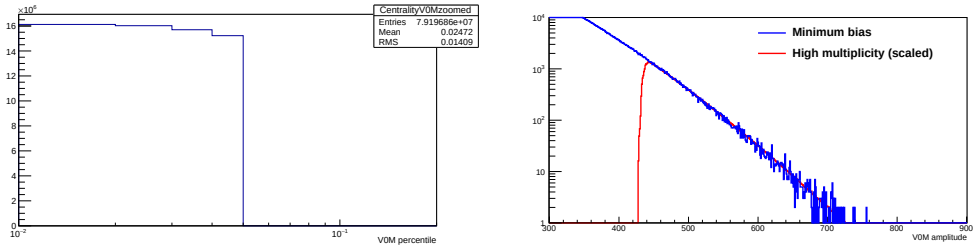

Figure 3.2: Left: V0M percentile distribution in high-multiplicity events (selection on 0–0.05% is applied). Right: V0M amplitude distributions in minimum-bias (tail of the distribution) and high-multiplicity events.

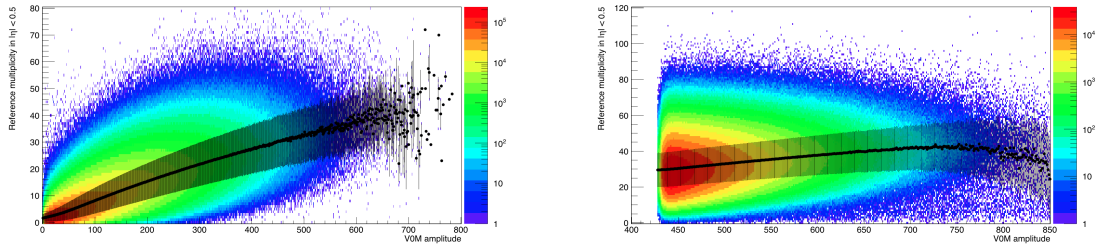

Figure 3.3: Correlation between V0M amplitude and reference multiplicity at mid-rapidity in minimum-bias (left) and high-multiplicity (right) events. Black points show mean values of reference multiplicity for each V0M amplitude value, and the error bars correspond to RMS of the distribution.

amplitude range. As a result, the multiplicity enhancement factor of the collected data samples measured with V0 detector amounts to ~ 5.4, which transforms to a multiplicity enhancement factor at mid-rapidity of:

$$\mathrm{d}N_{\mathrm{ch}}^{\mathrm{acc}}/\mathrm{d}\eta(\mathrm{HM})/\langle \mathrm{d}N_{\mathrm{ch}}^{\mathrm{acc}}/\mathrm{d}\eta(\mathrm{MB})\rangle|_{\eta=0} = 4.54$$

The conditions of pp data taking such as the inelastic interaction rate, the number of colliding bunches or the average number of inelastic collisions varied during 2016 and 2017, as can be seen in Fig. 3.4 for 2016 pp data. A proper rejection of background events such as beam-gas interactions or collisions with debunched protons is an essential part of the event analysis. Moreover, several pp collisions happened close in time can produce a "pile-up" of events in slow detectors such as the TPC, which is reconstructed as single event with artificially enhanced multiplicity. Such events can originate either from collisions of protons from different bunch crossings (when the separation between proton bunches circulating in the LHC is small, i. e. when the number of colliding bunches

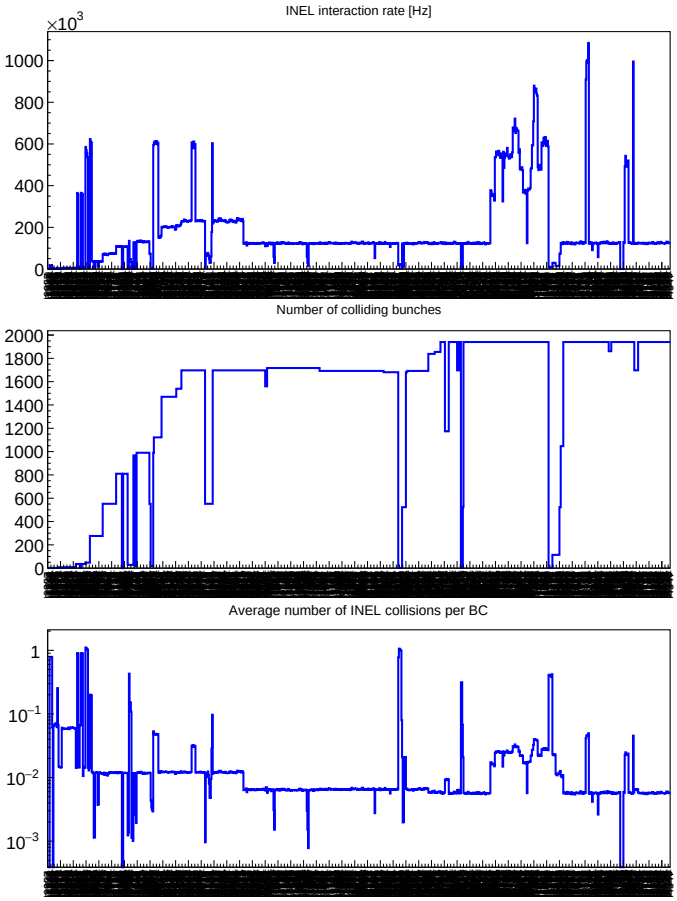

Figure 3.4: The data-taking conditions as a function of run number in 2016. All runs from 2016 data are shown, including those which are not used for the current analysis [173].

and the inelastic interaction rate are high) or from multiple collisions within the same bunch (when the average number of inelastic collisions per bunch crossing is high). In order to reject these events, several criteria based on the information from fast detectors (V0 and SPD) are required to be fulfilled by each collision, so that only good physical events pass the selection. Figure 3.5 shows as an example the correlation between the number of SPD tracklets (i. e. track segments of two hits extrapolated back to the beam line) and the number of SPD clusters in minimum-bias and high-multiplicity triggered events. In contrast to the number of SPD tracklets, which are required to point back to the reconstructed primary vertex, the number of SPD clusters is sensitive to pile-up events and beam-gas interactions, so such events appear as outliers from the main diagonal correlation. Moreover, events are rejected if a secondary pile-up interaction vertex is reconstructed with SPD tracklets using a multiplicity-dependent algorithm. The

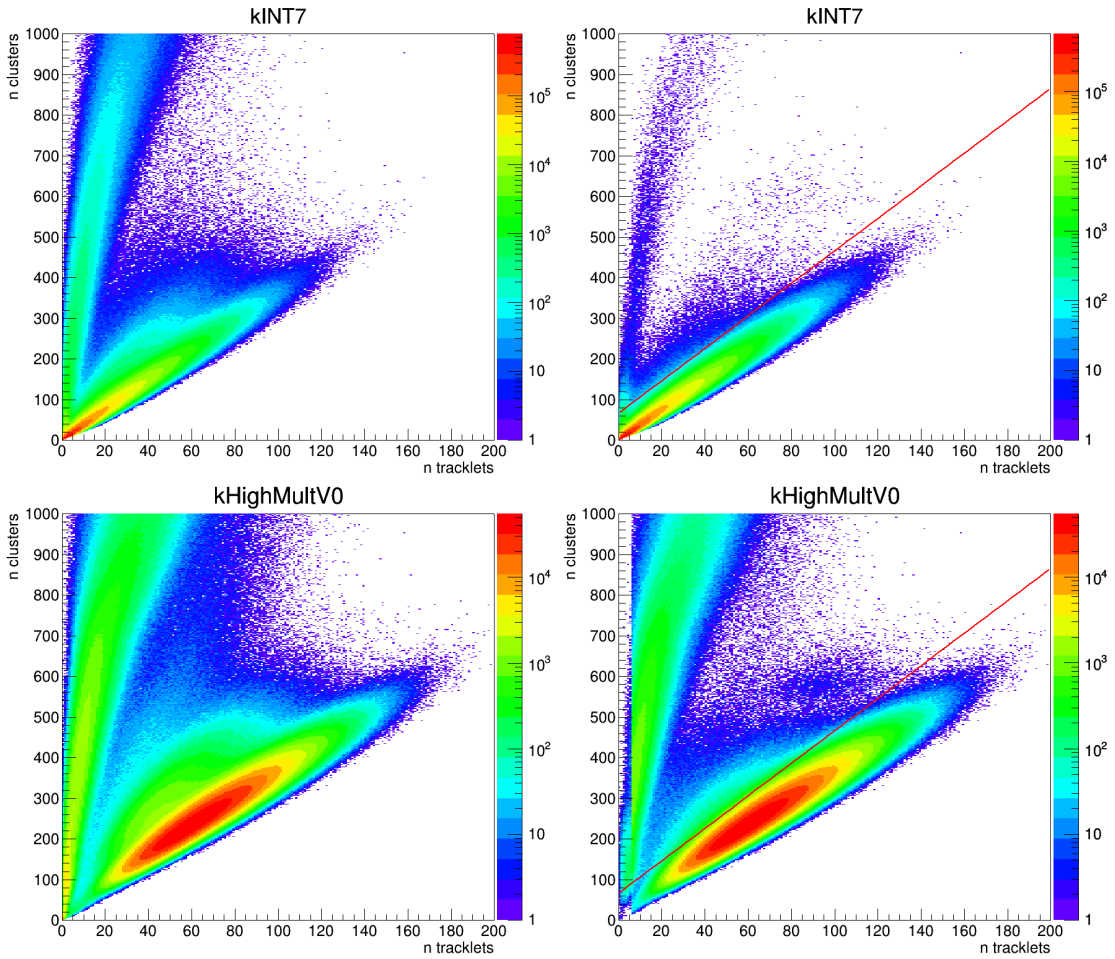

Figure 3.5: The correlation between the number of SPD tracklets and the number of SPD clusters in all triggered events (left) and in events cleaned up by other background rejection criteria but SPD tracklet-vs-cluster correlation (right) [173]. The top row shows minimum-bias events, the bottom row shows results for high-multiplicity events, the red line on the right plots shows the final SPD tracklet-vs-cluster selection applied to the data (all events above the line are rejected).

minimum number of SPD tracklets contributing to the secondary vertex reconstruction is required to be ≥ 3 for low-multiplicity events and ≥ 5 for events with high multiplicities in order to avoid higher false rejection of good high-multiplicity events.

The primary vertex position, which is reconstructed with SPD tracklets, may be further improved based on the information provided by tracks reconstructed in the ITS and TPC. To assure that all detectors involved in the analysis cover the $|\eta| < 0.8$ pseudorapidity range, the vertex position is restricted to $\pm 10\,\mathrm{cm}$ along the beam direction

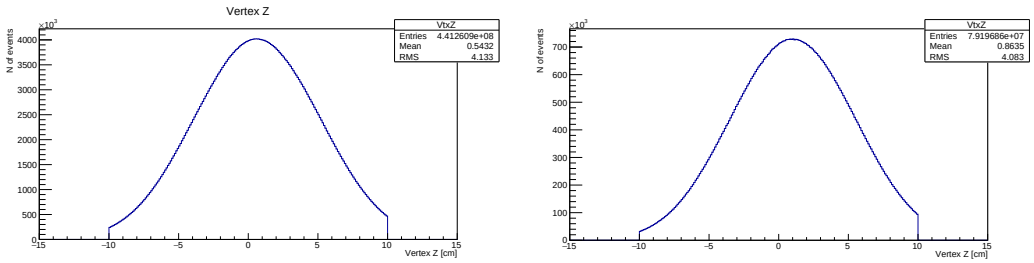

Figure 3.6: Distribution of vertex z position in minimum-bias (left) and high-multiplicity (right) events.

around the nominal interaction point (Fig. 3.6). The primary vertex should also fulfil the following additional requirements:

- At least 1 track or tracklet contributes to the vertex reconstruction
- Rejection of SPD vertices, for which only z coordinate is reconstructed and is determined with poor resolution
- Rejection of SPD vertices reconstructed with large dispersion (the size of the window opened to define the tracklets used in the determination of the vertex, with max. dispersion $= 0.03\,\mathrm{cm}$)
- Rejection of events if the vertices reconstructed with tracks and with SPD tracklets differ by large absolute distance (with max. displacement along z axis of $0.5\,\mathrm{cm}$)

As an example of these requirements, Fig. 3.7 shows the correlation between SPD-tracklet- and track-based vertex positions. Large distances between vertex positions reconstructed with two methods may indicate the presence of a secondary pile-up vertex, so such events are rejected from the analysis.

Various Monte Carlo (MC) simulated data are used in the analysis for the investigation of detector effects and its inefficiency. Every MC production is "anchored" to the corresponding data taking period in the sense that one tries to reproduce the same detector configuration, extracted from the Offline Conditions DataBase, in all details in the simulation, including active ITS zones and dead pixels, voltage settings, noisy channels and other detector-specific aspects. For this purpose, pp events are generated with e. g. Pythia event generator [174, 175] which is also used in this thesis. Pythia is a program widely used for the generation of high-energy collisions of e^+, e^-, proton and anti-proton in various combinations. It contains theory and models for a number of physics aspects, including hard and soft interactions, parton distributions, initial- and final-state parton showers, multiparton interactions, fragmentation and decay. Resulting particles are propagated through a detector simulation using Geant 3 package [176]. More details on MC analysis are presented in Section 3.4.

Several checks based on the detector performance, track matching, calibration etc. are performed for all reconstructed data by the ALICE Quality Assurance group in a centralised way. The results of such checks are recorded in the Run Condition Table

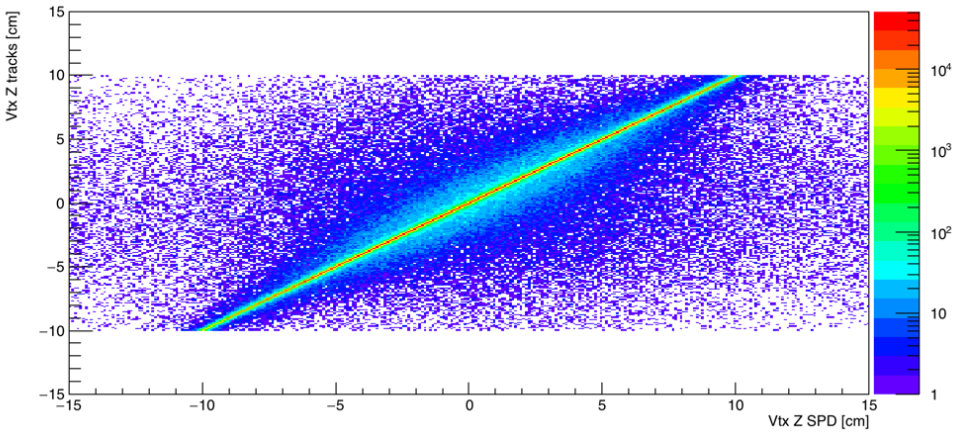

Figure 3.7: Correlation between vertex z positions reconstructed with tracks or SPD tracklets. Results are shown for kINT7 triggered events after physics selection and other vertex requirements (the vertex cuts on resolution/dispersion and displacement are not applied).

(RCT) as quality flags for each detector and each "run", which is the shortest period of continuous data-taking with stable conditions and detector performance. In this analysis only runs marked in the RCT as good are used, with a positive detector QA status for ITS, TPC, TOF and V0. In order to make sure that the detector performance is stable across all data-taking periods in 2016 and 2017, on top of these selections additional custom run-by-run checks are performed for all variables relevant for this analysis at event, track and PID levels. In principle, even a good (according to RCT) run can significantly differ from the rest of the period in terms of variables relevant for this analysis due to non-stable data-taking conditions or detector performance. It is therefore important to check that such deviations are properly described by Monte Carlo simulations, otherwise a run needs to be excluded from the analysis. For this purpose, mean values of different variables on event, track and pair levels are extracted for each run, both in experimental and in Monte Carlo simulated data, and their trends are analysed as a function of time (run number). As a result, several runs are excluded from the analysis due to significant deviations from the typical mean for the rest of the runs, if such deviations are not reproduced by Monte Carlo simulations.

An example of such run-by-run quality assurance is shown in Fig. 3.8, where the mean number of electron candidates per event is shown as a function of run number in 2016 pp data. The trend observed in experimental data is shown on the top plot, and it is well reproduced by Monte Carlo simulations on reconstruction level, i. e. after the propagation through the detector. A run is excluded from the analysis if at least one important parameter (such as the number of electron candidates, reference multiplicity

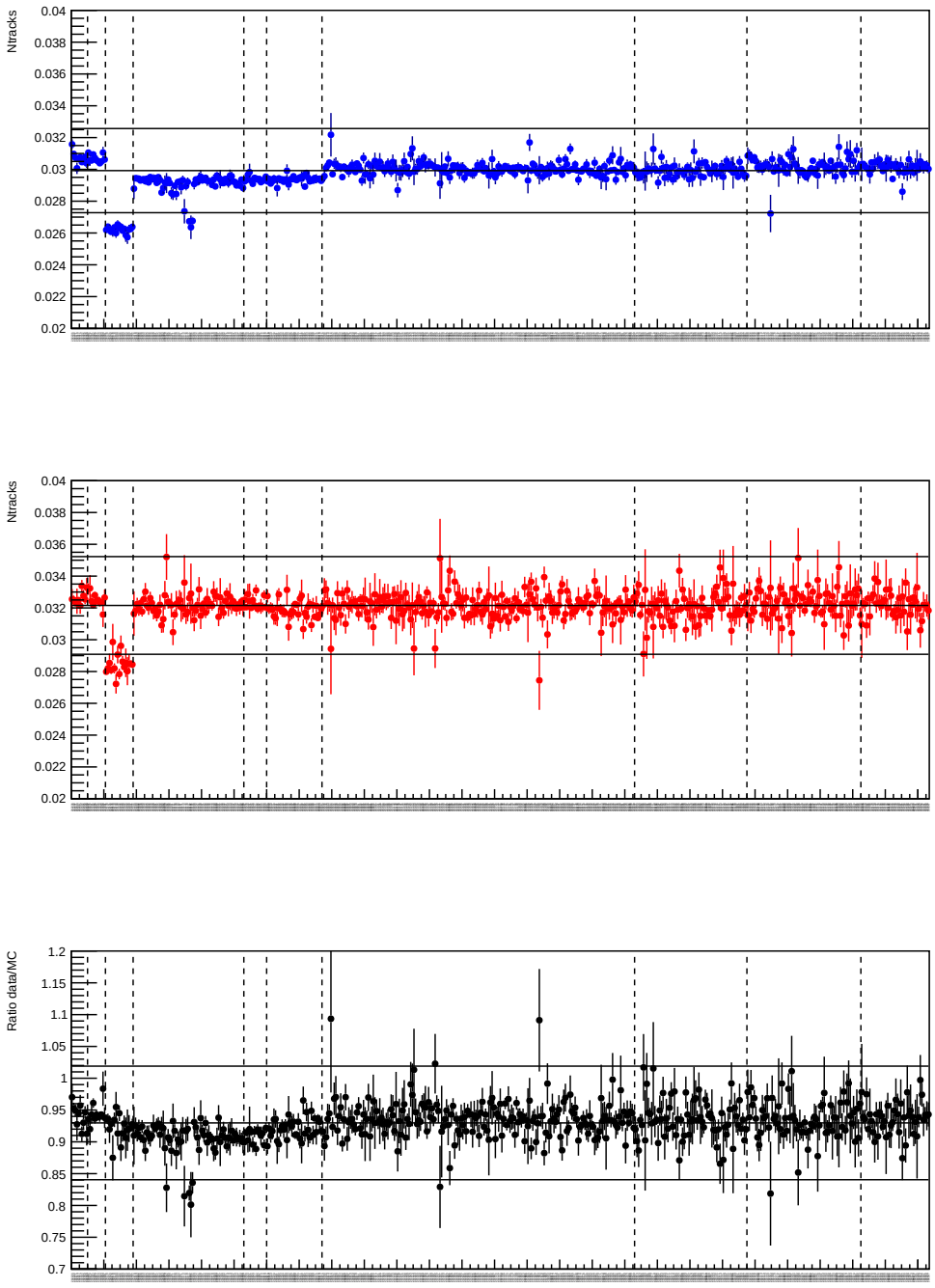

Figure 3.8: The mean number of electron and positron candidates as a function of run number in experimental data (blue) and in Monte Carlo simulated data (red); the ratio data / Monte Carlo is shown in black. Vertical dashed lines separate different data-taking periods in 2016, horizontal lines show the median and $\pm 3 \times$ RMS values.

at mid-rapidity, TPC and ITS tracking variables and the PID performance of the TPC and TOF detectors) is $> 3 \times$ RMS away from the value calculated as median of all runs and this deviation is not described by Monte Carlo simulations. The overall loss of statistics after such run-by-run checks is only $\sim 5\%$, which means that the performance of all relevant detectors was uniform and/or well described by Monte Carlo simulations.

At the time of the analysis a complete list of needed Monte Carlo simulations was available only for 2016 data. For this reason, for the analysis of dielectron spectra *corrected* for reconstruction efficiency only collisions recorded in 2016 are used in this thesis, which corresponds to a total number of 441×10^6 minimum-bias pp events and 79.2×10^6 high-multiplicity pp events. However, since efficiency-related corrections cancel to large extend in the ratio of dielectron spectra in Eq. 4.2, for the analysis of high-multiplicity collisions also raw (uncorrected) spectra can be used, which allows to add 2017 data without corresponding Monte Carlo simulations. This results in a total of 715×10^6 minimum-bias pp events and 153.8×10^6 high-multiplicity pp events used for high-multiplicity studies.

3.2 Track Selection and Particle Identification

In proton–proton collisions at LHC energies, many particles are produced within the acceptance of the ALICE central barrel spectrometer, but only some of them actually relate to the physical process of interest. The role of track selection criteria listed below in Table 3.1 is to select well-reconstructed tracks originating from the primary interaction vertex and to suppress secondary tracks from conversions of real photons and other processes not relevant for this analysis such as weak decays of strange hadrons, while keeping at the same time particles originating from charm and beauty hadrons.

Charged-particle tracks are reconstructed in the ITS and TPC in the kinematic range $|\eta| < 0.8$ and $p_{\mathrm{T}} > 0.2$ GeV/c which defines the detector aperture. Below $p_{\mathrm{T}} = 0.2$ GeV/c particles deflected in the magnetic field of $B = 0.5\,\mathrm{T}$ do not leave enough information in the TPC detector. Several further TPC track quality criteria are applied to each track candidate, such as a sufficient number of measured space points (clusters) or number of crossed rows. The latter is defined as the number of clusters assigned to a track plus a number of missing (but in principle findable) clusters, for which good clusters are found in neighbouring pad rows. In some cases a track has a large number of TPC clusters shared with other track(s), which can indicate a single TPC track wrongly reconstructed twice, so such track candidates are also rejected from the analysis. Finally, a track is required to have a good fit quality, which is expressed in terms of χ^2 value per TPC cluster:

$$\chi^2/n_{cl}^{\mathrm{TPC}} = \frac{1}{n_{cl}^{\mathrm{TPC}}} \sum_{i=0}^{n_{cl}^{\mathrm{TPC}}} \frac{(xy)_{i,cl} - (xy)_{i,track}}{\sigma_{i,xy}^2} + \frac{z_{i,cl} - z_{i,track}}{\sigma_{i,z}^2}, \tag{3.1}$$

Table 3.1: Track selection criteria used in analysis. Track is accepted only if all listed criteria are fulfilled.

Variable	Requirement
p_{T}	$> 0.2\ \mathrm{GeV}/c$
$\lvert\eta\rvert$	< 0.8
TPC refit	Required
Number of TPC crossed rows	≥ 100
Number of TPC clusters	≥ 80
Ratio of TPC crossed rows / findable clusters	> 0.8
χ^2 per TPC cluster	< 4
Fraction of shared TPC clusters	< 0.4
ITS refit	Required
Hit in first SPD layer	Required
Number of ITS clusters	≥ 3
Maximum number of shared ITS clusters	0
χ^2 per ITS cluster	< 4.5
Reject kink daughters	Required
DCA_{xy}	$< 1.0\,\mathrm{cm}$
DCA_{z}	$< 3.0\,\mathrm{cm}$
Independent cut on DCA_{xy} and DCA_{z}	true

where σ_{xy} and σ_z are the corresponding space point resolutions in the xy plane (transverse to beam direction) and along the z (beam) axis, correspondingly.

Similar track quality requirements are also applied for ITS variables. Real photons produced in the same collision can convert in detector material into $\mathrm{e}^+\mathrm{e}^-$ pairs, which contaminate dielectron signal in the mass region below $\approx 100\,\mathrm{MeV}/c^2$. Moreover, electrons and positrons from real photon conversions significantly increase the combinatorial background and therefore reduce the signal-to-background ratio of the dielectron spectrum over the whole mass range (Section 3.3). To suppress the contribution from photon conversions already on the level of single tracks (i. e. before the pair analysis and estimation of combinatorial background), tracks are required to have a hit in the first SPD layer and no ITS clusters shared with other reconstructed tracks in the event. A requirement of a hit in the first SPD layer greatly suppresses real photon conversions occurring in detector material beyond this layer, but causes some efficiency loss because of inactive SPD modules as shown in Fig. 3.9. A small fraction of electrons and positrons from photon conversions in the second ITS layer may still have a hit in the first layer associated wrongly to their reconstructed track. A requirement of zero shared ITS clusters leads to

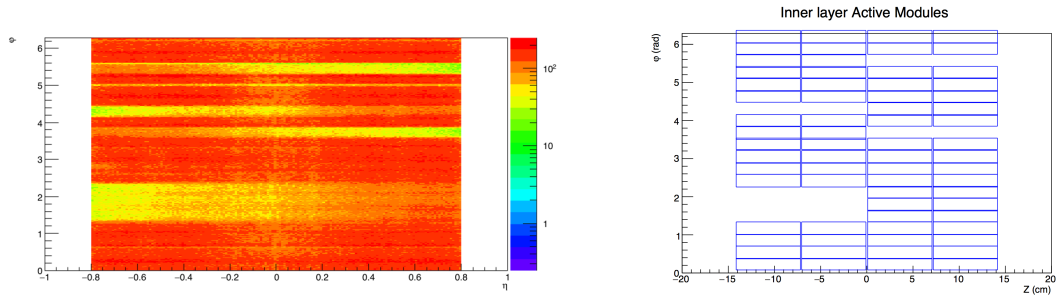

Figure 3.9: Left: $\eta - \phi$ distribution of charged-particle tracks after track selection. Right: active modules of the first SPD layer in 2016 and 2017 data.

further suppression of real photon conversions and improves the signal-to-background ratio of the dielectron spectrum (Section 3.3). This requirement also reduces the amount of conversion tracks from the first ITS layer or from the beam pipe.

The contribution from secondary tracks is reduced by requiring a maximum distance of closest approach (DCA) to the primary vertex in the transverse plane ($\mathrm{DCA_{xy}} < 1.0\,\mathrm{cm}$) and in the longitudinal direction ($\mathrm{DCA_{z}} < 3.0\,\mathrm{cm}$). These DCA cuts are chosen to be looser than the ones used typically in other analyses of primary particles in order to keep dielectron pairs from the decays of semileptonic open charm and beauty mesons, which have decay lengths of the order of hundred micrometers ($c\tau \approx 150\,\mu\mathrm{m}$ for D and $c\tau \approx 470\,\mu\mathrm{m}$ for B mesons). Some particles such as products of weak decays like $\mathrm{K}^+ \to \pi^+\pi^0$ are reconstructed in the detector as a continuous track with a pronounced "kink" topology: neutral particle, which cannot be directly reconstructed in the ITS and TPC, carries away some part of mother particle energy, and the track of second charged daughter (with the same charge as mother particle) is bent in the magnetic field in the same direction, but with smaller radius. Tracks which exhibit such kink topology are rejected from the analysis as well.

The same track selection is used for the analysis of high-multiplicity and minimum-bias data samples. A requirement of zero shared ITS clusters leads to a small ($\sim$2%) additional rejection of good signal pairs due to the higher average charged-particle multiplicity, which is taken into account in the systematic uncertainty (Section 3.6).

Electron[2] candidates are selected from charged-particle tracks using complementary PID information provided by the TPC and TOF detectors. The detector PID response, $n(\sigma_i^{\mathrm{DET}})$, is expressed in terms of the deviation between the measured and the expected value of the specific ionisation energy loss in the TPC or time-of-flight in the TOF for a given particle hypothesis i and momentum, normalised by the detector resolution σ^{DET}. For example, the TPC PID information for the electron hypothesis is given in units of $n(\sigma_{\mathrm{e}}^{\mathrm{TPC}})$ defined as:

[2]In the following, term 'electron' will be used for both electrons and positrons if not stated otherwise.

Table 3.2: PID selection of electron candidates used in analysis. Electron candidate is accepted if any of two sets of PID requirements is fulfilled.

Scheme	Detector	Particle	$n(\sigma)$ cut	p range [GeV/c]
A	TPC ($\mathrm{d}E/\mathrm{d}x$)	electron	$[-3.0, 3.0]$	$[0.2, \infty]$
	TPC ($\mathrm{d}E/\mathrm{d}x$)	pion	$[-\infty, 4.0]$	$[0.2, \infty]$
	TOF (β)	electron	$[-3.0, 3.0]$	$[0.4, \infty]$
B	TPC ($\mathrm{d}E/\mathrm{d}x$)	electron	$[-3.0, 3.0]$	$[0.2, \infty]$
	TPC ($\mathrm{d}E/\mathrm{d}x$)	pion	$[-\infty, 4.0]$	$[0.2, \infty]$
	TPC ($\mathrm{d}E/\mathrm{d}x$)	kaon	$[-\infty, -4.0]$ & $[4.0, \infty]$	$[0.2, \infty]$
	TPC ($\mathrm{d}E/\mathrm{d}x$)	proton	$[-\infty, -4.0]$ & $[4.0, \infty]$	$[0.2, \infty]$
	TOF (β)	electron	$[-3.0, 3.0]$ (if available)	$[0.4, \infty]$

$$n(\sigma_{\mathrm{e}}^{\mathrm{TPC}}) = \frac{(\mathrm{d}E/\mathrm{d}x)_{\mathrm{measured}} - \langle \mathrm{d}E/\mathrm{d}x(\mathrm{e}) \rangle_{\mathrm{expected}}}{\sigma_{\mathrm{e}}}. \tag{3.2}$$

The usage of supplementary information from different detectors allows one to reduce the fraction of hadrons in a sample of electron candidates to a minimum, while preserving a high electron efficiency for further pair analysis. To this purpose, a combined PID approach is used in this analysis, which utilises two supplementary PID cut settings each based on TPC and TOF requirements. These cut settings are discussed below, and the final sample of electron candidates consists of particles which passed either of two PID schemes (Table 3.2).

In both approaches electrons are selected in TPC with $\left|n(\sigma_{\mathrm{e}}^{\mathrm{TPC}})\right| < 3$ and pions are rejected by requiring $n(\sigma_{\pi}^{\mathrm{TPC}}) > 4$. Since electrons have a larger energy loss in the TPC than pions for momenta above 0.25 GeV/c, the $n(\sigma_{\pi}^{\mathrm{TPC}})$ requirement is asymmetric. Furthermore, in the selection scheme "A" kaons and protons are rejected by the strict requirement that the candidate is positively identified as an electron in the TOF ($\left|n(\sigma_{\mathrm{e}}^{\mathrm{TOF}})\right| < 3$). Since the TOF detector is located at $3.7 \lesssim R \lesssim 4.0$ m from the beam axis, the time-of-flight information is required only for particles with momentum above 0.4 GeV/c in order to minimise the rejection of good low-momentum tracks not reaching the detector or associated with mismatched TOF hits. Fig 3.10 (a) shows the resulting $n(\sigma_{\mathrm{e}}^{\mathrm{TPC}})$ distribution as a function of particle momentum for this PID approach.

The requirement of TOF PID information leads to significant loss of signal tracks, which is visible in Fig 3.10 (a) as a sharp drop of the number of electron candidates at $p = 0.4$ GeV/c. In order to increase the electron efficiency, the selection scheme "B" uses the TOF information to select electron candidates with $\left|n(\sigma_{\mathrm{e}}^{\mathrm{TOF}})\right| < 3$ only if the track has an associated hit in the TOF detector. The significant kaon and proton

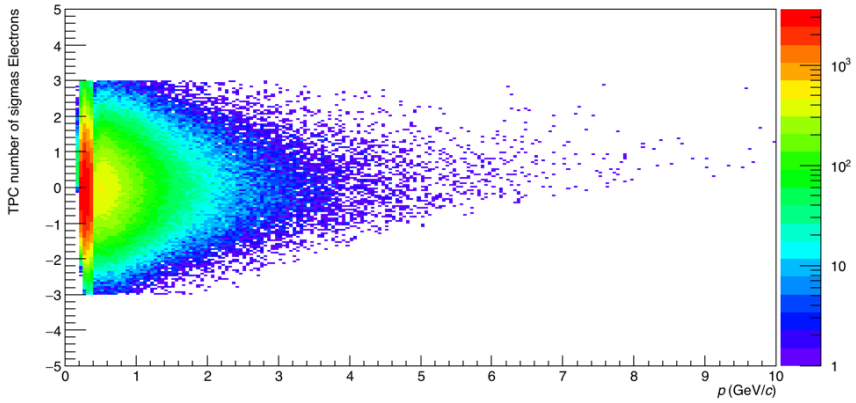

a)

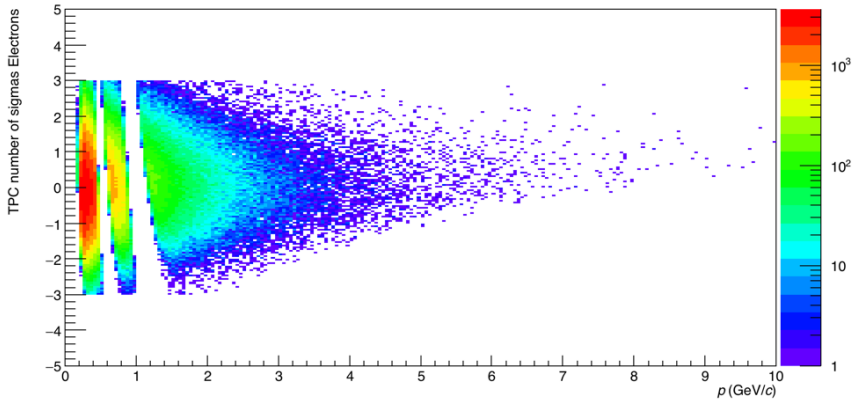

b)

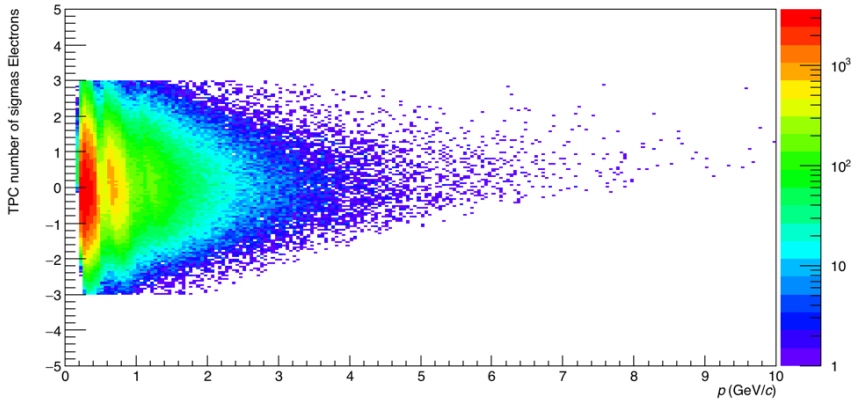

c)

Figure 3.10: $n(\sigma_{\mathrm{e}}^{\mathrm{TPC}})$ distributions as a function of particle momentum for electron candidates which fulfil the PID selection scheme A (a), B (b) or either of two (c).

contamination arising in this case around $p \approx 0.5$ and $p \approx 1.0$ GeV$/c$ is rejected with TPC requirements of $\left|n(\sigma_{\mathrm{K}}^{\mathrm{TPC}})\right| > 4$ and $\left|n(\sigma_{\mathrm{p}}^{\mathrm{TPC}})\right| > 4$ respectively. Fig. 3.10 (b) shows the corresponding $n(\sigma_{\mathrm{e}}^{\mathrm{TPC}})$ distribution, where the TPC hadron rejection bands are clearly visible.

The final sample of electron candidates is composed of particles which pass either of the two PID schemes, therefore the gaps created by the hadron rejection in the TPC seen in Fig. 3.10 (b) are "filled" with electron candidates which have a good TOF PID signal in these momentum regions and hence passed the PID selection "A" (Fig 3.10 (a)). The resulting $n(\sigma_{\mathrm{e}}^{\mathrm{TPC}})$ distribution for all electron candidates accepted for the analysis is shown in Fig. 3.10 (c). The same PID requirements are applied for the analyses of high-multiplicity and minimum-bias data samples, and in both cases a high electron purity is achieved (Section 3.6.4).

It is worth to mention that for the usage of such sophisticated PID approach a very good agreement of PID response between Monte Carlo simulations and experimental data is needed. In some phase-space regions, especially at low momentum and large pseudorapidities, the electron PID calibration of TPC and TOF detectors however is not perfect, and both real experimental data and Monte Carlo simulations show significant deviations of $n(\sigma_{\mathrm{e}}^{\mathrm{DET}})$ distributions from ideal case of mean $= 0$ and $\sigma = 1$. In order to improve the agreement and to ensure a consistent PID calibration, a special recalibration procedure is applied to PID response of TPC and TOF detectors, both in Monte Carlo and in experimental data. The $n(\sigma_{\mathrm{e}}^{\mathrm{TPC}})$ and $n(\sigma_{\mathrm{e}}^{\mathrm{TOF}})$ distributions are projected in different η and p intervals, and the width and mean values of the electron peak are extracted by fitting the distributions with two Gaussian fits (one for the signal and one for the background). Obtained values are used to re-calibrate the initial PID response, and a good PID calibration of both detectors close to ideal case of mean $= 0$ and $\sigma = 1$ is achieved in experimental data and in Monte Carlo simulations[3]. This procedure is described in more detail in Appendix B. After such re-calibration, Monte Carlo simulations are proven to describe the PID selection used in analysis precisely (Section 3.6).

3.3 Pair Analysis

Experimentally the origin of each electron or positron in an event is unknown, so all electron candidates from the same event are paired together considering combinations with unlike-sign (N_{+-}) and like-sign charge (N_{++} and N_{--}). Only a small fraction of unlike-sign pairs in N_{+-} originates from physical source of interest (like same mother decay or correlated pair from open heavy-flavour decays), which defines the signal S. Most of the electron pairs created in this way are of unphysical origin, i. e. a simple result of combining two electrons originating from different mother particles.

[3] In Monte Carlo data, PID recalibration of TPC detector is already a part of the analysis framework, so no additional work is needed in this case.

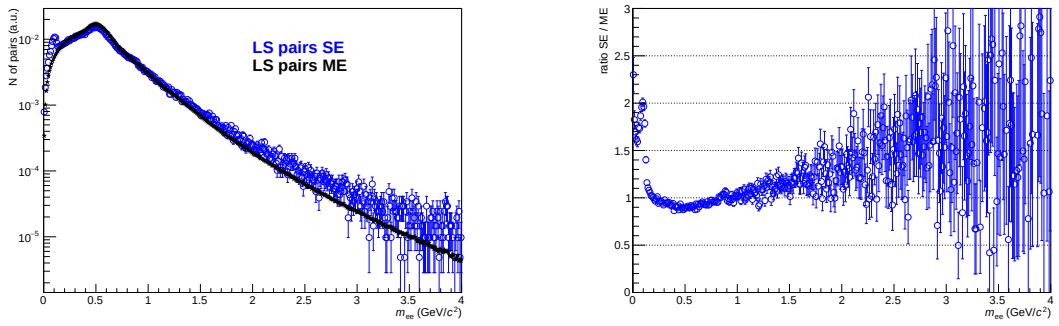

Figure 3.11: The shape of combinatorial background estimated with same-sign pairs from same events (blue) and with pairs from mixed events (black). The histograms are normalised by the number of entries, the ratio between two methods is shown on the right.

Such pairs give rise to the combinatorial background B, which needs to be properly estimated. Mathematically it can be shown that as long as electrons are created as e^+e^- pairs, such combinatorial background is described by the geometric mean of the like-sign background N_{++} and N_{--} of pairs from the same event, independent of the primary multiplicity distribution [76], as:

$$B_{\pm\pm} = 2\sqrt{N_{++} \cdot N_{--}}. \tag{3.3}$$

In contrast to the combinatorial background estimated by uncorrelated pairs from mixed events, i. e. by pairing electrons from different events with similar detector coverage, such estimation of background $B_{\pm\pm}$ also includes correlated background. In the low invariant-mass regions this can arise from e. g. π^0 decays with two e^+e^- pairs in the final state ($\pi^0 \to \gamma^{(*)}\gamma^{(*)} \to e^+e^-e^+e^-$), which includes decay channels with real photons and their subsequent conversion in detector material, or from pairs produced in the same jet. Such processes lead to unlike- and like-sign pairs at equal rate, so the corresponding contribution is taken into account in the estimation of $B_{\pm\pm}$. At higher invariant mass, correlated background arises from pairs produced in back-to-back jets. The comparison of background shapes estimated with same-sign pairs from same event and with pairs from mixed events is shown in Fig. 3.11. From the ratio between two methods one can clearly see a contribution of correlated background pairs, especially at low and high invariant masses. Compared to a mixed-event based approach, the disadvantage of the same-sign subtraction method is larger statistical uncertainties. However, with method based on mixed events one still needs to properly normalise the uncorrelated background yield and to estimate the contribution from correlated background, which can lead to additional uncertainties.

The background estimate in Eq. 3.3 needs to be corrected for the different detector acceptance of unlike- and like-sign pairs. Such differences may arise from the non-uniform azimuthal detector coverage convoluted with opposite curvature of positive and negative particles in the magnetic field. Since it is a purely acceptance effect, the corresponding correction factor R can be determined with the help of mixed events which preserve the acceptance effects. For this purpose, the yields of unlike-sign M_{+-} and like-sign $M_{\pm\pm}$ uncorrelated pairs from mixed events are divided in the following way:

$$R = \frac{M_{+-}}{2\sqrt{M_{++} \cdot M_{--}}}. \tag{3.4}$$

The physical signal is then obtained by:

$$S = N_{+-} - B = N_{+-} - 2R\sqrt{N_{++}N_{--}}, \tag{3.5}$$

where $B = 2R\sqrt{N_{++}N_{--}}$ represents the combinatorial background corrected for the acceptance differences.

The R-factor correction is applied as a function of invariant mass in different $p_{\mathrm{T,\,ee}}$ bins, but as a cross-check its behaviour is analysed also as a function of other pair variables such as $p_{\mathrm{T,\,ee}}$, η_{ee}, φ_{ee} and opening angle. In all cases the acceptance correction factor is found to be very stable and close to unity. To assure similar detector coverage for different events, which are mixed with each other, events are mixed within eight separate event classes defined by their vertex z position in $2.5\,\mathrm{cm}$ wide bins from $-10\,\mathrm{cm}$ to $10\,\mathrm{cm}$ and only within a given run. The resulting unlike-sign spectrum N_{+-}, combinatorial background B and R-factor in minimum-bias events are shown in Fig. 3.12. In order to avoid statistical fluctuations in the higher mass range, the R-factor is set to unity for $m_{\mathrm{ee}} > 0.5\ \mathrm{GeV}/c^2$ mass range, where no statistically significant deviations from 1 are observed.

In this analysis, electrons originating from real photon conversions are suppressed at the single track level by requiring a hit in first SPD layer and zero ITS clusters shared with other tracks. Since real photons do not have intrinsic physical mass, both decay products go basically in the same direction, and the magnetic field provides the only opening force. Thus pairs originating from conversions will most likely share ITS clusters with each other, and the requirement of no shared ITS clusters for single tracks improves signal-to-background ratio over whole mass region while preserving high efficiency: the signal pairs are affected only in the very low mass region below $200\ \mathrm{MeV}/c^2$ as it can be seen in Fig. 3.13. It indicates that this requirement indeed rejects mainly background pairs and only small fraction of physical dielectron signal in pp collisions.

In addition, dielectron pairs from photon conversions are characterised by a finite apparent invariant mass. Tracking algorithm assumes the particles to originate from the primary collision vertex, in which case electrons from conversions are tracked back to the

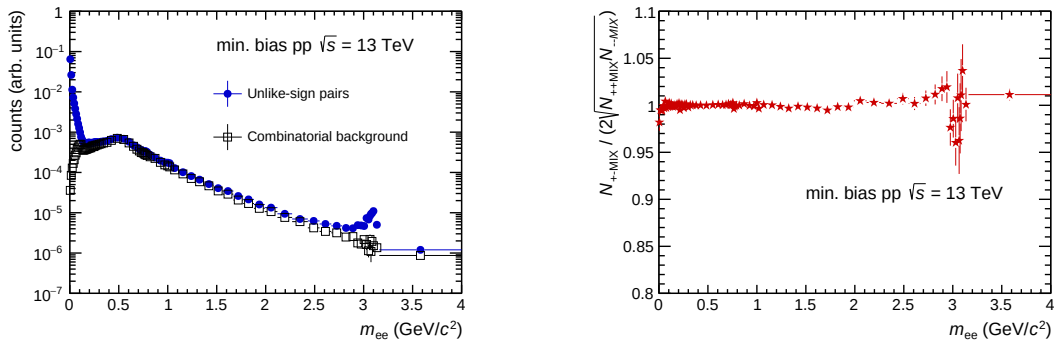

Figure 3.12: Unlike-sign spectrum N_{+-}, combinatorial background B and R-factor in minimum-bias events. Rejection of real photon conversions is not applied.

collision vertex rather than to the conversion vertex. This results in a non-vanishing artificial opening angle, which lies preferentially in the plane perpendicular to the magnetic field direction and can be used to further reject such conversion dielectron pairs [76]. To suppress such residual conversion pairs, the angle φ_V between the vector normal to the pair plane and the vector along the $\hat{z}$ axis, i. e. the magnetic field direction, is used in analysis:

$$\vec{u} = \frac{\vec{p}_+ + \vec{p}_-}{|\vec{p}_+ + \vec{p}_-|}, \tag{3.6a}$$

$$\vec{v} = \vec{p}_+ \times \vec{p}_-, \tag{3.6b}$$

$$\vec{w} = \vec{u} \times \vec{v}, \tag{3.6c}$$

$$\vec{u}_a = \frac{\vec{u} \times \hat{z}}{|\vec{u} \times \hat{z}|} \tag{3.6d}$$

$$\varphi_V = \arccos\left(\frac{\vec{w} \cdot \vec{u}_a}{|\vec{w}||\vec{u}_a|}\right). \tag{3.7}$$

Here $\vec{p}_-$ is the 3-momentum vector of the electron and $\vec{p}_+$ the 3-momentum vector of the positron. Fig. 3.14 shows the φ_V distributions of signal and conversion pairs in Monte Carlo data in different mass bins, where conversion pairs can be seen to peak at $\varphi_V \approx \pi$. However, Monte Carlo simulations do not reproduce perfectly the mass distribution of conversion pairs, with almost negligible contribution above $40\ \mathrm{MeV}/c^2$, whereas in experimental data conversion pairs can be seen also above that value. Therefore in this analysis a data-driven approach is used for the rejection of conversion pairs using φ_V.

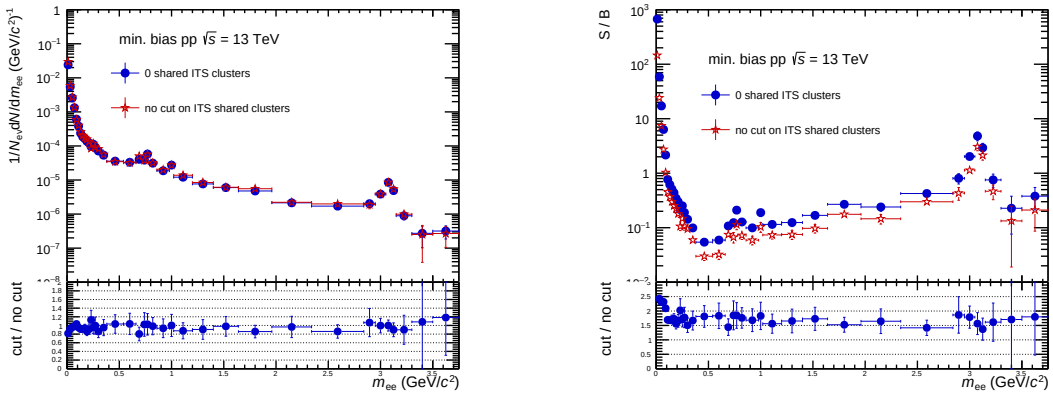

Figure 3.13: The comparison of raw signal (left) and signal-to-background ratio (right) in minimum-bias events showing effect of no shared ITS clusters requirement.

Fig. 3.15 shows the φ_V distributions of signal and background pairs in different mass bins in minimum-bias data sample, and the corresponding distributions in high-multiplicity events are shown in Fig. 3.16. Photon conversions can be seen in the signal φ_V distributions as pairs which peak at $\varphi_V \approx \pi$, with some traces from conversion pairs visible in mass bins up to 140 MeV/c^2 in high-multiplicity events. For consistency, in both analyses all pairs with $\varphi_V > 2.0$ and $m_{\mathrm{ee}} < 140$ MeV/c^2 are rejected from the signal calculation according to (3.5). The rejection is applied for unlike-sign as well as same-sign pairs in the same and mixed events as it is indicated by the vertical dashed line in Figs. 3.15 and 3.16.

The resulting unlike-sign spectrum, combinatorial background and R-factor with the applied φ_V cut are shown in Fig. 3.17 for minimum-bias events and in Fig. 3.18 for high-multiplicity data. Figures 3.19 and 3.20 show signal-to-background ratio and the statistical significance for dielectron signal in minimum-bias and high-multiplicity data correspondingly. The statistical significance is defined as $S/\sqrt{S+2B}$, where a factor 2 is present to take into account that the background is subtracted using the like-sign pairs. In the mass interval $0.2 < m_{\mathrm{ee}} < 3$ GeV/c^2, the signal-to-background ratio varies in minimum-bias events between 0.3 and 0.04, with a minimum around $m_{\mathrm{ee}} \approx 0.5$ GeV/c^2 (where the combinatorial background B is the highest) and is roughly constant at 0.2 in the intermediate mass range. In high-multiplicity events, the minimum reaches 0.01 and is about 0.08 in the intermediate mass range. Due to higher average event multiplicity, the signal-to-background ratio is lower than for minimum-bias events, while the statistical significance is comparable. This is consistent with a simple approximation of $S \sim N_{\mathrm{ch}}$ and $B \sim N_{\mathrm{ch}}^2$, where N_{ch} denotes charged-particle multiplicity. In background-dominated region this assumption leads to a roughly constant statistical sig-

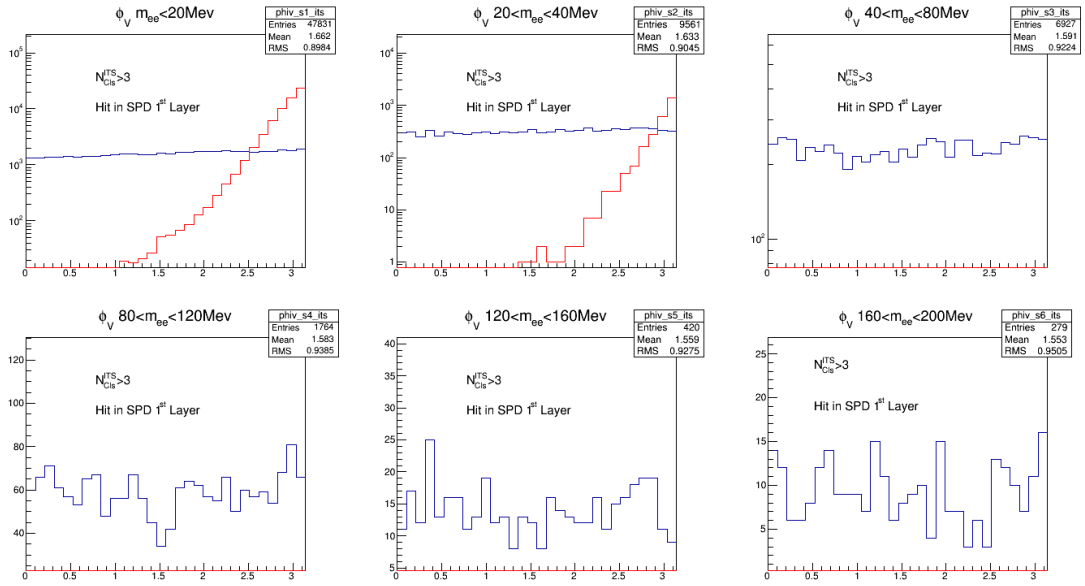

Figure 3.14: The φ_V distributions of signal (blue) and conversion pairs (red) in Monte Carlo simulations in different mass bins.

nificance $\sim S/\sqrt{B}$.

Finally, raw dielectron spectra in minimum-bias and high-multiplicity event classes normalised by the number of analysed events are shown in Figs. 3.21 and 3.22 for $p_{\mathrm{T,\,ee}} < 6$ GeV/c. All the analysis steps described above are also repeated in different $p_{\mathrm{T,\,ee}}$ bins, and the corresponding raw dielectron spectra are shown in Figs. 3.23 and 3.24. Photon conversion rejection is used as described above in this Section, and no signal loss correction due to the φ_V cut is applied yet. In the next step, these raw dielectron spectra are corrected for the detector reconstruction efficiency as described in Section 3.4.

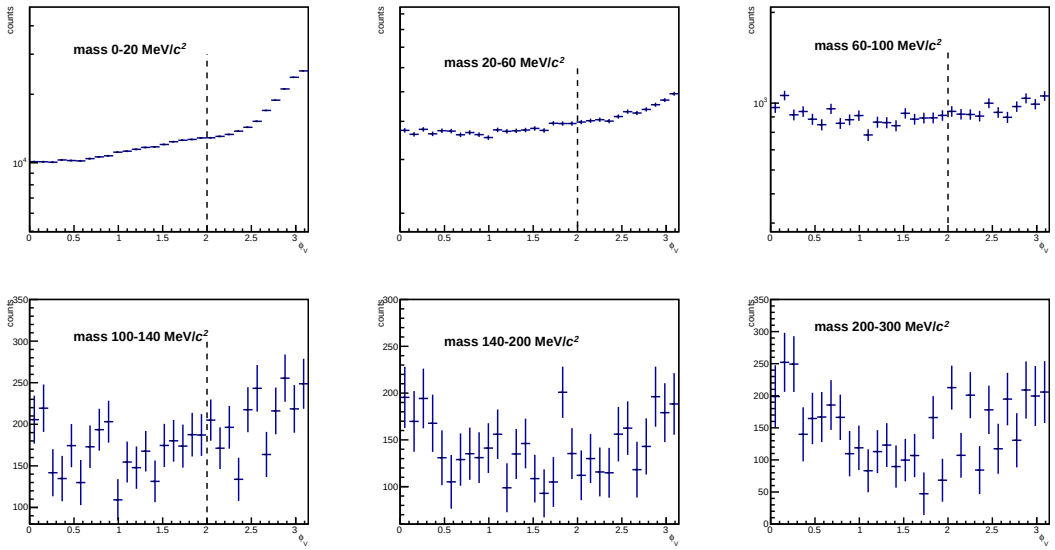

a)

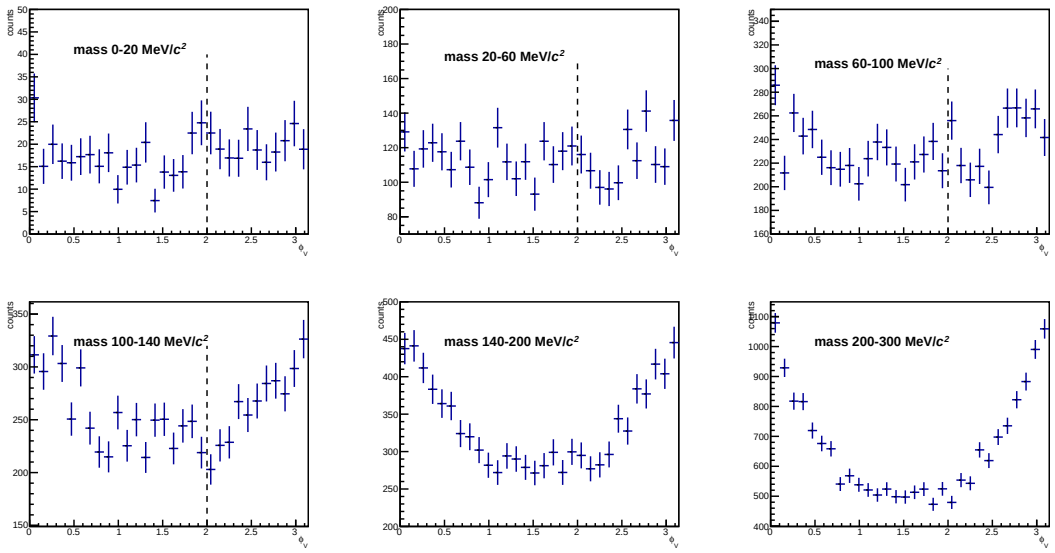

b)

Figure 3.15: φ_V distributions of a) signal and b) background pairs in minimum-bias events in different mass bins. Acceptance correction R-factor is applied. Vertical dashed line shows φ_V cut used in the analysis.

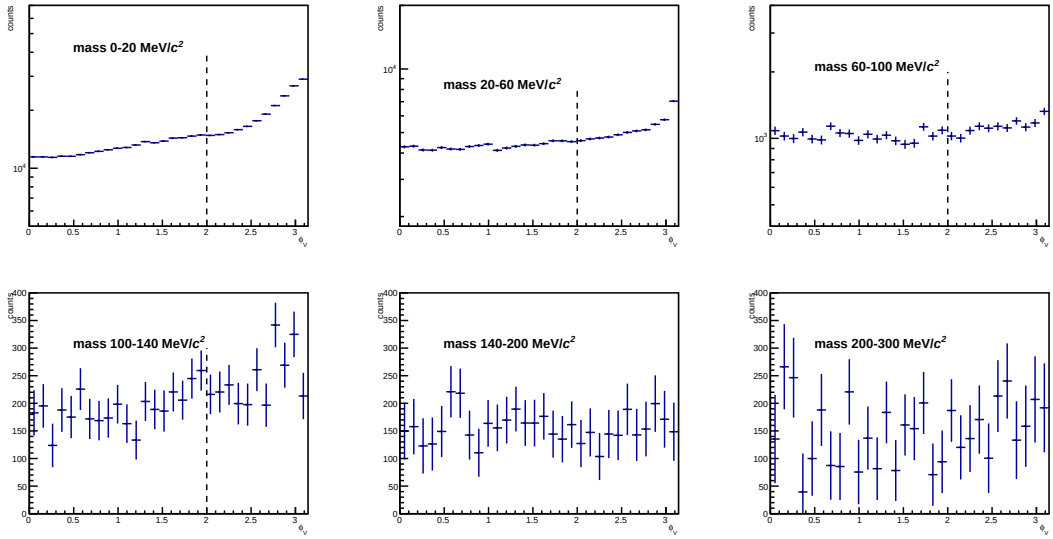

a)

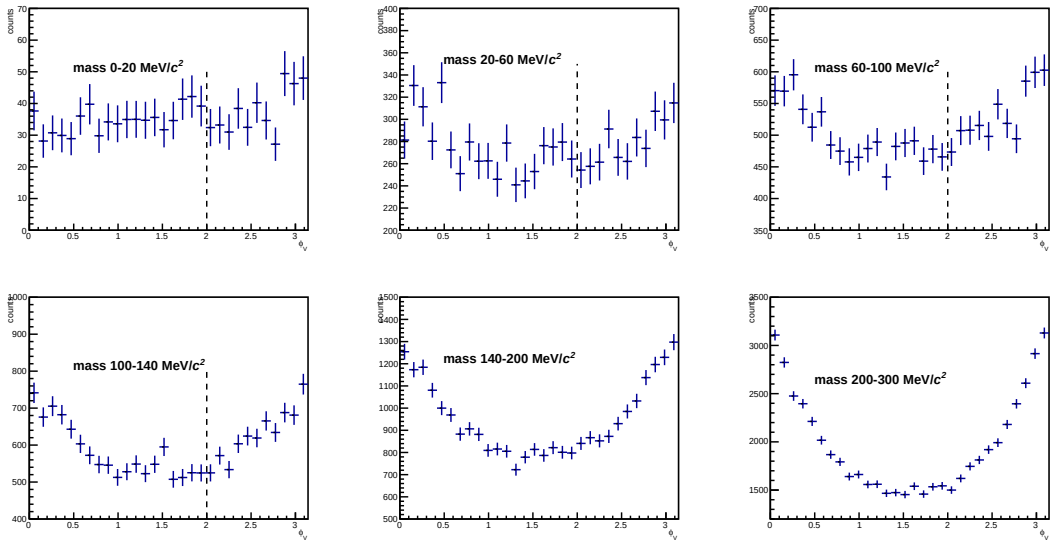

b)

Figure 3.16: φ_V distributions of a) signal and b) background pairs in high-multiplicity events in different mass bins. Acceptance correction R-factor is applied. Vertical dashed line shows φ_V cut used in the analysis.

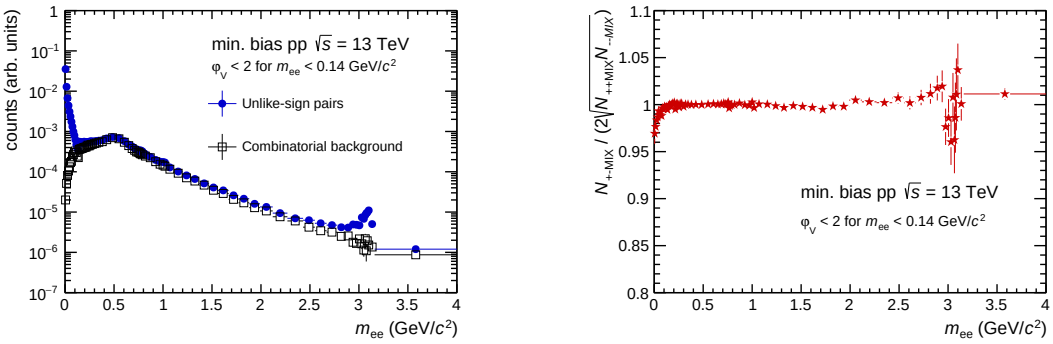

Figure 3.17: Unlike-sign spectrum N_{+-}, combinatorial background B and R-factor in minimum-bias events (p_{T}-integrated case).

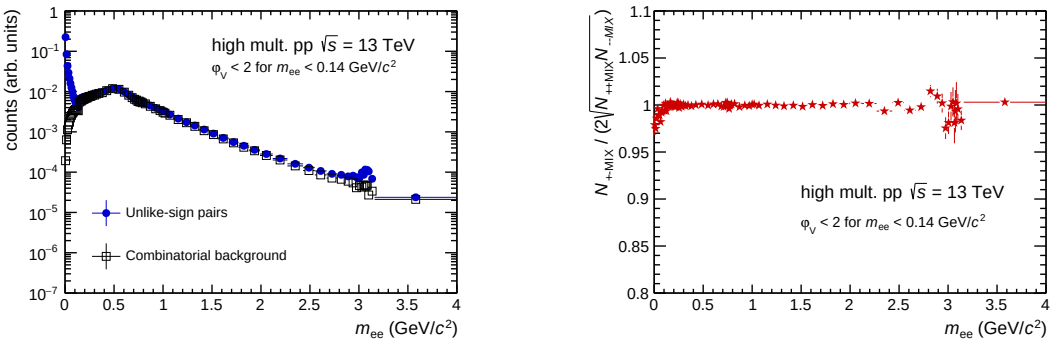

Figure 3.18: Unlike-sign spectrum N_{+-}, combinatorial background B and R-factor in high-multiplicity events (p_{T}-integrated case).

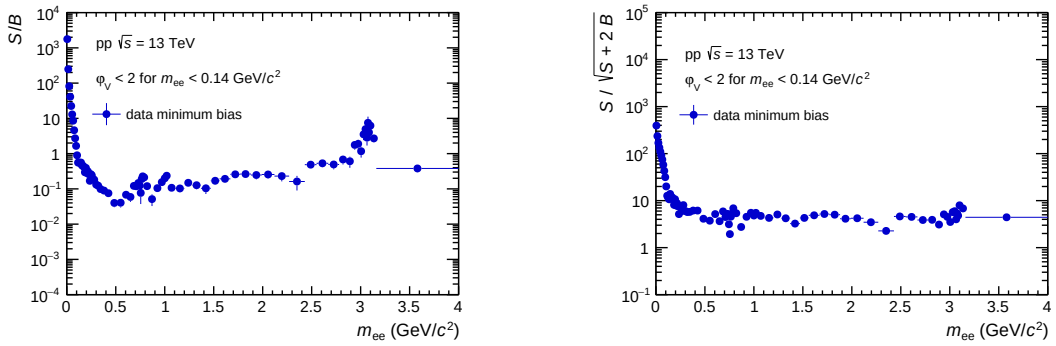

Figure 3.19: Signal-to-background ratio (left) and statistical significance (right) of di-electron signal in minimum-bias events.

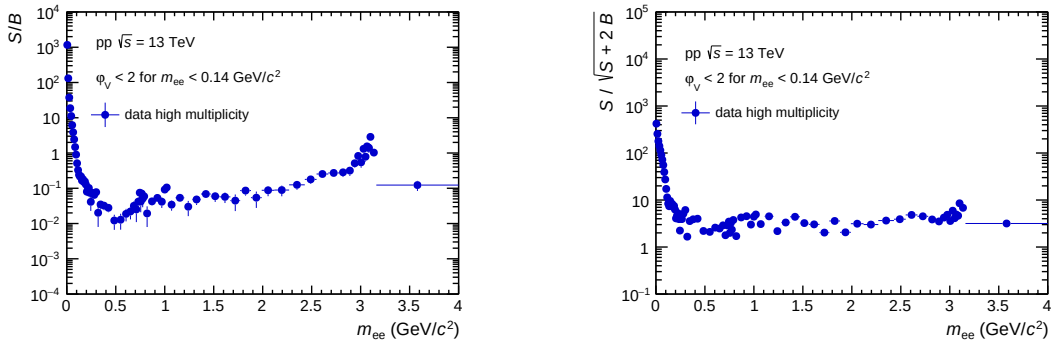

Figure 3.20: Signal-to-background ratio (left) and statistical significance (right) of di-electron signal in high-multiplicity events.

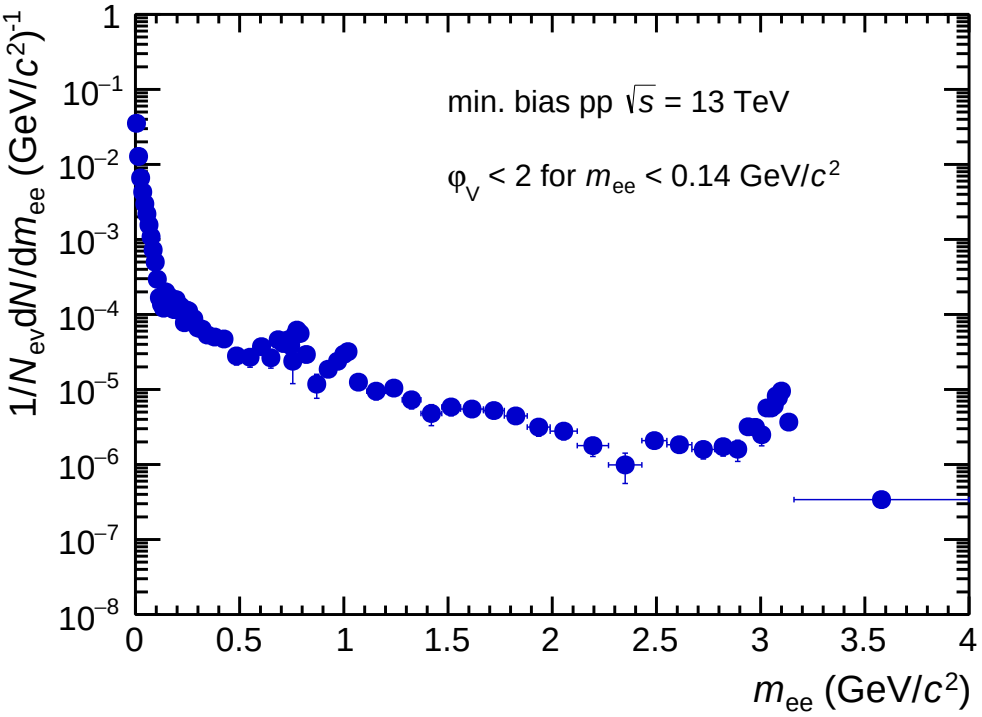

Figure 3.21: Raw dielectron signal normalised by the number of analysed minimum-bias events. Rejection of real photon conversions is applied as described in text, and no signal loss correction due to φ_V cut is applied.

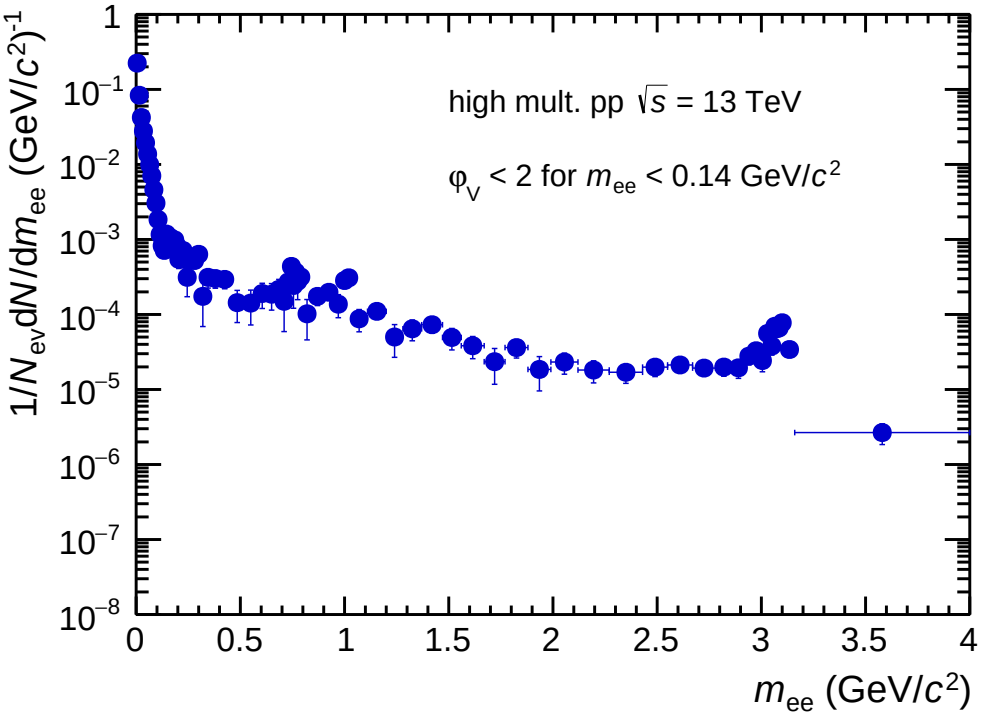

Figure 3.22: Raw dielectron signal normalised by number of analysed high-multiplicity events. Rejection of real photon conversions is applied as described in text, and no signal loss correction due to φ_V cut is applied.

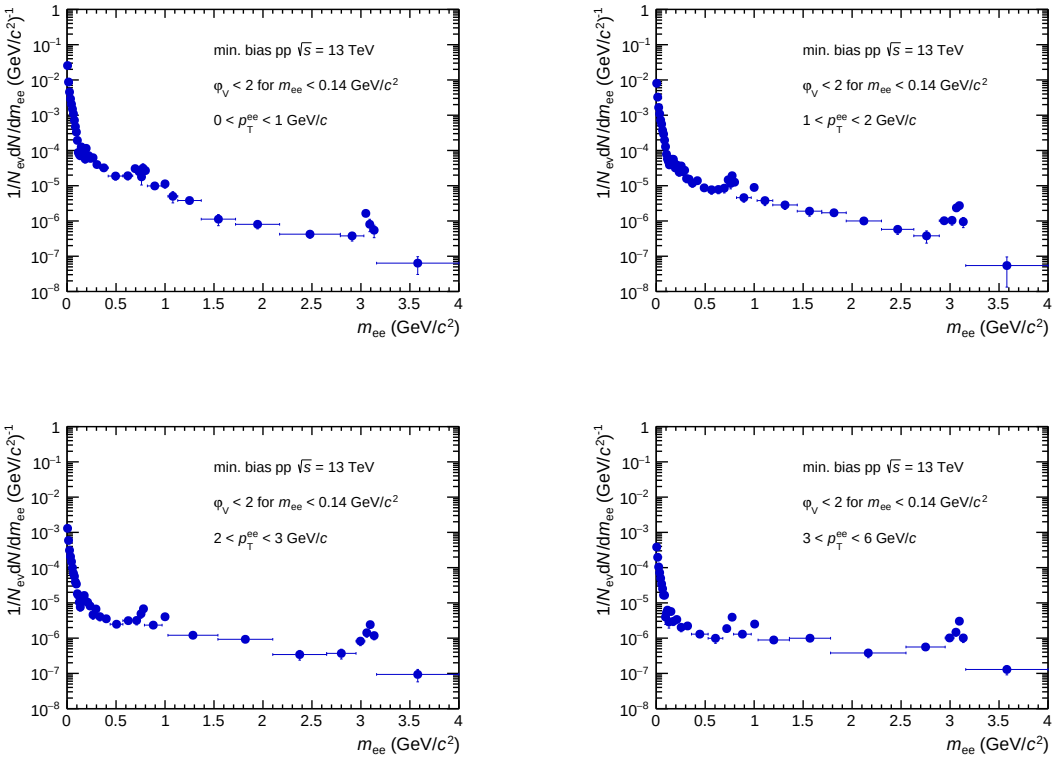

Figure 3.23: Raw dielectron signal normalised by number of analysed minimum-bias events in different $p_{\mathrm{T,\,ee}}$ bins. Rejection of real photon conversions is applied as described in text, and no signal loss correction due to φ_V cut is applied.

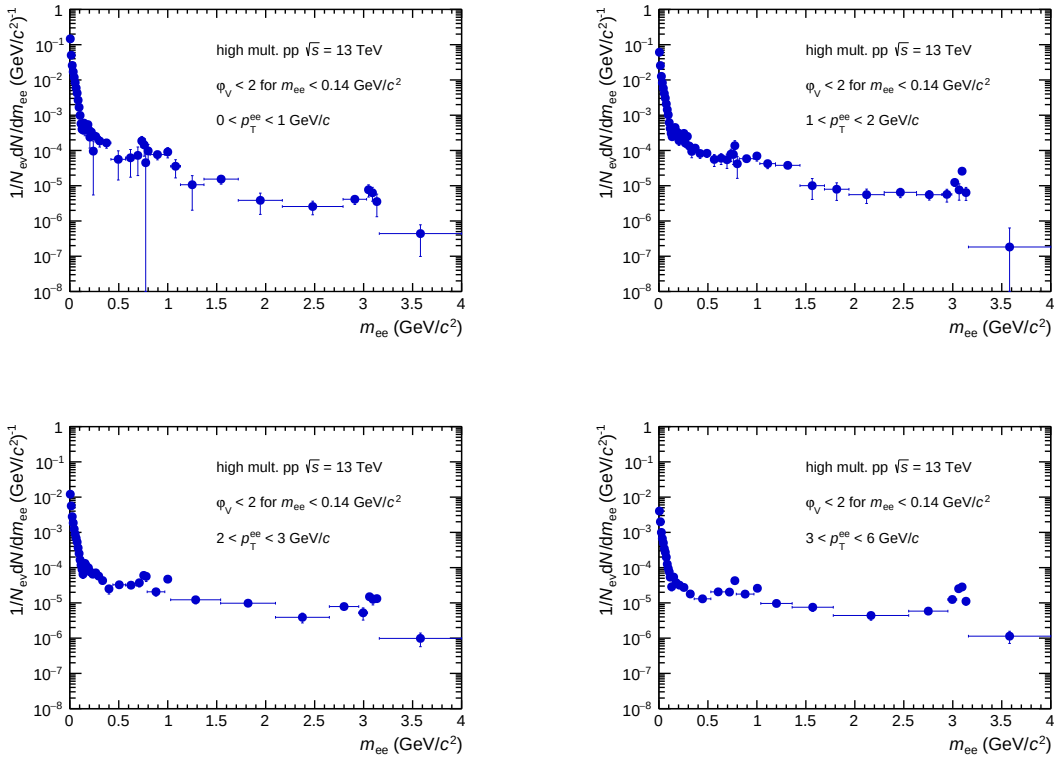

Figure 3.24: Raw dielectron signal normalised by number of analysed high-multiplicity events in different $p_{\mathrm{T,\,ee}}$ bins. Rejection of real photon conversions is applied as described in text, and no signal loss correction due to φ_V cut is applied.

3.4 Analysis of Monte Carlo Simulation

Before the dielectron spectrum can be compared with theoretical expectations, reconstruction efficiencies and detector effects should be taken into account and corrected for[4]. This section describes the analysis of Monte Carlo (MC) simulated data and the calculation of the corresponding dielectron signal efficiency.

In general, the reconstruction efficiency for single particle can be defined in MC as the ratio of reconstructed electrons that passed the selection criteria in Tables 3.1 and 3.2 over the number of generated electrons within acceptance ($p_{\mathrm{T,\,e}} > 0.2$ GeV/c and $|\eta_{\mathrm{e}}| < 0.8$) as a function of $x = p_{\mathrm{T}}, \eta, \varphi$:

$$\epsilon(x) = \frac{(\frac{\mathrm{d}N}{\mathrm{d}x})_{\mathrm{rec}}}{(\frac{\mathrm{d}N}{\mathrm{d}x})_{\mathrm{gen}}}. \tag{3.8}$$

However, as it will be shown later, electrons suffer from energy losses when traversing the ALICE detector, so that generated and reconstructed momenta can slightly differ: $p_{\mathrm{T}}^{\mathrm{gen}} \neq p_{\mathrm{T}}^{\mathrm{rec}}$. If one calculates single electron efficiency with $p_{\mathrm{T}}^{\mathrm{rec}}$ in enumerator and $p_{\mathrm{T}}^{\mathrm{gen}}$ in denominator, such calculation would then lead to a wrong estimation of efficiency. As a solution for this problem, in this thesis a special smearing procedure described in Section 3.4.2 is applied to all generated MC tracks to take into account energy losses and resolution, and the corresponding electron efficiency is always estimated in terms of "measurable" variables $p_{\mathrm{T}}, \eta, \varphi$, i. e. as they are reconstructed with the detector.

To correct experimental data for the reconstruction efficiencies, pp events are generated with the help of Pythia event generator [174, 175], with "Monash 2013" set of parameters (so-called tune) of Pythia 8 [177] for light hadron decays and "Perugia 2011" tune of Pythia 6.4 for heavy-flavour decays [178]. A choice of different Pythia versions is motivated by the fact that Monash 2013 tune reproduces many of the relevant light hadron multiplicities [179, 180]. It used recent experimental data from LHC for constraining the initial-state-radiation and multi-parton-interaction parameters and data from SPS and Tevatron to constrain the energy scaling. Perugia 2011 tune of Pythia 6.4 uses the same value of Λ_{QCD} for all shower activity (initial-state and final-state radiation) to simplify matching applications and was constrained by results from LEP, SPS and Tevatron experiments as well as by early data from LHC for minimum-bias and underlying-event activities in pp collisions at $\sqrt{s} = 0.9$ and 7 TeV. As a result, it describes reasonably well the transverse momentum spectra of heavy-flavour hadrons. The produced particles are propagated through the detector by Geant 3 package [176], which simulates in all detail the detector material and response. The signal reconstruction efficiency is studied as a function of m_{ee} and $p_{\mathrm{T,\,ee}}$ for the different $\mathrm{e}^+\mathrm{e}^-$ sources separately:

[4] In this thesis, only the reconstruction efficiency within the ALICE acceptance is discussed ($p_{\mathrm{T,\,e}} > 0.2$ GeV/c and $|\eta_{\mathrm{e}}| < 0.8$), i. e. no correction for the full 4π acceptance is applied.

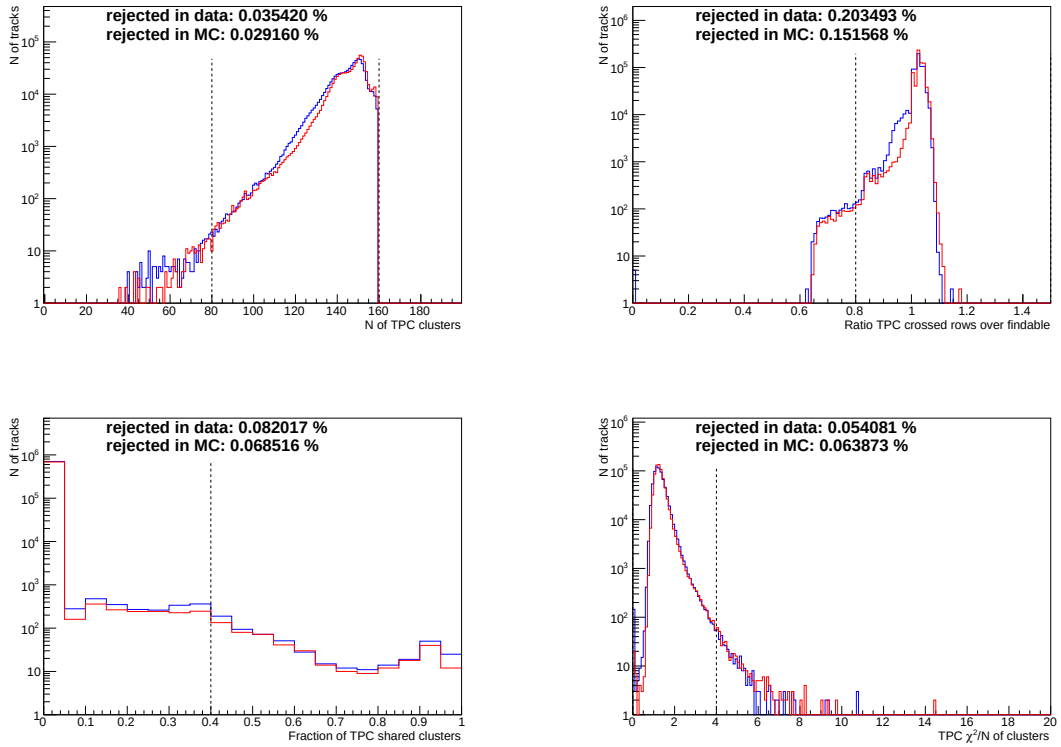

Figure 3.25: Distribution of TPC variables in data (blue) and in MC (red) for electrons. All other track selection criteria are applied except on the one shown on the plot as vertical dashed line. The relative number of tracks rejected by each selection is also listed.

resonance and Dalitz decays of light-flavour mesons, correlated semileptonic decays of charm and beauty hadrons, as well as J/ψ decays. The total signal reconstruction efficiency is obtained as a weighted average of efficiencies, with weights according to the expected contribution.

3.4.1 Monte Carlo Quality Assurance

To properly calculate the single electron and pair efficiencies, it is important to check first that the distributions of variables used for track selection (Table 3.1) are correctly reproduced in Monte Carlo simulations. Figure 3.25 shows as example a TPC variable distributions in real experimental data and in Monte Carlo data. In each panel, the same track and PID selection is applied both in Monte Carlo and in experimental data. Track selection criteria are applied according to Table 3.1 except on the variable that is shown

in the Figure. This is done in order to have a clean sample of track candidates in experimental data close to the final selection[5]. The results show distributions of the number of tracks passing the selection for approximately the same number of analysed events in experimental data and in Monte Carlo simulations. Not only the overall yield (i. e. multiplicity of electron candidates) and the shape of each distribution from experimental data is well reproduced in Monte Carlo data, but also the relative number of particles rejected by each cut (when other track cuts are applied) is found to be in good agreement. These checks are also done in different p_{T} intervals for the studies of systematic uncertainties on the track reconstruction (Section 3.6).

3.4.2 Simulation of Momentum Smearing

When a moving charged particle is deflected in an external electric or magnetic field, it emits electromagnetic radiation and hence loses part of its energy (synchrotron radiation). In addition to that, electrons, due to their low mass, especially suffer from Bremsstrahlung while traversing the ALICE detector, i. e. "braking" radiation produced by the deceleration of an electron when it's deflected by electromagnetic field of atomic nuclei in detector material. This effect can be seen in Fig. 3.26 where the difference between the generated $p_{\mathrm{T}}^{\mathrm{gen}}$ and the reconstructed $p_{\mathrm{T}}^{\mathrm{rec}}$ momenta is shown for electrons with a generated momentum in the range $0.5 < p_{\mathrm{T}}^{\mathrm{gen}} < 0.6$ GeV$/c$. Apart from the finite momentum resolution of the detector of about $\sim 1\%$, which results in finite width of $\Delta p_{\mathrm{T}}/p_{\mathrm{T}} = (p_{\mathrm{T}}^{\mathrm{gen}} - p_{\mathrm{T}}^{\mathrm{rec}})/p_{\mathrm{T}}^{\mathrm{gen}}$ around zero, this distribution shows also a tail produced by energy losses on the left side where $p_{\mathrm{T}}^{\mathrm{rec}} < p_{\mathrm{T}}^{\mathrm{gen}}$.

As a consequence, reconstructed momenta of electrons can differ slightly from the generated one. Due to energy losses, the p_{T} spectrum of reconstructed electrons is softer than the one of generated electrons, and the usage of reconstructed particle momentum in enumerator and pure generated momentum in denominator for electron efficiency calculation would then lead to a wrong estimation of efficiency, which results in an effective mass and $p_{\mathrm{T,\,ee}}$ shift of dielectron. Simultaneous unfolding of detector effects in multiple dimensions (invariant mass, $p_{\mathrm{T,\,ee}}$) is highly complicated for multiple sources, and even a simplified approach based on one-dimensional (e. g. invariant mass) unfolding methods cannot be performed for dielectron analysis due to instabilities of the existing algorithms in the resonance regions. Moreover, it is generally not done for previous experimental results presented in Section 1.4.

For a proper efficiency calculation, the smearing procedure is applied to the generated Monte Carlo electrons as detailed in [181]. The same smearing of generated particle values is also applied for the hadronic cocktail calculations for a consistent comparison of the dielectron spectrum with expected contributions. The transformation of the gener-

[5] In MC simulations one could easily reject background from secondary tracks by using information about the origin of each particle, but for direct comparison with experimental data it is not done in Fig. 3.25.

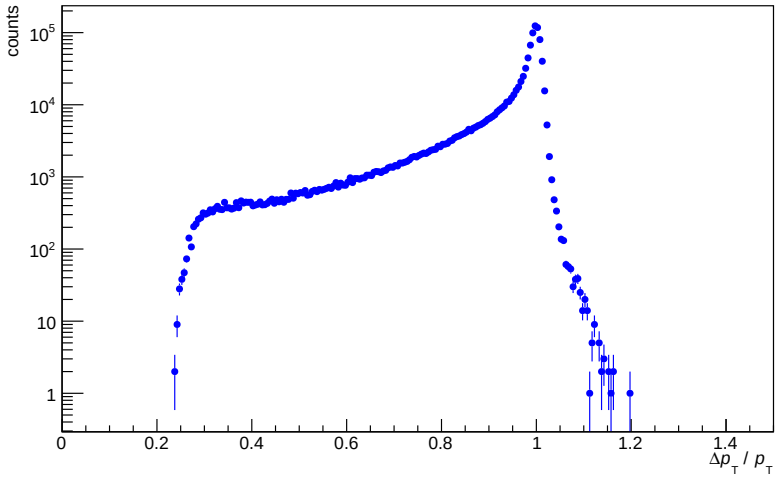

Figure 3.26: Distribution of $\Delta p_{\mathrm{T}}/p_{\mathrm{T}} = (p_{\mathrm{T}}^{\mathrm{gen}} - p_{\mathrm{T}}^{\mathrm{rec}})/p_{\mathrm{T}}^{\mathrm{gen}}$ for electrons with generated momentum of $0.5 < p_{\mathrm{T}}^{\mathrm{gen}} < 0.6$ GeV/c. The tail on the left side is produced by energy losses in the ALICE detector.

ated values of $p_{\mathrm{T,\,e}}^{\mathrm{gen}}$,$\eta_{\mathrm{e}}^{\mathrm{gen}}$ and $\varphi_{\mathrm{e}}^{\mathrm{gen}}$ into the corresponding "measurable" values (i. e. as it is reconstructed by detector) is done by using the detector response matrices (Figs. 3.27 and 3.28). They are two dimensional histograms containing the values of $p_{\mathrm{T,\,e}}^{\mathrm{rec}} - p_{\mathrm{T,\,e}}^{\mathrm{gen}}$, $\eta_{\mathrm{e}}^{\mathrm{rec}} - \eta_{\mathrm{e}}^{\mathrm{gen}}$ and $\varphi_{\mathrm{e}}^{\mathrm{rec}} - \varphi_{\mathrm{e}}^{\mathrm{gen}}$ as the function of generated particle transverse momentum.

For each given generated $p_{\mathrm{T,\,e}}^{\mathrm{gen}}$ the detector response matrices are projected onto the $\Delta p_{\mathrm{T,\,e}}$, $\Delta\eta_{\mathrm{e}}$ and $\Delta\varphi_{\mathrm{e}}$. Based on these projected distributions, three random numbers are extracted for each value of $\Delta p_{\mathrm{T,\,e}}$, $\Delta\eta_{\mathrm{e}}$ and $\Delta\varphi_{\mathrm{e}}$, which are then used to transform the generated values:

$$p_{\mathrm{T,\,e}}^{\mathrm{meas}} = p_{\mathrm{T,\,e}}^{\mathrm{gen}} + \Delta p_{\mathrm{T,\,e}} \tag{3.9}$$

$$\eta_{\mathrm{e}}^{\mathrm{meas}} = \eta_{\mathrm{e}}^{\mathrm{gen}} + \Delta\eta_{\mathrm{e}} \tag{3.10}$$

$$\varphi_{\mathrm{e}}^{\mathrm{meas}} = \varphi_{\mathrm{e}}^{\mathrm{gen}} + \Delta\varphi_{\mathrm{e}} \tag{3.11}$$

No significant dependence of the momentum or azimuthal angle resolution on pseudorapidity was observed, therefore the three variables are smeared independently. In order to take into account the smearing effects on the edges of central barrel acceptance ($p_{\mathrm{T}} > 0.2$ GeV/c and $|\eta| < 0.8$), such transformation is performed during the Monte Carlo analysis before acceptance cuts are applied. The corresponding smearing effect on generated pairs from same-mother resonance and Dalitz decays is shown in Fig. 3.29, where it can be clearly seen especially for narrow resonance states such as $\phi \to e^+e^-$ or J/$\psi \to e^+e^-$ decays. For reconstructed electrons, the smearing procedure can be

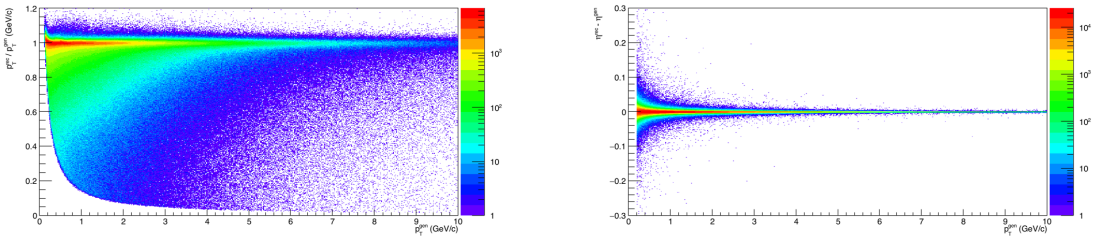

Figure 3.27: Resolution maps used for the smearing of MC generated values: transverse momentum (left) and pseudorapidity (right).

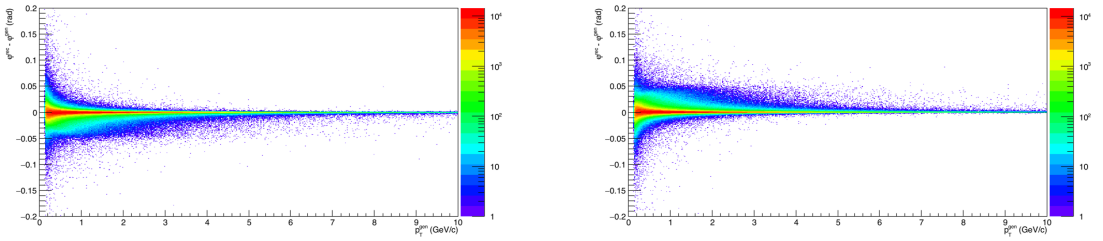

Figure 3.28: Resolution maps used for the smearing of MC generated values of azimuthal angle: for electrons (left) and for positrons (right). A slight shift between the reconstructed values for electrons and positrons is visible due to the opposite bending in the ALICE magnetic field.

verified by comparing the mass distributions obtained with $p_{\mathrm{T,\,e}}^{\mathrm{meas}}$ and with $p_{\mathrm{T,\,e}}^{\mathrm{rec}}$ values. A good agreement between two spectra can be seen in Fig. 3.30, which confirms that such transformation can reproduce the dielectron continuum as it is reconstructed by the detector.

3.4.3 Single Electron Efficiency

This subsection shows the results of single electron efficiency calculations which are used in the analysis for illustrative purposes only. The final signal efficiency is calculated as a function of mass using directly pairs originating either from same mother or from correlated semi-leptonic decays of heavy-flavour hadrons (see next subsection).

The single electron efficiency is defined as the ratio between reconstructed and generated electrons as a function of $x = p_{\mathrm{T}}, \eta, \varphi$, where for all generated particles the smearing procedure is applied ("measurable" values):

$$\epsilon(x) = \frac{\left(\frac{\mathrm{d}N}{\mathrm{d}x^{\mathrm{rec}}}\right)}{\left(\frac{\mathrm{d}N}{\mathrm{d}x^{\mathrm{meas}}}\right)}. \tag{3.12}$$

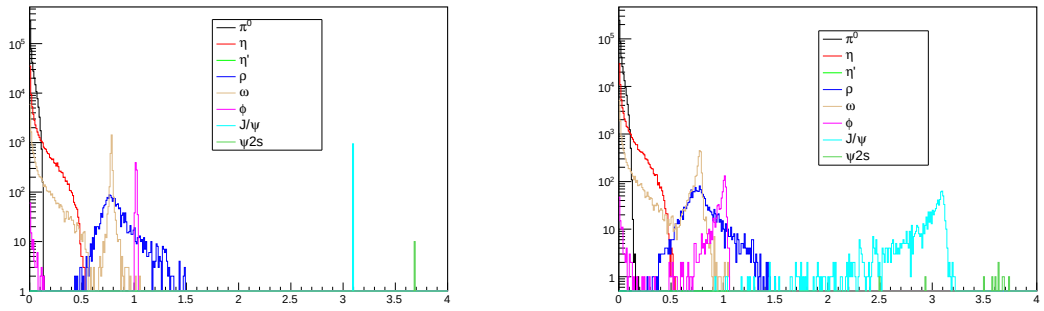

Figure 3.29: Invariant mass distribution of generated pairs from same mother decays obtained with true generated particle values (left) and with smeared ones (right).

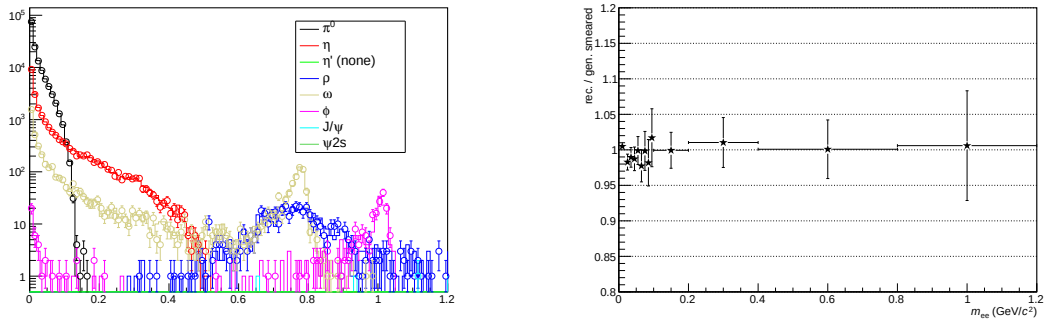

Figure 3.30: Comparison of the invariant mass distributions of pairs from same mother decays obtained with generated and smeared particle values (lines) and with directly reconstructed ones (open markers), the ratio between two methods is shown on the right plot. The comparison is done in Monte Carlo simulated data using exactly the same electrons.

For the calculation of the single electron (as well as pair) efficiency, only pure MC electrons originating from primary particles are used. It means that neither electrons from real photon conversions nor hadrons misidentified as electrons nor decay products of strange hadrons enter the equation above, and such contamination is removed in the experimental data from dielectron spectrum using data-driven methods. Figure 3.31 shows $p_{\mathrm{T,\,e}}^{\mathrm{gen}}$, $\eta_{\mathrm{e}}^{\mathrm{gen}}$ and $\varphi_{\mathrm{e}}^{\mathrm{gen}}$ distributions of generated electrons and positrons used for the efficiency calculation.

The track and PID selection listed in Tables 3.1 and 3.2 reduce hadron and secondary particle contamination, but cause a loss of signal electron tracks. Fig. 3.32 shows the re-

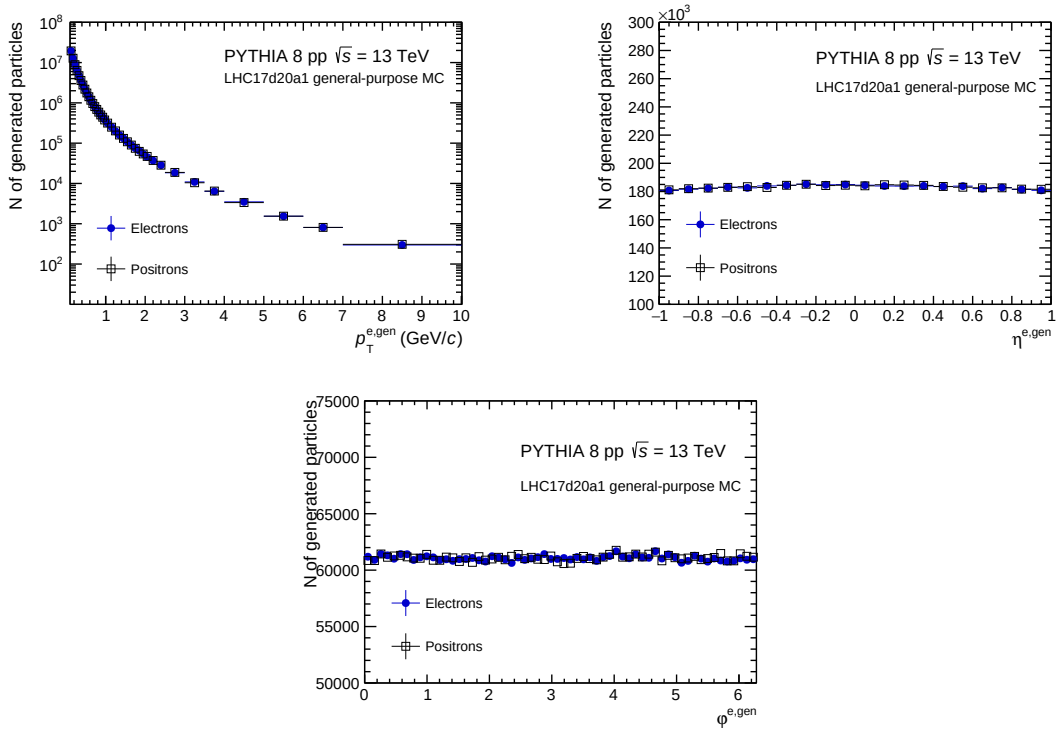

Figure 3.31: $p_{\mathrm{T,\,e}}^{\mathrm{gen}}$, $\eta_{\mathrm{e}}^{\mathrm{gen}}$ and $\varphi_{\mathrm{e}}^{\mathrm{gen}}$ distributions of generated electrons and positrons used for the efficiency calculation.

construction efficiency for electron and positron candidates as a function of $p_{\mathrm{T,\,e}}$, η_{e} and φ_{e}. Drops of efficiency as a function of particle momentum at $p_{\mathrm{T,\,e}}{\sim}0.5$ GeV/c and at $p_{\mathrm{T,\,e}}{\sim}1.0$ GeV/c reflect the rejection of hadron contamination, from kaons and protons, respectively, with the TPC detector and the requirement of good TOF PID signal in these crossing regions. The effect of the inactive areas in the ITS detector (and especially in the first SPD layer, Fig. 3.9), caused by some hardware-related problems during data taking, is clearly visible in the efficiency plot as a function of azimuthal angle φ_{e}. Small differences between electron and positron reconstruction efficiencies can be explained by the opposite curvature of electrons and positrons in the ALICE magnetic field folded with the non-symmetric detector geometry. The trend of the reconstruction efficiency as a function of the azimuthal angle between electrons and positrons is reversed for the opposite magnetic field polarity, which is also properly simulated.

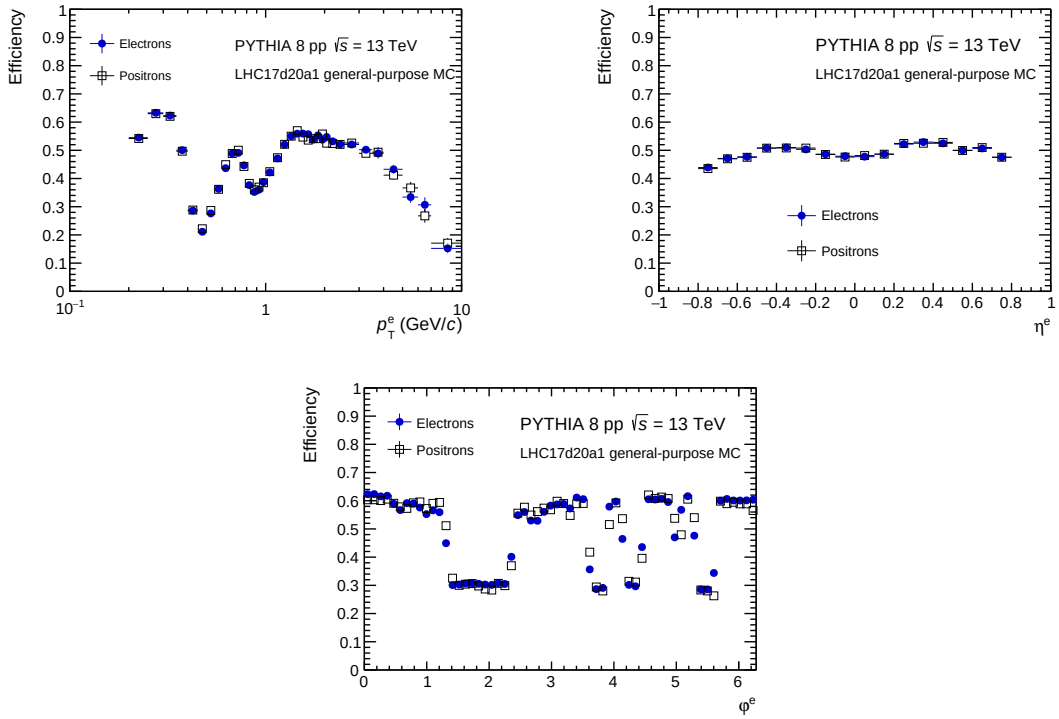

Figure 3.32: Single electron and positron reconstruction efficiencies as a function of $p_{\mathrm{T,\,e}}$, η_{e} and φ_{e}.

3.4.4 Pair Efficiency

The pair efficiency is defined as the ratio between the number of reconstructed and number of generated pairs after smearing procedure as a function of invariant mass and transverse momentum:

$$\epsilon(m_{\mathrm{ee}}, p_{\mathrm{T,\,ee}}) = \frac{\left(\frac{\mathrm{d}^2 N^{\mathrm{ee}}}{\mathrm{d}m_{\mathrm{ee}}^{\mathrm{rec}} \mathrm{d}p_{\mathrm{T}}^{\mathrm{ee,rec}}}\right)}{\left(\frac{\mathrm{d}^2 N^{\mathrm{ee}}}{\mathrm{d}m_{\mathrm{ee}}^{\mathrm{meas}} \mathrm{d}p_{\mathrm{T}}^{\mathrm{ee,meas}}}\right)}. \tag{3.13}$$

For the calculation of the pair reconstruction efficiency, only correlated MC pairs are used in the analysis. They originate either from the same light-flavour and J/ψ meson decays or from the correlated semi-leptonic decays of charmed and bottom hadrons.

Fig. 3.33 shows the mass spectrum of generated dielectron pairs from the same-mother decays of light-flavour hadrons and the corresponding pair reconstruction efficiency. For $\mathrm{J}/\psi \to e^+e^-$ decays, a special heavy-flavour enriched Monte Carlo production is used to extract the signal efficiency in the corresponding mass range. These J/ψ

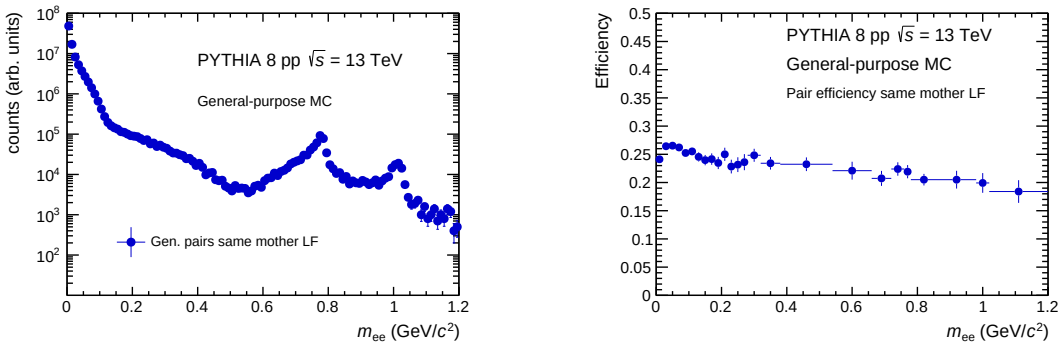

Figure 3.33: Mass spectrum of generated dielectron pairs from light-flavour meson decays (left) and the pair reconstruction efficiency (right). The smearing procedure is applied to every generated track.

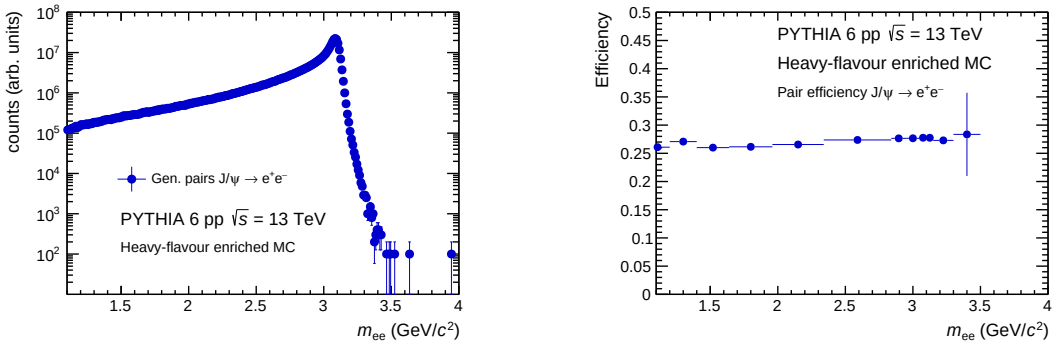

Figure 3.34: Mass spectrum of generated dielectron pairs from J/ψ decays (left) and the pair reconstruction efficiency (right). Decays include radiative $\mathrm{J}/\psi \to \gamma e^+e^-$ channel and feed-down from beauty hadrons. The smearing procedure is applied to every generated track.

decays include radiative channel $\mathrm{J}/\psi \to \gamma\, e^+e^-$, i. e. decays when γ is emitted by one of the electrons in final state, and the feed-down from beauty hadrons. The mass spectrum of generated dielectron pairs and the corresponding pair reconstruction efficiency are shown in Fig. 3.34.

In order to improve the statistical precision, for the studies of dielectron efficiency from open heavy-flavour decays a special heavy-flavour enriched Monte Carlo simulations are used. In these MC data, several dielectron production mechanisms are generated in each event with the following probabilities:

- $\mathrm{c\overline{c}} \rightarrow \mathrm{e^+e^-} + X$ (8%): a charm quark-antiquark pair is generated per event, and charmed hadrons (D mesons or Λ_c baryons) are forced to decay semileptonically, with a constraint on both produced electrons to be within $|y_\mathrm{e}| < 1.2$
- $\mathrm{b\overline{b}} \rightarrow \mathrm{e^+e^-} + X$ (8%): a beauty quark-antiquark pair is generated per event, and beauty hadrons (B mesons or Λ_b baryons) are forced to decay semileptonically, with a constraint on both electrons to be within $|y_\mathrm{e}| < 1.2$. The following decays of produced charmed hadrons are also forced to be semileptonic, but without any constraint on electron rapidity
- $\mathrm{b\overline{b}} \rightarrow \mathrm{e} + \mathrm{X}$ (66%): a beauty quark-antiquark pair is generated per event, and at least one electron in event originating from open heavy-flavour decay should be produced in $|y_\mathrm{e}| < 1.2$. Neither beauty nor charmed hadrons (if present) are forced to decay semileptonically, also no rapidity constraint is applied for any other electrons produced in event

During the analysis of Monte Carlo simulations, dielectron pairs originating from correlated semi-leptonic decays of heavy-flavour hadrons need a special treatment, since such pairs originate not simply from the same parent hadron but from a $Q\overline{Q}$ pair. At the quark level, the event history in Pythia simulations is sometimes unclear, especially in the case when several $Q\overline{Q}$ pairs are produced in a single event [182]. The reconstruction of the electron origin and the proper electron–positron pairing therefore becomes complicated, so for efficiency calculation the generated events are first pre-selected as described below.

For the study of $\mathrm{c\overline{c}} \rightarrow \mathrm{e^+e^-}$ pair efficiency, only events containing exactly one charmed hadron and one charmed anti-hadron are selected, and no beauty quark or hadron should be present in the generated event. In this way, the pairing of correlated electrons and positrons from charmed hadrons becomes straightforward (Fig. 1.8), and only unlike-sign pairs from charmed hadrons are produced[6]. These unlike-sign pairs are used for the calculation of $\mathrm{c\overline{c}} \rightarrow \mathrm{e^+e^-}$ pair efficiency shown in Fig. 3.35. As a cross-check, the $\mathrm{c\overline{c}} \rightarrow \mathrm{e^+e^-}$ pair efficiency is calculated in events with any number of produced charm hadrons (but still the presence of beauty quark/hadron is not allowed). In this case the like-sign combinatorial background is subtracted from both reconstructed and generated unlike-sign pairs in the same way as for experimental data (Section 3.3). The pair efficiency calculated in this way is found to be the same as the one obtained with "clean" $\mathrm{c\overline{c}}$ events containing only one charmed hadron and one charmed anti-hadron.

The studies of dielectron efficiency from open beauty decays are further complicated due to the significant probability of $\mathrm{B^0} \leftrightarrow \overline{\mathrm{B^0}}$ oscillations which create unlike-sign and like-sign dielectron pairs at various rates. For these studies, $\mathrm{b\overline{b}} \rightarrow \mathrm{e+X}$ events are used, in which one beauty quark-antiquark pair generated per event and at least one electron in event produced in $|y_\mathrm{e}| < 1.2$, without forcing semileptonic decays. To simplify the pairing of electrons from semi-leptonic decays of all produced charm and beauty

[6]Oscillation of $\mathrm{D^0}$ mesons with a small probability of $\sim 0.1\%$ [183, 184] was not simulated.

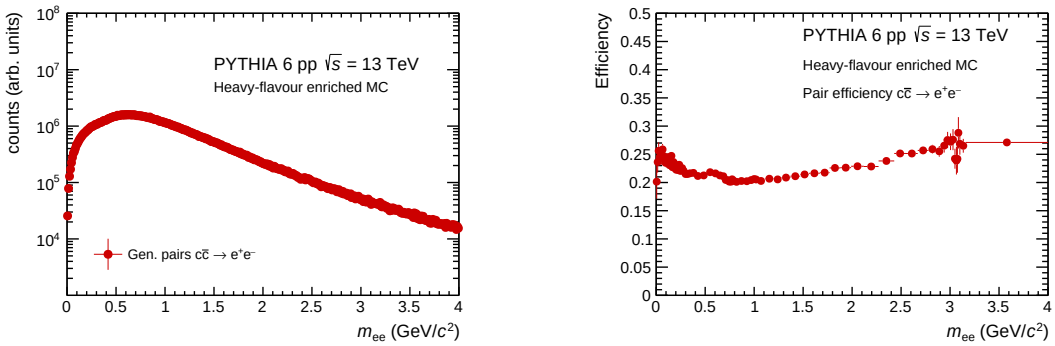

Figure 3.35: Mass spectrum of generated dielectron pairs from correlated semi-leptonic charm decays (left, arbitrary normalisation) and the corresponding reconstruction efficiency (right). The smearing procedure is applied to generated tracks.

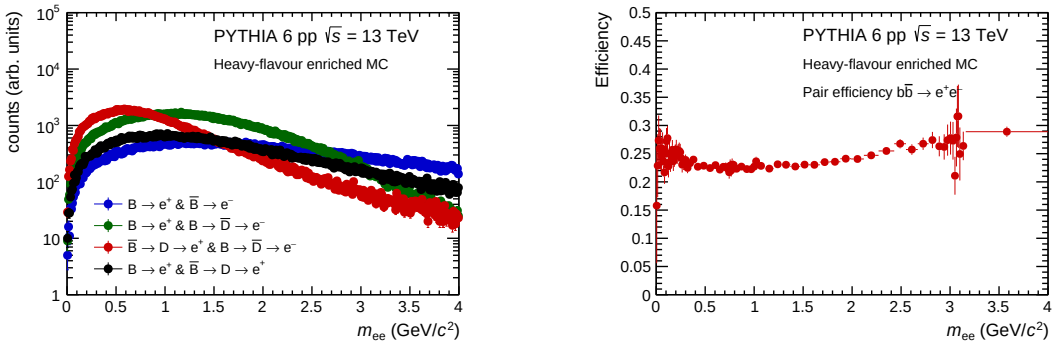

Figure 3.36: Mass spectra of generated dielectron pairs from correlated semi-leptonic beauty decays (left, arbitrary normalisation) and the corresponding pair reconstruction efficiency calculated with the like-sign subtraction method (right). Note that for green and black curves on the left plot only half of the contribution is shown, the second half (with the same yield) comes from charge-conjugated processes. The smearing procedure is applied to generated tracks.

hadrons, only events with exactly one beauty hadron and one beauty anti-hadron are used for the efficiency calculation, with no charm quarks present in the event and no oscillation of B mesons. The latter is implemented in Monte Carlo simulations as "wrong-sign" decays, i. e. as decays like $\mathrm{B} \rightarrow \mathrm{e}^-$ or $\overline{\mathrm{B}} \rightarrow \mathrm{e}^+$, which can be easily tagged and used as B meson oscillation veto. For consistency with the experimental data analysis, like-sign contributions originating from decays like $\mathrm{B} \rightarrow \mathrm{e}^+ \,\&\, \overline{\mathrm{B}} \rightarrow \mathrm{D} \rightarrow \mathrm{e}^+$ are subtracted both

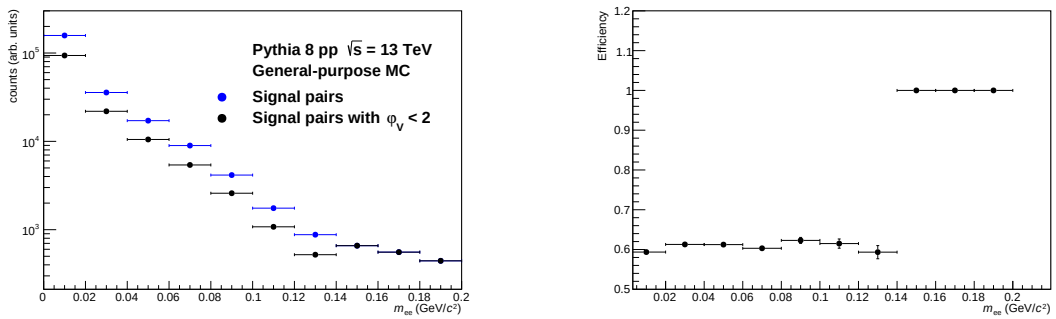

Figure 3.37: Mass spectrum of signal pairs in Monte Carlo data before and after $\varphi_V < 2$ requirement (left), and the corresponding signal efficiency (right). $\varphi_V < 2$ requirement is applied in the mass region below $m_{\rm ee} = 140\ {\rm MeV}/c^2$.

from generated and reconstructed unlike-sign pairs. The mass shapes of generated pairs and $\rm b\overline{b} \rightarrow e^+e^-$ pair efficiency are shown in Fig. 3.36. Different mass spectra represent different decay kinematics in various processes producing dielectron pair in the final state, e. g. $\rm B \rightarrow e^+$ & $\rm \overline{B} \rightarrow e^-$ or $\rm \overline{B} \rightarrow D \rightarrow e^+$ & $\rm B \rightarrow \overline{D} \rightarrow e^-$. As a cross-check, the $\rm b\overline{b} \rightarrow e^+e^-$ pair efficiency is calculated in events with any number of beauty hadrons produced in the event and with allowed oscillations of B mesons. The pair efficiency calculated again with like-sign subtraction method is found to be consistent to the one obtained with "clean" $\rm b\overline{b}$ events containing only one beauty hadron and one beauty anti-hadron with no oscillation.

On top of the single track selection criteria listed in Table 3.1, dielectron pairs originating from real photon conversions in detector material are removed from raw dielectron spectrum using a requirement on the pair orientation in the ALICE magnetic field (Section 3.3). This results also in the rejection of good signal pairs which are expected to have no preferred orientation with respect to the magnetic field. The impact of $\varphi_V < 2$ requirement on the signal pairs is studied in Monte Carlo simulations using only decays from light-flavour hadrons, and the corresponding signal efficiency due to φ_V cut is shown in Fig. 3.37. Such efficiency is found to be slightly lower than the $2/\pi$ value expected from a naive flat φ_V distribution, which comes from the acceptance minimum for low-mass pairs with $\varphi_V \sim \pi/2$, imposed by the finite pseudorapidity coverage $|\eta| < 0.8$ of the central barrel.

In order to obtain the final signal efficiency as a function of mass, the pair efficiencies for same mother and heavy flavour pairs are combined in the following way:

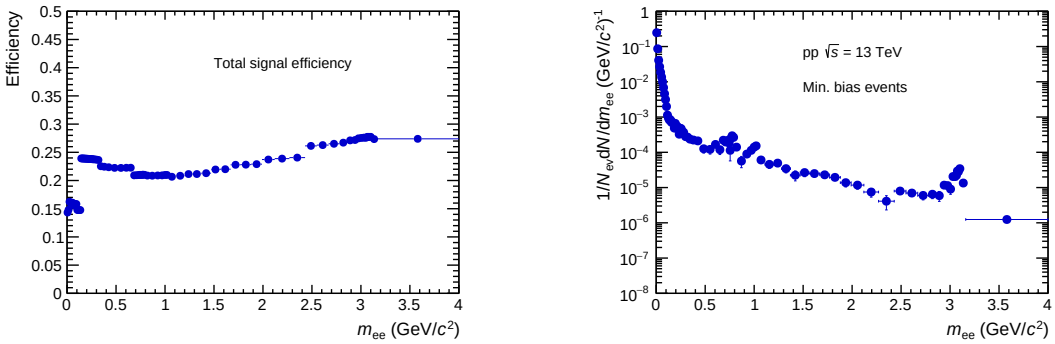

Figure 3.38: Total signal efficiency as a function of invariant mass (left) and the corrected dielectron spectrum normalised by the number of analysed events (right) in minimum-bias data for $p_{\mathrm{T,\,ee}} < 6\ \mathrm{GeV}/c$.

$$\epsilon(m_{\mathrm{ee}})_{total} = \epsilon(m_{\mathrm{ee}})_{LF}\frac{\mathrm{d}N^{ee}_{LF}}{\mathrm{d}N_{ee}} + \epsilon(m_{\mathrm{ee}})_{\mathrm{c\bar{c}}}\frac{\mathrm{d}N^{ee}_{\mathrm{c\bar{c}}}}{\mathrm{d}N_{ee}} + \epsilon(m_{\mathrm{ee}})_{\mathrm{b\bar{b}}}\frac{\mathrm{d}N^{ee}_{\mathrm{b\bar{b}}}}{\mathrm{d}N_{ee}} + \epsilon(m_{\mathrm{ee}})_{\mathrm{J/\psi}}\frac{\mathrm{d}N^{ee}_{\mathrm{J/\psi}}}{\mathrm{d}N_{ee}}, \tag{3.14}$$

where ϵ_{LF}, $\epsilon_{\mathrm{c\bar{c}}}$, $\epsilon_{\mathrm{b\bar{b}}}$ and $\epsilon_{\mathrm{J/\psi}}$ are shown in Figs. 3.33, 3.35, 3.36 and 3.34 respectively, and the corresponding relative contributions to the total signal are taken from hadronic cocktail calculations (Section 3.5). The total efficiency is calculated as a function of mass in each $p_{\mathrm{T,\,ee}}$ bin used in the analysis. Figure 3.38 shows the overall signal efficiency (also taking into account the efficiency due to the $\varphi_V < 2$ requirement in $m_{\mathrm{ee}} < 140\ \mathrm{MeV}/c^2$) and the corrected dielectron spectrum in minimum-bias data normalised by the number of analysed events for $p_{\mathrm{T,\,ee}} < 6\ \mathrm{GeV}/c$. The results in different $p_{\mathrm{T,\,ee}}$ bins are shown in Fig. 3.39.

The efficiency correction of high-multiplicity data sample is complicated due to the absence of specific Monte Carlo productions anchored to high-multiplicity data. Therefore, the same corrections as described in this Section are applied also to high-multiplicity raw dielectron spectra, and additional uncertainties are assigned to the corrected data points due to possible multiplicity dependence (Section 3.6). Corrected high-multiplicity data are used to extract the fraction of virtual direct photons as well as for the measurements of heavy-flavour production cross-sections as described in Chapter 4.

Finally, the dielectron spectrum in inelastic pp collisions also needs to be corrected for the fraction of collisions with a dielectron signal present that were lost. This can happen if such events either did not fulfil trigger condition or did not have a reconstructed interaction vertex. The corresponding efficiencies have been studied in Pythia simulations, considering all events that contained an electron–positron pair from the same

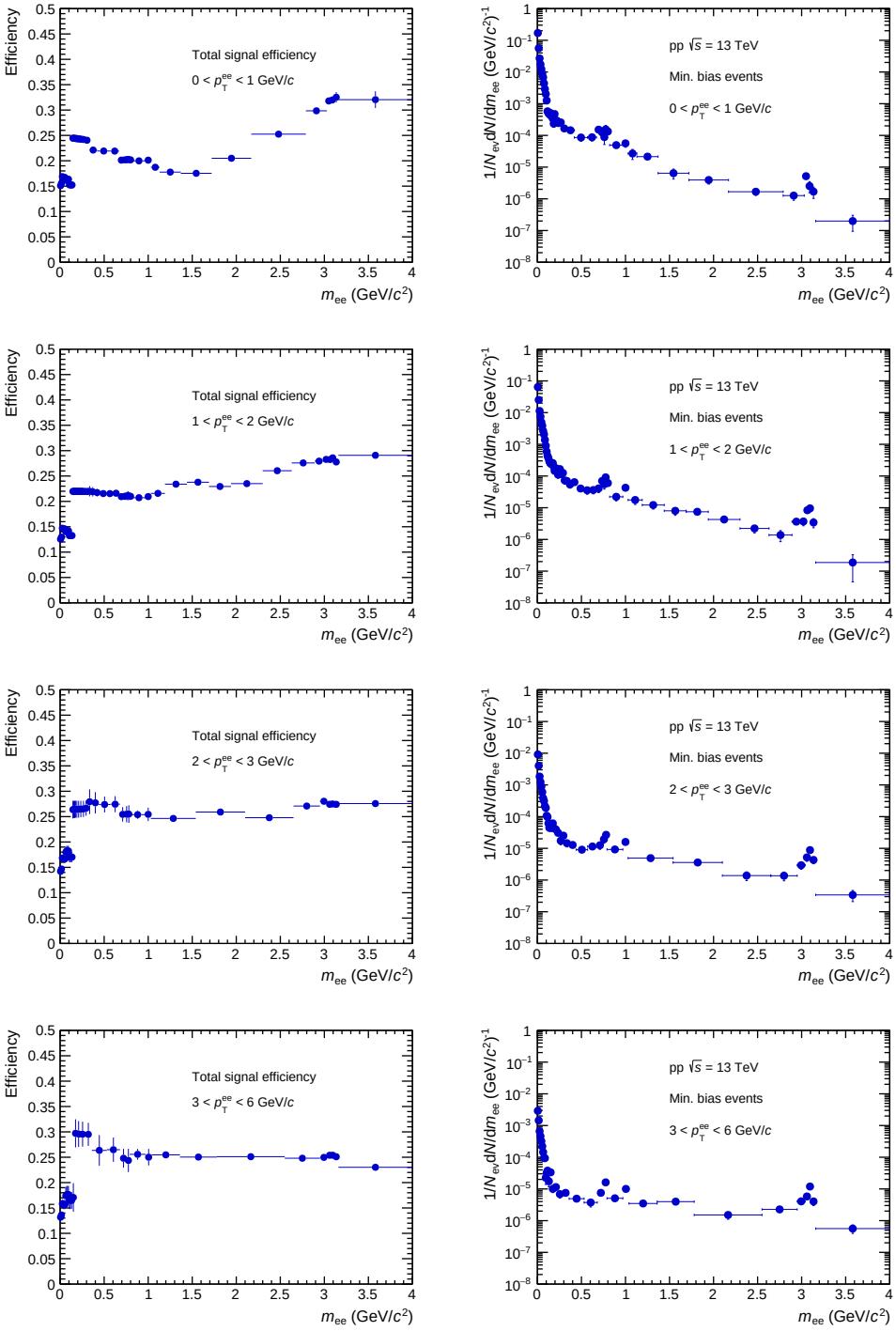

Figure 3.39: Total signal efficiency as a function of invariant mass (left) and corrected dielectron spectrum normalised by the number of analysed events (right) in minimum-bias data in different $p_{\mathrm{T,\,ee}}$ bins.

hadron decay, with both legs in the ALICE central barrel acceptance $|\eta_{\mathrm{e}}| < 0.8$ and $p_{\mathrm{T,\,e}} > 0.2$ GeV/c. The efficiency to fire minimum-bias trigger in such events was found to be $(99 \pm 1)\%$; open heavy-flavour events should have an even higher efficiency. A systematic uncertainty of 1% is therefore assigned to cover the possibility of a fully efficient minimum-bias trigger. In the same simulation, the vertex reconstruction efficiency in events with a dielectron and a minimum-bias trigger is found to be 100% with negligible uncertainties. For high-multiplicity data, the trigger and vertex reconstruction efficiencies are assumed to be 100% with negligible uncertainties.

3.5 Hadronic Cocktail

The measured dielectron spectrum is compared to the expectations from all known hadronic sources, i. e. the hadronic "cocktail", contributing to the dielectron spectrum in the ALICE central barrel acceptance ($|\eta_{\mathrm{e}}| < 0.8$ and $p_{\mathrm{T,\,e}} > 0.2$ GeV/c). This Section describes the cocktail calculations of light- and heavy-flavour meson decays with their vacuum properties (π^0, η, η', ρ, ω, ϕ, J/ψ and ψ(2S)) as well as the contributions from open heavy-flavour decays. Cocktail calculations for high-multiplicity pp collisions are discussed separately in Sections 3.5.3 (light-flavour part) and 3.5.4 (heavy-flavour decays).

3.5.1 Light-Flavour Decays

To estimate the contributions from light-flavour mesons, a fast Monte Carlo simulation is used as detailed in [157]. A dedicated phenomenological event generator "Exodus" [108] is implemented in the ALICE analysis framework, which simulates Dalitz and 2-body decays of light-flavour hadrons. A summary of light-flavour decays simulated in cocktail calculations is presented in Table 3.3. The following light-flavour hadron decays contribute to the dielectron signal:

- $\pi^0 \rightarrow \gamma\,\mathrm{e}^+\mathrm{e}^-$
- $\eta \rightarrow \gamma\,\mathrm{e}^+\mathrm{e}^-$
- $\rho^0 \rightarrow \mathrm{e}^+\mathrm{e}^-$
- $\omega \rightarrow \pi^0\,\mathrm{e}^+\mathrm{e}^-$ and $\omega \rightarrow \mathrm{e}^+\mathrm{e}^-$
- $\eta' \rightarrow \gamma\,\mathrm{e}^+\mathrm{e}^-$ and $\eta' \rightarrow \omega\,\mathrm{e}^+\mathrm{e}^-$
- $\phi \rightarrow \eta\,\mathrm{e}^+\mathrm{e}^-$, $\phi \rightarrow \pi^0\,\mathrm{e}^+\mathrm{e}^-$ and $\phi \rightarrow \mathrm{e}^+\mathrm{e}^-$

All mesons are assumed to be unpolarised, with flat rapidity distribution at mid-rapidity. The mass distribution of dielectron Dalitz decays follows the Kroll-Wada expression in Eq. 1.7 [69], with electromagnetic form factors measured by the NA60 Collaboration [192, 193]. The 2-body decays of ω and ϕ mesons are generated using Gounaris-Sakurai expression to describe their mass shape [194]. The ρ line shape has been studied in detail by the NA60 Collaboration [192], who confirmed the need for a Boltzmann

Table 3.3: Summary of light-flavour hadron decays contributing to dielectron spectrum.

Particle	Mass, MeV/c^2	Decay(s) (B.R.)	Ratio to π^0 at high p_{T}	Estimation method	References
π^0	134.9766 ± 0.0006	$\gamma\,\mathrm{e^+e^-}$ $(1.174 \pm 0.035)\%$	1	$\pi^{\pm}$ (extrapolated)	[42, 185–188]
η	547.862 ± 0.018	$\gamma\,\mathrm{e^+e^-}$ $(6.9 \pm 0.4)\times10^{-3}$	0.5 ± 0.1	η/π^0 at 7 TeV	[189]
ρ^0	775.26 ± 0.25	$\mathrm{e^+e^-}$ $(4.72 \pm 0.05)\times10^{-5}$	1.0 ± 0.2	ρ/π^0 (Pythia)	[180]
ω	782.65 ± 0.12	$\pi^0\,\mathrm{e^+e^-}$ $(7.7 \pm 0.6)\times10^{-4}$ $\mathrm{e^+e^-}$ $(7.28 \pm 0.14)\times10^{-5}$	0.85 ± 0.17	ω/π^0 (Pythia)	[179]
η'	957.78 ± 0.06	$\gamma\,\mathrm{e^+e^-}$ $(< 9 \times 10^{-4})$ $\omega\,\mathrm{e^+e^-}$ $(2.0 \pm 0.4)\times10^{-4}$	0.40 ± 0.08	m_{T} scaling	[190]
ϕ	1019.461 ± 0.019	$\eta\,\mathrm{e^+e^-}$ $(1.15 \pm 0.10)\times10^{-4}$ $\pi^0\,\mathrm{e^+e^-}$ $(1.12 \pm 0.28)\times10^{-5}$ $\mathrm{e^+e^-}$ $(2.954 \pm 0.030)\times10^{-4}$	0.13 ± 0.04	m_{T} scaling	[190, 191]

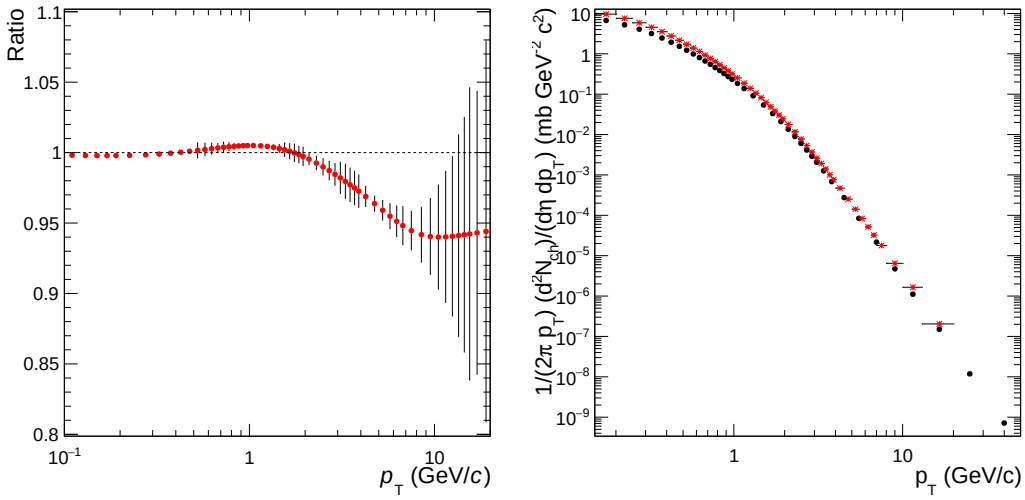

Figure 3.40: Left: the ratio between charged pion spectra extrapolated to $\sqrt{s} = 13$ TeV by using pion-to-hadron ratio from pp collisions at $\sqrt{s} = 7$ TeV [186, 187] or from pp collisions at $\sqrt{s} = 2.76$ TeV [186, 188]. Right: extrapolated charged pion spectrum at $\sqrt{s} = 13$ TeV in INEL (black points) and in INEL> 0 (red asterisk) event classes.

term beyond the standard description [195] and provided a precise measurement of the effective temperature parameter. Their parametrisation is used in this thesis as well.

By the time of this thesis only very limited (or no) data were available for the production cross-sections of relevant hadrons in pp collisions at $\sqrt{s} = 13$ TeV. Therefore, the production of each source listed in Table 3.3 is estimated by various methods described below. They are also summarised in Table 3.3 together with the references to relevant measurements or methods.

First, following the approach outlined in [185], the charged pion p_{T}-spectrum at $\sqrt{s} = 13$ TeV is approximated by scaling the p_{T}-spectrum of charged hadrons measured at $\sqrt{s} = 13$ TeV [42] by the pion-to-hadron ratio from pp collisions at $\sqrt{s} = 7$ TeV [186, 187]. The difference with respect to the same procedure based on the pion-to-hadron ratio measured at $\sqrt{s} = 2.76$ TeV [186, 188] is smaller than 1% at low p_{T} and reaches 5% at high p_{T} (Fig. 3.40 left). The difference in normalisation of the charged hadron p_{T}-spectra at $\sqrt{s} = 13$ TeV to INEL>0 events, i. e. inelastic collisions that produce at least one charged particle in $|\eta| < 1$, rather than inelastic events is corrected by the 21% difference in the p_{T} integrated $\mathrm{d}N_{\mathrm{ch}}/\mathrm{d}\eta$ values for these two event classes (5.31 ± 0.18 for INEL and 6.46 ± 0.19 for INEL>0 events, Fig. 3.40 right) [42]. A conservative uncertainty of 10% is assigned on this extrapolation. The resulting extrapolated charged-pion p_{T}-spectrum is fitted with a modified Hagedorn function [76, 196]:

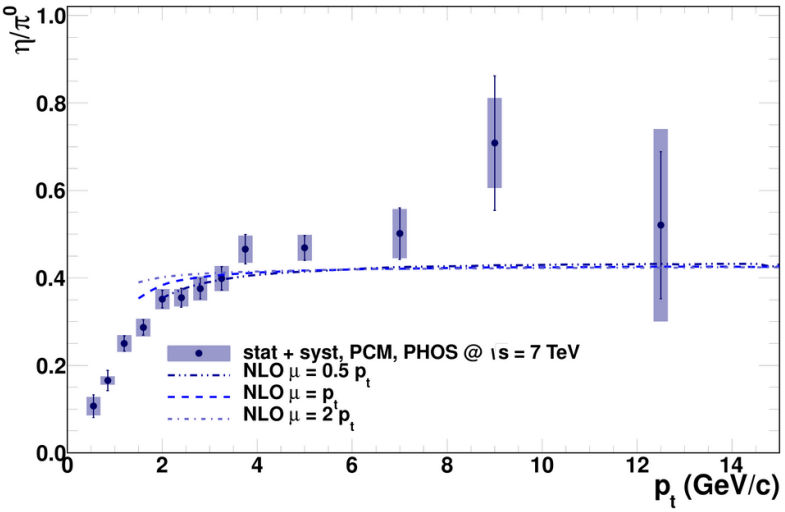

Figure 3.41: η/π^0 ratio measured in pp collisions at $\sqrt{s} = 7$ TeV compared to NLO pQCD predictions [189].

$$\frac{\mathrm{d}^2N}{\mathrm{d}y\mathrm{d}p_\mathrm{T}} = p_\mathrm{T} \times A \times \left(exp\left(ap_\mathrm{T} + bp_\mathrm{T}^2\right) + \frac{p_\mathrm{T}}{p_0} \right)^{-n} \tag{3.15}$$

This function approaches an exponential at low p_T and a power law at larger p_T and described very well the measured hadron spectra over the full p_T range [190]. The result of the fit is taken as proxy for the neutral-pion p_T-distribution, with the simulated cross section per unit rapidity for the π^0 of $\mathrm{d}\sigma/\mathrm{d}y|_{y=0} = 155.2$ mb.

For the η meson, a fit of the measured η/π^0 ratio in pp collisions at $\sqrt{s} = 7$ TeV is used (Fig. 3.41) [189] assuming that this ratio does not change between $\sqrt{s} = 7$ TeV and 13 TeV. The Monash 2013 tune of Pythia 8 is found to describe well the ρ/π^0 and ω/π^0 ratios measured in pp collisions at $\sqrt{s} = 2.76$ and 7 TeV, respectively [179, 180]. Therefore, MC simulations obtained with this tune at $\sqrt{s} = 13$ TeV are used to obtain the ρ/π^0 and ω/π^0 ratios. Based on the η/π^0, ρ/π^0 and ω/π^0 data, the ratios at high p_T are 0.5 ± 0.1, 1.0 ± 0.2 and 0.85 ± 0.17, respectively. Finally, η' and ϕ mesons are generated assuming m_T scaling, i. e. replacing p_T of the meson with $\sqrt{m^2 - m_\pi^2 + (p_\mathrm{T}/c)^2}$ [190]. For m_T scaling, particle yields are normalised at high p_T relative to the π^0 yield: 0.40 ± 0.08 for η' (based on Pythia calculations) and 0.13 ± 0.04 for ϕ [191].

The branching ratios for the decays into dielectrons are taken from the PDG [50]. The four-body decay $\eta' \to \pi^+\pi^-e^+e^-$ is neglected since its shape is not well established and its contribution is only marginal in the very low mass region (about two orders of magnitude lower than the π^0 contribution). Both four-body decay modes $\eta \to e^+e^-e^+e^-$ and $\eta \to \pi^+\pi^-e^+e^-$ are neglected as well for the same reasons.

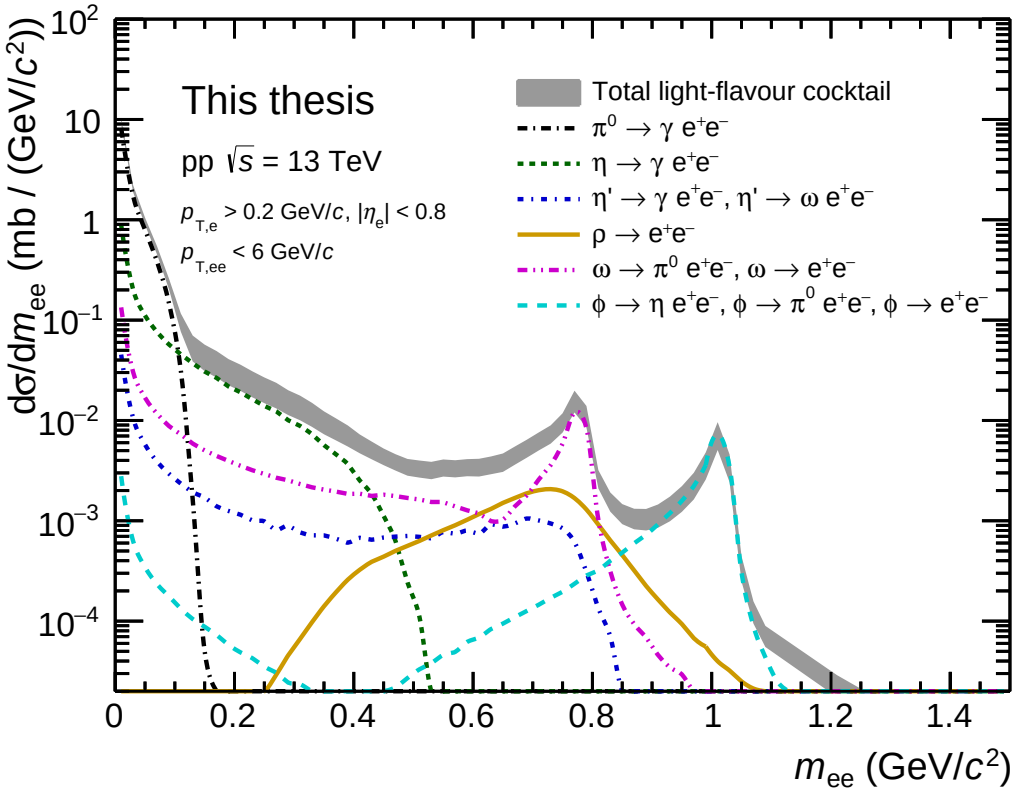

Figure 3.42: Mass spectra of the light-flavour hadronic cocktail in pp collisions at $\sqrt{s} = 13$ TeV after acceptance cuts and resolution smearing.

Acceptance cuts of $p_{\mathrm{T,\,e}} > 0.2$ GeV/c and $|\eta_{\mathrm{e}}| < 0.8$ are applied at the single track level as for the experimental data analysis. The momentum resolution and radiative corrections obtained with full-scale Monte Carlo simulations with 13 TeV are applied to the generated dielectron tracks before acceptance cuts in the same way as for experimental data analysis, independently for p_{T}, ϕ and η (Figs. 3.27 and 3.28). This results in a mass resolution of approximately 1%. The resulting mass shape of all light-flavour cocktail components after acceptance and resolution smearing is shown in Fig. 3.42.

The following sources of systematic uncertainties have been evaluated for light-flavour cocktail calculations: the input parameterisations of the measured spectra as a function of p_{T} ($\pi^{\pm}$, η/π^0 and ω/π^0), the branching fractions of all included decay modes, the scaling parameters at high p_{T} and the resolution smearing. The uncertainties from each of the considered sources in the light flavour mass spectrum are shown in 3.43, where it can be seen how the highest contribution to the total uncertainty comes from the variation of the scaling factors.

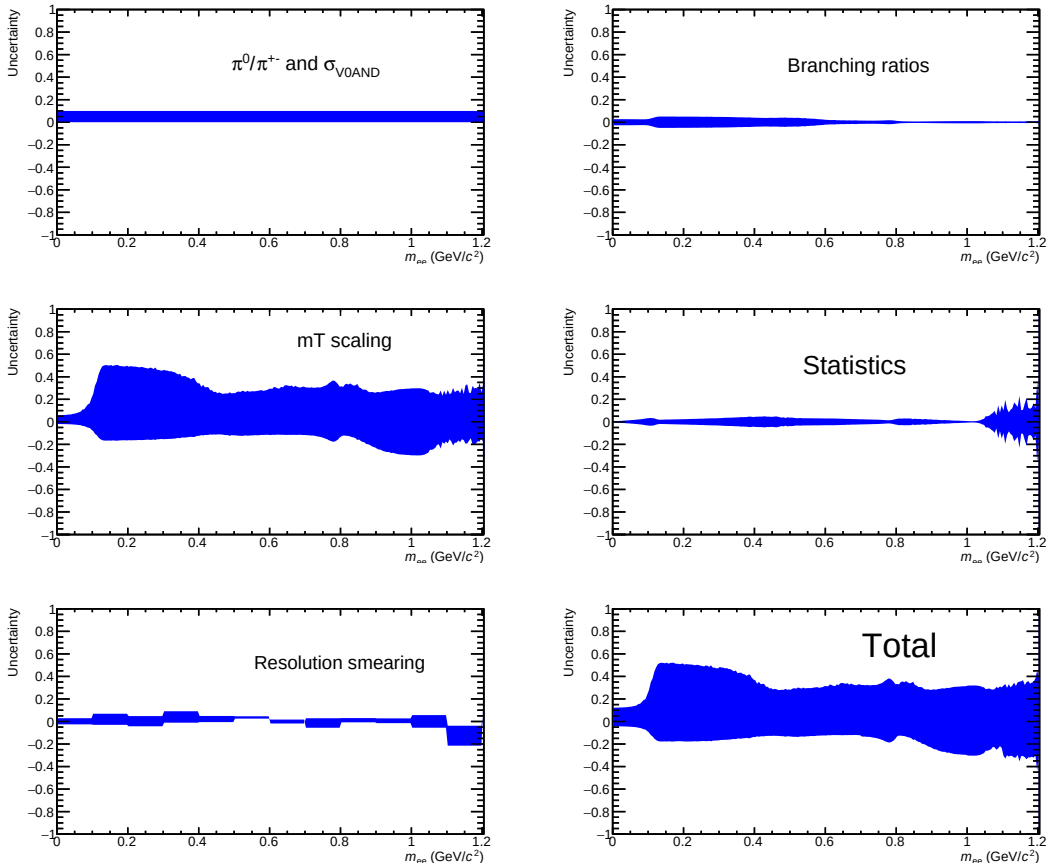

Figure 3.43: Relative uncertainties from different contributions evaluated for light-flavour cocktail.

3.5.2 Heavy-Flavour Decays

Electron pairs from the semi-leptonic decays of open heavy-flavour hadrons are simulated with two different Monte Carlo generators: the leading-order (LO) event generator Pythia 6.4.25 [174], which includes NLO parton showering processes, with Perugia 2011 tune [178] and the next-to-leading order (NLO) event generator Powheg [197–200]. Both generators were found to be consistent with FONLL calculations [30] and to reproduce the measurements within uncertainties [141].

For $2 \rightarrow 2$ processes, Pythia uses leading-order pQCD matrix elements with a leading-logarithmic p_{T}-ordered parton shower, and the underlying event simulation includes multiple parton interactions. The fragmentation and hadronisation of the charm and beauty quarks are based on the Lund string model. The Perugia 2011 set of parameters [178] was tuned on first LHC data, mainly from multiplicity and underlying-event related measurements. In this tune, the parton distribution functions are parametrised

with the CTEQ5L [201] functions.

In the Powheg (POsitive Weight Hardest Emission Generator) method, the hardest radiation is generated first using the exact NLO matrix elements. The Powheg output can then be interfaced to many modern Monte Carlo programs for parton shower generation (e. g. Pythia), which can be either p_{T}-ordered or allows the implementation of a p_{T} veto. In this work the Powheg BOX framework [198, 200] is used together with Perugia 2011 tune of Pythia 6.4 and CTEQ6.6 [202] functions for the input parton distribution functions.

In order to obtain the dielectron spectrum from open charm, a dedicated MC sample containing of at least one $\mathrm{c\overline{c}}$ pair per event with forced semi-leptonic decays is analysed (Section 3.4.4). All electrons, which come from the decay of a charm hadron and are within acceptance, are paired to unlike-sign and like-sign pairs. For a consistency with the experimental data analysis, the resulting like-sign spectrum is subtracted from the unlike-sign pairs in order to obtain the final dielectron spectrum. For the $\mathrm{b\overline{b}}$ MC sample, electrons are considered when coming from the decay of an intermediate charm or beauty meson, in order to take into account dielectron pairs with electrons coming from b quarks via intermediate charmed hadron, e. g. $\overline{\mathrm{B}} \rightarrow \mathrm{D} \rightarrow \mathrm{e}^{+}$ & $\mathrm{B} \rightarrow \overline{\mathrm{D}} \rightarrow \mathrm{e}^{-}$. Detector effects are implemented as for the light-hadron cocktail. The spectra are normalised to cross sections at midrapidity that are based on FONLL [30–32] extrapolations of the ALICE measurements at 7 TeV:

- $\frac{\mathrm{d}\sigma_{\mathrm{c\overline{c}}}}{\mathrm{d}y} = 954 \pm 69(\mathrm{stat.}) \pm 97(\mathrm{syst.})\ \mu\mathrm{b}$ [62]
- $\frac{\mathrm{d}\sigma_{\mathrm{b\overline{b}}}}{\mathrm{d}y} = 43 \pm 10\ \mu\mathrm{b}$ [140, 141].

Following the description in [203], a pQCD-driven $\sqrt{s}$-scaling of these measurements leads to the following cross sections per unit rapidity at $\sqrt{s} = 13\ \mathrm{TeV}$:

$$\frac{\mathrm{d}\sigma_{\mathrm{c\overline{c}}}}{\mathrm{d}y} = 1296^{+172}_{-162}\ \mu\mathrm{b}$$
$$\frac{\mathrm{d}\sigma_{\mathrm{b\overline{b}}}}{\mathrm{d}y} = 68^{+15}_{-16}\ \mu\mathrm{b}$$

The quoted uncertainties take into account both the measured uncertainty and the FONLL extrapolation uncertainties. The latter (dominated by scale uncertainties but also including PDF and mass uncertainties) are considered to be fully correlated between the two energies [204].

The branching fraction of charm-hadron decays to electrons is taken as $(9.6 \pm 0.4)\%$ [50]. An additional uncertainty of $\pm 0.9\%$ is added in quadrature to account for differences in the Λ_c/D^0 ratio measured by ALICE in pp collisions at $\sqrt{s} = 7\ \mathrm{TeV}$, which is 0.543 ± 0.061 (stat.) ± 0.160 (syst) for $p_{\mathrm{T}} > 1\ \mathrm{GeV}/c$ [205], and the LEP average of 0.113 ± 0.013 ± 0.006 [206]. This translates into a 22% uncertainty at the pair level. The branching fraction of bottom hadrons decaying into electrons, including via intermedi-

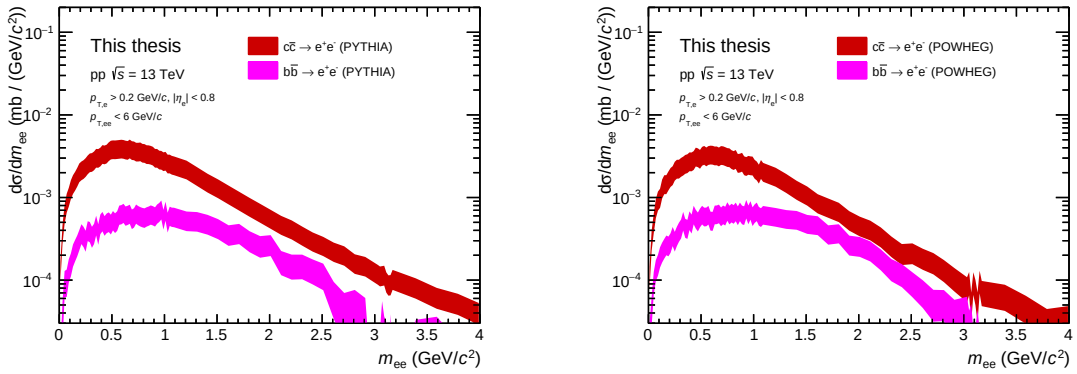

Figure 3.44: Dielectron mass spectra from correlated semi-leptonic decays of open charm and bottom hadrons using Pythia (left) and Powheg (right) simulations.

ate charm hadrons, is $(21.53 \pm 0.63)\%$ [50], which leads to a 6% uncertainty on the $\mathrm{b\bar{b}}$ contribution.

The resulting $\mathrm{e^+e^-}$ spectra from heavy-flavour correlated semi-leptonic decays are shown in Fig. 3.44 for both Pythia and Powheg simulations. The uncertainties on the spectra take into account the statistical uncertainty of the MC production added in quadrature to the uncertainty derived from the $\mathrm{c\bar{c}}$ and $\mathrm{b\bar{b}}$ cross sections at $\sqrt{s} = 13$ TeV, but do not include the uncertainty due to branching fraction to electrons (22% for charm and 6% for beauty decays).

The J/ψ contribution is simulated with Pythia 6.4 and normalised to the cross-section at $\sqrt{s} = 13$ TeV of $\frac{\mathrm{d}\sigma_{\mathrm{J}/\psi}}{\mathrm{d}y}|_{y=0} = 9.55^{+1.54}_{-1.57}$ µb. This cross-section is also obtained with FONLL [140] from the measurement at $\sqrt{s} = 7$ TeV by the ALICE Collaboration: $\frac{\mathrm{d}\sigma_{\mathrm{J}/\psi}}{\mathrm{d}y}|_{y=0} = 6.87^{+1.11}_{-1.13}$ µb [207]. The ψ(2S) contribution is normalised to J/ψ based on a cross section ratio of $\sigma(\psi(2S) \rightarrow \mathrm{e^+e^-})/\sigma(\mathrm{J}/\psi \rightarrow \mathrm{e^+e^-}) = 1.59 \pm 0.17\%$ [208]. Both contributions to the dielectron spectrum are shown in Fig. 3.45.

3.5.3 High-Multiplicity Light-Flavour Cocktail

A cocktail of hadronic dielectron sources is also used to estimate the expected dielectron mass spectrum in high-multiplicity events. For light-flavour hadrons the input hadron p_{T}-distributions are adjusted according to the measured modifications of the charged-hadron p_{T} spectra [42]. Figure 3.46 (left) shows the ratio of spectra measured in three intervals of raw (uncorrected) multiplicity $N_{\mathrm{ch}}^{\mathrm{acc}}$ ($1 \leq N_{\mathrm{ch}}^{\mathrm{acc}} < \langle N_{\mathrm{ch}}^{\mathrm{acc}} \rangle$, $\langle N_{\mathrm{ch}}^{\mathrm{acc}} \rangle \leq N_{\mathrm{ch}}^{\mathrm{acc}} < 2\langle N_{\mathrm{ch}}^{\mathrm{acc}} \rangle$ and $N_{\mathrm{ch}}^{\mathrm{acc}} > 2\langle N_{\mathrm{ch}}^{\mathrm{acc}} \rangle$) to the inclusive spectrum in INEL> 0 event class. For this ratio, the spectra are normalised by the integral prior to dividing. The data clearly show the correlation of the p_{T} spectrum with multiplicity for the whole p_{T} range. In particular, in events with $N_{\mathrm{ch}}^{\mathrm{acc}} > 2\langle N_{\mathrm{ch}}^{\mathrm{acc}} \rangle$ p_{T} spectrum becomes harder,

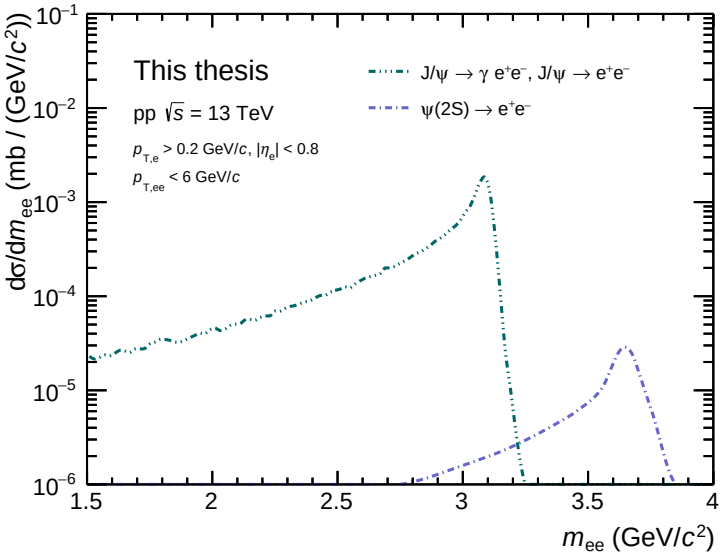

Figure 3.45: Dielectron mass spectra from J/ψ and ψ(2S) decays.

which in first order can be explained by large contribution from jets.

The modification of charged particle spectrum needs to be estimated for a multiplicity scaling factor obtained in this analysis. For raw (uncorrected) multiplicities in accepted high-multiplicity and minimum-bias events, this factor amounts to:

$$\mathrm{d}N_{\mathrm{ch}}^{\mathrm{acc}}/\mathrm{d}\eta(\mathrm{HM})/\langle \mathrm{d}N_{\mathrm{ch}}^{\mathrm{acc}}/\mathrm{d}\eta(\mathrm{MB})\rangle = 4.54$$

Two different weights have been used as lower and upper limit based on ratios of p_{T} distributions shown in Fig. 3.46 (left). The lower limit corresponds to the ratio of charged particle spectra in events with multiplicities $N_{\mathrm{ch}}^{\mathrm{acc}} \geq 2\langle N_{\mathrm{ch}}^{\mathrm{acc}}\rangle$, which is shown in red. In this multiplicity class, the corresponding multiplicity enhancement factor is $\approx$3. For the upper limit, the p_{T} spectrum in events with $N_{\mathrm{ch}}^{\mathrm{acc}} \geq 2\langle N_{\mathrm{ch}}^{\mathrm{acc}}\rangle$ is divided by the spectrum shown in blue in the same figure. The latter corresponds to the p_{T} spectrum of charged particles in events with multiplicities $1 \leq N_{\mathrm{ch}}^{\mathrm{acc}} < \langle N_{\mathrm{ch}}^{\mathrm{acc}}\rangle$, where the average multiplicity is reduced by a factor 2. In this way an upper limit corresponds roughly to an increase in the average multiplicity by a factor of $\approx$6.

To estimate individual hadron spectra, these p_{T} ratios are translated into an m_{T} dependence by using a mean hadron mass calculated for each p_{T} bin. This is done by using p_{T} spectra of pions, kaons and protons measured at midrapidity by ALICE at $\sqrt{s} = 7$ TeV [209] (Fig. 3.46 right) and by weighting their masses in each p_{T} bin according to the relative contributions. The resulting mean hadron mass is shown in Fig.3.47 (left), and the obtained m_{T}-dependent weights are shown in Fig.3.47 (right). The latter are applied to scale the production of all hadrons in the cocktail simulation.

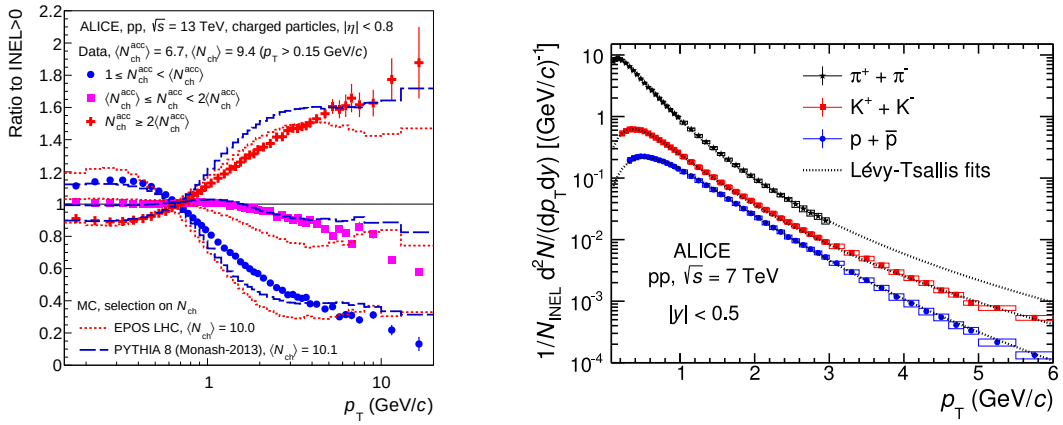

Figure 3.46: Left: the modification of charged-hadron p_{T} spectra in high-multiplicity pp collisions at $\sqrt{s} = 13$ TeV [42]. Right: p_{T} spectra of pions, kaons and protons in pp collisions at $\sqrt{s} = 7$ TeV [209].

The contributions from different hadrons are normalised in such a way that the relative contribution to the cocktail from each particle specie is kept the same between minimum-bias and high-multiplicity events. The uncertainties of high-multiplicity cocktail from light-hadron decays are about $\pm 15\%$, reaching up to $+50\%$ in the region dominated by the η meson due to uncertainties in the extrapolation to low p_{T}. The multiplicity dependence has an uncertainty that varies between about 12% at low p_{T} and 40% at high p_{T}.

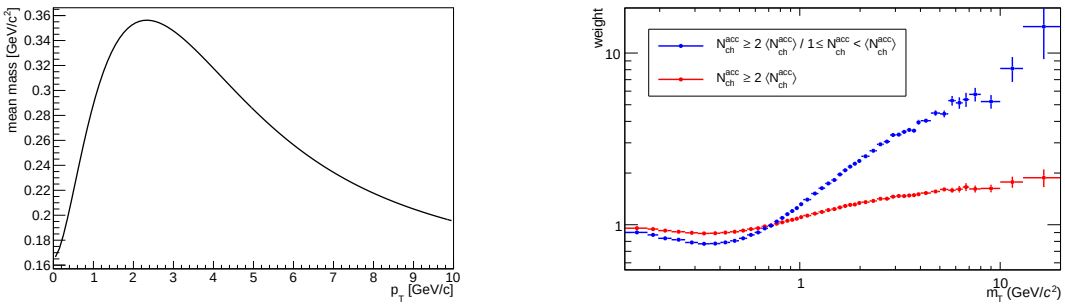

Figure 3.47: Mean hadron mass as a function of p_{T} (left) and the resulting m_{T} weights applied to the hadronic sources (right). Red and blue lines on the right panel correspond to lower and upper limits, see text for details.

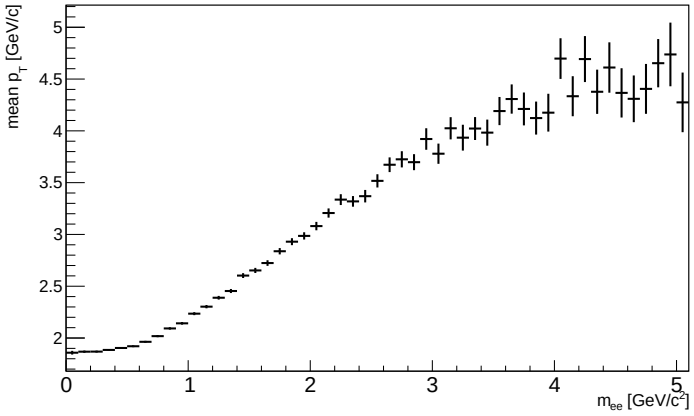

Figure 3.48: Average D meson p_{T} as a function of dielectron invariant mass in Pythia simulations.

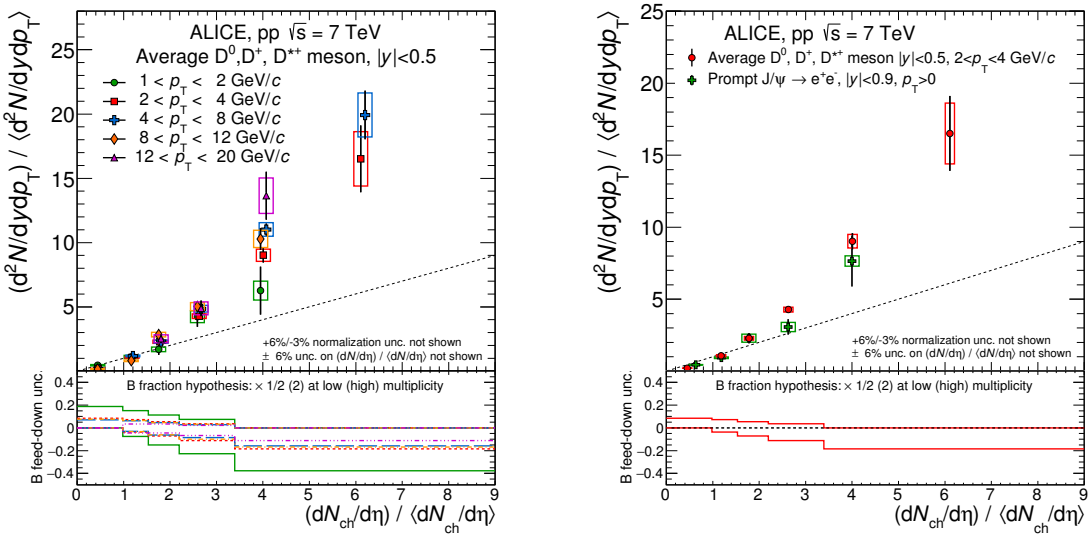

Figure 3.49: Left: average D meson relative yields as a function of the relative charged-particle multiplicity in different p_{T} intervals. Right: p_{T}-integrated relative yield of J/ψ as a function of the relative charged-particle multiplicity [43].

3.5.4 High-Multiplicity Heavy-Flavour Cocktail

For high-multiplicity heavy-flavour cocktail calculations, open charm contribution are simulated with Pythia and weighted as a function of p_{T} according to the measured enhancement of D mesons with $p_{\mathrm{T}} > 1$ GeV/c at $\sqrt{s} = 7$ TeV [43] (Fig. 3.49 left). The relative enhancement of D meson production is in fact shown here as a function

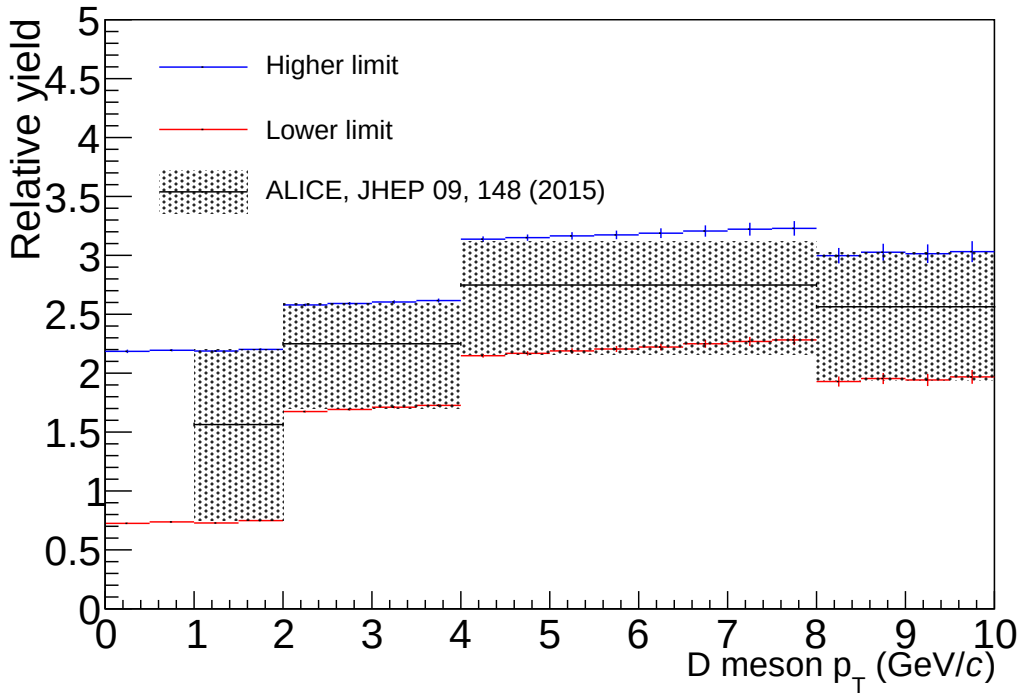

Figure 3.50: Enhancement factors applied to high-multiplicity heavy-flavour cocktail as a function of the D meson p_{T}. Blue and red lines represent upper and lower enhancements according to the measured values in [43] for a multiplicity increase of a factor 4, which are shown as grey shaded area. The same enhancement factors are also applied for open beauty mesons.

of $\mathrm{d}N_{\mathrm{ch}}^{\mathrm{acc}}/\mathrm{d}\eta(\mathrm{HM})/\langle \mathrm{d}N_{\mathrm{ch}}^{\mathrm{acc}}/\mathrm{d}\eta(\mathrm{INEL} > 0)$, so the results at relative charged-particle multiplicity of ≈ 4 are the ones closest to the multiplicity factor obtained in this analysis. These enhancement factors are applied as a function of D-meson p_{T} as shown in Fig. 3.50. Here, the blue and red lines represent the upper and lower enhancements simulated according to the measured values shown as grey shaded area. To bracket the expected enhancement, systematic and statistical errors of the measurement are added in quadrature. No measurement of the multiplicity dependence exists for D mesons with $p_{\mathrm{T}} < 1$ GeV/c. While they still can contribute to the dielectron spectrum, their contribution is expected to be relatively small: the average D meson p_{T} as a function of dielectron invariant mass has been evaluated using Pythia simulations, and the result is shown in Fig. 3.48. For the weighting of D mesons with $p_{\mathrm{T}} < 1$ GeV/c the measurement of D mesons with $1 < p_{\mathrm{T}} < 2$ GeV/c is assumed as a conservative estimate.

The same weights are also applied to the open beauty contribution as no significant difference between the production of D mesons and J/ψ from beauty-hadron decays

is observed [43]. For electrons originating from charm or beauty hadrons with $p_{\mathrm{T}} < 1$ GeV/c, the same weight as for $1 < p_{\mathrm{T}} < 2$ GeV/c is applied in the absence of a measurement. The same enhancement is also assumed for Λ_{c} baryon. The multiplicity dependence of heavy-flavour cocktail has an uncertainty that varies between about 40% at low p_{T} decreasing to 20% at high p_{T}.

Finally, the J/ψ contribution is scaled according to a dedicated, p_{T}-integrated measurement [43] at relative charged-particle multiplicity of ≈ 4, which is also shown in Fig. 3.49 (right).

With all ingredients taken into account, the expected ratio of dielectron spectra in high-multiplicity over minimum-bias events after acceptance cuts is shown in Fig. 3.51. The blue band on the upper panel represents the light-flavour uncertainty between the lower and upper multiplicities considered for the high-multiplicity cocktail, and magenta band corresponds to the heavy-flavour part of high-multiplicity cocktail. The light-flavour and heavy-flavour expectations are weighted according to their relative contributions, and the expectation for the dielectron spectra ratio from the combination of all sources can be seen in the lower panel.

3.6 Systematic Checks and Uncertainties

This Section describes analysis cross-checks and the evaluation of systematic uncertainties. Different aspects of the analysis are considered as sources for possible systematic biases: event, track and electron selection, hadron contamination, photon conversions, R-factor as well as integrated luminosity. Systematic uncertainties specific for the high-multiplicity data analysis are discussed separately in Section 3.6.9.

3.6.1 Event Selection

As described in Section 3.1, a physics selection with additional background rejection is applied to the experimental data. It was verified that this physics selection does not bias the selection of good physics events, and no additional correction or uncertainty is needed in the analysis [210]. On top of the physics selection, events are also rejected if a secondary (pile-up) interaction vertex is reconstructed with SPD tracklets. Another pile-up rejection tool is used as a cross-check. Instead of relying on the SPD information only, multiple vertices are reconstructed in the event with full ITS+TPC tracks (the so-called "multi-vertexer" algorithm); such algorithm has a wider time coverage than the SPD vertex finder and is therefore more sensitive to pile-up events from different bunch crossings. Depending on the data-taking period, the multi-vertexer leads to an additional rejection of $\lesssim 2\%$ of events compared to the SPD pile-up rejection, but with no significant effect on the dielectron spectrum (Fig. 3.52). Therefore no additional uncertainties due to pile-up rejection need to be assigned to the results.

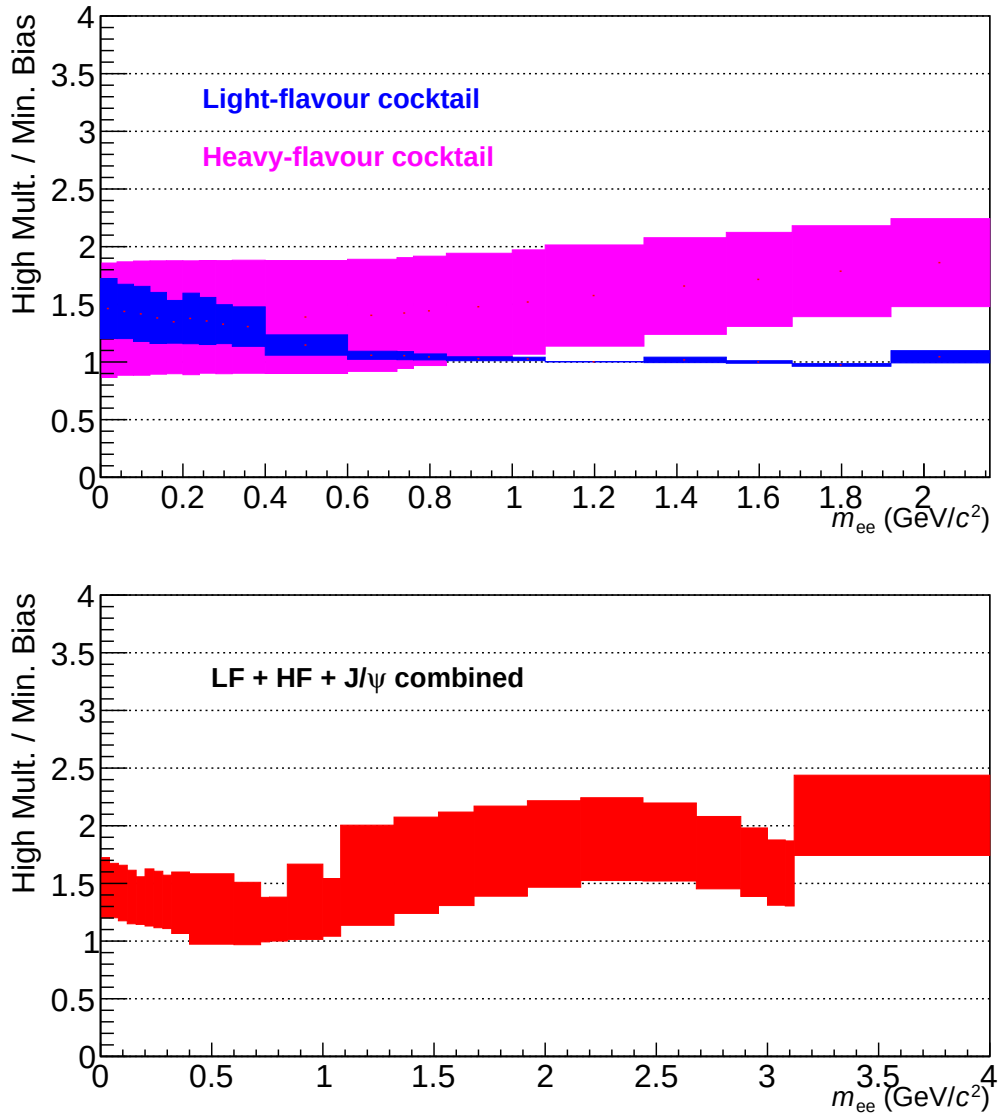

Figure 3.51: Upper panel: Ratio of the dielectron mass spectra for the light-flavour (blue) and heavy-flavour (magenta) hadronic sources. Lower panel: overall dielectron spectra ratio for all hadronic sources combined. Note the different x axis ranges.

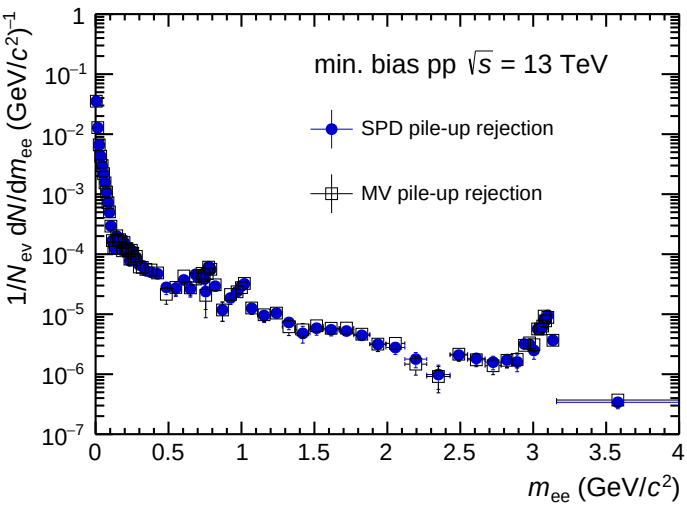

Figure 3.52: Dielectron spectra in minimum-bias events obtained with usage of different pile-up rejection tools.

3.6.2 Tracking

Several sources are considered for the systematic uncertainties due to the track selection. As a result of checks described below, residual disagreements between experimental data and Monte Carlo simulations add a 6.5% uncertainty on the single track level. Since such uncertainties are correlated for two electrons in a signal pair, this leads to a 13% uncertainty for pairs.

First, Monte Carlo simulations are checked to reproduce in detail the distributions of track variables used for track selection (Table 3.1). For this purpose, all such distributions are checked in different p_{T} ranges ($0.2 < p_{\mathrm{T}} < 0.4$ GeV/c, $0.4 < p_{\mathrm{T}} < 1.0$ GeV/c and $p_{\mathrm{T}} > 1.0$ GeV/c), and the number of tracks kept by each selection criteria (when other selection criteria are applied) is compared between Monte Carlo and experimental data. In all cases a very good agreement is found, and the relative differences for each cut variable are added quadratically, which results in only 1% of systematic uncertainty for single tracks with very small p_{T} dependence (2% for pairs). Fig. 3.53 shows an example of such comparison for the p_{T} interval $0.4 < p_{\mathrm{T}} < 1.0$ GeV/c for DCA- and ITS-related requirements.

Further systematic uncertainties due to track reconstruction are estimated by comparing the following efficiencies in MC simulations and in experimental data: a) ITS–TPC matching, b) requirement of a hit in the first SPD layer and c) requirement of zero ITS clusters shared with other tracks. The ITS–TPC matching efficiency is estimated as the ratio of the number of electron candidates with ITS+TPC tracking requirements over

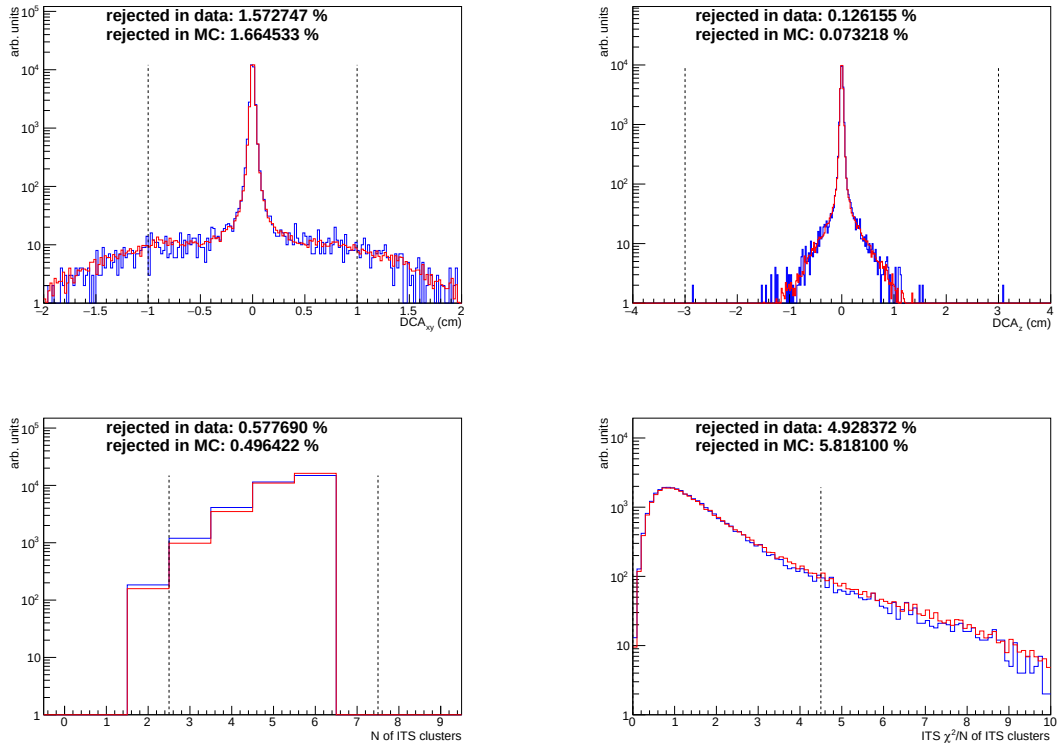

Figure 3.53: Distributions of DCA and ITS variables in data (blue) and in MC (red) for tracks with $0.4 < p_{\mathrm{T}} < 1.0\ \mathrm{GeV}/c$. All other track selection criteria are applied except the one shown on the plot as vertical dashed line. Relative number of tracks rejected by each selection is also listed.

the number of electron candidates with only TPC tracking requirements. Here the same TPC tracking requirements are used as in main analysis (Table 3.1), whereas for the ITS a hit in any SPD layer is required (the bias due to the requirement of a hit in the first SPD layer is estimated separately). In all cases very tight DCA requirements ($0.1\ \mathrm{cm}$) are applied in order to suppress the contribution from photon conversions, which may not be perfectly reproduced by Monte Carlo simulations. The results are shown in Fig. 3.54 (top left) as a function of single-track p_{T}. A good agreement between experimental data and Monte Carlo simulations is found in all cases. The overall difference of 1.5% (with negligible p_{T}-dependence) for single electrons leads to a 3% uncertainty for pairs.

The requirement of a hit in the first SPD layer is used in the analysis to suppress tracks originating from late photon conversions. The corresponding "SPD first" matching efficiency is estimated in a similar way as the number of electron candidates with a hit in the first SPD layer over the number of electron candidates with hit in any of the two

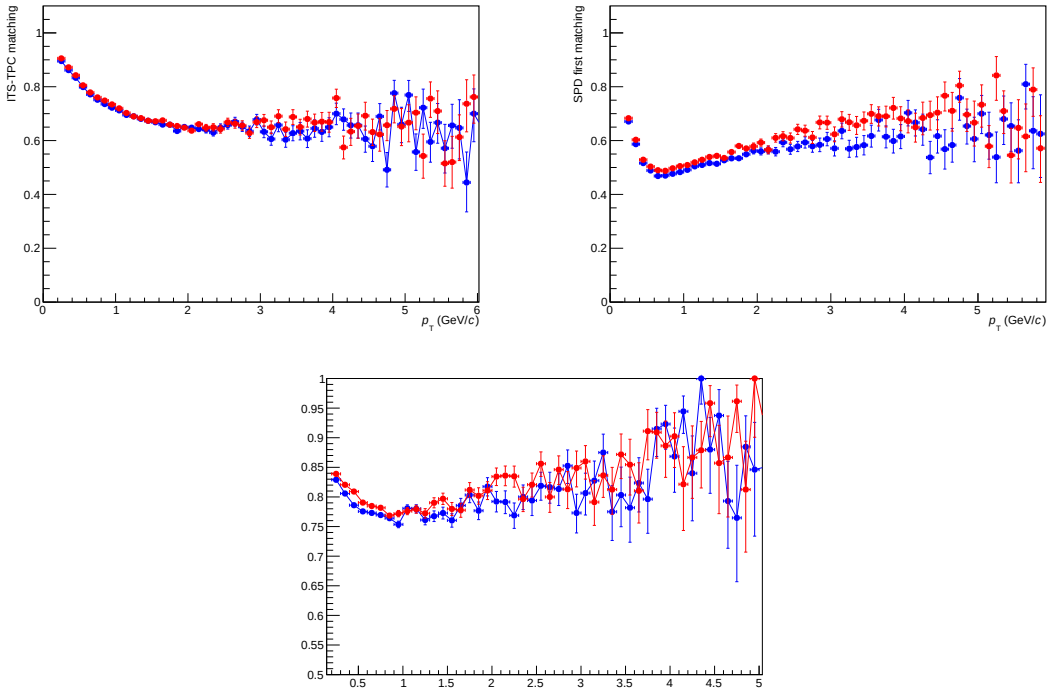

Figure 3.54: Fraction of electron candidates passing the requirement of ITS track cuts (top left panel), hit in first SPD layer (top right) and no shared ITS clusters (bottom) in experimental data (blue) and in Monte Carlo simulations (red) as a function of p_{T}, see text for details.

SPD layers. In both cases, tight DCA cuts are used again in order to suppress the contribution from real photon conversions. The relative difference between experimental data and Monte Carlo simulations of 3% (with a small p_{T}-dependence) for single electrons results in a 6% uncertainty for pairs (Fig. 3.54 top right).

The requirement of no ITS clusters shared with other tracks is also tested in a similar way in experimental data and in Monte Carlo simulations, and the corresponding fraction of electron candidates surviving this selection criterion is checked as a function of of p_{T} (Fig. 3.54 bottom panel). In all cases tight DCA cuts are used in order to suppress the contribution from real photon conversions. Again only small p_{T}-dependence is found in this case, and the relative difference between data and Monte Carlo simulations of $< 2\%$ for single electrons results in a 4% uncertainty for pairs.

All the uncertainties described above have been tested in hadronic cocktail simulations, which have shown that a small p_{T} dependence of tracking uncertainty results in a negligible dependence of the dielectron signal uncertainty on m_{ee} and $p_{\mathrm{T,\,ee}}$.

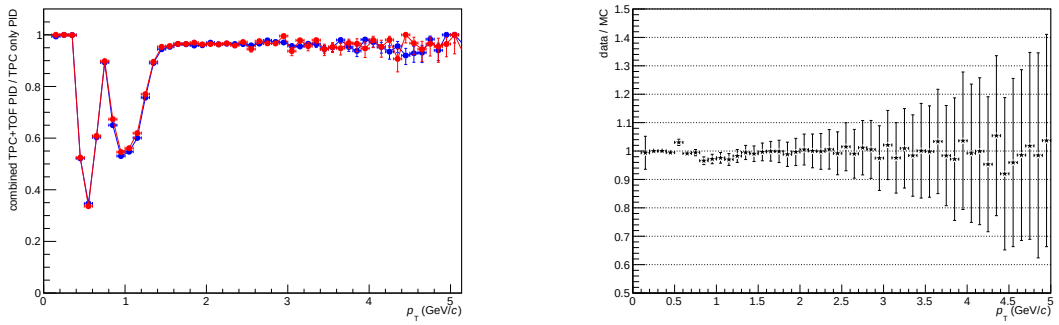

Figure 3.55: Fraction of electrons passing PID requirements in experimental data (blue) and in Monte Carlo simulations (red) as a function of p_{T}; see text for details. The ratio "data / MC" is shown on the right plot.

3.6.3 Electron Identification

The PID selection leads to a significant drop of the single electron efficiency at $p_{\mathrm{T}} \approx 0.5$ GeV/c and at $p_{\mathrm{T}} \approx 1.0$ GeV/c (Fig. 3.32) due to the rejection of hadrons in the TPC. To check that all the details of the PID selection are properly described by Monte Carlo simulations, the following test is performed in experimental and in Monte Carlo data.

For the studies of systematic uncertainties due to tracking described previously, one needs a sample of primary tracks originating from event vertex, so photon conversions are suppressed by tight DCA requirements. However, in order to test the PID response of the TPC and TOF detectors, one would need only a clean sample of electrons (to minimise hadron contamination and therefore any possible biases due to non-perfect particle abundances in Monte Carlo data) without tight requirements on their origin. Such a clean sample of electrons can be obtained in experimental data with electrons from photon conversions.

Late conversions in outer ITS layers or in detector material before the TPC are reconstructed with a special "V0 finder" algorithm, which in general searches for secondary vertices of neutral particle decays into two charged tracks. After that, a PID selection including only TPC requirements for electrons and pions (first two lines in Table 3.2, which are common for schemes "A" and "B") is already sufficient to obtain a very clean sample of electrons from conversions in experimental data, since neither kaons nor protons pass the "V0 finder" reconstruction requirements. Although in Monte Carlo one could select pure electrons directly by using MC information, for a proper comparison with the experimental data the same "V0 finder" algorithm is used in MC to select electrons from photon conversions. TPC PID response is checked to reproduce in detail all characteristics of such clean electrons as a function of their p_{T} and η, both in MC and in

experimental data. The ITS tracking requirements, which would reject a large fraction of such late conversions, are not applied to the tracks, whereas TPC track requirements are the same as in main analysis.

After that, all PID requirements used in the analysis are applied according to Table 3.2 to the sample of electrons described above, and the fraction of electrons survived PID requirements is checked in Monte Carlo and in experimental data (Fig. 3.55). Since all sources of possible biases are suppressed as described above, such a ratio directly represents the combined PID efficiency of the TPC and TOF detectors for electrons in experimental data and in MC simulations. Very good agreement is found over whole p_{T} range, with maximum difference of up to 3% in kaon ($p_{\mathrm{T}} \approx 0.5$ GeV/c) and proton ($p_{\mathrm{T}} \approx 1$ GeV/c) crossing regions. Simulations of this uncertainty with hadronic cocktail have shown that it leads to a $\lesssim 2\%$ difference in dielectron signal, which is taken as a conservative estimate for the corresponding systematic uncertainty in whole mass range.

It is worth to mention that such a good agreement, especially in the hadron rejection region, is also a result of the careful PID re-calibration of TPC and TOF detectors described in Apendix B. The uncertainty shown in Fig. 3.55 (right) also includes possible uncertainties introduced by the PID re-calibration procedure.

3.6.4 Hadron Contamination

This Section describes an approach to evaluate hadron contamination as a function of p, which is then converted to pair and signal purity. A high purity of electron sample reached both in minimum-bias and in high-multiplicity events minimises the effect of hadron contamination on the dielectron spectrum. Moreover, most of the contaminated pairs are subtracted from dielectron spectrum during the pair analysis, since as a rule they are of uncorrelated origin. Therefore, the main problem is correlated contamination, which arise from e. g. $\phi \to \mathrm{K}^{+}\mathrm{K}^{-}$ decays when both kaons are mis-identified as electrons.

For particle momenta below 400 MeV/c, where electron identification relies only on the TPC energy loss, the main contamination comes from pions passing the $n(\sigma_{\pi}^{\mathrm{TPC}})$ rejection. To evaluate this background, the $n(\sigma_{\mathrm{e}}^{\mathrm{TPC}})$ distribution from experimental data is fitted in momentum slices with a skew normal distribution defined as

$$f(x) = \frac{1}{\sqrt{2\pi\sigma^2}} \exp\left(-\frac{(x-\mu)^2}{2\sigma^2}\right) \left(1 + \mathrm{erf}\left(\frac{\alpha(x-\mu)}{\sqrt{2\sigma^2}}\right)\right) \tag{3.16}$$

both for the electron signal and the pion background with a total of 8 free parameters in the range $-4 < n(\sigma_{\mathrm{e}}^{\mathrm{TPC}}) < 4$. The result of the fit is then evaluated in the nominal $-3 < n(\sigma_{\mathrm{e}}^{\mathrm{TPC}}) < 3$ range used for the electron selection.

The hadron contamination for momenta above 400 MeV/c is dominated by kaons in the range 400–800 MeV/c, protons in 800–1200 MeV/c and pions above 1200 MeV/c.

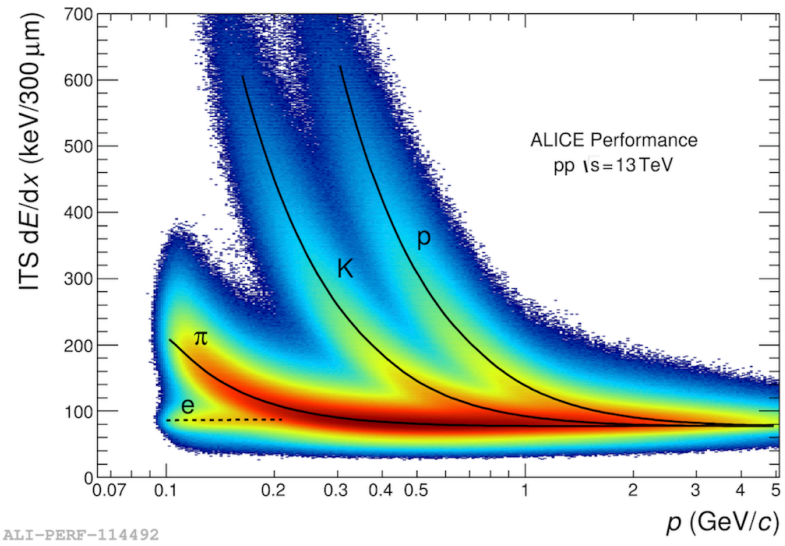

Figure 3.56: ITS $\mathrm{d}E/\mathrm{d}x$ in pp collisions at $\sqrt{s} = 13$ TeV [166].

Those hadrons can pass the selection criteria, if they originate from fake matches between ITS+TPC tracks and TOF hits. Even with a TOF PID requirement $|n(\sigma_{\mathrm{e}}^{\mathrm{TPC}})| < 3$ some true electrons identified by TOF could be matched to a hadron track reconstructed in ITS+TPC. The mismatch probability is expected to be slightly higher in high-multiplicity data sample. Since in the TPC kaons and protons completely overlap in the corresponding crossing regions, this contamination is evaluated by fitting $n(\sigma_{\mathrm{e}}^{\mathrm{ITS}})$ distributions from experimental data. Thanks to different specific energy loss in silicon ITS layers than in TPC gas, kaons and protons have different $\mathrm{d}E/\mathrm{d}x$ than electrons also in TPC crossing regions (Fig. 3.56). The $n(\sigma_{\mathrm{e}}^{\mathrm{ITS}})$ distribution is fitted in momentum slices with the following contributions:

- Monte Carlo templates of $n(\sigma_{\mathrm{e}}^{\mathrm{ITS}})$ for kaons and protons; the kaon template is included in fits below 800 MeV/c and the proton template above
- A skew normal distribution for the electron signal from Eq. 3.16
- A total of 5 parameters for each fit, 4 from the signal distribution and one additional for the background normalisation
- Additional constrains in momentum bins with large overlap of signal and hadrons, which rely on the shape of momentum spectra for kaons and protons passing the electron selection criteria in Monte Carlo simulations

Finally, the pion contamination in the momentum range above 400 MeV/c is evaluated by fitting the $n(\sigma_{\pi}^{\mathrm{TPC}})$ distribution from experimental data in momentum slices, with both the signal (that in this case is the true electron signal plus the kaon/proton contamination to avoid its double counting) and the pion background fitted by skew normal distributions. The fit contains therefore in total 8 free parameters and is performed in the range $-3 < n(\sigma_{\pi}^{\mathrm{TPC}}) < 20$. The results of the fit is then evaluated in the nominal

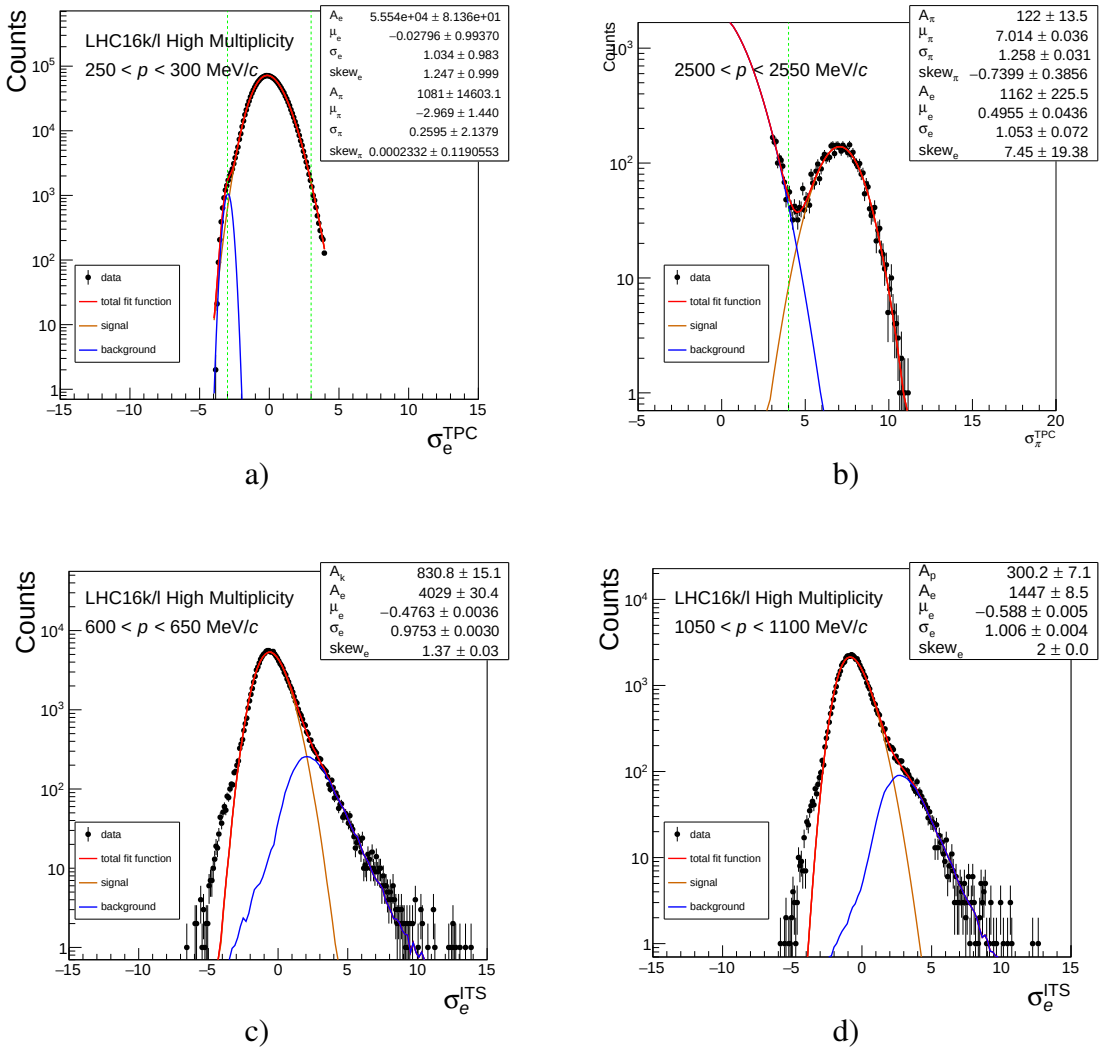

Figure 3.57: Example of the fits of $n(\sigma_{\mathrm{e}}^{\mathrm{TPC}})$ (a) and $n(\sigma_{\pi}^{\mathrm{TPC}})$ (b) used to evaluate pion background below and above 400 MeV/c, respectively. $n(\sigma_{\mathrm{e}}^{\mathrm{ITS}})$ distribution is used for the evaluation of kaon/proton contamination ((c) and (d)).

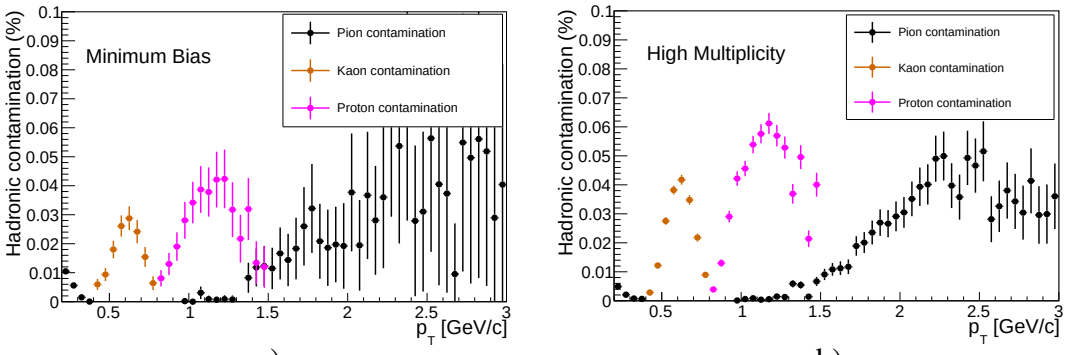

a) b)

Figure 3.58: Pion, kaon and proton contamination in minimum-bias (a) and high-multiplicity (b) events.

$n(\sigma_{\pi}^{\mathrm{TPC}}) > 4$ range used for electron selection.

Examples of the fits can be seen in Fig. 3.57 showing the pion shape in $n(\sigma_{\mathrm{e}}^{\mathrm{TPC}})$ and kaon/proton shapes in $n(\sigma_{\mathrm{e}}^{\mathrm{ITS}})$. The obtained hadron contamination in minimum-bias and high-multiplicity events is summarised in Fig. 3.58 for all fitted momentum bins. The purity of the electron sample is $>93\%$ in all p_{T} bins, with a p_{T}-integrated hadron contamination of about 4% for both event classes. The obtained single-electron purity is used afterwards in Monte Carlo simulations to estimate the contamination of final dielectron signal.

Due to the non-perfect simulation of particle abundances, single electron purity was found in Monte Carlo data to be higher than the one obtained from the data-driven approach described above (Fig. 3.59). Therefore, in order to reproduce the purity seen in experimental data, each hadron contaminating electron sample is re-weighted in MC (Fig. 3.59) to obtain the pair purity using true MC information about the origin of each particle. The pair contamination is estimated separately for pairs originating from light-flavour hadron decays and for pairs from semi-leptonic heavy-flavour decays.

For light-flavour decays, the dielectron signal is defined as a true electron and positron pair originating from the same-mother decay, and hadron contamination as a pair of particles from same-mother decay where at least one leg is a mis-identified hadron. No such contaminated pairs have been found in a sample of more than 350×10^3 pairs using Monte Carlo simulations of inelastic pp events. The pair contamination becomes significant when one uses relaxed PID selection, e. g. the exclusion of kaons and protons in the TPC with $|n(\sigma_{\mathrm{K,p}}^{\mathrm{TPC}})| > 2$ requirement (instead of default 4). Figure 3.60 shows the true dielectron signal and all unlike-sign pairs originating from light-flavour same-mother decays in case of such relaxed PID selection. One can see that significant hadron contamination leads in this case to a peak at $\sim$250 MeV/c^2 originating from $\phi \rightarrow \mathrm{K}^{+}\mathrm{K}^{-}$

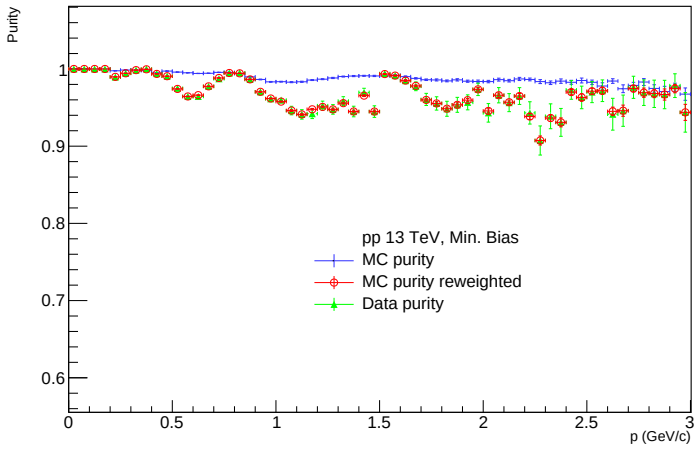

Figure 3.59: Electron purity in experimental data and in Monte Carlo simulations (unweighted and re-weighted).

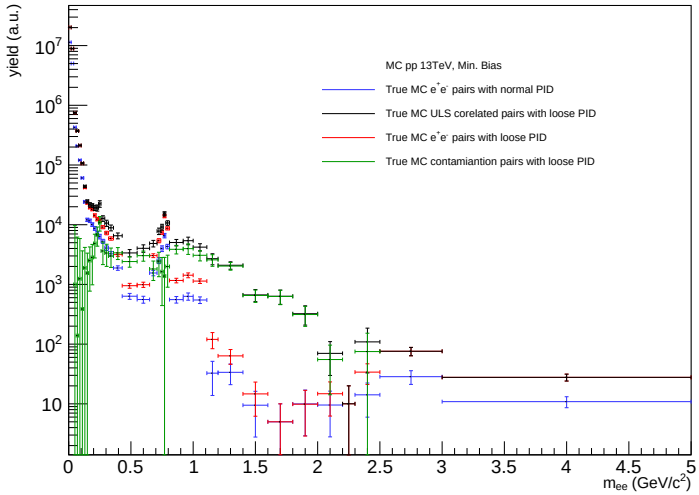

Figure 3.60: True dielectron signal (red) and all unlike-sign correlated pairs (black) originating from same decay of light-flavour hadrons in case of relaxed PID selection, see text for details. The resulting pair contamination is shown in green. True dielectron signal with standard PID selection is shown in blue (with zero contaminated pairs).

decay, where both kaons are misidentified as electrons with the wrong mass assigned to each leg. Other electron-hadron and hadron-hadron pairs create a continuum over a wide mass range.

Table 3.4: Summary of hadron contamination for heavy-flavour decays

PID scheme	Event Type	ULS pairs (contamination)	LS pairs (contamination)
A	$c\bar{c}$	14314 (1)	0 (0)
	$b\bar{b}$ no osc.	19124 (9)	7925 (1)
	$b\bar{b}$ with osc.	9546 (4)	5778 (3)
B	$c\bar{c}$	3958 (1)	0 (0)
	$b\bar{b}$ no osc.	6380 (3)	2310 (1)
	$b\bar{b}$ with osc.	2826 (2)	1831 (1)

For heavy-flavour decays, the contamination has been investigated for 3 different cases: $c\bar{c}$, $b\bar{b}$ with no oscillation and $b\bar{b}$ with at least one oscillation. To select only correlated pairs, in all cases events are filtered to ensure that one and only one type of heavy-flavour pair has been created during the generation. The pair contamination is found to be negligible for both $c\bar{c}$ and $b\bar{b}$ events (Table 3.4). For $b\bar{b}$ events also like-sign pairs are checked to have negligible hadron contamination.

As a result, hadron contamination on dielectron signal is found to be negligible and no systematic uncertainty or correction is applied to the final dielectron spectrum.

3.6.5 Photon Conversion Rejection

In order to ensure that conversion pairs are rejected in experimental data, a $\varphi_V < 2$ requirement is applied for all pairs in the mass region below 140 MeV/c^2. As a cross-check, a tighter selection of $\varphi_V < \pi/2$ is used for pure signal pairs in Monte Carlo data and for unlike-sign pairs in experimental data (Fig. 3.61). The fraction of pairs kept by $\varphi_V < \pi/2$ requirement relative to the default requirement is found to be in good agreement between data and Monte Carlo simulations, which implies only a small residual fraction of photon conversions that survive the default requirement. The relative difference of less than 2% is taken as an uncertainty (below 140 MeV/c^2) for the final results.

3.6.6 R-Factor Calculation

Since the R-factor enters directly in the signal calculation (Eq. 3.5), a possible bias in its estimation leads to a systematic uncertainty in final dielectron signal, which depends inversely on the signal-to-background ratio:

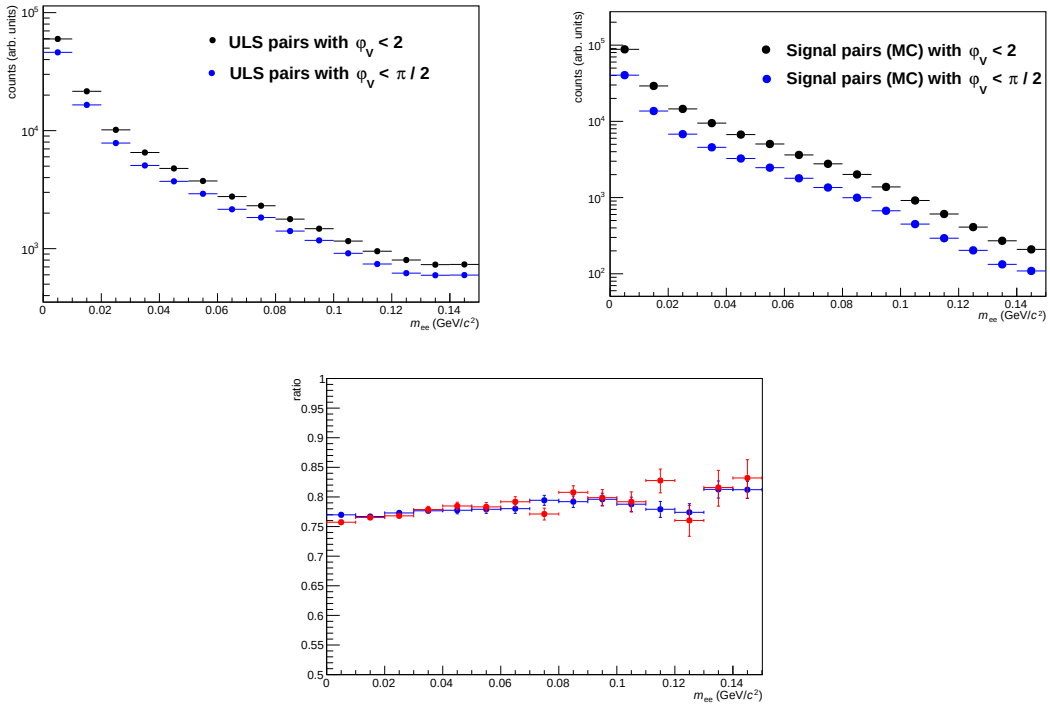

Figure 3.61: Unlike-sign pairs in experimental data (top left) and signal pairs in Monte Carlo simulations (top right) for two different φ_V requirements. The relative fraction of pairs with $\varphi_V < \pi/2$ is shown on the bottom panel in experimental data (blue) and in MC (red).

$$\Delta S = \Delta R \cdot B/S. \tag{3.17}$$

Therefore, several checks have been done in order to evaluate any possible uncertainty in the R-factor calculation. As a result, an uncertainty of 2% on the dielectron signal is used as an estimate of total systematic uncertainty due to R-factor calculation.

To check the dependence of the R-factor on $p_{\mathrm{T,\,ee}}$ and its effect on the raw dielectron spectrum, the signal extraction procedure is done in each $p_{\mathrm{T,\,ee}}$ bin ($0-1$, $1-2$, $2-3$ and $3-6$ GeV$/c$) using the corresponding R-factors extracted from data. The sum of raw signals in $p_{\mathrm{T,\,ee}}$ bins is compared then to the dielectron spectrum obtained in $p_{\mathrm{T,\,ee}} < 6$ GeV$/c$ bin using the $p_{\mathrm{T,\,ee}}$-independent R-factor. The results are shown in Fig. 3.62, where no significant difference is seen between two approaches. Therefore, no uncertainty is assigned to the final data points, and for the final results for $p_{\mathrm{T,\,ee}} < 6$ GeV$/c$ case are calculated as the sum of dielectron spectra in different $p_{\mathrm{T,\,ee}}$ bins.

In order to minimise the effect of statistical fluctuations, the R-factor is set to unity

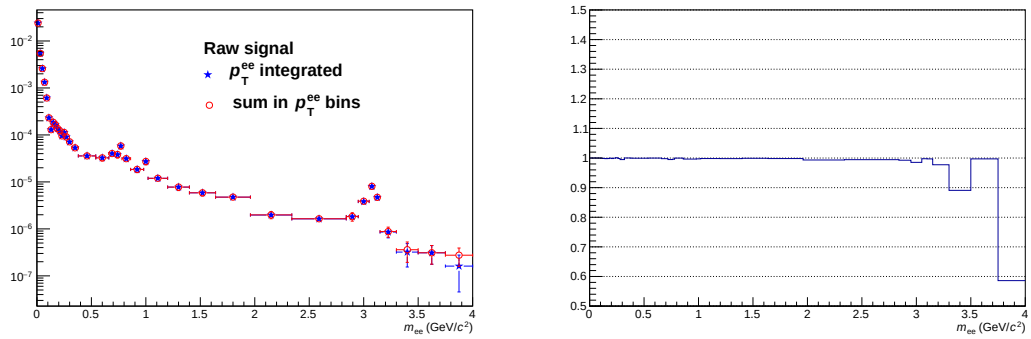

Figure 3.62: Left: raw dielectron spectra calculated as the sum in different $p_{\mathrm{T,\,ee}}$ bins with corresponding R-factors or in $p_{\mathrm{T,\,ee}} < 6$ GeV/c. The ratio between two approaches is shown on the right.

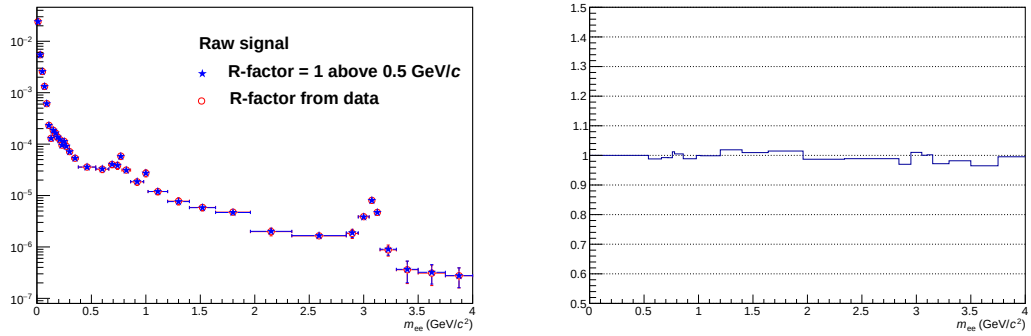

Figure 3.63: Left: raw dielectron spectra calculated with different R-factors: from data itself or set to unity in $m_{\mathrm{ee}} > 0.5$ GeV/c^2. The ratio between two methods is shown on the right. Below $m_{\mathrm{ee}} = 0.5$ GeV/c^2 two methods give the same results by construction.

for $m_{\mathrm{ee}} > 0.5$ GeV/c^2 where no statistically significant deviations from 1 are observed (Fig. 3.12 right). As a cross-check, the signal extraction procedure is repeated without assumption $R = 1$, and the resulting effect on the dielectron mass spectrum as a function of the invariant mass is shown in Fig. 3.63. No significant difference is found between two approaches as expected.

Assuming that R-factor represents only detector acceptance effects and does not depend on multiplicity, a small difference observed between R-factors from high-multiplicity and minimum-bias data samples (Fig. 3.64) results in systematic uncertainty of 2%.

To test the R-factor dependence on the number of event mixing bins and the vertex position, the event mixing is done in 20 vertex z position bins each 1.0 cm wide (from -10 cm to 10 cm). The results are compared to the default approach using 8 bins each 2.5 cm wide. No significant difference can be seen between two approaches (Fig. 3.65),

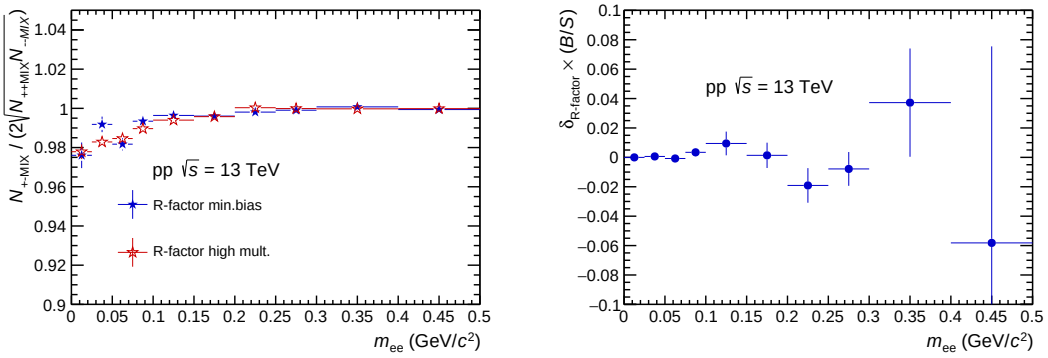

Figure 3.64: R-factor in high-multiplicity and minimum-bias events (left) and the corresponding difference scaled by B/S (right).

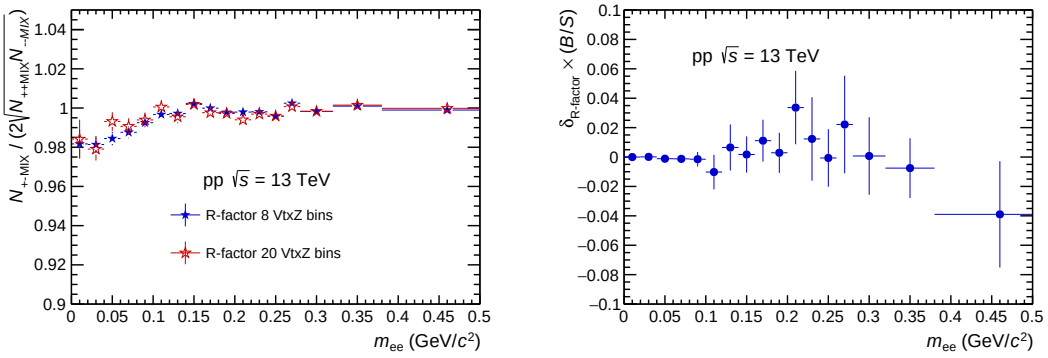

Figure 3.65: R-factor calculated with different number of vertex z position bins (left) and the corresponding difference scaled by B/S (right).

so no further systematic uncertainty is assigned.

3.6.7 Integrated Luminosity

The minimum-bias trigger described in Section 3.1 requires simultaneous signal in both V0 detectors. Let us denote such event class as "V0AND" (i. e. events which fulfil V0A *and* V0C trigger requirement), then the integrated luminosity of analysed minimum-bias data sample is calculated as:

$$\mathcal{L}_{\mathrm{int}}^{\mathrm{MB}} = N_{\mathrm{V0AND}} / \sigma_{\mathrm{pp}}^{\mathrm{V0AND}}, \tag{3.18}$$

i. e. the ratio of the measured V0AND cross section ($\sigma_{\mathrm{pp}}^{\mathrm{V0AND}} = 57.8 \pm 2.9\,\mathrm{mb}$), obtained from a van-der-Meer scan [211], and the number of V0AND (i. e. minimum-bias)

Table 3.5: Uncertainties assigned to dielectron spectrum in inelastic pp collisions.

Source	Uncertainty
Tracking	13%
PID selection	2%
Conversion rejection ($m_{\mathrm{ee}} < 0.14\ \mathrm{GeV}/c^2$)	2%
R-factor	2%
Total	13.5%

triggered events (N_{V0AND}). The latter is calculated as the number of minimum-bias events considered for the analysis ($N_{\mathrm{evt}} = 441.26 \times 10^6$), i. e. triggered events with a reconstructed interaction vertex and passing the physics event selection, corrected for the vertex reconstruction efficiency ($\varepsilon_{\mathrm{evt}}^{\mathrm{vtx}}$):

$$N_{\mathrm{V0AND}} = N_{\mathrm{evt}}/\varepsilon_{\mathrm{evt}}^{\mathrm{vtx}}. \tag{3.19}$$

While the efficiency to reconstruct the collision vertex is basically 100% when two electrons are present in the event, this is not generally true for V0AND triggered events. The latter efficiency is found to be $\varepsilon_{\mathrm{evt}}^{\mathrm{vtx}} = 97.0 \pm 0.5\%$, the difference observed between various methods (based either on Pythia MC simulations or on data-driven approaches) has been used as systematic uncertainty. This leads to an integrated luminosity of $\mathcal{L}_{\mathrm{int}}^{\mathrm{MB}} = 7.87 \pm 0.40\ \mathrm{nb}^{-1}$ for the minimum-bias pp data sample. The luminosity uncertainty is a global uncertainty and is therefore omitted from the point-to-point uncertainties; instead, it is explicitly mentioned in the figures.

3.6.8 Total Systematic Uncertainty

As a result of the checks described above, no significant variation of systematic uncertainties on m_{ee} or $p_{\mathrm{T,\,ee}}$ is observed in the analysis, and the same total uncertainty of 13.5% is assigned as point-to-point correlated uncertainties on the differential dielectron cross section in inelastic pp collisions. All sources of uncertainties are summarised in Table 3.5.

3.6.9 High-Multiplicity Analysis

The analysis of the high-multiplicity data sample carries additional systematic uncertainties which are discussed below. As a result, the total systematic uncertainty adds up to 15% for the corrected high-multiplicity dielectron spectra.

A shift in the vertex z position of about $\sim$0.3 cm towards higher positive values is found in high-multiplicity events compared to the minimum-bias data (Fig. 3.6). It can

be explained by the non-symmetric geometry of the V0 scintillators (Fig. 2.10): the V0A detector is located $340\,\mathrm{cm}$ from the vertex on the negative z side whereas V0C is fixed to the front face of the hadron absorber of muon arm, $90\,\mathrm{cm}$ from the vertex on the positive z side. Despite the smaller active area of V0C detector ($0.315\,\mathrm{m}^2$ compared to $0.548\,\mathrm{m}^2$ for V0A), its solid angle visible from the nominal interaction point at $z = 0\,\mathrm{cm}$ is much larger: 0.39 for V0C compared to 0.047 for V0A. The online V0 multiplicity is calculated as the sum of two signals from V0A and V0C, and the constant threshold value for this sum is used to trigger events with high multiplicities. This fact gives events closer to V0C (i. e. with higher positive vertex z values) a higher chance to produce a multiplicity above threshold, which leads to the observed bias in the vertex z position.

For the estimation of this effect, the mean reference multiplicity is calculated for events in $\pm 4.1\,\mathrm{cm}$ around the mean vertex z position, which corresponds to the RMS of the vertex z distribution shown in Fig. 3.6. This range is shifted afterwards by $1\,\mathrm{cm}$ (3 times more than the observed shift between minimum-bias and high-multiplicity events) towards larger and smaller vertex Z values. In both minimum-bias and high-multiplicity events this leads to a change of less than 0.5% for the reference multiplicity measured in $|\eta| < 0.5$ (top row of Fig. 3.66). However, the total number of electron and positron candidates measured in $|\eta| < 0.8$ and additionally affected by the PID efficiency of TPC and TOF detectors changes by 3% in each event class (bottom row of Fig. 3.66). Since no dedicated MC simulation was performed for the analysis of high-multiplicity pp collisions to take into account this effect, the final result includes uncertainty of 6%.

The requirement of no ITS clusters shared with other tracks leads to further rejection of good signal pairs in high-multiplicity data sample due to higher average multiplicity in the event. The ratio of the raw dielectron spectrum with such a cut over the dielectron spectrum without cut is checked in minimum-bias and in high-multiplicity events (Fig. 3.67). The difference of $\sim 2\%$ observed between the results is assigned as a systematic uncertainty to the corrected spectrum.

For the corrected high-multiplicity dielectron spectra, the same systematic uncertainties as listed in Table 3.5 are assigned to the data points. In addition, 6% uncertainty is used because of the shift of the vertex z position, 6% due to the multiplicity dependence of the single track reconstruction efficiency and electron identification [212] and 2% due to multiplicity dependence of the no shared ITS clusters requirement. Added in quadrature, this amounts to a total uncertainty of 15%. However, since the multiplicity-independent uncertainties cancel in the ratio (Eq. 4.2), the systematic uncertainty on the dielectron spectra ratio is reduced to $\sim 9\%$. It is dominated by the shift of the vertex z position and the multiplicity dependence of tracking and PID selection.

For high-multiplicity triggered events (with a total number of events 79.2×10^6), the vertex reconstruction efficiency is 100% with negligible uncertainties. Offline information from the V0 detector is used to select 0.05% of $\sigma_{\mathrm{pp}}^{\mathrm{V0AND}}$ cross-section, which results in an integrated luminosity of $\mathcal{L}_{\mathrm{int}}^{\mathrm{HM}} = 2.79 \pm 0.15\ \mathrm{pb}^{-1}$ for high-multiplicity data sam-

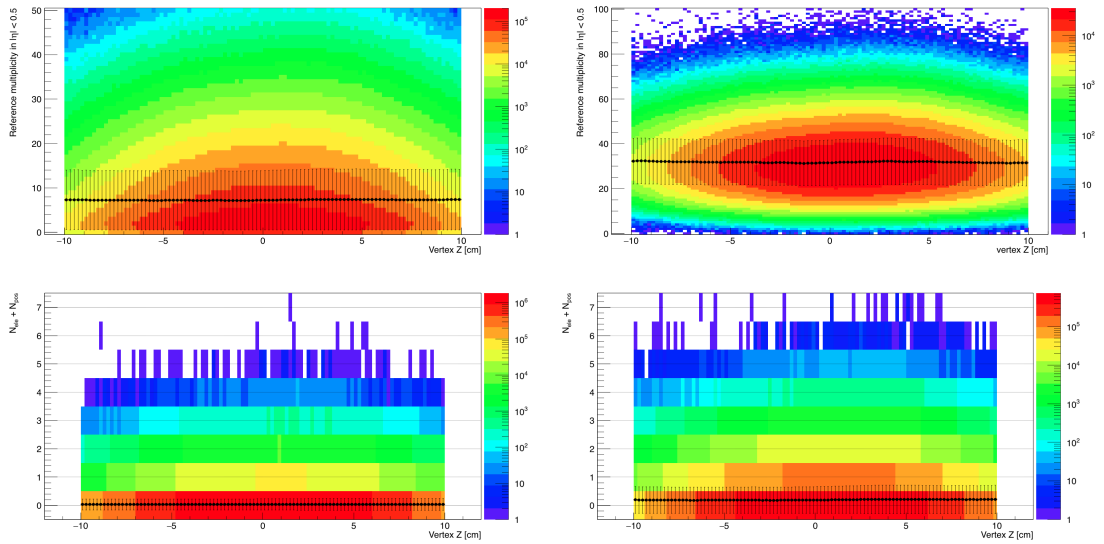

Figure 3.66: Top row: correlation between the reference multiplicity in $|\eta| < 0.5$ and the vertex z position. Bottom row: correlation between the number of electrons and the vertex z position. Results in minimum-bias events are shown on the left, right panels correspond to high-multiplicity pp collisions. Black points show the mean values of reference multiplicity or number of electrons for each vertex z position, and the error bars correspond to RMS of distribution. Note the different y axis scale for two plots on the top row.

ple collected in 2016. However, for the analysis of high-multiplicity pp collisions also raw uncorrected dielectron spectra can be used in Eq. 4.2, which allows to consider also 2017 data without corresponding Monte Carlo simulations. This results in a total of 715×10^6 minimum-bias pp events and 153.8×10^6 high-multiplicity pp events which are used for high-multiplicity studies only. These values correspond to integrated luminosities of $\mathcal{L}^{\mathrm{MB}}_{\mathrm{int,2016+2017}} = 12.37 \pm 0.63\ \mathrm{nb}^{-1}$ and $\mathcal{L}^{\mathrm{HM}}_{\mathrm{int,2016+2017}} = 5.42 \pm 0.29\ \mathrm{pb}^{-1}$.

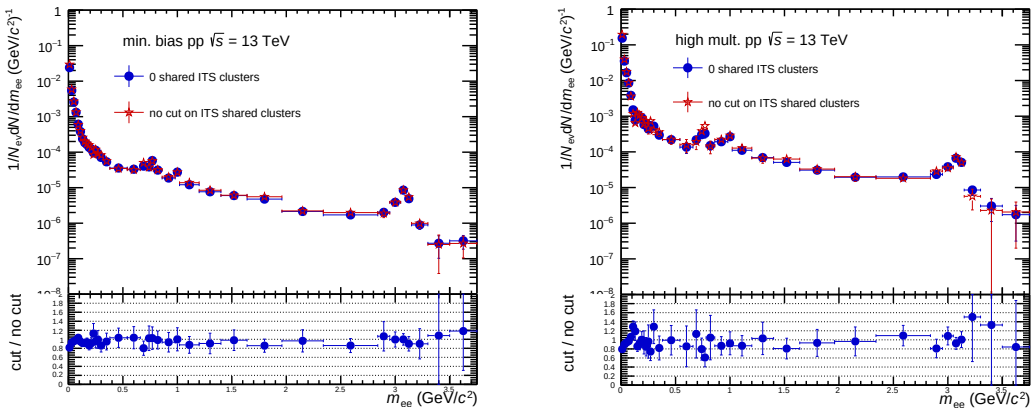

Figure 3.67: The effect of no shared ITS clusters requirement on raw dielectron spectrum in minimum-bias (left) and high-multiplicity (right) events. The difference between ratios of $\sim 2\%$ is taken as systematic uncertainty for high-multiplicity data analysis.

Table 3.6: Uncertainties assigned to dielectron spectrum in high-multiplicity pp collisions.

Source	Uncertainty
Min. bias analysis	13.5%
Vertex Z shift	6%
Multiplicity dependence of eff. and PID	6%
ITS shared cluster	2%
Total	15%

4 Results

This Chapter presents the results of the analyses of inelastic and high-multiplicity pp collisions. The dielectron mass, m_{ee}, and transverse momentum, $p_{\mathrm{T,\,ee}}$, spectra in inelastic collisions are shown in Section 4.1, followed by the discussion of the dielectron spectrum modification in high-multiplicity collisions in Section 4.2. The extraction of charm and beauty production cross sections in both event classes is presented in Section 4.3. Finally, the fraction of direct photons in the inclusive photon spectrum is discussed in Section 4.4.

4.1 Dielectron Cross Sections in Inelastic Events

The differential dielectron cross section is reported in the form of:

$$\frac{\mathrm{d}^2\sigma_{\mathrm{ee}}}{\mathrm{d}m_{\mathrm{ee}}\mathrm{d}p_{\mathrm{T,\,ee}}} = \frac{1}{\mathcal{L}_{\mathrm{int}}} \frac{S(m_{\mathrm{ee}}, p_{\mathrm{T,\,ee}})}{\Delta m_{\mathrm{ee}} \varepsilon_{\mathrm{ee}}^{\mathrm{trig}} \varepsilon_{\mathrm{ee}}^{\mathrm{vtx}} \varepsilon_{\mathrm{ee}}^{\mathrm{rec}}(m_{\mathrm{ee}}, p_{\mathrm{T,\,ee}})}, \tag{4.1}$$

where:

- $S(m_{\mathrm{ee}}, p_{\mathrm{T,\,ee}})$ is the measured dielectron signal yield defined in (3.5);
- $\mathcal{L}_{\mathrm{int}} = 7.87 \pm 0.40\ \mathrm{nb}^{-1}$ is the integrated luminosity of the pp data set as discussed in Section 3.6.7;
- Δm_{ee} and $\Delta p_{\mathrm{T,\,ee}}$ is the bin width in GeV;
- $\varepsilon_{\mathrm{ee}}^{\mathrm{trig}} = 0.99 \pm 0.01$ is the V0AND efficiency to trigger on a pp collisions containing an $\mathrm{e}^+\mathrm{e}^-$ pair in the acceptance (Section 3.4.4);

- $\varepsilon_{\rm ee}^{\rm vtx} = 1$ is the vertex reconstruction efficiency in events that contain an $\rm e^+e^-$ pair in the acceptance and that fired the V0AND trigger (Section 3.4.4);
- $\varepsilon_{\rm ee}^{\rm rec}(m_{\rm ee}, p_{\rm T,\,ee})$ is the reconstruction efficiency defined in (3.14), i. e. the mass- and $p_{\rm T,\,ee}$-dependent efficiency to reconstruct an $\rm e^+e^-$ pair in events with a reconstructed vertex that fired the V0AND trigger and that had an $\rm e^+e^-$ pair in the acceptance.

The results are shown either as $\rm d\sigma/d\it m_{\rm ee}$ (integrated over $p_{\rm T,\,ee} < 6$ GeV/c or over some limited $p_{\rm T,\,ee}$ range) or as $\rm d\sigma/d\it p_{\rm T,\,ee}$ (integrated over some mass bin). The dielectron cross sections are presented within the ALICE central barrel acceptance $|\eta_{\rm e}| < 0.8$ and $p_{\rm T,\,e} > 0.2$ GeV/c, i. e. without correction to full phase space which largely depends on the models used to extrapolate the results.

In each $p_{\rm T,\,ee}$ bin, the mass binning of the dielectron spectra presented below is defined by the requirement for *expected* statistical significance to be above a certain threshold. To calculate the expected value for statistical significance $S/\sqrt{S+2B}$, the raw signal S is estimated as a signal from cocktail calculations multiplied by dielectron reconstruction efficiency $\varepsilon_{\rm ee}^{\rm rec}(m_{\rm ee}, p_{\rm T,\,ee})$, and the combinatorial background B is taken from data. The resulting significance is then investigated in narrow $m_{\rm ee}$ bins of $\Delta m_{\rm ee} = 10$ MeV/c^2 width to see how wide each final $m_{\rm ee}$ bin has to be in order to reach the expected significance $\geq 5\sigma$. It this way one obtains an unbiased estimation of dielectron mass spectrum binning. Of course, the actual statistical significance of dielectron signal can be below 5σ as it is shown in Fig. 3.19. Similar studies are done for the high-multiplicity data analysis as well.

The dielectron spectrum, integrated over $p_{\rm T,\,ee} < 6$ GeV/c, is shown as a function of $m_{\rm ee}$ in Fig. 4.1. The experimental data are compared to the expectation from the hadronic decay cocktail discussed in Section 3.5 using Pythia simulations for the heavy-flavour decays. The global scale uncertainty on the pp luminosity (5%) is not shown. The data are in agreement within uncertainties with the expectation from the hadron decay cocktail over the whole mass range. Good agreement between data and cocktail calculations is also found as a function of $p_{\rm T,\,ee}$, which can be seen for $p_{\rm T,\,ee}$-spectra in different $m_{\rm ee}$ intervals in Fig. 4.2 and for mass spectra in different $p_{\rm T,\,ee}$-bins in Fig. 4.3. This confirms that the measured dielectron distributions can be described with the hadronic decays. Similar good agreement with cocktail expectations is also found for the Powheg-based simulations of open heavy-flavour contribution (Figs. 4.4 and 4.5).

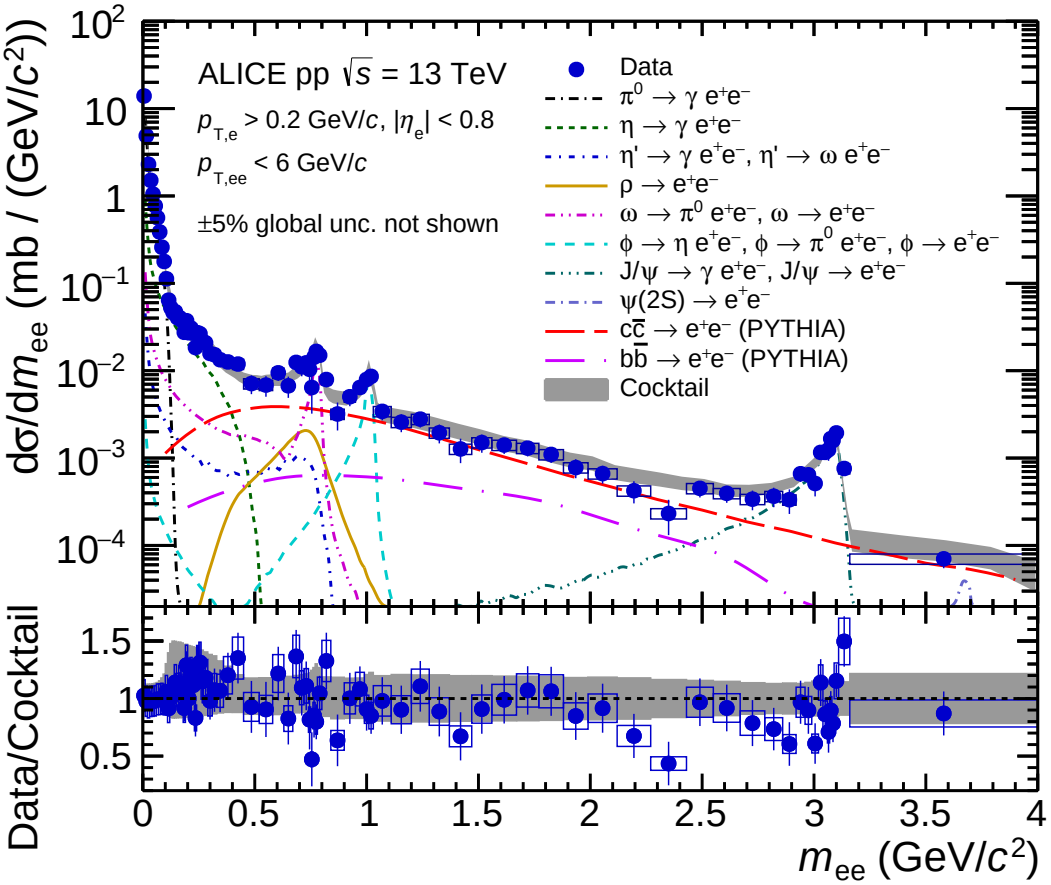

Figure 4.1: The dielectron cross section in inelastic pp collisions at $\sqrt{s} = 13$ TeV as a function of invariant mass m_{ee} using Pythia simulations to estimate open heavy-flavour decays. The global scale uncertainty on the pp luminosity (5%) is not shown. The statistical and systematic uncertainties of the data are shown as vertical bars and boxes. The expectation from the hadronic decay cocktail is shown as a band, and the bottom plot shows the data-to-cocktail ratio together with the cocktail uncertainty.

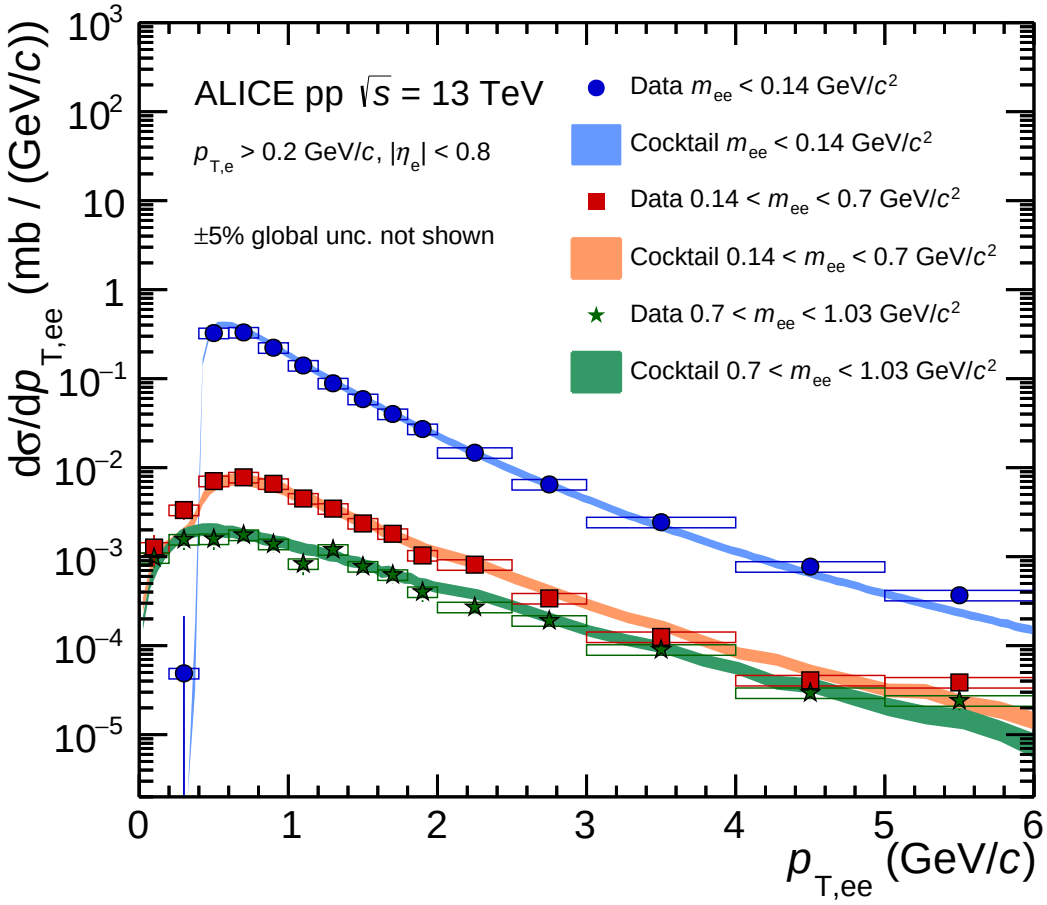

Figure 4.2: The dielectron cross section in inelastic pp collisions at $\sqrt{s} = 13$ TeV as a function of pair transverse momentum $p_{\mathrm{T,\,ee}}$ in different mass intervals using Pythia simulations to estimate open heavy-flavour decays. The global scale uncertainty on the pp luminosity (5%) is not shown. The statistical and systematic uncertainties of the data are shown as vertical bars and boxes. The expectations from the hadronic decay cocktail are shown as bands. Acceptance effect of the $p_{\mathrm{T,\,e}} > 0.2$ GeV/c requirement is visible in the low mass regions at $p_{\mathrm{T,\,ee}} < 0.4$ GeV/c.

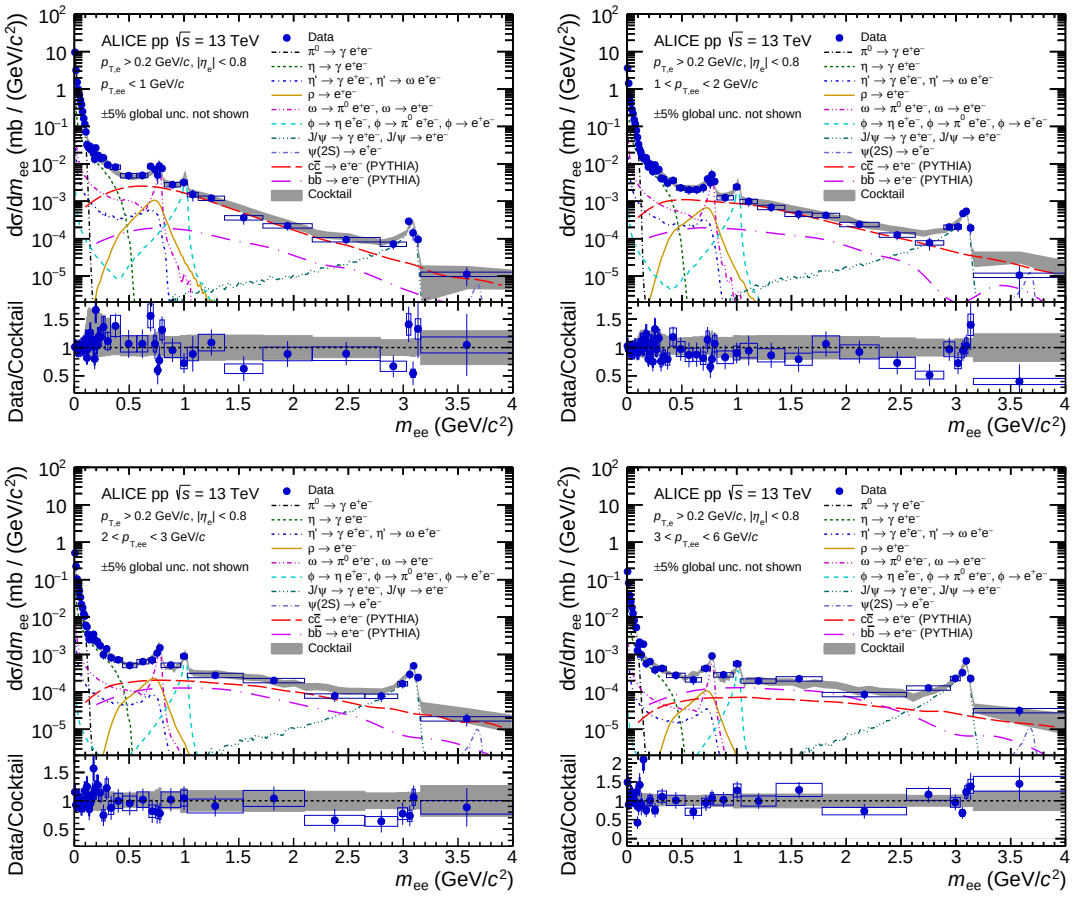

Figure 4.3: The dielectron cross section in inelastic pp collisions at $\sqrt{s} = 13$ TeV as a function of invariant mass in different $p_{\mathrm{T,\,ee}}$ intervals using Pythia simulations to estimate open heavy-flavour decays. The global scale uncertainty on the pp luminosity (5%) is not shown. The statistical and systematic uncertainties of the data are shown as vertical bars and boxes. The expectation from the hadronic decay cocktail is shown as a band, and the data-to-cocktail ratio is presented below together with the cocktail uncertainty.

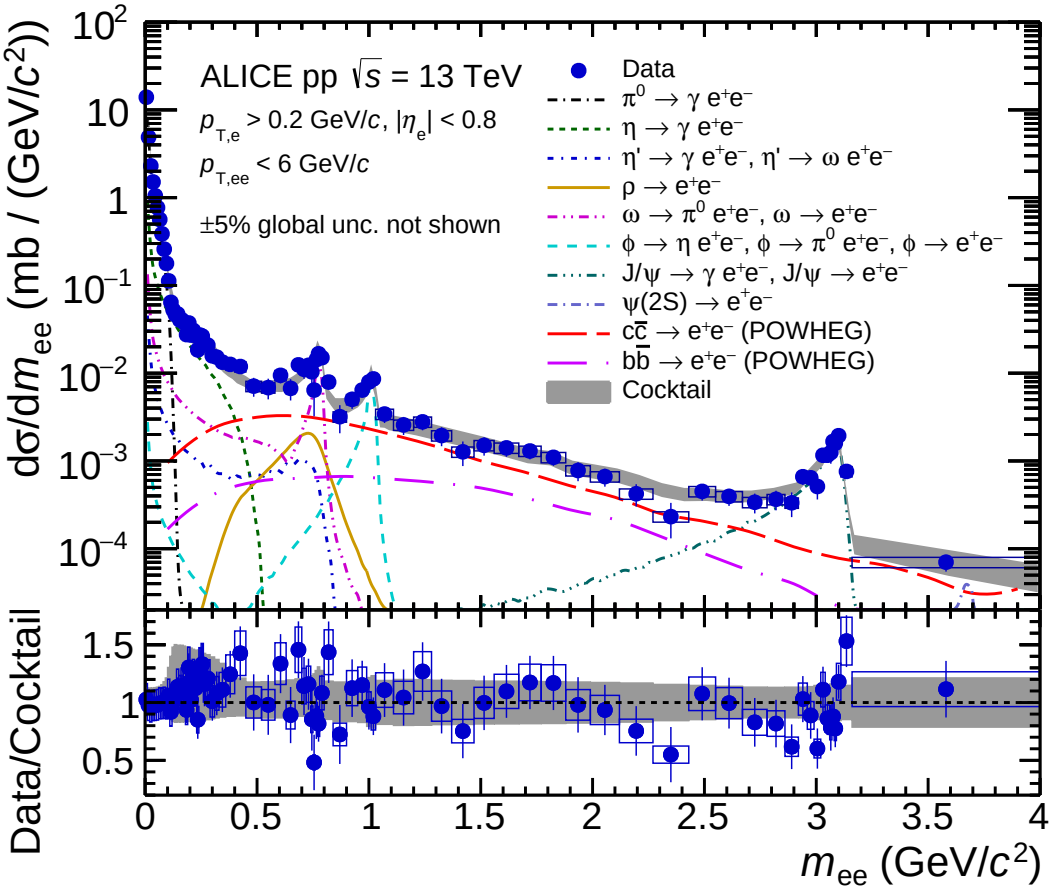

Figure 4.4: The dielectron cross section in inelastic pp collisions at $\sqrt{s} = 13$ TeV as a function of invariant mass using Powheg simulations to estimate open heavy-flavour decays. The global scale uncertainty on the pp luminosity (5%) is not shown. The statistical and systematic uncertainties of the data are shown as vertical bars and boxes. The expectation from the hadronic decay cocktail is shown as a band, and the data-to-cocktail ratio is presented below together with the cocktail uncertainty.

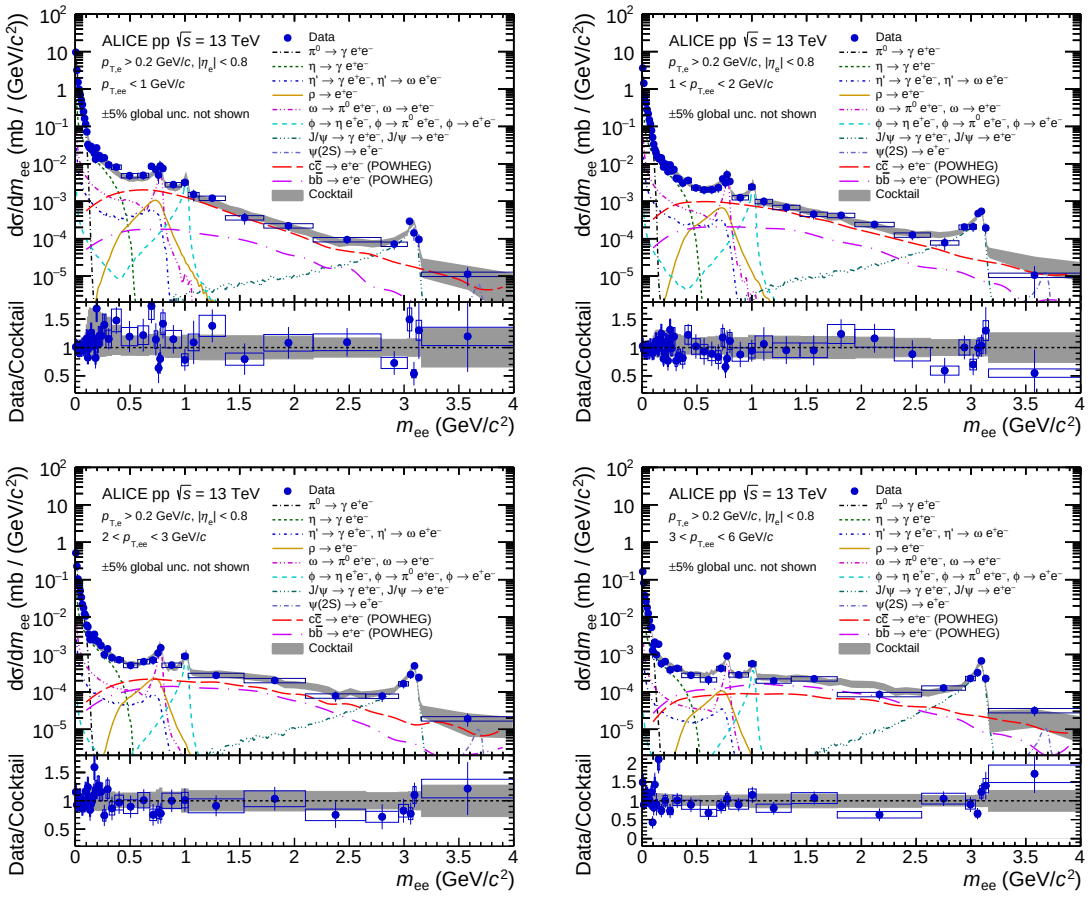

Figure 4.5: The dielectron cross section in inelastic pp collisions at $\sqrt{s} = 13$ TeV as a function of invariant mass in different $p_{\mathrm{T,\,ee}}$ intervals using Powheg simulations to estimate open heavy-flavour decays. The global scale uncertainty on the pp luminosity (5%) is not shown. The statistical and systematic uncertainties of the data are shown as vertical bars and boxes. The expectation from the hadronic decay cocktail is shown as a band, and the data-to-cocktail ratio is presented below together with the cocktail uncertainty.

4.2 High-Multiplicity pp Collisions

Modifications of the dielectron spectrum in high-multiplicity pp collisions are investigated in experimental data as the ratio of the dielectron spectrum in high-multiplicity events over the spectrum in inelastic collisions:

$$\frac{N_{\mathrm{ee}}(\mathrm{HM})/\langle N_{\mathrm{ch}}(\mathrm{HM})\rangle}{N_{\mathrm{ee}}(\mathrm{INEL})/\langle N_{\mathrm{ch}}(\mathrm{INEL})\rangle} = \frac{\langle N_{\mathrm{ch}}(\mathrm{INEL})\rangle}{\langle N_{\mathrm{ch}}(\mathrm{HM})\rangle} \times \frac{1/N_{\mathrm{HM}}\,\mathrm{d}N_{\mathrm{ee}}/\mathrm{d}m_{\mathrm{ee}}|_{\mathrm{HM}}}{1/N_{\mathrm{INEL}}\,\mathrm{d}N_{\mathrm{ee}}/\mathrm{d}m_{\mathrm{ee}}|_{\mathrm{INEL}}}. \quad (4.2)$$

The results are compared to a dedicated cocktail simulation of light- and heavy-flavour production (Sections 3.5.3 and 3.5.4). To account for the trivial scaling with charged-particle multiplicity, the ratio is scaled by the multiplicity factor, which for corrected multiplicities in inelastic and in high-multiplicity pp collisions amounts to:

$$\mathrm{d}N_{\mathrm{ch}}/\mathrm{d}\eta(\mathrm{HM})/\langle \mathrm{d}N_{\mathrm{ch}}/\mathrm{d}\eta(\mathrm{INEL})\rangle = 6.27 \pm 0.22, \quad (4.3)$$

where $\mathrm{d}N_{\mathrm{ch}}/\mathrm{d}\eta(\mathrm{HM}) = 33.29 \pm 0.39$ and $\langle \mathrm{d}N_{\mathrm{ch}}/\mathrm{d}\eta(\mathrm{INEL})\rangle = 5.31 \pm 0.18$ are the charged-particle multiplicities in $|\eta_{\mathrm{ch}}| < 0.5$ measured in high-multiplicity and inelastic pp collisions, respectively [42]. Figures 4.6 and 4.7 show the ratios of the dielectron spectra in high-multiplicity over inelastic events as a function of m_{ee} for different $p_{\mathrm{T,\,ee}}$ intervals. The ratio is found to be in good agreement with the hadronic decay cocktail calculations over the whole measured m_{ee} and $p_{\mathrm{T,\,ee}}$ range.

For light-flavour mesons, and in particular for π^0 and η, this confirms the hypothesis that different light mesons have the same multiplicity dependence as a function of m_{T}, which was used in the construction of the high-multiplicity hadron cocktail (Section 3.5.3). At low invariant mass, both data and cocktail simulations exhibit a ratio above 1, which comes from the low-p_{T} cut of $p_{\mathrm{T,\,e}} > 0.2$ GeV/c convoluted with the hardening of charged-particle p_{T} spectrum with multiplicity shown in Fig. 3.46.

In the intermediate mass range, the ratio is in good agreement with the cocktail calculations based on measured single D meson production at similar relative multiplicity (Section 3.5.4). From the agreement between data and cocktail in the high-p_{T} range ($3 < p_{\mathrm{T,\,ee}} < 6$ GeV/c^2), which is dominated by open beauty, it can be also concluded that at measured multiplicity enhancement open beauty production at high p_{T} has a multiplicity dependence similar to that of open charm.

While not the primary goal on this thesis, the results are also happen to be the first measurement of J/ψ production in high-multiplicity pp collisions in different p_{T} intervals. The p_{T} dependence of enhancement can be seen in Fig. 4.7 in the mass bin around $m_{\mathrm{ee}} \approx 3.1$ GeV/c^2, which is compared to the cocktail expectations based on previous p_{T}-integrated J/ψ measurements at $\sqrt{s} = 7$ TeV at similar relative multiplicity [44]. The results in different p_{T} intervals are found to be in good agreement with preliminary results from a dedicated J/ψ analysis in high-multiplicity pp collisions at $\sqrt{s} = 13$ TeV [213].

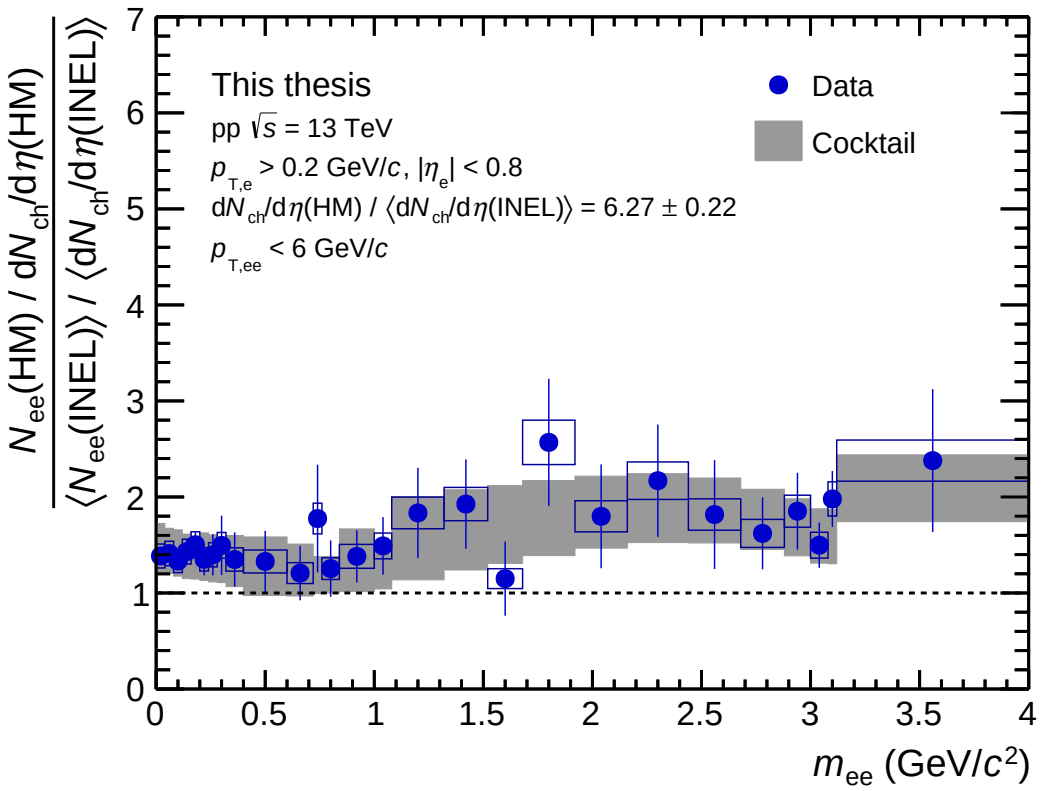

Figure 4.6: Ratio of dielectron spectra in HM and INEL events scaled by the charged-particle multiplicity. The statistical and systematic uncertainties of the data are shown as vertical bars and boxes. The expectation from the hadronic decay cocktail calculation is shown as a grey band.

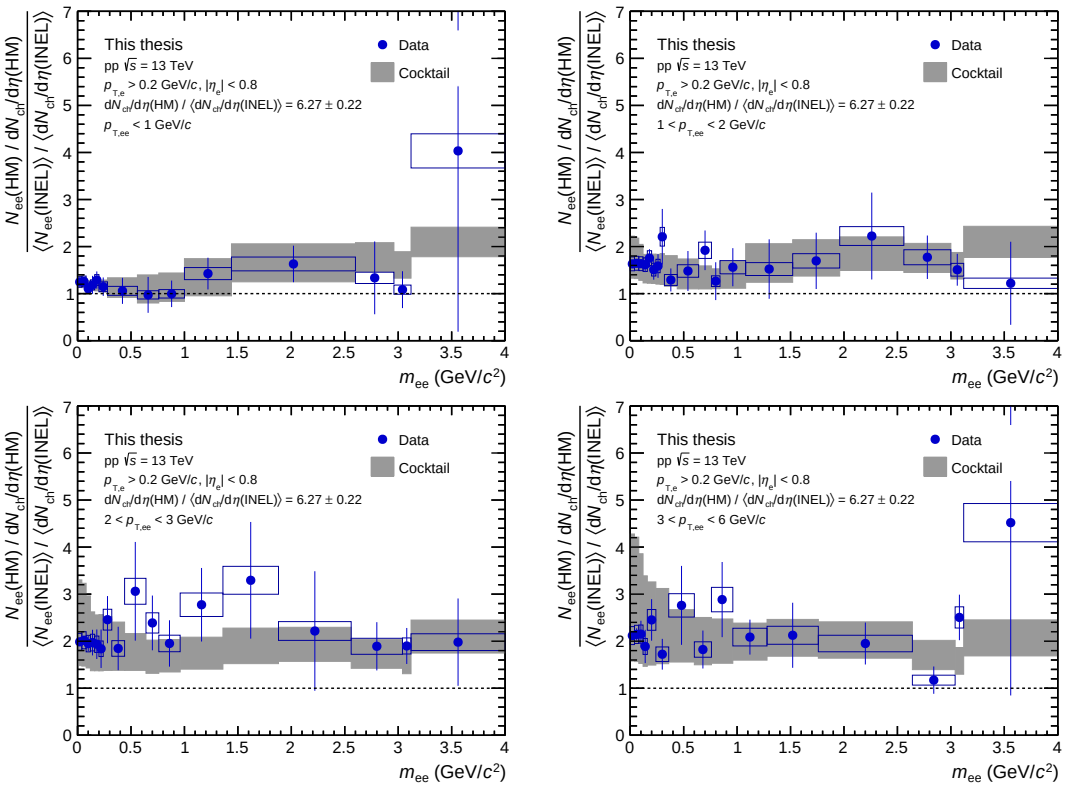

Figure 4.7: Ratio of dielectron spectra in HM and INEL events scaled by the charged-particle multiplicity in different $p_{\mathrm{T,\,ee}}$ intervals. The statistical and systematic uncertainties of the data are shown as vertical bars and boxes. The expectation from the hadronic decay cocktail calculation is shown as a grey band.

4.3 Charm and Beauty Production Cross Sections

The charm and beauty production cross sections, $\sigma_{\mathrm{c\bar{c}}}$ and $\sigma_{\mathrm{b\bar{b}}}$, can be extracted from the dielectron spectrum in intermediate mass region, which is dominated by open heavy-flavour decays. In this thesis, the production cross-sections are extracted at mid-rapidity, i. e. $\mathrm{d}\sigma_{\mathrm{c\bar{c}}}/\mathrm{d}y|_{y=0}$ and $\mathrm{d}\sigma_{\mathrm{b\bar{b}}}/\mathrm{d}y|_{y=0}$. For this purpose, data are fitted simultaneously in m_{ee} ($1.03 < m_{\mathrm{ee}} < 2.86$ GeV/c^2) and $p_{\mathrm{T,\,ee}}$ ($p_{\mathrm{T,\,ee}} < 6$ GeV/c) with Pythia and Powheg templates of open charm and beauty production. Light-flavour and J/ψ contributions from hadronic cocktail calculations are kept fixed, which introduces negligible uncertainties on the resulting heavy-flavour cross section. The fit is performed with the sum of two contributions:

$$f^{GEN} = S_{c\bar{c}} f^{GEN}_{c\bar{c}} + S_{b\bar{b}} f^{GEN}_{b\bar{b}}, \tag{4.4}$$

where $f^{GEN}_{c\bar{c}}$ and $f^{GEN}_{b\bar{b}}$ are the cross sections of dielectron pairs from charm and beauty-hadron decays calculated with the event generator GEN and normalised to $\mathrm{d}\sigma_{\mathrm{c\bar{c}}}/\mathrm{d}y|^{\mathrm{REF}}_{y=0} = 1296^{+172}_{-162}\,\mu$b and $\mathrm{d}\sigma_{\mathrm{b\bar{b}}}/\mathrm{d}y|^{\mathrm{REF}}_{y=0} = 68^{+15}_{-16}\,\mu$b, respectively (Section 3.5.2). The two fit parameters are the scaling factors $S_{c\bar{c}}$ and $S_{b\bar{b}}$ defined as:

$$\mathrm{d}\sigma_{\mathrm{c\bar{c}}}/\mathrm{d}y|_{y=0} = S_{c\bar{c}} \times \mathrm{d}\sigma_{\mathrm{c\bar{c}}}/\mathrm{d}y|_{y=0}{}^{\mathrm{REF}}, \tag{4.5}$$

$$\mathrm{d}\sigma_{\mathrm{b\bar{b}}}/\mathrm{d}y|_{y=0} = S_{b\bar{b}} \times \mathrm{d}\sigma_{\mathrm{b\bar{b}}}/\mathrm{d}y|_{y=0}{}^{\mathrm{REF}}. \tag{4.6}$$

For each combination of scaling factors $S_{c\bar{c}}$ and $S_{b\bar{b}}$, the χ^2 value is calculated as follows:

$$\chi^2 = \sum_{i=1}^{n} \left(\frac{x_i - \mu_i}{\sqrt{(\sigma^{stat}_{x_i})^2 + (\sigma^{stat}_{\mu_i})^2}} \right)^2 . \tag{4.7}$$

The values of the data points and MC calculations in bin i are given by x_i and μ_i respectively, while $\sigma^{stat}_{x_i}$ and $\sigma^{stat}_{\mu_i}$ represent their statistical uncertainties. The result of the fit is determined by the minimum of the χ^2 value.

The Pythia and Powheg fits of dielectron spectra in inelastic events projected over $p_{\mathrm{T,\,ee}}$ and m_{ee} are shown in the left and right panels of Fig. 4.8, respectively. The fit using Pythia templates leads to the following rescale factors:

$$S_{\mathrm{c\bar{c}}} = 0.75 \pm 0.11(\mathrm{stat.}),$$
$$S_{\mathrm{b\bar{b}}} = 1.16 \pm 0.21(\mathrm{stat.}).$$

High quality of the fit ($\chi^2/\mathrm{ndf} = 57.8/66$) has been confirmed in detailed studies as described in [182]. These two parameters are found to be highly anti-correlated ($\rho = -0.70$), so future studies should utilise the impact parameter information $\mathrm{DCA_{ee}}$ for a

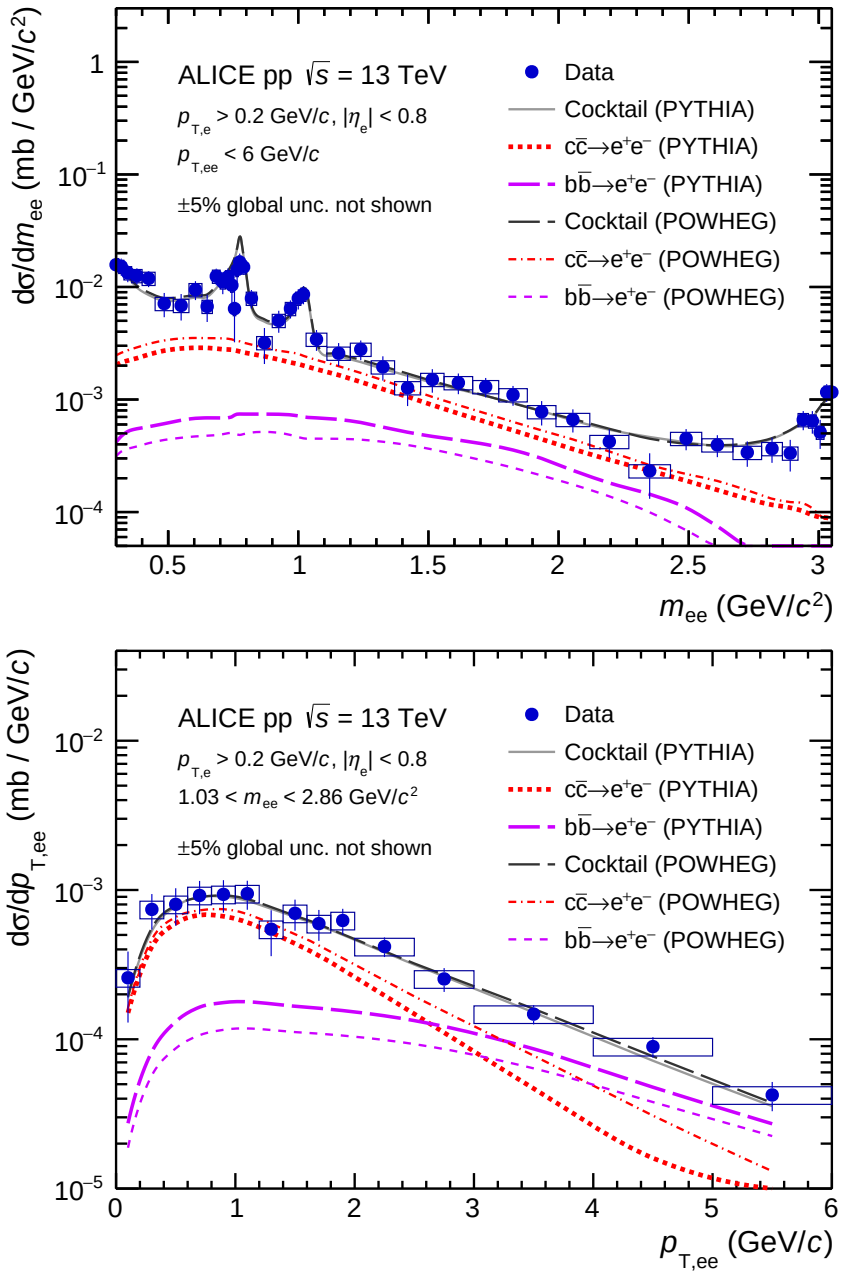

Figure 4.8: Projection of the heavy-flavour dielectron fit (grey line) in inelastic pp collisions at $\sqrt{s} = 13$ TeV onto the dielectron mass (top panel) and $p_{\mathrm{T,\,ee}}$ (bottom panel) using Pythia and Powheg event generators. The lines show the charm (red) and beauty (magenta) contributions after the fit. The global scale uncertainty on the pp luminosity (5%) is not shown. The statistical and systematic uncertainties of the data are shown as vertical bars and boxes.

more precise measurement [157]. The current statistics is not enough for a 3-dimensional simultaneous fit in m_{ee}, $p_{\mathrm{T,\,ee}}$ and $\mathrm{DCA_{ee}}$, while the standalone $\mathrm{DCA_{ee}}$ fit is roughly as precise as the 2-dimensional fit in m_{ee} and $p_{\mathrm{T,\,ee}}$ [157].

To take into account the systematic uncertainties of the data, which are highly correlated from bin to bin, the fit is repeated twice, having moved all data by $\pm 1\sigma$ of the systematic uncertainties. The resulting cross sections are:

$$\left.\frac{\mathrm{d}\sigma_{\mathrm{c\bar{c}}}}{\mathrm{d}y}\right|_{y=0} = 974 \pm 138\,(\mathrm{stat.}) \pm 140\,(\mathrm{syst.})\ \mu\mathrm{b},$$
$$\left.\frac{\mathrm{d}\sigma_{\mathrm{b\bar{b}}}}{\mathrm{d}y}\right|_{y=0} = 79 \pm 14\,(\mathrm{stat.}) \pm 11\,(\mathrm{syst.})\ \mu\mathrm{b},$$

where the first uncertainty is the statistical uncertainty from the data and the second is the systematic uncertainty on the data.

The cross-section extraction from the fit to the data was repeated using the heavy-flavour templates from Powheg event generator. The fit (with $\chi^2/\mathrm{ndf} = 52.6/66$) leads to rescale factors of:

$$S_{\mathrm{c\bar{c}}} = 1.09 \pm 0.14(\mathrm{stat.})$$
$$S_{\mathrm{b\bar{b}}} = 0.71 \pm 0.21(\mathrm{stat.}).$$

Again, the two parameters are found to be highly anti-correlated ($\rho = -0.77$). The data have been moved by $\pm 1\sigma$ of the statistical uncertainties, and the fit was repeated in order to take into account the systematic uncertainties of the data. The resulting cross-sections are:

$$\left.\frac{\mathrm{d}\sigma_{\mathrm{c\bar{c}}}}{\mathrm{d}y}\right|_{y=0} = 1417 \pm 184\,(\mathrm{stat.}) \pm 204\,(\mathrm{syst.})\ \mu\mathrm{b},$$
$$\left.\frac{\mathrm{d}\sigma_{\mathrm{b\bar{b}}}}{\mathrm{d}y}\right|_{y=0} = 48 \pm 14\,(\mathrm{stat.}) \pm 7\,(\mathrm{syst.})\ \mu\mathrm{b},$$

i.e. with Powheg one obtains substantially larger $\mathrm{c\bar{c}}$ and lower $\mathrm{b\bar{b}}$ cross-sections than with Pythia.

The resulting cross sections are summarised in Table 4.1. Both event generators are able to reproduce the (m_{ee}, $p_{\mathrm{T,\,ee}}$) spectra reasonably well and give similar minimum χ^2 per number of degree of freedom (0.88 for Pythia and 0.80 for Powheg). The results are consistent with extrapolations from lower energies based on FONLL pQCD calculations discussed in Section 3.5.2.

The sizeable difference in the cross sections between two MC event generators are comparable to what is observed for dielectron measurements in pp collisions at $\sqrt{s} = 7\ \mathrm{TeV}$ [157]. The different cross sections obtained from fits with Pythia and Powheg

	Pythia	Powheg
$\mathrm{d}\sigma_{\mathrm{c\bar{c}}}/\mathrm{d}y\|_{y=0}$	$974\pm138\,(\mathrm{stat.})\pm140\,(\mathrm{syst.})\ \mu\mathrm{b}$	$1417\pm184\,(\mathrm{stat.})\pm204\,(\mathrm{syst.})\ \mu\mathrm{b}$
$\mathrm{d}\sigma_{\mathrm{b\bar{b}}}/\mathrm{d}y\|_{y=0}$	$79\pm14\,(\mathrm{stat.})\pm11\,(\mathrm{syst.})\ \mu\mathrm{b}$	$48\pm14\,(\mathrm{stat.})\pm7(\mathrm{syst.})\ \mu\mathrm{b}$
$\mathrm{d}\sigma_{\mathrm{c\bar{c}}}/\mathrm{d}y\|_{y=0}^{\mathrm{HM}}$	$4.14\pm0.67\,(\mathrm{stat.})\pm0.66\,(\mathrm{syst.})\ \mu\mathrm{b}$	$5.95\pm0.91\,(\mathrm{stat.})\pm0.95\,(\mathrm{syst.})\ \mu\mathrm{b}$
$\mathrm{d}\sigma_{\mathrm{b\bar{b}}}/\mathrm{d}y\|_{y=0}^{\mathrm{HM}}$	$0.29\pm0.07\,(\mathrm{stat.})\pm0.05\,(\mathrm{syst.})\ \mu\mathrm{b}$	$0.17\pm0.07\,(\mathrm{stat.})\pm0.03\,(\mathrm{syst.})\ \mu\mathrm{b}$

Table 4.1: Heavy-flavour production cross sections in inelastic and high-multiplicity pp collisions at $\sqrt{s} = 13$ TeV. The 24% (6%) branching fraction uncertainty for charm (beauty) decays into electrons is not listed. Like statistical and systematic uncertainties, it is fully correlated between the Pythia and Powheg based results.

simulations are caused by acceptance differences of $\mathrm{e^+e^-}$ pairs from heavy-flavour hadron decays in these two event generators because of different kinematic correlations of the heavy quark pairs, in particular in rapidity [157]. Since the hadronization of the charm and beauty quarks as well as the decay kinematics of the heavy-flavour hadrons is in both cases performed by Pythia, this points to important differences in the heavy-quark production mechanisms implemented in the two generators. It can result in different kinematic correlations of the $q\bar{q}$ pair and therefore in different probabilities for the $\mathrm{e^+e^-}$ pair to enter the detector acceptance. The result of the fit depends also on the $p_{\mathrm{T,\,ee}}$ distributions of correlated $\mathrm{e^+e^-}$ pairs from charm and beauty-hadron decays, which are harder in Powheg than in Pythia.

It should be stressed that single heavy-flavour measurements are insensitive to these differences as the cross sections obtained from such measurements agree between Pythia and Powheg based extrapolations [139, 142, 153]. Here, dielectron measurements can give further constraints on the MC event generators. When such complementary information on heavy-flavour production provided by dielectrons is properly modelled, measurements of production cross sections with Pythia and Powheg should lead to consistent results.

Table 4.1 also summarises the corresponding cross sections for the high-multiplicity data. In case of Pythia, the measured charm cross section translates into a p_{T}-integrated enhancement of $1.86 \pm 0.40\,(\mathrm{stat.}) \pm 0.40\,(\mathrm{syst.})$ relative to the charged-particle multiplicity increase. This is consistent with the modelled multiplicity dependence used as input for the cocktail in Figs. 4.6 and 4.7. For the beauty cross section, the observed p_{T}-integrated enhancement is $1.63 \pm 0.50\,(\mathrm{stat.}) \pm 0.35\,(\mathrm{syst.})$. This is consistent with the multiplicity dependence observed for open charm, but a scaling with charged-particle multiplicity cannot be excluded.

4.4 Direct Photons

As discussed in Section 1.2.4, the fraction of real direct photons to inclusive photons can be extracted from the dielectron spectrum at small invariant masses assuming the equivalence between this fraction and the ratio of virtual direct photons to inclusive photons. To this purpose, the data are fitted, in bins of $p_{\mathrm{T,\,ee}}$, with the sum of the light-flavour cocktail ($f_{\mathrm{LF}}(m_{\mathrm{ee}})$), open heavy-flavour contribution ($f_{\mathrm{HF}}(m_{\mathrm{ee}})$) and a virtual direct photon component ($f_{\mathrm{direct}}(m_{\mathrm{ee}})$) using the following expression:

$$\mathrm{d}\sigma/\mathrm{d}m_{\mathrm{ee}} = r f_{\mathrm{dir}}(m_{\mathrm{ee}}) + (1-r) f_{\mathrm{LF}}(m_{\mathrm{ee}}) + f_{\mathrm{HF}}(m_{\mathrm{ee}}). \tag{4.8}$$

The normalisation of the open heavy-flavour component f_{HF} is fixed to the measured open charm and beauty cross sections presented above, using the Pythia simulations for the nominal fit (as systematic uncertainty estimate, the Powheg simulation is used instead). The light-flavour cocktail f_{LF} and virtual direct photon templates f_{dir} are normalised independently to the data in $m_{\mathrm{ee}} < 0.04$ GeV$/c^2$, i. e. in a mass window in which Dalitz decays and direct photons have the same $\sim 1/m_{\mathrm{ee}}$ dependence (Eq. 1.7). These normalisation factors are unity within $\simeq 1.5\%$ thanks to the good agreement between data and cocktail. The direct photon fraction r is then the only fit parameter, which is extracted by fitting the data in the mass interval $0.14 < m_{\mathrm{ee}} < 0.32$ GeV$/c^2$ (i. e. above the π^0 mass to suppress the most dominant hadron background) in $p_{\mathrm{T,\,ee}}$ bins of $1-2$, $2-3$ and $3-6$ GeV$/c$.

The following sources of systematic uncertainties are considered: the fit range, the systematic uncertainties of the data and of the hadronic cocktail components, as well as the normalisation range. Among them, the largest contribution comes from the systematic uncertainty due to hadronic cocktail calculations. In the mass region of $100-300$ MeV$/c^2$ (dominated by η decays), the relative cocktail uncertainty reaches $\sim 20-30\%$.

Figures 4.9 and 4.10 show the fits to minimum-bias and high-multiplicity data in each p_{T} bin, and Fig. 4.11 shows the results for r in inelastic and high-multiplicity events. The results are consistent with unity within the statistical and systematic uncertainties, which also prevent any conclusions on the scaling of direct-photon production with charged-particle multiplicity. The results in inelastic pp collisions are compared with a NLO pQCD calculation [214] shown as grey band in Fig. 4.11 (left), which is performed with the CT10 PDFs [215–217]. The width of the theory band is given by the variations of the factorisation and renormalisation scales from $\mu = p_{\mathrm{T}}$ to $\mu = 0.5p_{\mathrm{T}}$ and $\mu = 2p_{\mathrm{T}}$ (for $\mu = 0.5p_{\mathrm{T}}$ the calculation is limited to $p_{\mathrm{T}} > 2$ GeV$/c$). These calculations predict a small fraction of direct photons over the measured p_{T} range, compatible with the measurements within uncertainties. The pQCD results for $\mu = p_{\mathrm{T}}$ in each p_{T} bin are summarised in Table 4.2.

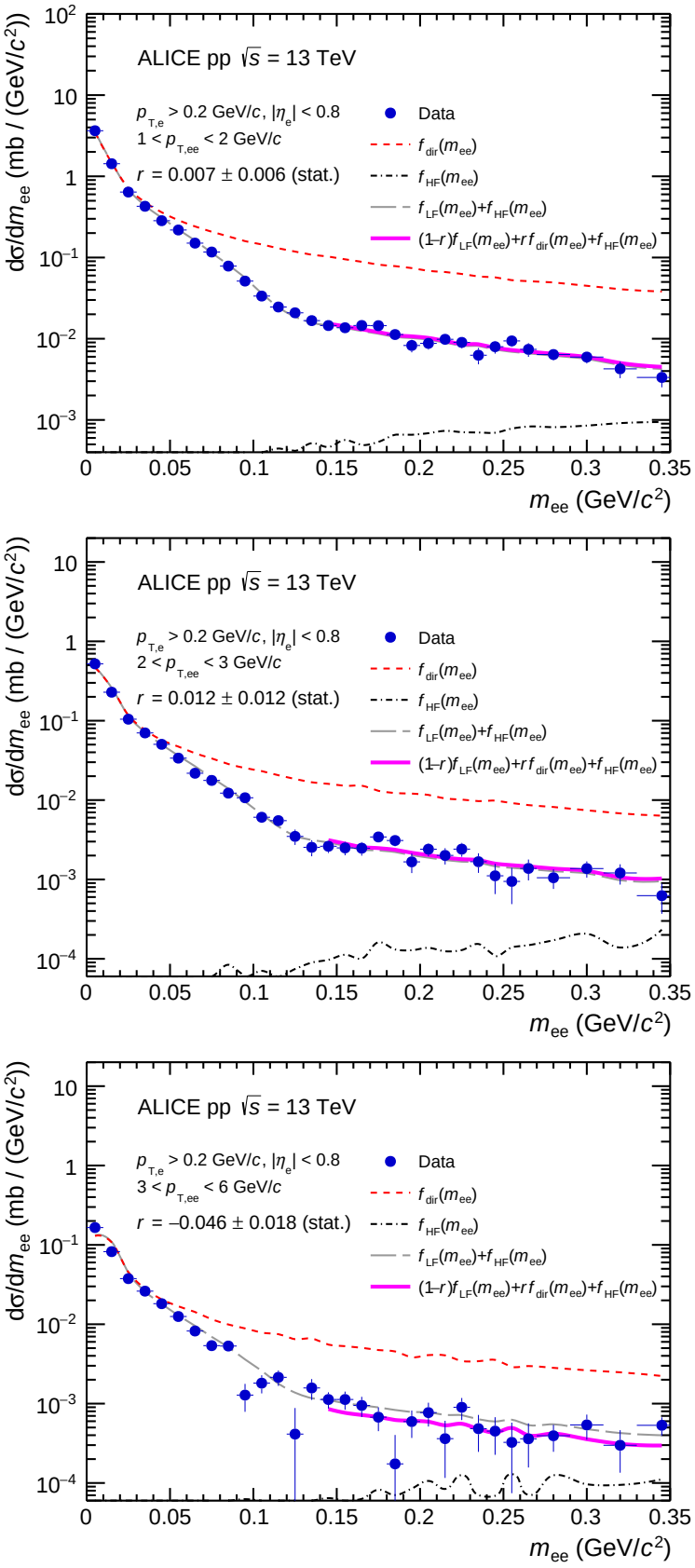

Figure 4.9: Fit of the minimum-bias data sample in different $p_{\mathrm{T,\,ee}}$ intervals with a three-component fit function to extract the fraction of direct photons to inclusive photons.

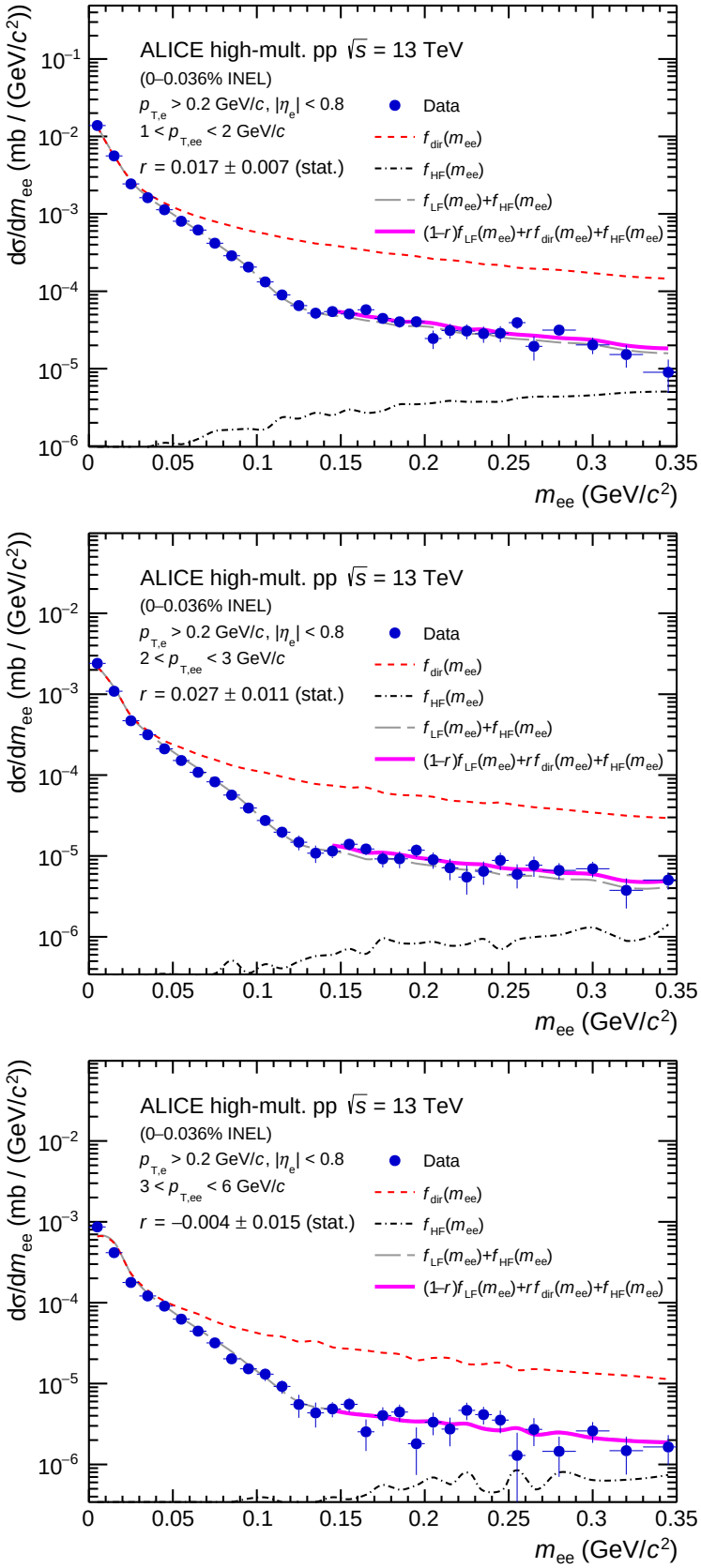

Figure 4.10: Fit of the high-multiplicity data sample in different $p_{\mathrm{T,\,ee}}$ intervals with a three-component fit function to extract the fraction of direct photons to inclusive photons.

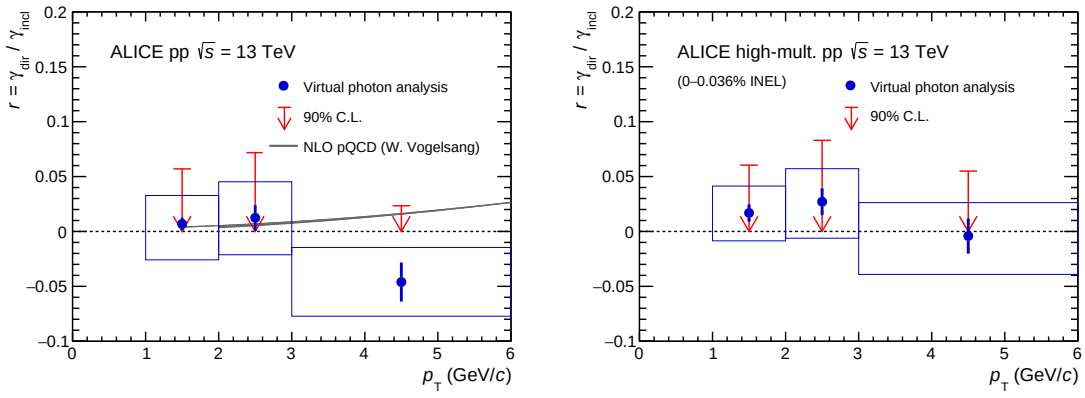

Figure 4.11: Ratio of direct to inclusive photon cross sections extracted from the dielectron spectra in inelastic (left) and high-multiplicity (right) pp collisions at $\sqrt{s} = 13\,\mathrm{TeV}$. The result in inelastic pp collisions is compared with a NLO pQCD calculation [214]. Statistical and systematic uncertainties are shown as vertical bars and boxes.

Data sample	$1<p_{\mathrm{T,\,ee}}<2$ GeV/c	$2<p_{\mathrm{T,\,ee}}<3$ GeV/c	$3<p_{\mathrm{T,\,ee}}<6$ GeV/c
Minimum-bias	0.057	0.072	0.023
High-multiplicity	0.060	0.083	0.055
pQCD	0.003	0.007	0.013

Table 4.2: Upper limits at 90% C.L. on the direct-photon fractions in comparison with the expectation in inelastic pp collisions based on a NLO pQCD calculation for a factorisation and renormalisation scale choice of $\mu = p_{\mathrm{T}}$ [214].

Since no significant direct photon contribution is observed in neither the inelastic nor the high-multiplicity events, the upper limits for direct photon production are extracted at 90% confidence level (C.L.) using the Feldman–Cousins method [218]. For this purpose, statistical and systematic uncertainties are treated independently as Gaussian distributions and summed in quadrature. The obtained upper limits are summarised in Table 4.2 and are also shown graphically in Fig. 4.11.

5
Summary and Outlook

This thesis presented the first measurement of dielectron production at midrapidity in proton–proton collisions at $\sqrt{s} = 13\ \mathrm{TeV}$, the highest collider energy ever studied. The dielectron continuum in inelastic pp collisions can be well described by the expected contributions from decays of light- and heavy-flavour hadrons, which validates the hadronic cocktail calculation and the assumptions used for it.

The charm and beauty production cross sections are extracted for the first time at midrapidity integrated over all p_{T} at $\sqrt{s} = 13\ \mathrm{TeV}$ using templates from two event generators, and the results are consistent with extrapolations from measurements at lower energies based on pQCD calculations. The differences observed between Powheg and Pythia imply different kinematic correlations of the heavy-quark pairs in these two event generators. Here, dielectron measurements are uniquely sensitive to the heavy quark production mechanisms and can provide further constraints on the MC event generators, which aim at describing the production of open heavy-flavour hadrons.

The dielectron production has been also studied in pp collisions with high charged-particle multiplicities. This is the first measurement sensitive to the production of π^0, η, ω and ϕ in high-multiplicity pp collisions. The result confirms the hypothesis that these light mesons have the same multiplicity dependence as a function of m_{T}. The agreement between data and cocktail in the high-p_{T} range, which is dominated by open beauty, provides for the first time constraints on the scaling of beauty production with multiplicity, validating the assumption that at least at high p_{T} it scales like charm production. Previous measurements via non-prompt J/ψ had no significant constraining power [43], in particular in the multiplicity regime $\mathrm{d}N_{\mathrm{ch}}/\mathrm{d}\eta(\mathrm{HM})/\langle \mathrm{d}N_{\mathrm{ch}}/\mathrm{d}\eta(\mathrm{INEL})\rangle = 6.27 \pm 0.22$ investigated in this thesis. This puts additional constraints on mechanisms used to de-

scribe heavy-flavour production in high-multiplicity pp collisions, such as multiple parton interactions, percolation or hydrodynamic models.

It is also the first attempt to estimate the production of direct photons in high-multiplicity pp collisions. The fraction of direct photons in the inclusive photon spectrum has been extracted from dielectron mass spectra, and the results are found to be consistent with zero within experimental uncertainties. The current uncertainties prevent any conclusion on the multiplicity scaling of direct photon production. In inelastic pp collisions, upper limits on direct photon production are in agreement with predictions from perturbative quantum chromodynamics calculations.

The $\mathrm{e^+e^-}$ pair production will be further studied in pp, p–Pb and Pb–Pb collisions with the LHC Run-2 data, which are currently being recorded (2015–2018). The studies of the full pp data sample from Run-2, with about 4 times more events and with future, more precise measurements of hadron production as cocktail input, might already allow one to measure the direct photon production at low p_{T} in inelastic and high-multiplicity pp collisions. For this, especially a precise η measurement would be needed in order to reduce the current systematic uncertainties of the direct photon measurement. Detailed dielectron studies of heavy-flavour production cross sections, with reduced statistical and systematic uncertainties, will provide an important constraint for Monte Carlo generators and probably will be able to exclude one of the model in favour of other: the information on pair $\mathrm{DCA_{ee}}$, successfully tested recently in pp analysis at $\sqrt{s} = 7\ \mathrm{TeV}$ [157], can be used simultaneously with m_{ee} and $p_{\mathrm{T,\,ee}}$ to further improve the fit results and to pin down the difference between Monte Carlo generators. With high enough statistics, angular correlations between dielectrons from open heavy-flavour decays also have the potential to provide more discrimination power between models [111].

To fully exploit the scientific potential of LHC, a wide ALICE physics program is proposed for the LHC Run-3 period (2021–2023) and beyond [219]. High statistics Pb–Pb measurements will be accompanied by precision measurements in pp and p–Pb collisions, which will serve both as a quantitative base for comparison with results from Pb–Pb collisions and as further fundamental studies of QCD. The statistics of pp collisions collected in Run-3 will allow for precise dielectron studies sensitive to heavy-flavour production mechanisms, for which an increase of factor of $\sim$100 in statistics would be needed compared to Run-2 [182]. Measurements of thermal radiation with dielectrons in small systems, if produced, may also be possible with the full Run-3 statistics. However, for such measurement the definition of a proper reference, which would include direct photon production from MPI and all other non-thermal sources, most probably will be complicated. Here, a possible approach could be e. g. an assumption of direct photon production scaling at high p_{T}.

One of the main objectives of the ALICE physics program for the LHC Run-3 and beyond will be the precise measurement of dielectron production in heavy-ion collisions. After a major upgrade of main detector systems, the ALICE experiment will

collect about 100 times more data in central Pb–Pb collisions [220–223]. A new Inner Tracking System will greatly improve the capabilities of DCA measurements and low-p_{T} tracking [223], which are needed to study open heavy-flavour production in detail and to enhance the discrimination power between prompt and non-prompt dielectron sources. Anticipated interaction rates up to $50\,\mathrm{kHz}$ (a factor $\sim$50 higher compared to Run-2) make it also necessary to upgrade the current TPC read-out, which in the future will be based on Gas Electron Multipliers (GEMs) [221, 222]. In order to further increase the acceptance of dielectrons with low mass and transverse momentum, part of the Pb–Pb data will be recorded with a magnetic field in the central barrel solenoid reduced from 0.5 T to 0.2 T. Simulations of the detector performance indicate that from the analysis of the low-mass region a detailed study of the in-medium properties of the ρ meson will be possible. The initial QGP temperature is expected to be measured with a precision of 10–20% from an exponential fit to the intermediate mass region of the dielectron spectrum, where the contribution from charm decays will be strongly suppressed by the improved secondary vertex resolution of the upgraded detectors.

Acknowledgements

The results presented in this thesis could not have been achieved without the help and support of many people who have been accompanying me over the past years. Foremost, I would like to gratefully thank my supervisor Torsten Dahms for his endless support and careful guidance through complicated and fascinating field of low-mass dielectron physics. His extremely wide knowledge of the topic and the ability to solve analysis difficulties were the key ingredients of the final success. He has always been ready to help me with any of my questions, both related to physics and about life in Germany. It was also a pleasure to be a part of his research group and to work together with Oton Vazquez Doce, Anisa Dashi and Alex Chauvin. We have been working really as one team, and I would like to thank them for this wonderful experience. In particular, I am grateful to Oton for his invaluable contribution to hadronic cocktail calculations.

I would like to express my deepest thanks to Prof. Laura Fabbietti. Her passion for physics, strong requirements for high-quality analyses and conference talks and immense support of every group member make it very special to be a part of her group. I thank her for great opportunities and for all the trust, it will be a pleasure for me to continue the journey as a group member. I would also like to extend my thanks to all members of the group for useful debates and for all the fun during our group meetings, both at Physics Department and outside Garching Research Centre. Special thanks to my office colleagues and ALICE collaborators Ante Bilandzic, Oliver Arnold, Cristiane Jahnke, Dimitar Mihaylov, Valentina Mantovani Sarti, Andreas Mathis and Bernhard Hohlweger for fruitful discussions and nice atmosphere in the office, I believe we have been a perfect example of how a large international collaboration works on small scale. I would like to express my acknowledgement to my colleagues from the Physics Analysis Group "Low-mass dielectrons" Taku Gunji, Michael Weber and Raphaelle Bailhache for detailed analysis review and important suggestions which have substantially improved the results of the analysis.

Already before this journey has started, Ilia Kolevatov has motivated me to apply for this position and helped me a lot with bureaucratic procedures, for which I'm very grateful to him. I would like to thank Elena Zerner-Käning for the support and guidance during the first days of my life in new country. I also want to express my very special thanks to our International Russian-Ukrainian-German Union with headquarters in IPP Guesthouses, Garching, and in particular to Anton Bogomolov, Serhiy Mochalskyy and

Alexey Arkhipov, for all the fun on the slopes and the moments we shared together. I'm very grateful to my parents for their love, support and trust.

Finally, I would like to thank my wife Svetlana. Here, I just cannot put into simple words what she means to me.

This research was supported by the DFG cluster of excellence "Origin and Structure of the Universe".

Bibliography

[1] R. Hagedorn, "Statistical thermodynamics of strong interactions at high-energies," *Nuovo Cim. Suppl.* **3** (1965) 147–186. Cited on page(s): 1

[2] A. Chodos, R. L. Jaffe, K. Johnson, C. B. Thorn, and V. F. Weisskopf, "A New Extended Model of Hadrons," *Phys. Rev.* **D9** (1974) 3471–3495. Cited on page(s): 2

[3] F. Karsch, "Lattice simulations of the thermodynamics of strongly interacting elementary particles and the exploration of new phases of matter in relativistic heavy ion collisions," *J. Phys. Conf. Ser.* **46** (2006) 122–131, arXiv:hep-lat/0608003 [hep-lat]. Cited on page(s): 2

[4] **Wuppertal-Budapest** Collaboration, S. Borsanyi, Z. Fodor, C. Hoelbling, S. D. Katz, S. Krieg, C. Ratti, and K. K. Szabo, "Is there still any T_c mystery in lattice QCD? Results with physical masses in the continuum limit III," *JHEP* **09** (2010) 073, arXiv:1005.3508 [hep-lat]. Cited on page(s): 2

[5] S. Borsanyi, G. Endrodi, Z. Fodor, A. Jakovac, S. D. Katz, S. Krieg, C. Ratti, and K. K. Szabo, "The QCD equation of state with dynamical quarks," *JHEP* **11** (2010) 077, arXiv:1007.2580 [hep-lat]. Cited on page(s): 2

[6] **HotQCD** Collaboration, A. Bazavov *et al.*, "Equation of state in (2+1)-flavor QCD," *Phys. Rev.* **D90** (2014) 094503, arXiv:1407.6387 [hep-lat]. Cited on page(s): 2

[7] K. Fukushima and T. Hatsuda, "The phase diagram of dense QCD," *Rept. Prog. Phys.* **74** (2011) 014001, arXiv:1005.4814 [hep-ph]. Cited on page(s): 2

[8] T. Boeckel and J. Schaffner-Bielich, "A little inflation at the cosmological QCD phase transition," *Phys. Rev.* **D85** (2012) 103506, arXiv:1105.0832 [astro-ph.CO]. Cited on page(s): 2

[9] M. J. Fromerth and J. Rafelski, "Hadronization of the quark Universe," arXiv:astro-ph/0211346 [astro-ph]. Cited on page(s): 2

[10] J. Schukraft and R. Stock, "Toward the Limits of Matter: Ultra-relativistic nuclear collisions at CERN," *Adv. Ser. Direct. High Energy Phys.* **23** (2015) 61–87, arXiv:1505.06853 [nucl-ex]. Cited on page(s): 3

[11] P. Braun-Munzinger, V. Koch, T. Schäfer, and J. Stachel, "Properties of hot and dense matter from relativistic heavy ion collisions," *Phys. Rept.* **621** (2016) 76–126, arXiv:1510.00442 [nucl-th]. Cited on page(s): 3

[12] **PHENIX** Collaboration, S. S. Adler *et al.*, "Nuclear modification of electron spectra and implications for heavy quark energy loss in Au+Au collisions at s(NN)**(1/2) - 200-GeV," *Phys. Rev. Lett.* **96** (2006) 032301, arXiv:nucl-ex/0510047 [nucl-ex]. Cited on page(s): 3

[13] **PHENIX** Collaboration, A. Adare *et al.*, "Energy Loss and Flow of Heavy Quarks in Au+Au Collisions at s(NN)**(1/2) = 200-GeV," *Phys. Rev. Lett.* **98** (2007) 172301, arXiv:nucl-ex/0611018 [nucl-ex]. Cited on page(s): 3

[14] **PHENIX** Collaboration, A. Adare *et al.*, "Enhanced production of direct photons in Au+Au collisions at $\sqrt{s_{\rm NN}} = 200$ GeV and implications for the initial temperature," *Phys. Rev. Lett.* **104** (2010) 132301, arXiv:0804.4168 [nucl-ex]. Cited on page(s): 3, 14

[15] **ALICE** Collaboration, J. Adam *et al.*, "Direct photon production in Pb-Pb collisions at $\sqrt{s_{\rm NN}} = 2.76$ TeV," *Phys. Lett.* **B754** (2016) 235–248, arXiv:1509.07324 [nucl-ex]. Cited on page(s): 3, 14, 16, 27, 28

[16] **PHENIX** Collaboration, S. S. Adler *et al.*, "Elliptic flow of identified hadrons in Au+Au collisions at s(NN)**(1/2) = 200-GeV," *Phys. Rev. Lett.* **91** (2003) 182301, arXiv:nucl-ex/0305013 [nucl-ex]. Cited on page(s): 3

[17] **STAR** Collaboration, J. Adams *et al.*, "Azimuthal anisotropy in Au+Au collisions at s(NN)**(1/2) = 200-GeV," *Phys. Rev.* **C72** (2005) 014904, arXiv:nucl-ex/0409033 [nucl-ex]. Cited on page(s): 3

[18] **ALICE** Collaboration, K. Aamodt *et al.*, "Elliptic flow of charged particles in Pb-Pb collisions at 2.76 TeV," *Phys. Rev. Lett.* **105** (2010) 252302, arXiv:1011.3914 [nucl-ex]. Cited on page(s): 3

[19] http://madai.msu.edu. Last accessed: 2018-08-26. Cited on page(s): 4

[20] R. Rapp, J. Wambach, and H. van Hees, "The Chiral Restoration Transition of QCD and Low Mass Dileptons," *Landolt-Bornstein* **23** (2010) 134, arXiv:0901.3289 [hep-ph]. Cited on page(s): 4, 10, 13

[21] I. Tserruya, "Electromagnetic Probes," *Landolt-Bornstein* **23** (2010) 176, arXiv:0903.0415 [nucl-ex]. Cited on page(s): 4

[22] M. Gyulassy and M. Plumer, "Jet Quenching in Dense Matter," *Phys. Lett.* **B243** (1990) 432–438. Cited on page(s): 5

[23] R. Baier, Y. L. Dokshitzer, A. H. Mueller, S. Peigne, and D. Schiff, "Radiative energy loss and p(T) broadening of high-energy partons in nuclei," *Nucl. Phys.* **B484** (1997) 265–282, arXiv:hep-ph/9608322 [hep-ph]. Cited on page(s): 5

[24] M. H. Thoma and M. Gyulassy, "Quark Damping and Energy Loss in the High Temperature QCD," *Nucl. Phys.* **B351** (1991) 491–506. Cited on page(s): 5

[25] E. Braaten and M. H. Thoma, "Energy loss of a heavy fermion in a hot plasma," *Phys. Rev.* **D44** (1991) 1298–1310. Cited on page(s): 5

[26] E. Braaten and M. H. Thoma, "Energy loss of a heavy quark in the quark - gluon plasma," *Phys. Rev.* **D44** no. 9, (1991) R2625. Cited on page(s): 5

[27] V. Greco, C. M. Ko, and R. Rapp, "Quark coalescence for charmed mesons in ultrarelativistic heavy ion collisions," *Phys. Lett.* **B595** (2004) 202–208, arXiv:nucl-th/0312100 [nucl-th]. Cited on page(s): 5

[28] A. Andronic, P. Braun-Munzinger, K. Redlich, and J. Stachel, "Statistical hadronization of charm in heavy ion collisions at SPS, RHIC and LHC," *Phys. Lett.* **B571** (2003) 36–44, arXiv:nucl-th/0303036 [nucl-th]. Cited on page(s): 5

[29] S. Batsouli, S. Kelly, M. Gyulassy, and J. L. Nagle, "Does the charm flow at RHIC?," *Phys. Lett.* **B557** (2003) 26–32, arXiv:nucl-th/0212068 [nucl-th]. Cited on page(s): 5

[30] M. Cacciari, M. Greco, and P. Nason, "The p_{T} spectrum in heavy flavor hadroproduction," *JHEP* **05** (1998) 007, arXiv:hep-ph/9803400 [hep-ph]. Cited on page(s): 5, 27, 93, 94

[31] M. Cacciari, S. Frixione, and P. Nason, "The p_{T} spectrum in heavy flavor photoproduction," *JHEP* **03** (2001) 006, arXiv:hep-ph/0102134 [hep-ph]. Cited on page(s): 5, 27, 94

[32] M. Cacciari, S. Frixione, N. Houdeau, M. L. Mangano, P. Nason, and G. Ridolfi, "Theoretical predictions for charm and bottom production at the LHC," *JHEP* **10** (2012) 137, arXiv:1205.6344 [hep-ph]. Cited on page(s): 5, 12, 13, 27, 94

[33] C. Loizides, "Experimental overview on small collision systems at the LHC," *Nucl. Phys. A* **956** (2016) 200, arXiv:1602.09138 [nucl-ex]. Cited on page(s): 6, 16

[34] J. L. Nagle and W. A. Zajc, "Small System Collectivity in Relativistic Hadron and Nuclear Collisions," arXiv:1801.03477 [nucl-ex]. Invited review prepared for Annual Review of Nuclear and Particle Science 68. Cited on page(s): 6, 16

[35] **CMS** Collaboration, V. Khachatryan *et al.*, "Observation of long-range near-side angular correlations in pp collisions at the LHC," *JHEP* **09** (2010) 091, arXiv:1009.4122 [hep-ex]. Cited on page(s): 6, 16

[36] **CMS** Collaboration, V. Khachatryan *et al.*, "Evidence for collectivity in pp collisions at the LHC," *Phys. Lett. B* **765** (2017) 193, arXiv:1606.06198 [nucl-ex]. Cited on page(s): 6, 16

[37] **ALICE** Collaboration, B. Abelev *et al.*, "Multiplicity dependence of two-particle azimuthal correlations in pp collisions at the LHC," *JHEP* **09** (2013) 049, arXiv:1307.1249 [nucl-ex]. Cited on page(s): 6, 16

[38] **ATLAS** Collaboration, G. Aad *et al.*, "Observation of long-range elliptic azimuthal anisotropies in $\sqrt{s} = 13$ and 2.76 TeV pp collisions with the ATLAS detector," *Phys. Rev. Lett.* **116** (2016) 172301, arXiv:1509.04776 [hep-ex]. Cited on page(s): 6, 16

[39] **ATLAS** Collaboration, M. Aaboud *et al.*, "Measurements of long-range azimuthal anisotropies and associated Fourier coefficients for pp collisions at $\sqrt{s} = 5.02$ and 13 TeV and p–Pb collisions at $\sqrt{s_{\mathrm{NN}}} = 5.02$ TeV with the ATLAS detector," *Phys. Rev. C* **96** (2017) 024908, arXiv:1609.06213 [nucl-ex]. Cited on page(s): 6, 16

[40] **ATLAS** Collaboration, M. Aaboud *et al.*, "Measurement of multi-particle azimuthal correlations in pp, p–Pb and low-multiplicity Pb–Pb collisions with the ATLAS detector," *Eur. Phys. J. C* **77** (2017) 428, arXiv:1705.04176 [hep-ex]. Cited on page(s): 6, 16

[41] **ALICE** Collaboration, J. Adam *et al.*, "Enhanced production of multi-strange hadrons in high-multiplicity pp collisions," *Nature Phys.* **13** (2017) 535, arXiv:1606.07424 [nucl-ex]. Cited on page(s): 6, 16

[42] **ALICE** Collaboration, J. Adam *et al.*, "Pseudorapidity and transverse-momentum distributions of charged particles in pp collisions at

$\sqrt{s} = 13$ TeV," *Phys. Lett. B* **753** (2016) 319, arXiv:1509.08734 [nucl-ex]. Cited on page(s): 6, 17, 47, 89, 90, 95, 97, 126

[43] **ALICE** Collaboration, J. Adam *et al.*, "Measurement of charm and beauty production at central rapidity versus charged-particle multiplicity in pp collisions at $\sqrt{s} = 7$ TeV," *JHEP* **09** (2015) 148, arXiv:1505.00664 [nucl-ex]. Cited on page(s): 6, 17, 18, 98, 99, 100, 137

[44] **ALICE** Collaboration, B. Abelev *et al.*, "J/ψ production as a function of charged particle multiplicity in pp collisions at $\sqrt{s} = 7$ TeV," *Phys. Lett. B* **712** (2012) 165, arXiv:1202.2816 [hep-ex]. Cited on page(s): 6, 18, 126

[45] T. Sjostrand and M. van Zijl, "A Multiple Interaction Model for the Event Structure in Hadron Collisions," *Phys. Rev.* **D36** (1987) 2019. Cited on page(s): 6, 18

[46] P. Bartalini and L. Fano, eds., *Proceedings, 1st International Workshop on Multiple Partonic Interactions at the LHC (MPI08)*, DESY. DESY, Hamburg, 2009. arXiv:1003.4220 [hep-ex]. https://inspirehep.net/record/849580/files/arXiv:1003.4220.pdf. Cited on page(s): 6, 18

[47] **CDF** Collaboration, D. Acosta *et al.*, "The underlying event in hard interactions at the Tevatron $\bar{p}p$ collider," *Phys. Rev.* **D70** (2004) 072002, arXiv:hep-ex/0404004 [hep-ex]. Cited on page(s): 6

[48] **CMS** Collaboration, V. Khachatryan *et al.*, "First Measurement of the Underlying Event Activity at the LHC with $\sqrt{s} = 0.9$ TeV," *Eur. Phys. J.* **C70** (2010) 555–572, arXiv:1006.2083 [hep-ex]. Cited on page(s): 6

[49] **ATLAS** Collaboration, G. Aad *et al.*, "Measurement of underlying event characteristics using charged particles in pp collisions at $\sqrt{s} = 900GeV$ and 7 TeV with the ATLAS detector," *Phys. Rev.* **D83** (2011) 112001, arXiv:1012.0791 [hep-ex]. Cited on page(s): 6

[50] **Particle Data Group**, C. Patrignani, *et al.*, "Review of Particle Physics," *Chin. Phys. C* **40** (2016) 100001. Cited on page(s): 8, 9, 40, 91, 94, 95

[51] F. Karsch, "Lattice QCD at high temperature and density," *Lect. Notes Phys.* **583** (2002) 209–249, arXiv:hep-lat/0106019 [hep-lat]. Cited on page(s): 8

[52] **Fermilab Lattice, HPQCD, UKQCD, MILC** Collaboration, C. T. H. Davies *et al.*, "High precision lattice QCD confronts experiment," *Phys. Rev. Lett.* **92** (2004) 022001, arXiv:hep-lat/0304004 [hep-lat]. Cited on page(s): 8

[53] T. R. Klassen, "The (Lattice) QCD potential and coupling: How to accurately interpolate between multiloop QCD and the string picture," *Phys. Rev.* **D51** (1995) 5130–5152, arXiv:hep-lat/9408016 [hep-lat]. Cited on page(s): 9

[54] Y. Nambu and G. Jona-Lasinio, "Dynamical Model of Elementary Particles Based on an Analogy with Superconductivity. 1.," *Phys. Rev.* **122** (1961) 345–358. [,127(1961)]. Cited on page(s): 10

[55] S. Klimt, M. F. M. Lutz, and W. Weise, "Chiral phase transition in the SU(3) Nambu and Jona-Lasinio model," *Phys. Lett.* **B249** (1990) 386–390. Cited on page(s): 10

[56] G. E. Brown and M. Rho, "Scaling effective Lagrangians in a dense medium," *Phys. Rev. Lett.* **66** (1991) 2720–2723. Cited on page(s): 10

[57] R. Rapp and J. Wambach, "Chiral symmetry restoration and dileptons in relativistic heavy ion collisions," *Adv. Nucl. Phys.* **25** (2000) 1, arXiv:hep-ph/9909229 [hep-ph]. Cited on page(s): 10

[58] G. Hering, *Dielectron production in heavy ion collisions at 158-GeV/c per nucleon*. PhD thesis, Darmstadt, Tech. Hochsch., 2001. arXiv:nucl-ex/0203004 [nucl-ex]. https://inspirehep.net/record/571210/files/arXiv:nucl-ex_0203004.pdf. Cited on page(s): 10

[59] S. D. Drell and T.-M. Yan, "Massive Lepton Pair Production in Hadron-Hadron Collisions at High-Energies," *Phys. Rev. Lett.* **25** (1970) 316–320. [Erratum: Phys. Rev. Lett.25,902(1970)]. Cited on page(s): 11

[60] **CMS** Collaboration, S. Chatrchyan *et al.*, "Measurement of the Drell-Yan Cross Section in pp Collisions at $\sqrt{s} = 7$ TeV," *JHEP* **10** (2011) 007, arXiv:1108.0566 [hep-ex]. Cited on page(s): 11

[61] **CMS** Collaboration, V. Khachatryan *et al.*, "Measurements of differential and double-differential Drell-Yan cross sections in proton-proton collisions at 8 TeV," *Eur. Phys. J.* **C75** no. 4, (2015) 147, arXiv:1412.1115 [hep-ex]. Cited on page(s): 11

[62] **ALICE** Collaboration, S. Acharya *et al.*, "Measurement of D-meson production at mid-rapidity in pp collisions at $\sqrt{s} = 7$ TeV," *Eur. Phys. J. C* **77** (2017) 550, arXiv:1702.00766 [hep-ex]. Cited on page(s): 12, 13, 26, 94

[63] A. Andronic *et al.*, "Heavy-flavour and quarkonium production in the LHC era: from proton–proton to heavy-ion collisions," *Eur. Phys. J.* **C76** no. 3, (2016) 107, arXiv:1506.03981 [nucl-ex]. Cited on page(s): 12, 16

[64] P. Petreczky, "Lattice QCD at non-zero temperature," *J. Phys.* **G39** (2012) 093002, arXiv:1203.5320 [hep-lat]. Cited on page(s): 13

[65] C. A. Dominguez, M. Loewe, and Y. Zhang, "Chiral symmetry restoration and deconfinement in QCD at finite temperature," *Phys. Rev.* **D86** no. 3, (2012) 034030, arXiv:1205.3361 [hep-ph]. [Erratum: Phys. Rev.D90,no.3,039903(2014)]. Cited on page(s): 13

[66] P. M. Hohler and R. Rapp, "Is ρ-Meson Melting Compatible with Chiral Restoration?," *Phys. Lett.* **B731** (2014) 103–109, arXiv:1311.2921 [hep-ph]. Cited on page(s): 13, 24

[67] J. J. Sakurai, "Theory of strong interactions," *Annals Phys.* **11** (1960) 1–48. Cited on page(s): 14

[68] F.-M. Liu and S.-X. Liu, "Quark-gluon plasma formation time and direct photons from heavy ion collisions," *Phys. Rev.* **C89** no. 3, (2014) 034906, arXiv:1212.6587 [nucl-th]. Cited on page(s): 14

[69] N. M. Kroll and W. Wada, "Internal pair production associated with the emission of high-energy gamma rays," *Phys. Rev.* **98** (1955) 1355. Cited on page(s): 14, 88

[70] L. G. Landsberg, "Electromagnetic decays of light mesons," *Phys. Rept.* **128** (1985) 301. Cited on page(s): 14

[71] R. H. Dalitz, "On an alternative decay process for the neutral pi-meson, Letters to the Editor," *Proc. Phys. Soc.* **A64** (1951) 667–669. Cited on page(s): 14

[72] **STAR** Collaboration, L. Adamczyk *et al.*, "Direct virtual photon production in Au–Au collisions at $\sqrt{s_{\mathrm{NN}}} = 200$ GeV," *Phys. Lett. B* **770** (2017) 451, arXiv:1607.01447 [nucl-ex]. Cited on page(s): 14

[73] **ALICE** Collaboration, S. Acharya *et al.*, "Direct photon production at low transverse momentum in pp collisions at $\sqrt{s} = 2.76$ and 8 TeV," arXiv:1803.09857 [nucl-ex]. Cited on page(s): 14, 27

[74] U. A. Wiedemann, "Jet Quenching in Heavy Ion Collisions," arXiv:0908.2306 [hep-ph]. [Landolt-Bornstein23,521(2010)]. Cited on page(s): 16

[75] S. A. Voloshin, A. M. Poskanzer, and R. Snellings, "Collective phenomena in non-central nuclear collisions," *Landolt-Bornstein* **23** (2010) 293–333, arXiv:0809.2949 [nucl-ex]. Cited on page(s): 16

[76] **PHENIX** Collaboration, A. Adare *et al.*, "Detailed measurement of the e^+e^- pair continuum in $p+p$ and Au+Au collisions at $\sqrt{s_{NN}} = 200$ GeV and implications for direct photon production," *Phys. Rev.* **C81** (2010) 034911, arXiv:0912.0244 [nucl-ex]. Cited on page(s): 16, 22, 23, 24, 26, 27, 61, 63, 90

[77] **CMS** Collaboration, S. Chatrchyan *et al.*, "Observation of sequential Upsilon suppression in PbPb collisions," *Phys. Rev. Lett.* **109** (2012) 222301, arXiv:1208.2826 [nucl-ex]. [Erratum: Phys. Rev. Lett.120,no.19,199903(2018)]. Cited on page(s): 16

[78] E. G. Ferreiro, "Charmonium dissociation and recombination at LHC: Revisiting comovers," *Phys. Lett. B* **731** (2014) 57, arXiv:1210.3209 [hep-ph]. Cited on page(s): 17

[79] **HADES** Collaboration, T. Galatyuk, "Low-mass e^+e^- mass distributions from 1.23 A GeV Au+Au collisions with HADES," *Nucl. Phys.* **A967** (2017) 680–683. Cited on page(s): 18, 19

[80] **HADES** Collaboration, G. Agakishiev *et al.*, "Inclusive dielectron production in proton-proton collisions at 2.2 GeV beam energy," *Phys. Rev.* **C85** (2012) 054005, arXiv:1203.2549 [nucl-ex]. Cited on page(s): 18

[81] **HADES** Collaboration, G. Agakishiev *et al.*, "Inclusive dielectron spectra in p+p collisions at 3.5 GeV," *Eur. Phys. J.* **A48** (2012) 64, arXiv:1112.3607 [nucl-ex]. Cited on page(s): 18

[82] **HADES** Collaboration, G. Agakishiev *et al.*, "Dielectron production in Ar+KCl collisions at 1.76A GeV," *Phys. Rev.* **C84** (2011) 014902, arXiv:1103.0876 [nucl-ex]. Cited on page(s): 18, 19

[83] **HADES** Collaboration, G. Agakishiev *et al.*, "Origin of the low-mass electron pair excess in light nucleus-nucleus collisions," *Phys. Lett.* **B690** (2010) 118–122, arXiv:0910.5875 [nucl-ex]. Cited on page(s): 18, 19

[84] **HADES** Collaboration, G. Agakishiev *et al.*, "Study of dielectron production in C+C collisions at 1-A-GeV," *Phys. Lett.* **B663** (2008) 43–48, arXiv:0711.4281 [nucl-ex]. Cited on page(s): 18

[85] **HADES** Collaboration, G. Agakichiev *et al.*, "Dielectron production in C-12+C-12 collisions at 2-AGeV with HADES," *Phys. Rev. Lett.* **98** (2007) 052302, arXiv:nucl-ex/0608031 [nucl-ex]. Cited on page(s): 18

[86] T. Galatyuk, P. M. Hohler, R. Rapp, F. Seck, and J. Stroth, "Thermal Dileptons from Coarse-Grained Transport as Fireball Probes at SIS Energies," *Eur. Phys. J.* **A52** no. 5, (2016) 131, arXiv:1512.08688 [nucl-th]. Cited on page(s): 19

[87] S. Endres, H. van Hees, J. Weil, and M. Bleicher, "Dilepton production and reaction dynamics in heavy-ion collisions at SIS energies from coarse-grained transport simulations," *Phys. Rev.* **C92** no. 1, (2015) 014911, arXiv:1505.06131 [nucl-th]. Cited on page(s): 19

[88] **CERES** Collaboration, G. Agakichiev *et al.*, "Enhanced production of low mass electron pairs in 200-GeV/u S - Au collisions at the CERN SPS," *Phys. Rev. Lett.* **75** (1995) 1272–1275. Cited on page(s): 20

[89] **NA38** Collaboration, C. Lourenco *et al.*, "J / psi, psi-prime and muon pair production in p - W and S - U collisions," *Nucl. Phys.* **A566** (1994) 77C–85C. Cited on page(s): 20

[90] **CERES/NA45** Collaboration, G. Agakishiev *et al.*, "Low mass e+ e- pair production in 158/A-GeV Pb - Au collisions at the CERN SPS, its dependence on multiplicity and transverse momentum," *Phys. Lett.* **B422** (1998) 405–412, arXiv:nucl-ex/9712008 [nucl-ex]. Cited on page(s): 20

[91] **CERES/NA45** Collaboration, D. Adamova *et al.*, "Enhanced production of low mass electron pairs in 40-AGeV Pb - Au collisions at the CERN SPS," *Phys. Rev. Lett.* **91** (2003) 042301, arXiv:nucl-ex/0209024 [nucl-ex]. Cited on page(s): 20

[92] G.-Q. Li, C. M. Ko, and G. E. Brown, "Enhancement of low mass dileptons in heavy ion collisions," *Phys. Rev. Lett.* **75** (1995) 4007–4010, arXiv:nucl-th/9504025 [nucl-th]. Cited on page(s): 20

[93] R. Rapp, G. Chanfray, and J. Wambach, "Medium modifications of the rho meson at CERN SPS energies," *Phys. Rev. Lett.* **76** (1996) 368–371, arXiv:hep-ph/9508353 [hep-ph]. Cited on page(s): 20

[94] **CERES** Collaboration, G. Agakichiev *et al.*, "e+ e- pair production in Pb - Au collisions at 158-GeV per nucleon," *Eur. Phys. J.* **C41** (2005) 475–513, arXiv:nucl-ex/0506002 [nucl-ex]. Cited on page(s): 20

[95] **HELIOS** Collaboration, M. Masera, "Dimuon production below mass 3.1-GeV/c**2 in p W and S W interactions at 200-A/GeV/c," *Nucl. Phys.* **A590** (1995) 93C–102C. Cited on page(s): 20

[96] **HELIOS/3** Collaboration, A. L. S. Angelis *et al.*, "Excess of continuum dimuon production at masses between threshold and the J / Psi in S - W interactions at 200-GeV/c/nucleon," *Eur. Phys. J.* **C13** (2000) 433–452. Cited on page(s): 20

[97] **NA50** Collaboration, E. Scomparin *et al.*, "Intermediate mass muon pair continuum in Pb Pb collisions at 158-GeV/c," *Nucl. Phys.* **A610** (1996) 331C–341C. Cited on page(s): 20

[98] **NA60** Collaboration, R. Arnaldi *et al.*, "First measurement of the rho spectral function in high-energy nuclear collisions," *Phys. Rev. Lett.* **96** (2006) 162302, arXiv:nucl-ex/0605007 [nucl-ex]. Cited on page(s): 21

[99] **NA60** Collaboration, R. Shahoyan, "Evidence for the production of thermal dimuons with masses above 1-GeV/c**2 in 158A-GeV In-In collisions," *Nucl. Phys.* **A827** (2009) 353C–355C. [,507(2009)]. Cited on page(s): 21, 22

[100] **NA60** Collaboration, S. Damjanovic *et al.*, "NA60 results on the rho spectral function in In-In collisions," *Nucl. Phys.* **A783** (2007) 327–334, arXiv:nucl-ex/0701015 [nucl-ex]. Cited on page(s): 21

[101] **NA60** Collaboration, R. Arnaldi *et al.*, "NA60 results on thermal dimuons," *Eur. Phys. J.* **C61** (2009) 711–720, arXiv:0812.3053 [nucl-ex]. Cited on page(s): 21

[102] **NA60** Collaboration, R. Arnaldi *et al.*, "Evidence for radial flow of thermal dileptons in high-energy nuclear collisions," *Phys. Rev. Lett.* **100** (2008) 022302, arXiv:0711.1816 [nucl-ex]. Cited on page(s): 21, 25

[103] H. van Hees and R. Rapp, "Dilepton Radiation at the CERN Super Proton Synchrotron," *Nucl. Phys.* **A806** (2008) 339–387, arXiv:0711.3444 [hep-ph]. Cited on page(s): 22

[104] J. Ruppert, C. Gale, T. Renk, P. Lichard, and J. I. Kapusta, "Low mass dimuons produced in relativistic nuclear collisions," *Phys. Rev. Lett.* **100** (2008) 162301, arXiv:0706.1934 [hep-ph]. Cited on page(s): 22

[105] K. Dusling, D. Teaney, and I. Zahed, "Thermal dimuon yields at NA60," *Phys. Rev.* **C75** (2007) 024908, arXiv:nucl-th/0604071 [nucl-th]. Cited on page(s): 22

[106] T. Renk and J. Ruppert, "Dimuon transverse momentum spectra as a tool to characterize the emission region in heavy-ion collisions," *Phys. Rev.* **C77** (2008) 024907, arXiv:hep-ph/0612113 [hep-ph]. Cited on page(s): 22

[107] D. Adamova *et al.*, "Modification of the rho-meson detected by low-mass electron-positron pairs in central Pb-Au collisions at 158-A-GeV/c," *Phys. Lett.* **B666** (2008) 425–429, arXiv:nucl-ex/0611022 [nucl-ex]. Cited on page(s): 22

[108] **PHENIX** Collaboration, A. Adare *et al.*, "Dilepton mass spectra in pp collisions at $\sqrt{s} = 200\ \mathrm{GeV}$ and the contribution from open charm," *Phys. Lett. B* **670** (2009) 313, arXiv:0802.0050 [hep-ex]. Cited on page(s): 22, 28, 88

[109] **STAR** Collaboration, L. Adamczyk *et al.*, "Di-electron spectrum at mid-rapidity in $p + p$ collisions at $\sqrt{s} = 200$ GeV," *Phys. Rev.* **C86** (2012) 024906, arXiv:1204.1890 [nucl-ex]. Cited on page(s): 22

[110] **PHENIX** Collaboration, A. Adare *et al.*, "Cross section for $\mathrm{b\bar{b}}$ production via dielectrons in d–Au collisions at $\sqrt{s_{\mathrm{NN}}} = 200\ \mathrm{GeV}$," *Phys. Rev. C* **91** (2015) 014907, arXiv:1405.4004 [nucl-ex]. Cited on page(s): 22, 28

[111] **PHENIX** Collaboration, A. Adare *et al.*, "Measurements of $\mathrm{e^+e^-}$ pairs from open heavy flavor in pp and dA collisions at $\sqrt{s_{\mathrm{NN}}} = 200\ \mathrm{GeV}$," *Phys. Rev. C* **96** (2017) 024907, arXiv:1702.01084 [nucl-ex]. Cited on page(s): 22, 23, 28, 138

[112] **PHENIX** Collaboration, A. Adare *et al.*, "Direct photon production in d+Au collisions at $\sqrt{s_{NN}} = 200$ GeV," *Phys. Rev.* **C87** (2013) 054907, arXiv:1208.1234 [nucl-ex]. Cited on page(s): 23

[113] **PHENIX** Collaboration, A. Adare *et al.*, "Dielectron production in Au+Au collisions at $\sqrt{s_{NN}}$=200 GeV," *Phys. Rev.* **C93** no. 1, (2016) 014904, arXiv:1509.04667 [nucl-ex]. Cited on page(s): 23, 24, 26

[114] **STAR** Collaboration, L. Adamczyk *et al.*, "Dielectron Mass Spectra from Au+Au Collisions at $\sqrt{s_{\mathrm{NN}}}$ = 200 GeV," *Phys. Rev. Lett.* **113** no. 2, (2014) 022301, arXiv:1312.7397 [hep-ex]. [Addendum: Phys. Rev. Lett.113,no.4,049903(2014)]. Cited on page(s): 23, 26

[115] **STAR** Collaboration, L. Adamczyk *et al.*, "Measurements of Dielectron Production in Au+Au Collisions at $\sqrt{s_{\mathrm{NN}}}$ = 200 GeV from the STAR Experiment," *Phys. Rev.* **C92** no. 2, (2015) 024912, arXiv:1504.01317 [hep-ex]. Cited on page(s): 23, 26

[116] O. Linnyk, W. Cassing, J. Manninen, E. L. Bratkovskaya, and C. M. Ko, "Analysis of dilepton production in Au+Au collisions at $\sqrt{s_{NN}} = 200$ GeV within the Parton-Hadron-String Dynamics (PHSD) transport approach," *Phys. Rev.* **C85** (2012) 024910, arXiv:1111.2975 [nucl-th]. Cited on page(s): 23

[117] **PHENIX** Collaboration, A. Adare *et al.*, "Centrality dependence of low-momentum direct-photon production in Au+Au collisions at $\sqrt{s_{_{NN}}} = 200$ GeV," *Phys. Rev.* **C91** no. 6, (2015) 064904, arXiv:1405.3940 [nucl-ex]. Cited on page(s): 24

[118] R. Rapp, "Signatures of thermal dilepton radiation at RHIC," *Phys. Rev.* **C63** (2001) 054907, arXiv:hep-ph/0010101 [hep-ph]. Cited on page(s): 24, 30

[119] K. Dusling and I. Zahed, "Low mass dilepton radiation at RHIC," *Nucl. Phys.* **A825** (2009) 212–221, arXiv:0712.1982 [nucl-th]. Cited on page(s): 24

[120] W. Liu and R. Rapp, "Low-energy thermal photons from meson-meson bremsstrahlung," *Nucl. Phys.* **A796** (2007) 101–121, arXiv:nucl-th/0604031 [nucl-th]. Cited on page(s): 24

[121] C. Shen, U. W. Heinz, J.-F. Paquet, and C. Gale, "Thermal photons as a quark-gluon plasma thermometer reexamined," *Phys. Rev.* **C89** no. 4, (2014) 044910, arXiv:1308.2440 [nucl-th]. Cited on page(s): 24, 27

[122] D. G. d'Enterria and D. Peressounko, "Probing the QCD equation of state with thermal photons in nucleus-nucleus collisions at RHIC," *Eur. Phys. J.* **C46** (2006) 451–464, arXiv:nucl-th/0503054 [nucl-th]. Cited on page(s): 24

[123] **PHENIX** Collaboration, A. Adare *et al.*, "Observation of direct-photon collective flow in $\sqrt{s_{NN}} = 200$ GeV Au+Au collisions," *Phys. Rev. Lett.* **109** (2012) 122302, arXiv:1105.4126 [nucl-ex]. Cited on page(s): 25

[124] **PHENIX** Collaboration, A. Adare *et al.*, "Azimuthally anisotropic emission of low-momentum direct photons in Au+Au collisions at $\sqrt{s_{_{NN}}} = 200$ GeV," *Phys. Rev.* **C94** no. 6, (2016) 064901, arXiv:1509.07758 [nucl-ex]. Cited on page(s): 25

[125] H. van Hees, C. Gale, and R. Rapp, "Thermal Photons and Collective Flow at the Relativistic Heavy-Ion Collider," *Phys. Rev.* **C84** (2011) 054906, arXiv:1108.2131 [hep-ph]. Cited on page(s): 25

[126] R. Chatterjee, E. S. Frodermann, U. W. Heinz, and D. K. Srivastava, "Elliptic flow of thermal photons in relativistic nuclear collisions," *Phys. Rev. Lett.* **96** (2006) 202302, arXiv:nucl-th/0511079 [nucl-th]. Cited on page(s): 25

[127] O. Linnyk, W. Cassing, and E. L. Bratkovskaya, "Centrality dependence of the direct photon yield and elliptic flow in heavy-ion collisions at $\sqrt{s_{NN}} = 200$ GeV," *Phys. Rev.* **C89** no. 3, (2014) 034908, arXiv:1311.0279 [nucl-th]. Cited on page(s): 25

[128] G. Basar, D. Kharzeev, D. Kharzeev, and V. Skokov, "Conformal anomaly as a source of soft photons in heavy ion collisions," *Phys. Rev. Lett.* **109** (2012) 202303, arXiv:1206.1334 [hep-ph]. Cited on page(s): 25

[129] K. Tuchin, "Electromagnetic radiation by quark-gluon plasma in a magnetic field," *Phys. Rev.* **C87** no. 2, (2013) 024912, arXiv:1206.0485 [hep-ph]. Cited on page(s): 25

[130] S. Turbide, C. Gale, and R. J. Fries, "Azimuthal Asymmetry of Direct Photons in High Energy Nuclear Collisions," *Phys. Rev. Lett.* **96** (2006) 032303, arXiv:hep-ph/0508201 [hep-ph]. Cited on page(s): 25

[131] **STAR** Collaboration, L. Adamczyk *et al.*, "Energy dependence of acceptance-corrected dielectron excess mass spectrum at mid-rapidity in Au+Au collisions at $\sqrt{s_{NN}} = 19.6$ and 200 GeV," *Phys. Lett.* **B750** (2015) 64–71, arXiv:1501.05341 [hep-ex]. Cited on page(s): 25

[132] R. Rapp and H. van Hees, "Thermal Dileptons as Fireball Thermometer and Chronometer," *Phys. Lett.* **B753** (2016) 586–590, arXiv:1411.4612 [hep-ph]. Cited on page(s): 25

[133] **STAR** Collaboration, P. Huck, "Beam Energy Dependence of Dielectron Production in Au + Au Collisions from STAR at RHIC," *Nucl. Phys.* **A931** (2014) 659–664, arXiv:1409.5675 [nucl-ex]. Cited on page(s): 25

[134] **NA60** Collaboration, R. Arnaldi *et al.*, "Evidence for the production of thermal-like muon pairs with masses above 1-GeV/c**2 in 158-A-GeV Indium-Indium Collisions," *Eur. Phys. J.* **C59** (2009) 607–623, arXiv:0810.3204 [nucl-ex]. Cited on page(s): 25

[135] **STAR** Collaboration, J. Adam *et al.*, "Low-p_T e^+e^- pair production in Au+Au collisions at $\sqrt{s_{NN}} = 200$ GeV and U+U collisions at $\sqrt{s_{NN}} = 193$ GeV at STAR," arXiv:1806.02295 [hep-ex]. Cited on page(s): 26

[136] **ALICE** Collaboration, B. Abelev *et al.*, "Measurement of charm production at central rapidity in proton–proton collisions at $\sqrt{s} = 2.76$ TeV," *JHEP* **07** (2012) 191, arXiv:1205.4007 [hep-ex]. Cited on page(s): 26

[137] **ALICE** Collaboration, B. Abelev *et al.*, "Beauty production in pp collisions at $\sqrt{s} = 2.76$ TeV measured via semi-electronic decays," *Phys. Lett. B* **738** (2014) 97, arXiv:1405.4144 [nucl-ex]. [Erratum: Phys. Lett. B 763 (2016) 507]. Cited on page(s): 26

[138] **ALICE** Collaboration, B. Abelev *et al.*, "Measurement of electrons from semileptonic heavy-flavor hadron decays in pp collisions at $\sqrt{s} = 2.76$ TeV," *Phys. Rev. D* **91** (2015) 012001, arXiv:1405.4117 [nucl-ex]. Cited on page(s): 26

[139] **ALICE** Collaboration, J. Adam *et al.*, "D-meson production in p–Pb collisions at $\sqrt{s_{\rm NN}} = 5.02$ TeV and in pp collisions at $\sqrt{s} = 7$ TeV," *Phys. Rev. C* **94** (2016) 054908, arXiv:1605.07569 [nucl-ex]. Cited on page(s): 26, 27, 132

[140] **ALICE** Collaboration, B. Abelev *et al.*, "Measurement of prompt J/ψ and beauty hadron production cross sections at mid-rapidity in pp collisions at $\sqrt{s} = 7$ TeV," *JHEP* **11** (2012) 065, arXiv:1205.5880 [hep-ex]. Cited on page(s): 26, 27, 94, 95

[141] **ALICE** Collaboration, B. Abelev *et al.*, "Measurement of electrons from beauty hadron decays in pp collisions at $\sqrt{s} = 7$ TeV," *Phys. Lett. B* **721** (2013) 13, arXiv:1208.1902 [hep-ex]. [Erratum: Phys. Lett. B 763 (2016) 507]. Cited on page(s): 26, 93, 94

[142] **ATLAS** Collaboration, G. Aad *et al.*, "Measurement of $\rm D^{*\pm}$, $\rm D^{\pm}$ and $\rm D_s^{\pm}$ meson production cross sections in pp collisions at $\sqrt{s} = 7$ TeV with the ATLAS detector," *Nucl. Phys. B* **907** (2016) 717, arXiv:1512.02913 [hep-ex]. Cited on page(s): 26, 132

[143] **CMS** Collaboration, V. Khachatryan *et al.*, "Measurement of the + production cross section in pp collisions at $\sqrt{s} = 7$ TeV," *Phys. Rev. Lett.* **106** (2011) 112001, arXiv:1101.0131 [hep-ex]. Cited on page(s): 26

[144] **CMS** Collaboration, V. Khachatryan *et al.*, "Inclusive b-hadron production cross section with muons in pp collisions at $\sqrt{s} = 7$ TeV," *JHEP* **03** (2011) 090, arXiv:1101.3512 [hep-ex]. Cited on page(s): 26

[145] **CMS** Collaboration, S. Chatrchyan *et al.*, "Measurement of the 0 production cross section in pp collisions at $\sqrt{s} = 7$ TeV," *Phys. Rev. Lett.* **106** (2011) 252001, arXiv:1104.2892 [hep-ex]. Cited on page(s): 26

[146] **CMS** Collaboration, S. Chatrchyan *et al.*, "J/ψ and ψ(2S) production in pp collisions at $\sqrt{s} = 7$ TeV," *JHEP* **02** (2012) 011, arXiv:1111.1557 [hep-ex]. Cited on page(s): 26

[147] **CMS** Collaboration, S. Chatrchyan *et al.*, "Suppression of non-prompt J/ψ, prompt J/ψ, and Υ(1S) in Pb–Pb collisions at $\sqrt{s_{\rm NN}} = 2.76$ TeV," *JHEP* **05** (2012) 063, arXiv:1201.5069 [nucl-ex]. Cited on page(s): 26

[148] **CMS** Collaboration, S. Chatrchyan *et al.*, "Measurement of the cross section for production of $\mathrm{b\bar{b}}X$, decaying to muons in pp collisions at $\sqrt{s} = 7$ TeV," *JHEP* **06** (2012) 110, arXiv:1203.3458 [hep-ex]. Cited on page(s): 26

[149] **CMS** Collaboration, A. M. Sirunyan *et al.*, "Measurement of the $\pm$ meson nuclear modification factor in Pb–Pb collisions at $\sqrt{s_{\mathrm{NN}}} = 5.02$ TeV," *Phys. Rev. Lett.* **119** (2017) 152301, arXiv:1705.04727 [hep-ex]. Cited on page(s): 26

[150] **CMS** Collaboration, A. M. Sirunyan *et al.*, "Nuclear modification factor of D^0 mesons in Pb–Pb collisions at $\sqrt{s_{\mathrm{NN}}} = 5.02$ TeV," arXiv:1708.04962 [nucl-ex]. Cited on page(s): 26

[151] **CMS** Collaboration, A. M. Sirunyan *et al.*, "Measurement of prompt and nonprompt charmonium suppression in PbPb collisions at 5.02 TeV," *Eur. Phys. J.* **C78** no. 6, (2018) 509, arXiv:1712.08959 [nucl-ex]. Cited on page(s): 26

[152] **LHCb** Collaboration, R. Aaij *et al.*, "Production of J/ψ and Υ mesons in pp collisions at $\sqrt{s} = 8$ TeV," *JHEP* **06** (2013) 064, arXiv:1304.6977 [hep-ex]. Cited on page(s): 26

[153] **LHCb** Collaboration, R. Aaij *et al.*, "Measurements of prompt charm production cross-sections in pp collisions at $\sqrt{s} = 13$ TeV," *JHEP* **03** (2016) 159, arXiv:1510.01707 [hep-ex]. [Erratum: JHEP05,074(2017)]. Cited on page(s): 26, 132

[154] **LHCb** Collaboration, R. Aaij *et al.*, "Measurements of prompt charm production cross-sections in pp collisions at $\sqrt{s} = 5$ TeV," *JHEP* **06** (2017) 147, arXiv:1610.02230 [hep-ex]. Cited on page(s): 26

[155] **LHCb** Collaboration, R. Aaij *et al.*, "Measurement of the b-quark production cross-section in 7 and 13 TeV pp collisions," *Phys. Rev. Lett.* **118** (2017) 052002, arXiv:1612.05140 [hep-ex]. [Erratum: Phys. Rev. Lett. 119 (2017) 169901]. Cited on page(s): 26

[156] **ALICE** Collaboration, S. Acharya *et al.*, "Direct photon elliptic flow in Pb-Pb collisions at $\sqrt{s_{\mathrm{NN}}}$ = 2.76 TeV," arXiv:1805.04403 [nucl-ex]. Cited on page(s): 28

[157] **ALICE** Collaboration, S. Acharya *et al.*, "Dielectron production in proton-proton collisions at $\sqrt{s} = 7$ TeV," arXiv:1805.04391 [hep-ex]. Cited on page(s): 28, 29, 88, 131, 132, 138

[158] **ALICE** Collaboration, S. Acharya *et al.*, "Dielectron and heavy-quark production in inelastic and high-multiplicity proton-proton collisions at $\sqrt{s_{\mathrm{NN}}} =$ 13 TeV," arXiv:1805.04407 [hep-ex]. Cited on page(s): 28

[159] **ALICE** Collaboration, S. Acharya *et al.*, "Measurement of dielectron production in central Pb-Pb collisions at $\sqrt{s_{\mathrm{NN}}} = 2.76$ TeV," arXiv:1807.00923 [nucl-ex]. Cited on page(s): 28, 30, 31

[160] R. Rapp, "Dilepton Spectroscopy of QCD Matter at Collider Energies," *Adv. High Energy Phys.* **2013** (2013) 148253, arXiv:1304.2309 [hep-ph]. Cited on page(s): 30

[161] T. Song, W. Cassing, P. Moreau, and E. Bratkovskaya, "Open charm and dileptons from relativistic heavy-ion collisions," *Phys. Rev.* **C97** no. 6, (2018) 064907, arXiv:1803.02698 [nucl-th]. Cited on page(s): 30

[162] **ALICE** Collaboration, P. Cortese *et al.*, "ALICE: Physics Performance Report, Volume I," *J. Phys. G* **30** (2004) 1517. Cited on page(s): 33, 37

[163] **ALICE** Collaboration, C. W. Fabjan *et al.*, "ALICE: Physics Performance Report, Volume II," *J. Phys. G* **32** (2006) 1295. Cited on page(s): 33, 43

[164] **ALICE** Collaboration, K. Aamodt *et al.*, "The ALICE experiment at the CERN LHC," *JINST* **3** (2008) S08002. Cited on page(s): 33, 38, 39, 41, 43, 45

[165] **ALICE** Collaboration, B. Abelev *et al.*, "Performance of the ALICE Experiment at the CERN LHC," *Int. J. Mod. Phys.* **A29** (2014) 1430044, arXiv:1402.4476 [nucl-ex]. Cited on page(s): 33, 42

[166] http://aliceinfo.cern.ch/Figure/. Last accessed: 2018-08-26. Cited on page(s): 34, 41, 44, 107

[167] R. Fruhwirth, "Application of Kalman filtering to track and vertex fitting," *Nucl. Instrum. Meth.* **A262** (1987) 444–450. Cited on page(s): 34

[168] **ALICE** Collaboration, K. Aamodt *et al.*, "Alignment of the ALICE Inner Tracking System with cosmic-ray tracks," *JINST* **5** (2010) P03003, arXiv:1001.0502 [physics.ins-det]. Cited on page(s): 36, 37

[169] **ALICE** Collaboration, J. Adam *et al.*, "Study of cosmic ray events with high muon multiplicity using the ALICE detector at the CERN Large Hadron Collider," *JCAP* **1601** (2016) 032, arXiv:1507.07577 [astro-ph.HE]. Cited on page(s): 36

[170] W. Blum, L. Rolandi, and W. Riegler, *Particle detection with drift chambers*. Particle Acceleration and Detection. 2008. http://www.springer.com/physics/elementary/book/978-3-540-76683-4. Cited on page(s): 40

[171] A. Akindinov *et al.*, "The multigap resistive plate chamber as a time-of-flight detector," *Nucl. Instrum. Meth.* **A456** (2000) 16–22. Cited on page(s): 42

[172] **ALICE** Collaboration, J. Adam *et al.*, "Determination of the event collision time with the ALICE detector at the LHC," *Eur. Phys. J. Plus* **132** (2017) 99, arXiv:1610.03055 [physics.ins-det]. Cited on page(s): 43

[173] http://aliqaevs.web.cern.ch/aliqaevs. Last accessed: 2018-08-26. Cited on page(s): 48, 50, 51

[174] T. Sjostrand, S. Mrenna, and P. Z. Skands, "PYTHIA 6.4 physics and manual," *JHEP* **05** (2006) 026, arXiv:hep-ph/0603175 [hep-ph]. Cited on page(s): 52, 74, 93

[175] T. Sjöstrand, S. Ask, J. R. Christiansen, R. Corke, N. Desai, P. Ilten, S. Mrenna, S. Prestel, C. O. Rasmussen, and P. Z. Skands, "An Introduction to PYTHIA 8.2," *Comput. Phys. Commun.* **191** (2015) 159–177, arXiv:1410.3012 [hep-ph]. Cited on page(s): 52, 74

[176] R. Brun, R. Hagelberg, M. Hansroul, and J. C. Lassalle, *Simulation program for particle physics experiments, GEANT: User guide and reference manual*. CERN, Geneva, 1978. https://cds.cern.ch/record/118715. Cited on page(s): 52, 74

[177] P. Skands, S. Carrazza, and J. Rojo, "Tuning PYTHIA 8.1: the Monash 2013 Tune," *Eur. Phys. J. C* **74** (2014) 3024, arXiv:1404.5630 [hep-ph]. Cited on page(s): 74

[178] P. Z. Skands, "Tuning Monte Carlo generators: The Perugia tunes," *Phys. Rev. D* **82** (2010) 074018, arXiv:1005.3457 [hep-ph]. Cited on page(s): 74, 93

[179] **ALICE** Collaboration, "Production of $\omega(782)$ in pp collisions at $\sqrt{s} = 7$ TeV," May, 2018, ALICE-PUBLIC-2018-004. https://cds.cern.ch/record/2316785. Cited on page(s): 74, 89, 91

[180] **ALICE** Collaboration, S. Acharya *et al.*, "Production of the $\rho(770)^0$ meson in pp and Pb-Pb collisions at $\sqrt{s_{\rm NN}} = 2.76$ TeV," arXiv:1805.04365 [nucl-ex]. Cited on page(s): 74, 89, 91

[181] **ALICE** Collaboration, "Momentum transformation matrix for dielectron simulations in Pb-Pb collisions at $\sqrt{s_{\mathrm{NN}}} = 2.76$ TeV,". https://cds.cern.ch/record/2289779. Cited on page(s): 76

[182] A. Dashi, "Constraining heavy flavour production with dielectrons in pp collisions at $\sqrt{s} = 13$ TeV," Master's thesis, Technische Universität München, April, 2018. Cited on page(s): 83, 129, 138

[183] **LHCb** Collaboration, R. Aaij *et al.*, "Observation of $D^0 - \overline{D}^0$ oscillations," *Phys. Rev. Lett.* **110** no. 10, (2013) 101802, arXiv:1211.1230 [hep-ex]. Cited on page(s): 83

[184] **LHCb** Collaboration, R. Aaij *et al.*, "Updated determination of D^0-$\overline{D}^0$ mixing and CP violation parameters with $D^0 \to K^+\pi^-$ decays," *Phys. Rev.* **D97** no. 3, (2018) 031101, arXiv:1712.03220 [hep-ex]. Cited on page(s): 83

[185] **ALICE** Collaboration, S. Acharya *et al.*, "Transverse momentum spectra and nuclear modification factors of charged particles in pp, p–Pb and Pb–Pb collisions at the LHC," arXiv:1802.09145 [nucl-ex]. Cited on page(s): 89, 90

[186] **ALICE** Collaboration, B. Abelev *et al.*, "Energy dependence of the transverse momentum distributions of charged particles in pp collisions measured by ALICE," *Eur. Phys. J. C* **73** (2013) 2662, arXiv:1307.1093 [nucl-ex]. Cited on page(s): 89, 90

[187] **ALICE** Collaboration, J. Adam *et al.*, "Multiplicity dependence of charged pion, kaon, and (anti)proton production at large transverse momentum in p–Pb collisions at $\sqrt{s_{\mathrm{NN}}} = 5.02$ TeV," *Phys. Lett. B* **760** (2016) 720, arXiv:1601.03658 [nucl-ex]. Cited on page(s): 89, 90

[188] **ALICE** Collaboration, B. Abelev *et al.*, "Production of charged pions, kaons and protons at large transverse momenta in pp and Pb–Pb collisions at $\sqrt{s_{\mathrm{NN}}} = 2.76$ TeV," *Phys. Lett. B* **736** (2014) 196, arXiv:1401.1250 [nucl-ex]. Cited on page(s): 89, 90

[189] **ALICE** Collaboration, B. Abelev *et al.*, "Neutral pion and η meson production in pp collisions at $\sqrt{s} = 0.9$ TeV and $\sqrt{s} = 7$ TeV," *Phys. Lett. B* **717** (2012) 162, arXiv:1205.5724 [hep-ex]. Cited on page(s): 89, 91

[190] L. Altenkämper, F. Bock, C. Loizides, and N. Schmidt, "Applicability of transverse mass scaling in hadronic collisions at energies available at the CERN Large Hadron Collider," *Phys. Rev. C* **96** (2017) 064907, arXiv:1710.01933 [hep-ph]. Cited on page(s): 89, 91

[191] **ALICE** Collaboration, B. Abelev *et al.*, "Production of $K^*(892)^0$ and $\phi(1020)$ in pp collisions at $\sqrt{s} = 7$ TeV," *Eur. Phys. J. C* **72** (2012) 2183, arXiv:1208.5717 [hep-ex]. Cited on page(s): 89, 91

[192] **NA60** Collaboration, R. Arnaldi *et al.*, "Precision study of the $\eta \to \mu^+\mu^-\gamma$ and $\omega \to \mu^+\mu^-\pi^0$ electromagnetic transition form-factors and of the $\rho \to \mu^+\mu^-$ line shape in NA60," *Phys. Lett.* **B757** (2016) 437–444, arXiv:1608.07898 [hep-ex]. Cited on page(s): 88

[193] **NA60** Collaboration, R. Arnaldi *et al.*, "Study of the electromagnetic transition form-factors in eta —> mu+ mu- gamma and omega —> mu+ mu- pi0 decays with NA60," *Phys. Lett.* **B677** (2009) 260–266, arXiv:0902.2547 [hep-ph]. Cited on page(s): 88

[194] G. J. Gounaris and J. J. Sakurai, "Finite width corrections to the vector meson dominance prediction for rho —> e+ e-," *Phys. Rev. Lett.* **21** (1968) 244–247. Cited on page(s): 88

[195] J. Knoll, "Transport dynamics of broad resonances," *Prog. Part. Nucl. Phys.* **42** (1999) 177–186, arXiv:nucl-th/9811099 [nucl-th]. [,177(1998)]. Cited on page(s): 90

[196] P. K. Khandai, P. Sett, P. Shukla, and V. Singh, "Transverse Mass Spectra and Scaling of Hadrons at RHIC and LHC Energies," arXiv:1205.0648 [hep-ph]. Cited on page(s): 90

[197] P. Nason, "A new method for combining NLO QCD with shower Monte Carlo algorithms," *JHEP* **11** (2004) 040, arXiv:hep-ph/0409146 [hep-ph]. Cited on page(s): 93

[198] S. Frixione, P. Nason, and G. Ridolfi, "A positive-weight next-to-leading-order Monte Carlo for heavy flavour hadroproduction," *JHEP* **09** (2007) 126, arXiv:0707.3088 [hep-ph]. Cited on page(s): 93, 94

[199] S. Frixione, P. Nason, and C. Oleari, "Matching NLO QCD computations with Parton Shower simulations: the POWHEG method," *JHEP* **11** (2007) 070, arXiv:0709.2092 [hep-ph]. Cited on page(s): 93

[200] S. Alioli, P. Nason, C. Oleari, and E. Re, "A general framework for implementing NLO calculations in shower Monte Carlo programs: The POWHEG BOX," *JHEP* **06** (2010) 043, arXiv:1002.2581 [hep-ph]. Cited on page(s): 93, 94

[201] **CTEQ** Collaboration, H. L. Lai, J. Huston, S. Kuhlmann, J. Morfin, F. I. Olness, J. F. Owens, J. Pumplin, and W. K. Tung, "Global QCD analysis of parton

structure of the nucleon: CTEQ5 parton distributions," *Eur. Phys. J.* **C12** (2000) 375–392, arXiv:hep-ph/9903282 [hep-ph]. Cited on page(s): 94

[202] P. M. Nadolsky, H.-L. Lai, Q.-H. Cao, J. Huston, J. Pumplin, D. Stump, W.-K. Tung, and C. P. Yuan, "Implications of CTEQ global analysis for collider observables," *Phys. Rev.* **D78** (2008) 013004, arXiv:0802.0007 [hep-ph]. Cited on page(s): 94

[203] R. Averbeck, N. Bastid, Z. C. del Valle, P. Crochet, A. Dainese, and X. Zhang, "Reference heavy flavour cross sections in pp collisions at $\sqrt{s} = 2.76$ TeV, using a pQCD-driven $\sqrt{s}$-scaling of ALICE measurements at $\sqrt{s} = 7$ TeV," arXiv:1107.3243 [hep-ph]. Cited on page(s): 94

[204] M. Cacciari, M. L. Mangano, and P. Nason, "Gluon PDF constraints from the ratio of forward heavy-quark production at the LHC at $\sqrt{s} = 7$ and 13 TeV," *Eur. Phys. J. C* **75** (2015) 610, arXiv:1507.06197 [hep-ph]. Cited on page(s): 94

[205] **ALICE** Collaboration, S. Acharya *et al.*, "Λ_c^+ production in pp collisions at $\sqrt{s} = 7$ TeV and in p–Pb collisions at $\sqrt{s_{NN}} = 5.02$ TeV," arXiv:1712.09581 [nucl-ex]. Cited on page(s): 94

[206] L. Gladilin, "Fragmentation fractions of c and b quarks into charmed hadrons at LEP," *Eur. Phys. J. C* **75** (2015) 19, arXiv:1404.3888 [hep-ex]. Cited on page(s): 94

[207] **ALICE** Collaboration, K. Aamodt *et al.*, "Rapidity and transverse momentum dependence of inclusive J/ψ production in pp collisions at $\sqrt{s} = 7$ TeV," *Phys. Lett. B* **704** (2011) 442, arXiv:1105.0380 [hep-ex]. [Erratum: Phys. Lett. B 718 (2012) 692]. Cited on page(s): 95

[208] **ALICE** Collaboration, J. Adam *et al.*, "Inclusive quarkonium production at forward rapidity in pp collisions at $\sqrt{s} = 8$ TeV," *Eur. Phys. J.* **C76** no. 4, (2016) 184, arXiv:1509.08258 [hep-ex]. Cited on page(s): 95

[209] **ALICE** Collaboration, J. Adam *et al.*, "Measurement of pion, kaon and proton production in pp collisions at $\sqrt{s} = 7\,TeV$," *Eur. Phys. J. C* **75** (2016) 226, arXiv:1504.00024 [nucl-ex]. Cited on page(s): 96, 97

[210] M. Floris private communication. Cited on page(s): 100

[211] **ALICE** Collaboration, "ALICE luminosity determination for pp collisions at $\sqrt{s} = 13$ TeV," Public Note, Jun, 2016. https://cds.cern.ch/record/2160174. Cited on page(s): 114

[212] **ALICE** Collaboration, B. Abelev *et al.*, "Multiplicity dependence of pion, kaon, proton and lambda production in p–Pb collisions at $\sqrt{s_{\rm NN}} = 5.02$ TeV," *Phys. Lett. B* **728** (2014) 25, arXiv:1307.6796 [nucl-ex]. Cited on page(s): 116

[213] **ALICE** Collaboration, C. Jahnke, "J/ψ production as a function of event multiplicity in pp collisions at $\sqrt{s} = 13$ TeV using EMCal-triggered events with ALICE at the LHC," in *14th International Workshop on Hadron Physics (Hadron Physics 2018) Florianopolis, Santa Catarina, Brazil, March 18-23, 2018*. 2018. arXiv:1805.00841 [hep-ex]. https://inspirehep.net/record/1671075/files/1805.00841.pdf. Cited on page(s): 126

[214] L. E. Gordon and W. Vogelsang, "Polarized and unpolarized prompt photon production beyond the leading order," *Phys. Rev. D* **48** (1993) 3136. Cited on page(s): 133, 136

[215] H.-L. Lai, M. Guzzi, J. Huston, Z. Li, P. M. Nadolsky, J. Pumplin, and C. P. Yuan, "New parton distributions for collider physics," *Phys. Rev.* **D82** (2010) 074024, arXiv:1007.2241 [hep-ph]. Cited on page(s): 133

[216] J. Gao, M. Guzzi, J. Huston, H.-L. Lai, Z. Li, P. Nadolsky, J. Pumplin, D. Stump, and C. P. Yuan, "CT10 next-to-next-to-leading order global analysis of QCD," *Phys. Rev.* **D89** no. 3, (2014) 033009, arXiv:1302.6246 [hep-ph]. Cited on page(s): 133

[217] M. Guzzi, P. Nadolsky, E. Berger, H.-L. Lai, F. Olness, and C. P. Yuan, "CT10 parton distributions and other developments in the global QCD analysis," arXiv:1101.0561 [hep-ph]. Cited on page(s): 133

[218] G. J. Feldman and R. D. Cousins, "Unified approach to the classical statistical analysis of small signals," *Phys. Rev. D* **57** (1998) 3873, arXiv:physics/9711021 [physics.data-an]. Cited on page(s): 136

[219] **ALICE** Collaboration, B. Abelev *et al.*, "Upgrade of the ALICE Experiment: Letter Of Intent," *J. Phys.* **G41** (2014) 087001. Cited on page(s): 138

[220] P. Buncic, M. Krzewicki, and P. Vande Vyvre, "Technical Design Report for the Upgrade of the Online-Offline Computing System," Tech. Rep. CERN-LHCC-2015-006. ALICE-TDR-019, Apr, 2015. https://cds.cern.ch/record/2011297. Cited on page(s): 139

[221] **ALICE** Collaboration, "Upgrade of the ALICE Time Projection Chamber," Tech. Rep. CERN-LHCC-2013-020. ALICE-TDR-016, Oct, 2013. https://cds.cern.ch/record/1622286. Cited on page(s): 139

[222] **ALICE** Collaboration, "Addendum to the Technical Design Report for the Upgrade of the ALICE Time Projection Chamber," Tech. Rep. CERN-LHCC-2015-002. ALICE-TDR-016-ADD-1, Feb, 2015. https://cds.cern.ch/record/1984329. Cited on page(s): 139

[223] L. Musa, "Upgrade of the Inner Tracking System Conceptual Design Report. Conceptual Design Report for the Upgrade of the ALICE ITS," Tech. Rep. CERN-LHCC-2012-013. LHCC-P-005, CERN, Geneva, Aug, 2012. https://cds.cern.ch/record/1475244. Cited on page(s): 139

Appendices

A
Kinematic Variables

This Appendix introduces relevant kinematic variables used throughout this thesis. If not stated otherwise, in the following the natural units of $\hbar = c = k_B = 1$ are used. Only the case of particle collision going in opposite directions is considered.

In general, any particle can be described by its 4-momentum vector defined as:

$$p^\mu = (p^0, p^1, p^2, p^3) = (E, \vec{p}), \tag{A.1}$$

where E and $\vec{p} = (p_x, p_y, p_z)$ are particle's energy and momentum, a superscript (subscript) denotes the contravariant (covariant) variables, and axes x, y and z defines the coordinate system. A natural choice of such a system in a collision of two particles is the one with the z axis along the beam (particle) direction. The particle's momentum transverse to the beam direction is then $\vec{p}_{\mathrm{T}} = (p_x, p_y)$, with an absolute value of $p_{\mathrm{T}} = \sqrt{p_x^2 + p_y^2}$. The Lorentz transformation between two frames with relative velocity v leads to a change of particle's 4-momentum $p = (E, \vec{p}_{\mathrm{T}}, p_z) \rightarrow p' = (E', \vec{p}_{\mathrm{T}}{}', p_z{}')$ according to:

$$E' = \gamma(E - \beta p_z), \tag{A.2}$$
$$p_z{}' = \gamma(p_z - \beta E), \tag{A.3}$$
$$\vec{p}_{\mathrm{T}}{}' = \vec{p}_{\mathrm{T}}, \tag{A.4}$$

where $\beta = v/c$ and $\gamma = 1/\sqrt{1-\beta^2}$ is the Lorentz factor. The transverse momentum $\vec{p}_{\mathrm{T}}$ and the transverse mass defined as $m_{\mathrm{T}} = \sqrt{m^2 + p_{\mathrm{T}}^2}$ are Lorentz invariant under

longitudinal transformation along axis z, so therefore these variables are useful for the studies of particle production in various experiments. Another essential characteristic of each particle is its rapidity y defined as:

$$y = \frac{1}{2} \ln \frac{E + p_z}{E - p_z}, \tag{A.5}$$

which for small velocities when $p_z \ll E$ approaches $y \approx \beta_{\mathrm{L}} = p_z/E$. Under Lorentz transformations $y \to y'$ rapidity possesses a simple transformation property. Consider a laboratory system S and a system S' moving along the z axis with a relative velocity $\beta \equiv \beta_{S'}$ and an object with rapidity y' measured in S', then:

$$y = \frac{1}{2} \ln \frac{E + p_z}{E - p_z} = \frac{1}{2} \ln \frac{\gamma(E' + \beta {p_z}') + \gamma({p_z}' + \beta E')}{\gamma(E' + \beta {p_z}') - \gamma({p_z}' + \beta E')} = \frac{1}{2} \ln \frac{(1+\beta)(E' + {p_z}')}{(1-\beta)(E' - {p_z}')}$$

$$= \frac{1}{2} \ln \frac{1+\beta}{1-\beta} + \frac{1}{2} \ln \frac{E' + {p_z}'}{E' - {p_z}'}, \tag{A.6}$$

i. e. $y = y' + y_{S'}$. In experiment, however, the measurement of y requires the knowledge about particle mass m, so instead another variable called pseudorapidity η is widely used. It is defined through the polar angle θ between the particle 3-momentum $\vec{p}$ and the beam axis as:

$$\eta = -\ln \left(\tan \left(\frac{\theta}{2} \right) \right). \tag{A.7}$$

Pseudorapidity η therefore amounts to zero for particles produced at $\theta = 90^\circ$ and tends towards infinity for small angles. For massless particles $\eta = y$, which is also approximately true for particles with $|\vec{p}| \gg m$:

$$y = \frac{1}{2} \ln \frac{E + |\vec{p}| \cos\theta}{E - |\vec{p}| \cos\theta} \approx \frac{1}{2} \ln \frac{1 + \cos\theta}{1 - \cos\theta} = \frac{1}{2} \ln \frac{2\cos^2 \theta/2}{2\sin^2 \theta/2} = -\ln \tan \frac{\theta}{2} = \eta \tag{A.8}$$

In a collision of two particles with momenta $\vec{p}_1$ and $\vec{p}_2$ one can always choose a frame in which $\vec{p}_1 = -\vec{p}_2$, i. e. the centre-of-mass frame CM. The Lorentz-invariant Mandelstam variable s is defined as:

$$s = (p_1 + p_2)^2 = \left(E_1^{\mathrm{CM}} + E_2^{\mathrm{CM}}\right)^2, \tag{A.9}$$

where $p_1 = (E_1, \vec{p}_1)$ and $p_2 = (E_2, \vec{p}_2)$ are the particle 4-momenta. Therefore, $\sqrt{s}$ represents the total energy available in a collision in the centre-of-mass frame. For fixed-target experiments, when a particle 1 with $p_1 = (E_1^{lab}, \vec{p}_1^{\,\mathrm{lab}})$ collides with a target particle 2 $p_2 = (m_2, 0)$, s equals to:

$$\begin{aligned} s &= \left[\begin{pmatrix} E_1^{\mathrm{lab}} \\ \vec{p}_1^{\,\mathrm{lab}} \end{pmatrix} + \begin{pmatrix} m_2 \\ \vec{0} \end{pmatrix} \right]^2 = (E_1^{\mathrm{lab}})^2 + 2E_1^{\mathrm{lab}} m_2 + m_2^2 - (\vec{p}_1^{\,\mathrm{lab}})^2 = \\ &= m_1^2 + m_2^2 + 2E_1^{\mathrm{lab}} m_2. \end{aligned} \tag{A.10}$$

The total energy available in a collision in the centre-of-mass frame is:

$$\sqrt{s} = \sqrt{m_1^2 + m_2^2 + 2E_1^{\mathrm{lab}} m_2} \tag{A.11}$$

For collider experiments the incoming particles can be described with $p_1 = (E_1, \vec{p}_1)$ and $p_1 = (E_2, \vec{p}_2)$, therefore:

$$\begin{aligned} s &= \left[\begin{pmatrix} E_1 \\ \vec{p}_1 \end{pmatrix} + \begin{pmatrix} E_2 \\ \vec{p}_2 \end{pmatrix} \right]^2 = E_1^2 + 2E_1E_2 + E_2^2 - (\vec{p}_1^{\,2} + 2\vec{p}_1\vec{p}_2 + \vec{p}_2^{\,2}) \\ &= m_1^2 + m_2^2 + 2E_1E_2 - 2\vec{p}_1\vec{p}_2. \end{aligned} \tag{A.12}$$

For $m_1 = m_2$ the centre-of-mass frame $\vec{p}_1 = -\vec{p}_2$ in such a collision is the same as the laboratory frame, and $\sqrt{s} = 2E_1 = 2E_2 = 2E$.

For a direct comparison with nucleon–nucleon collisions such as pp, it is useful to normalise the centre-of-mass energy $\sqrt{s}$ available in heavy-ion collisions by the number of nucleon–nucleon pairs, i. e. $\sqrt{s_{\mathrm{NN}}} = \sqrt{s}/A$, where A denotes the atomic number of a nucleus, e. g. for Pb it amounts to $A = 208$.

The invariant mass of the parent particle decaying into two daughters with E_1, $\vec{p}_1$ and E_2, $\vec{p}_2$ is the sum of their 4-momenta squared:

$$\begin{aligned} m_{\mathrm{parent}}^2 = s &= \left[\begin{pmatrix} E_1 \\ \vec{p}_1 \end{pmatrix} + \begin{pmatrix} E_2 \\ \vec{p}_2 \end{pmatrix} \right]^2 = (E_1 + E_2)^2 - (\vec{p}_1 + \vec{p}_2)^2 = \\ &= m_1^2 + m_2^2 + 2E_1E_2 - 2\vec{p}_1 \cdot \vec{p}_2 \end{aligned} \tag{A.13}$$

Finally, the pair transverse momentum of the parent particle is calculated as:

$$p_{\mathrm{T,parent}}^2 = (p_{\mathrm{x},1} + p_{\mathrm{x},2})^2 + (p_{\mathrm{y},1} + p_{\mathrm{y},2})^2 \tag{A.14}$$

B

TPC and TOF Post-Calibration

This Appendix describes the TPC and TOF re-calibration procedure in experimental data and in Monte Carlo simulations.

In this procedure the sample of electron candidates passed the PID Schema "A" is used. The $n(\sigma_{\mathrm{e}}^{\mathrm{TPC}})$ and $n(\sigma_{\mathrm{e}}^{\mathrm{TOF}})$ distributions are projected in different η and p intervals in the range $|\eta| < 0.8$ and $p < 1.5$ GeV/c. The width w (in terms of detector resolution σ) and the mean m values of the electron peak are extracted by fitting the projections with two Gaussian fits (one for signal and one for background) as shown in Figs. B.1 and B.2. Good overall quality of the fit expressed in terms of χ^2 per degree of freedom is found in each $p - \eta$ bin. The mean and width values extracted in this way are shown in Fig. B.3 for $n(\sigma_{\mathrm{e}}^{\mathrm{TPC}})$ and in Fig. B.4 for $n(\sigma_{\mathrm{e}}^{\mathrm{TOF}})$ on left panels. In order to suppress the statistical fluctuations, these $p - \eta$ maps are smoothed in $p > 1.0$ GeV/c range.

No significant dependence of such correction maps on data-taking period has been found. To re-calibrate the initial detector parametrisation of $n(\sigma_{\mathrm{e}}^{\mathrm{DET}})$ distribution, the obtained m and w values are applied to the data according to the following transformation:

$$n(\sigma_{\mathrm{e}}^{\mathrm{DET}}) \rightarrow \frac{n(\sigma_{\mathrm{e}}^{\mathrm{DET}}) - m}{w}. \tag{B.1}$$

As it can be seen in Figs. B.3 and B.4 on the right panels, both the mean and the width values of $n(\sigma_{\mathrm{e}}^{\mathrm{TPC}})$ and $n(\sigma_{\mathrm{e}}^{\mathrm{TOF}})$ distributions are close to ideal case of $m = 0$ and $w = 1$ after re-calibration. The mean values are also found to be stable and close

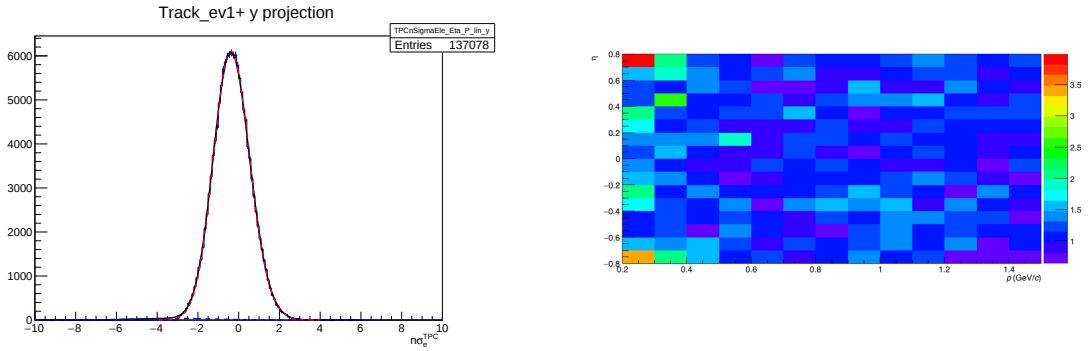

Figure B.1: Example of $n(\sigma_{\mathrm{e}}^{\mathrm{TPC}})$ distribution fit (in $-0.2 < \eta < -0.1$ and in $0.3 < p < 0.4$ GeV/c interval, left) and χ^2 of the fit in all $p - \eta$ bins (right).

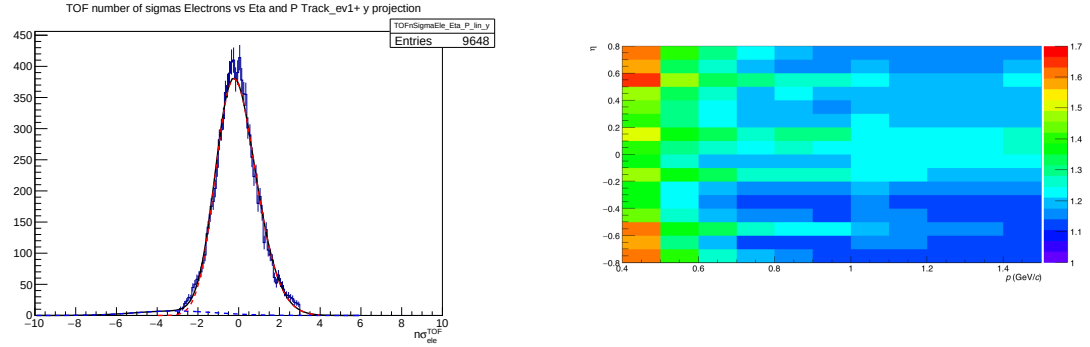

Figure B.2: Example of $n(\sigma_{\mathrm{e}}^{\mathrm{TOF}})$ distribution fit (in $-0.1 < \eta < 0.0$ and in $1.2 < p < 1.3$ GeV/c interval, left) and χ^2 of the fit in all $p - \eta$ bins (right).

to zero as a function of run number after the re-calibration procedure as it is shown in Fig. B.5.

Similar re-calibration procedure of TOF PID response is applied for the Monte Carlo simulations, for which the corresponding mean and width values of $n(\sigma_{\mathrm{e}}^{\mathrm{TOF}})$ distribution are shown in Fig. B.6. The values show different behaviour with respect to the one observed in data (Fig. B.4). The results of the re-calibration procedure are shown in Fig. B.6 on the right side.

For MC simulations, the re-calibration procedure of $n(\sigma_{\mathrm{e}}^{\mathrm{TPC}})$ values is implemented as a part of analysis framework when one analyses MC data with a so-called "tuneOnData" option enabled. It takes into account the parameterisations of expected signals (TPC "splines") of the corresponding data-taking period, which are extracted directly from the experimental data and sampled (according to a parameterised resolution) to

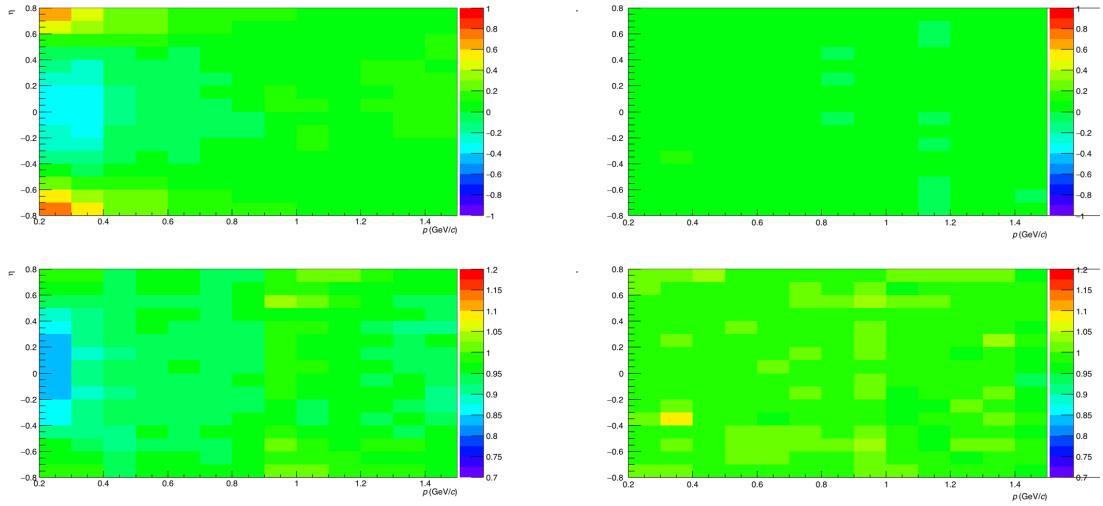

Figure B.3: Mean (top panels) and width (bottom panels) values of $n(\sigma_{\mathrm{e}}^{\mathrm{TPC}})$ distribution as a function of p and η. The results before and after the re-calibration are shown on the left and on the right, correspondingly.

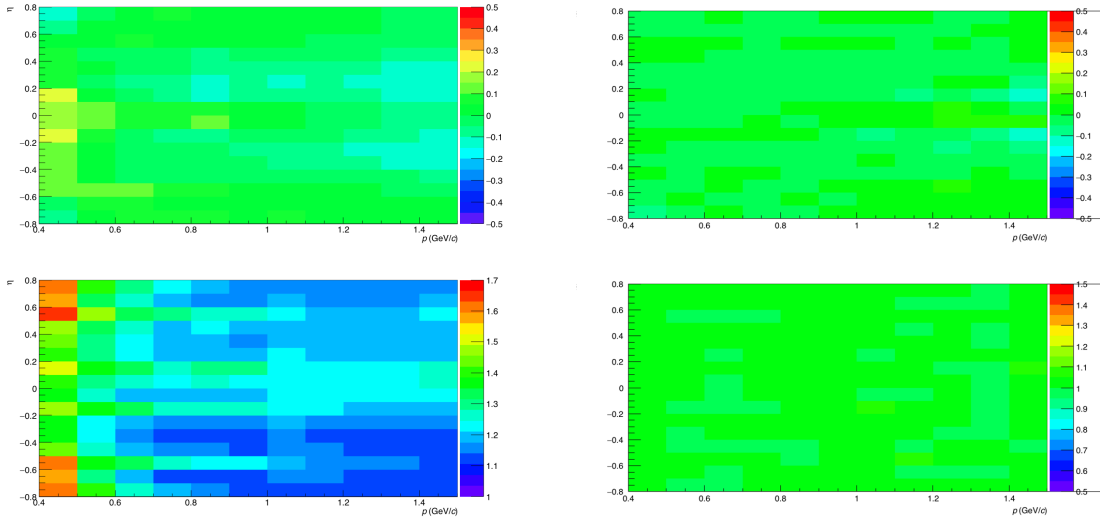

Figure B.4: Mean (top panels) and width (bottom panels) values of $n(\sigma_{\mathrm{e}}^{\mathrm{TOF}})$ distribution as a function of p and η. The results before and after the re-calibration are shown on the left and on the right, correspondingly.

generate a gaussian PID signal around them. The corresponding $n(\sigma_{\mathrm{e}}^{\mathrm{TPC}})$ values are found to be close to the perfect case and stable vs run number (Fig. B.7).

The PID re-calibration procedure is also applied in the analysis of high-multiplicity

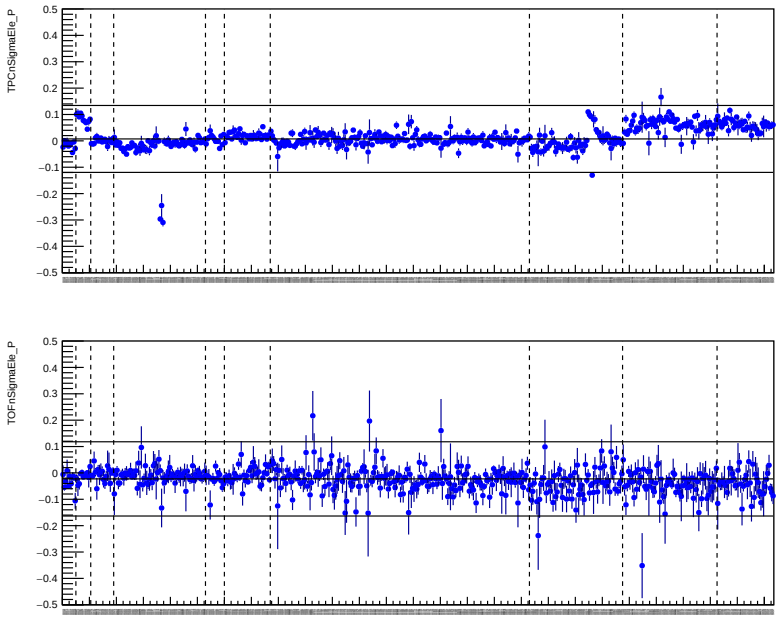

Figure B.5: The mean $n(\sigma_{\mathrm{e}}^{TPC})$ (top panel) and $n(\sigma_{\mathrm{e}}^{\mathrm{TOF}})$ (bottom panel) values in experimental data as a function of run number after re-calibration.

data sample. No significant dependence of correction maps on multiplicity has been found, and the correction maps extracted from the minimum-bias data sample are also used in high-multiplicity data analysis.

As a result of re-calibration procedure, the TPC and TOF PID information is consistent between the experimental data and the Monte Carlo simulations, and the mean and width values show stable behaviour as a function of run number, track momentum and pseudorapidity. The re-calibration procedure impact on the corrected dielectron spectrum is found to be $\sim$6% in the very low-mass range below $100\ \mathrm{MeV}/c^2$ and non-significant at higher masses. As it was mentioned in Section 3.6.3, any possible uncertainties introduced by re-calibration procedure are included in the uncertainty shown in Fig. 3.55.

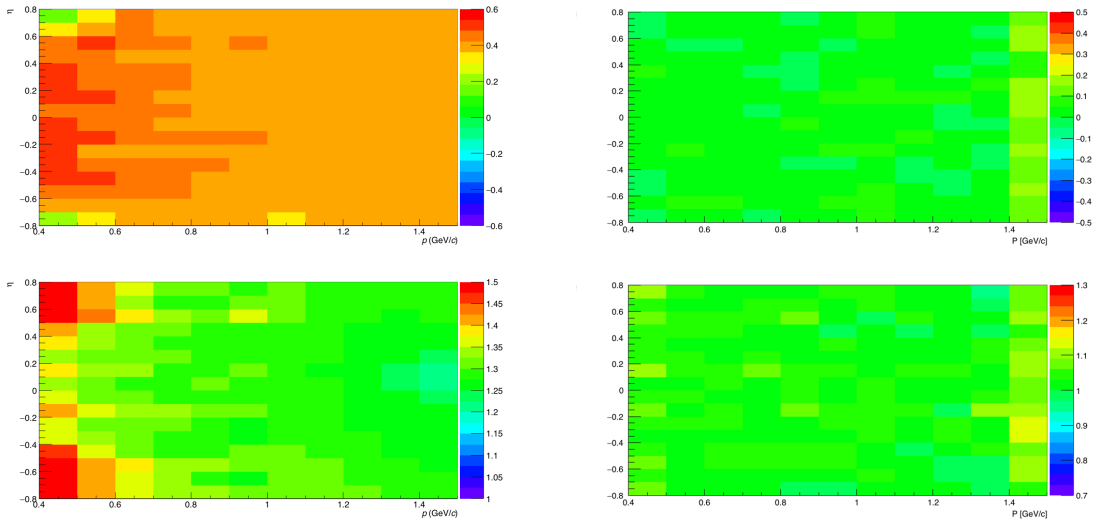

Figure B.6: Mean (top panels) and width (bottom panels) values of $n(\sigma_{\mathrm{e}}^{\mathrm{TOF}})$ distribution as a function of p and η in MC simulations. The results before and after re-calibration are shown on the left and on the right, correspondingly.

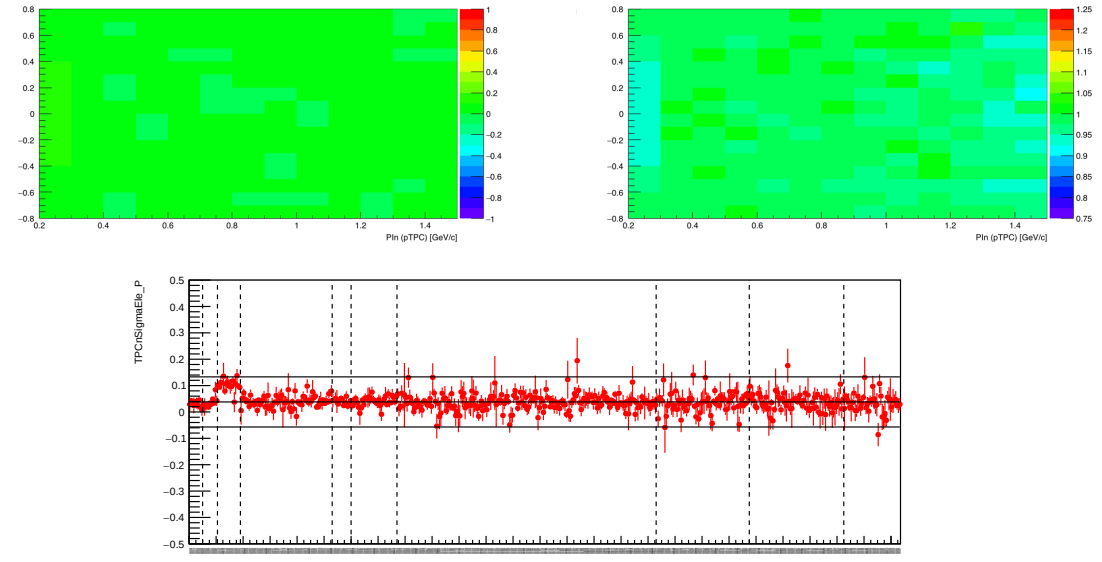

Figure B.7: Mean (top left) and width (top right) of $n(\sigma_{\mathrm{e}}^{\mathrm{TPC}})$ as a function of p and η in Monte Carlo data with "TuneOnData" option enabled. Bottom panel shows the behaviour of the mean value as a function of run number.